

AN ABSTRACT OF THE DISSERTATION OF

Valmikanathan Onbattuvelli for the degree of Doctor of Philosophy in
Industrial Engineering presented on December 9, 2010.

Title: The Effects of Nanoparticle Addition on the Processing, Structure and
Properties of SiC and AlN

Abstract approved:

Sundar Atre

Silicon carbide (SiC) and aluminum nitride (AlN) exhibit a combination of thermal and mechanical properties that are relevant to applications in electronics, aerospace, defense and automotive industries. However, the successful translation of these properties into final applications lies in the net-shaping of these ceramics into fully dense microstructures. Increasing the packing density of the starting powders is one effective route to achieve high sintered density and dimensional precision. The current research presents an in-depth study on the effects of nanoparticle addition on the powder injection molding (PIM) of SiC and AlN powder-polymer mixtures. In particular, bimodal mixtures of nanoscale (n) and sub-micrometer (μ) particles were

found to have significantly increased powder packing characteristics (solids loading) in the powder-polymer mixtures.

The influence of nanoparticle addition on the multi-step PIM process was examined by comparing the rheological and thermal properties of the novel bimodal μ -n powder-polymer mixtures to conventional monomodal μ powder-polymer mixtures. Additionally, the effect of nanoparticle addition on the mold filling behavior of the powder-polymer mixtures was examined. Subsequently, the effects of increased powder content and reduced particle size owing to nanoparticle addition were studied in the context of the polymer removal kinetics. Finally, nanoparticle addition was found to expedite the liquid phase formation during the sintering stage. The sintered parts of bimodal μ -n mixtures exhibited higher sintered densities, lower shrinkage and better thermal properties than the corresponding monomodal powder mixtures. The above results provide new perspectives which could impact a wide range of materials, powder processing techniques and applications.

© Copyright by Valmikanathan Onbattuvelli

December 9, 2010

All Rights Reserved

The Effects of Nanoparticle Addition on the Processing, Structure and Properties of
SiC and AlN

by
Valmikanathan Onbattuvelli

A DISSERTATION

submitted to

Oregon State University

in partial fulfillment of
the requirements for the
degree of

Doctor of Philosophy

Presented December 9, 2010

Commencement June 2011

Doctor of Philosophy dissertation of Valmikanathan Onbattuvelli presented
on December 9, 2010.

APPROVED:

Major Professor, representing Industrial Engineering

Head of the School of Mechanical, Industrial and Manufacturing Engineering

Dean of the Graduate School

I understand that my dissertation will become part of the permanent collection of Oregon State University libraries. My signature below authorizes release of my dissertation to any reader upon request.

Valmikanathan Onbattuvelli, Author

ACKNOWLEDGEMENTS

The completion of this dissertation would not have been accomplished without the support and guidance of Dr. Sundar Atre. I am very grateful to Dr. Sundar Atre whose tutelage provided the opportunity to do this research work and the drive to do stuff which I would not have done otherwise. Covering a wide spectrum of research areas, I received technical contributions from the inter-disciplinary research groups in OSU, industrial collaborators, academic and national lab partners. I would like to take this opportunity to thank each of them for their support to my research.

I am very thankful to Dr. John Simonsen for guiding me through the use of torque rheometry and for his support to my research. I would like to thank Dr. Skip Rochefort in helping me master the thermogravimetric analysis and differential scanning calorimetry techniques which played a predominant role in my research. Special thanks to Dr. Bill Warnes and David Cann for allowing me use their instrumentation facility to measure mechanical properties. I thank Dr. Mas Subramanian for helping with the thermal conductivity measurements. I would like to thank Teresa Sawyer in training me on the SEM facility. I would like to extend my gratitude to Sriram Ramamoorthi, James Eilertsen, Dan Foster, Negar Monfared, Grant Kim and Greg Purdy for their support during this work.

My sincere thanks to Dr T.S. Sudarshan of Materials Modification Inc., (Fairfax, VA) for his continuous financial and technical support during my PhD program. I am very thankful to Dean Elliott and Linda Campbell of Entek Extruders (Lebanon, OR) for their technical support in feedstock scale-up process. I am very grateful to Tim McCabe, Joel Strong and Laureano Gonsalves of Kinetics Inc., (Wilsonville, OR) in helping me perform pilot scale injection molding cycles at their facility. I am thankful to Sachin Laddha and Kevin Simmons of PNNL (Richland, WA) for helping me with the sintering experiments. I also thank Dr. Seong Jin Park and Dr. Randall M. German with their invaluable guidance throughout the research. Finally, I thank all my lab mates, fellow graduate students and my friends who were responsible for great ideas, useful discussions and constant support.

TABLE OF CONTENTS

<u>Chapter</u>		<u>Page</u>
1	Introduction.....	1
2	Review on net shape fabrication techniques for silicon carbide and aluminum nitride.....	4
2.1	Introduction.....	5
2.2	Net-shaping of thermally conducting ceramics.....	7
2.2.1	Ceramic injection molding.....	7
2.2.2	Field assisted sintering.....	8
2.2.3	Pyrolysis of cast pre-ceramic polymers.....	9
2.3	Literature review on the densification of SiC and AlN.....	10
2.3.1	Material parameters.....	10
2.3.2	Process parameters.....	12
2.4	Conclusions.....	14
2.5	References.....	14
3	Sintering nanoscale powders.....	47
3.1	Introduction.....	48
3.2	Nanoscale powder consolidation processes.....	49
3.2.1	Field assisted compaction.....	49
3.2.2	Microwave sintering.....	50
3.2.3	Explosion/shock wave compaction.....	51
3.3	Attributes of nanoscale powder sintering.....	51
3.3.1	Material Parameters.....	53
3.3.2	Process parameters.....	54
3.4	Sintering models.....	55

TABLE OF CONTENTS (continued)

<u>Chapter</u>		<u>Page</u>
3.5	Structure –property relationships for sintered nanoscale powders	60
3.5.1	Hardness and yield strength.....	60
3.5.2	Creep resistance.....	61
3.5.3	Superplasticity.....	61
3.5.4	Thermal diffusivity.....	61
3.6	Potential application of sintered nanoscale powders.....	62
3.7	Future trends.....	63
3.7.1	Material informatics.....	63
3.7.2	Integration of bulk synthesis with nanoscale powder processing	63
3.8	Concluding remarks.....	64
3.9	References.....	65
4	The effect of nanoparticle addition on the solids loading of SiC and AlN powder-polymer mixtures.....	86
4.1	Introduction.....	87
4.2	Experimental section.....	87
4.2.1	Materials.....	87
4.2.2	Instrumentation.....	88
4.2.3	Torque rheometry- experimental procedure.....	88
4.3	Results and discussion.....	89
4.4	Conclusions.....	93
4.5	References.....	93
5	The effect of nanoparticle addition on the properties of SiC and AlN feedstocks for powder injection molding.....	116
5.1	Introduction.....	117

TABLE OF CONTENTS (continued)

<u>Chapter</u>		<u>Page</u>
5.2	Experimental section.....	118
5.2.1	Materials.....	118
5.2.2	Feedstock formulation and scale-up.....	118
5.2.3	Instrumentation.....	118
5.3	Results and discussion.....	119
5.3.1	Thermal properties.....	119
5.3.2	Rheological properties.....	119
5.3.3	PVT measurements.....	121
5.3.4	Injection molding simulations.....	122
5.4	Conclusions.....	123
5.5	References.....	124
6	The effect of nanoparticle addition on binder removal from injection molded SiC and AlN.....	145
6.1	Introduction.....	146
6.2	Experimental section.....	147
6.2.1	Materials.....	147
6.2.2	Sample preparation.....	147
6.2.3	Debinding procedure.....	147
6.3	Results and discussion.....	148
6.3.1	Confirmation Studies.....	148
6.3.2	Effect of nanoparticle addition on the solvent debinding kinetics	149
6.3.3	Thermal debinding of solvent debound samples.....	150
6.4	Conclusions.....	151
6.5	References.....	151

TABLE OF CONTENTS (continued)

<u>Chapter</u>		<u>Page</u>
7	The effect of nanoparticle addition on the densification and properties of SiC.....	172
7.1	Introduction.....	173
7.2	Experimental section.....	174
7.2.1	Materials.....	174
7.2.2	Sample preparation.....	174
7.2.3	Instrumentation.....	174
7.3	Results and discussion.....	174
7.4	Conclusions.....	178
7.5	References.....	178
8	The effect of nanoparticle addition on the sintering and properties of AlN.....	196
8.1	Introduction.....	197
8.2	Experimental section.....	198
8.2.1	Materials.....	198
8.2.2	Sample preparation.....	198
8.2.3	Characterization.....	198
8.3	Results and discussion.....	198
8.4	Conclusions.....	201
8.5	References.....	202
9	Conclusions and future work.....	215
9.1	Conclusions.....	215
9.1.1	Powder bimodality.....	215
9.1.2	Properties of powder-polymer mixtures.....	215
9.1.3	Polymer removal of injection molded bimodal samples.....	216

TABLE OF CONTENTS (continued)

<u>Chapter</u>		<u>Page</u>
9.1.4	Densification and properties of bimodal μ -n SiC.....	216
9.1.5	Densification and properties of bimodal μ -n AlN.....	217
9.2	Directions for future research.....	217
9.2.1	Effect of varying the binder composition.....	217
9.2.2	Effect of varying the initial particle size.....	217
9.2.3	Effect of nanosized sintering additives.....	218
9.2.4	Green micromachining of injection molded bimodal samples.....	218
9.2.5	Extension of powder bimodality concept to other systems.....	218
9.2.6	Densification of bimodal μ -n SiC and AlN under pressure and electric field.....	219
9.3	References.....	219
	Appendix.....	228

LIST OF FIGURES

<u>Figure</u>		<u>Page</u>
2.1	Schematic of a plasma-pressure compaction apparatus.....	21
2.2	The effect of initial particle size on the densification and fracture toughness of SiC.....	22
2.3	Densification of SiC with an initial particle size, a. 0.42 μm (sintered grain size: 0.7 μm), b. 0.5 μm (sintered grain size: 1.1 μm) and c. 0.7 μm (sintered grain size: 1.5 μm), indicating that the smaller particle size leads to finer microstructures.....	23
2.4	The effect of using different SiC polytypes over the microstructure indicating that the aspect ratio of the grains increases with increase in β -SiC content.....	24
2.5	The effect of initial β -SiC content (wt.%) on fracture toughness and flexural strength.....	25
2.6	The effect of different sintering additives on the density and thermal conductivity of AlN.....	26
2.7	The effect of sintering additive concentration on the thermal conductivity of SiC and AlN.....	27
2.8	Processing window for sintering conditions for SiC(a) and AlN (b).....	28
2.9	Growth of SiC grains with increment in the sintering temperature; a. 1850 $^{\circ}\text{C}$, b. 1875 $^{\circ}\text{C}$, c. 1900 $^{\circ}\text{C}$, d. 1950 $^{\circ}\text{C}$	30
2.10	The effect of sintering temperature on the weight loss experienced during SiC sintering.....	31
2.11	Growth of AlN grains with an increase in the hold time (1830 $^{\circ}\text{C}$); a. 25 min, b. 100 min, c. 240 min, d. 720 min.....	32
2.12	The effect of hold time on the size and aspect ratio of SiC grains pressureless sintered at 1950 $^{\circ}\text{C}$	33
2.13	SiC sintering at 1700 $^{\circ}\text{C}$ for 1 hr by plasma pressure compaction with an external pressure of a. 10MPa, b. 30 MPa, c. 50 MPa.....	34
2.14	β -SiC sintered at 1950 $^{\circ}\text{C}$ for 60 minutes in, a. Ar and b. N ₂	35

LIST OF FIGURES (continued)

<u>Figure</u>	<u>Page</u>
3.1 An example of integrating bulk synthesis with nanoscale powders consolidation.....	76
4.1 Torque rheometry plot for 100% μ -AlN (a) and 100% μ -SiC (b) with the insets showing the resulting mixtures.....	97
4.2a Effect of n-AlN addition to μ -AlN on the maximum powder fraction in the powder-polymer mixture.....	98
4.2b Effect of n-SiC addition to μ -SiC on the maximum powder fraction in the powder-polymer mixture.....	99
4.3 Comparison of powder packing behavior in monomodal (a) and bimodal (b) AlN powder-polymer mixtures.....	100
4.4 Comparison of powder packing behavior in monomodal (a) and bimodal (b) SiC powder-polymer mixtures.....	101
4.5 Effect of nanoparticle addition on the mixing torque of AlN(a) and SiC(b) powder-polymer mixtures.....	102
4.6 Viscosity of extruded monomodal (a) and bimodal (b) AlN powder-polymer mixtures at different shear rate and temperature combinations, exhibiting pseudo-plastic behavior.....	103
4.7 Viscosity of extruded monomodal (a) and bimodal (b) SiC powder-polymer mixtures at different shear rate and temperature combinations, exhibiting pseudo-plastic behavior.....	104
4.8 Viscosity of the binder mixture at different shear rate and temperature combinations.....	106
4.9a Comparison of viscosity (calculated by the Krieger-Dougherty model) as a function of solids loading for monomodal and bimodal AlN powder-polymer mixtures at 160 °C for the shear rates of (i) 800/s, (ii) 400/s and (iii) 160/s.....	107
4.9b Comparison of viscosity (calculated by the Krieger-Dougherty model) as a function of solids loading for monomodal and bimodal SiC powder-polymer mixtures at 160 °C for the shear rates of (i) 800/s, (ii) 400/s and (iii) 160/s.....	108

LIST OF FIGURES (continued)

<u>Figure</u>	<u>Page</u>
4.10a Comparison of viscosity (calculated by the simplified Krieger-Dougherty model) as a function of solids loading for monomodal and bimodal AlN powder-polymer mixtures at 160 °C for the shear rates of (i) 800/s, (ii) 400/s and (iii) 160/s.....	109
4.10b Comparison of viscosity (calculated by the simplified Krieger-Dougherty model) as a function of solids loading for monomodal and bimodal SiC powder-polymer mixtures at 160 °C for the shear rates of (i) 800/s, (ii) 400/s and (iii) 160/s.....	110
4.11a Comparison of viscosity (calculated by the modified Eiler's model) as a function of solids loading for monomodal and bimodal AlN powder-polymer mixtures at 160 °C for the shear rates of (i) 800/s, (ii) 400/s and (iii) 160/s.....	111
4.11b Comparison of viscosity (calculated by the modified Eiler's model) as a function of solids loading for monomodal and bimodal SiC powder-polymer mixtures at 160 °C for the shear rates of (i) 800/s, (ii) 400/s and (iii) 160/s.....	112
5.1 DSC of the monomodal and bimodal SiC (a) and AlN (b) feedstocks	127
5.2 TGA of the monomodal and bimodal SiC (a) and AlN (b) feedstocks	128
5.3 Viscosity of monomodal (a) and bimodal (b) SiC feedstocks at different shear rate and temperature combinations, displaying pseudo-plastic behavior.....	129
5.4 Viscosity of monomodal (a) and bimodal (b) AlN feedstocks at different shear rate and temperature combinations, confirming its pseudo-plastic behavior.....	130
5.5 Comparison of powder packing behavior in monomodal (a) and bimodal (b) SiC feedstocks.....	131
5.6 Comparison of powder packing behavior in monomodal (a) and bimodal (b) AlN feedstocks.....	132
5.7 PVT relationship for monomodal (a) and bimodal (b) SiC feedstocks	133
5.8 PVT relationship for monomodal (a) and bimodal (b) AlN feedstocks	134
5.9 Progressive filling pattern during the injection molding of monomodal SiC feedstock at 170°C, (a) 25% fill, (b) 50% fill, (c): 75% fill and (d) 100% fill.....	135

LIST OF FIGURES (continued)

<u>Figure</u>	<u>Page</u>	
5.10	Fill time vs. injection temperature for all feedstocks, revealing that nanoparticle addition slows the mould filling process.....	136
5.11	Melt velocity vs. injection temperature for all feedstocks indicating that nanoparticle addition slows down the melt's fluidity thereby increasing the mould fill time.....	137
5.12	Shear stress at the wall vs. injection temperature for all feedstocks, indicating that nanoparticle addition increases the shear stress on the walls.....	138
5.13	Multi-slotted parts injection molded with the monomodal SiC feedstock.....	139
6.1	Effect of immersion time on the solvent debinding of monomodal μ -SiC samples with different Ψ ratios at (a) RT, (b) 40 °C and (c) 60 °C	154
6.2	Effect of immersion time on the solvent debinding of monomodal μ -AlN samples with different Ψ ratios at (a) RT, (b) 40 °C and (c) 60 °C	155
6.3	The effect of immersion time on the solvent debinding of bimodal μ -n SiC samples with different Ψ ratios at (a) RT, (b) 40 °C and (c) 60 °C	156
6.4	The effect of immersion time on the solvent debinding of bimodal μ -n AlN samples with different Ψ ratios at (a) RT, (b) 40 °C and (c) 60 °C	157
6.5	TGA runs on solvent-debound monomodal μ - SiC (a) and μ -AlN (b) samples ($\Psi = 1.22/\text{mm}$) indicating the increasing removal of soluble binder components with increased immersion time.....	158
6.6	TGA runs on solvent-debound bimodal μ -n SiC (a) and μ -n AlN (b) samples ($\Psi = 1.22/\text{mm}$) indicating the increasing removal of soluble binder components with increased immersion time.....	159
6.7	SEM micrographs of monomodal μ -SiC samples ($\Psi = 1.22/\text{mm}$) after debinding in heptane at 60 °C as function of immersion time.....	160
6.8	SEM micrographs of monomodal μ -n SiC samples ($\Psi = 1.22/\text{mm}$) after debinding in heptane at 60 °C as function of immersion time.....	161
6.9	SEM micrographs of monomodal μ -AlN samples ($\Psi = 1.22/\text{mm}$) after debinding in heptane at 60 °C as function of immersion time.....	162

LIST OF FIGURES (continued)

<u>Figure</u>	<u>Page</u>
6.10 SEM micrographs of monomodal μ -n AlN samples ($\Psi = 1.22/\text{mm}$) after debinding in heptane at 60 °C as function of immersion time.....	163
6.11 The effect of solids loading on the permeability of monomodal and bimodal SiC (a) and AlN (b) samples.....	164
6.12 Diffusion coefficients as a function of solvent temperature for SiC (a) and AlN (b) samples ($\Psi = 1.22/\text{mm}$).....	165
6.13 Diffusion coefficients as a function of solvent temperature for the SiC (a) and AlN (b) samples ($\Psi = 0.64/\text{mm}$).....	166
6.14 Diffusion coefficients as a function of solvent temperature for the SiC (a) and AlN (b) samples ($\Psi = 0.52/\text{mm}$).....	167
7.1 Processing window for sintering conditions for SiC based on literature reports.....	182
7.2 Effect of sintering temperatures on the densification of bimodal (a) and monomodal (b) SiC.....	183
7.3 SEM images revealing the transition of bimodal SiC samples from thermally debound stage to the onset of liquid phase formation, (a) 500 °C, (b) 1100 °C, (c) 1300 °C and (d) 1550 °C.....	184
7.4 SEM images revealing the transition of monomodal SiC samples from thermally debound stage to the onset of liquid phase formation, (a) 500 °C, (b) 1100 °C, (c) 1300 °C and (d) 1550 °C.....	185
7.5 Weight loss experienced by bimodal (a) and monomodal (b) SiC as a function of sintering temperature.....	186
7.6 Isometric shrinkage of bimodal (a) and monomodal (b) SiC as a function of sintering temperature.....	187
7.7 Vickers hardness of bimodal (a) and monomodal (b) SiC as a function of sintering temperature.....	188
7.8 Indentation toughness of bimodal (a) and monomodal (b) SiC as a function of sintering temperatures.....	189
7.9 Thermal diffusivity of bimodal (a) and monomodal (b) SiC as a function of sintering temperatures.....	190
7.10 Cp of bimodal (a) and monomodal (b) SiC as a function of sintering temperatures.....	191

LIST OF FIGURES (continued)

<u>Figure</u>	<u>Page</u>
7.11 Thermal conductivity of bimodal (a) and monomodal (b) SiC as a function of sintering temperatures.....	192
8.1 Effect of sintering temperature on the pressureless densification of AlN.....	205
8.2 SEM images revealing the transition of bimodal AlN samples from thermally debound stage to the onset of liquid phase formation.....	206
8.3 SEM images revealing the grain growth in the bimodal AlN samples with the increase in the sintering temperatures.....	207
8.4 Effect of sintering temperature on weight loss during AlN densification.....	208
8.5 Effect of sintering temperature on shrinkage during AlN densification	209
8.4 Effect of sintering temperature on weight loss during AlN densification.....	208
8.5 Effect of sintering temperature on shrinkage during AlN densification	209
8.6 Thermal diffusivity of AlN samples as a function of sintering temperature.....	210
8.7 Cp of AlN samples as a function of sintering temperature.....	211
8.8 Thermal conductivity of AlN samples as a function of sintering temperature.....	212
8.9 Mechanical properties of bimodal AlN samples as a function of sintering temperature.....	213
9.1 Nanorod formation in monomodal AlN at 1100 °C (a) and monomodal SiC at 1550 °C (b).....	221
9.2 Micromachined green bimodal μ -n AlN samples.....	222
9.3 Sintered micromachined bimodal μ -n AlN samples.....	223
9.4 Global market for powder injection molded products.....	224
9.5 SEM micrographs of sintered microchannels (a), microgrids (b) and microwells (c) net-shaped by PIM of bimodal μ -n BaTiO ₃	225

LIST OF TABLES

<u>Table</u>	<u>Page</u>
2.1 Characteristics of SiC polytypes.....	36
2.2 Quantitative comparison of the properties of thermally conducting ceramics.....	37
2.3 Comparison of the processing of organic binders and pre-ceramic polymers.....	38
2.4 Comparison of ceramic net-shaping processes.....	39
2.5 Prior reports on additive-assisted sintering of SiC.....	40
2.6 Prior reports on additive-assisted sintering of AlN.....	43
2.7 Pros and cons of applying external pressure to densify SiC and AlN.....	46
3.1 Chemical methods for synthesizing ceramic nanoparticles.....	78
3.2 Comparison of the ceramic net-shaping processes.....	79
3.3 Effects of material and process parameters on densification and grain growth for conventional processes.....	80
3.4 Effect of materials and process parameters on densification and grain growth for recent processes.....	81
3.5 The effect of particle size and specific area on green density.....	82
3.6 Example of nanoscale sintering models.....	83
3.7 Applications of sintering models.....	84
4.1 Conditions used for scaling up of SiC and AlN powder-polymer mixtures.....	113
4.2 Slopes of the viscosity plots of powder-polymer mixtures and binders representing the power law coefficient “n” values.....	114
4.3 Comparison of experimental and theoretical Φ_c values for SiC and AlN powder-polymer mixtures.....	115

LIST OF TABLES (continued)

<u>Table</u>	<u>Page</u>
5.1	Properties of sintered SiC and AlN ceramics..... 140
5.2	Comparison of the net-shaping processes for SiC and AlN..... 141
5.3	Conditions used for scaling up of SiC and AlN feedstocks..... 142
5.4	Values of different rheological constants for SiC and AlN feedstocks... 143
5.5	PVT coefficients for SiC and AlN Feedstocks..... 144
6.1	Literature review on binder formulations used in the multi-step debinding process..... 168
6.2	Composition of SiC and AlN samples tested in the current study..... 169
6.3	Dissolution and diffusion coefficients of monomodal and bimodal SiC and AlN samples at room temperature with different aspect ratios..... 170
6.4	The effect of hold time on the % residual weight of the SiC and AlN samples during the thermal debinding..... 171
7.1	Literature review on the liquid phase formation temperature for SiC densification..... 193
7.2	Prior reports on additive-assisted pressureless sintering of SiC..... 194
7.3	Prior reports on the mechanical properties of monomodal SiC..... 195
8.1	Literature review on YAG formation temperature for AlN densification 214
9.1	Elemental composition of nanorods formed during the monomodal AlN sintering..... 226
9.2	Elemental composition of nanorods formed during the sintering of monomodal SiC..... 227

I dedicate this dissertation to
my Onbattuvelli and Rogers family

CHAPTER 1

Introduction

Silicon carbide (SiC) and aluminum nitride (AlN) have a useful combination of properties including high thermal conductivity, low coefficient of thermal expansion, mechanical strength and chemical inertness. In order to translate these properties into demanding applications in electronic, energy and transportation sectors, it is necessary to develop net shaping processes that result in fully dense microstructures.

Chapter 2 of the dissertation reviews and compares the net-shaping techniques available to fabricate SiC and AlN. Among the techniques, powder injection molding (PIM) is considered to be well-suited for mass production of dimensionally precise, complex part geometries. PIM is a multi-step process that combines the processability of plastics and superior material properties of metals and ceramics to form high performance components. Ceramic or metal powder is compounded with polymers and used to mold parts in an injection molding machine, in a manner analogous to the forming of conventional thermoplastics. The molded part is then subjected to polymer removal (debinding). The debound part is then sintered under controlled time, temperature and atmospheric conditions to get the final part of desired dimensions, density, microstructure and properties. However, the successful application of PIM to SiC and AlN faces many hurdles, which are addressed in this thesis. Similar to the polymer injection molding, defects are possible in the injection-molded components. During debinding, the goal is to remove the polymers in the shortest time with the least impact on the molded part. Additionally, SiC and AlN cannot be sintered easily due to covalent bonding. Additives are used in such systems to drive the densification by forming a liquid phase. The literature review presented in the **Chapter 2** has been accepted for publication in the journal, “*Materials and Manufacturing Processes*”. The review helped in selecting the sintering additive content and sintering conditions in the present thesis.

Irrespective of the fabrication techniques, prior reports focused on achieving maximum sintered density, a precursor to sintered properties. Previous studies explored this issue by varying sintering additives and sintering conditions. The concept of powder bimodality based on nanoparticle additions is specifically explored in the current dissertation. **Chapter 3** focuses on the advantages and limitations of using nanoparticles. This detailed review on the ceramic nanoparticles has been accepted for publication as an invited chapter in the book, “*Application of Nanomaterials*” (American Scientific Publishers).

The primary focus of this dissertation is to study the effects of nanoparticle addition on the PIM of SiC and AlN. In **Chapter 4**, bimodal microscale (μ) and nanoscale (n) powder mixtures of AlN and SiC were mixed in different ratios along with a polymer phase. The effect of the nanoparticle content on powder packing was studied and the bimodal μ -n powder mixture providing the maximum powder-binder mixture density was determined. These experiments show a surprising result that mixtures of fine particles with poor packing characteristics display vastly increased powder content in the polymer mixtures. Additionally, a comparative study between the monomodal and bimodal powder-binder mixtures was performed to understand the effect of nanoparticle addition on the rheological properties. Results from **Chapter 4** were presented in international conferences including, *NSTI Nanotech 2010* and *PowderMet 2010*. A research article based on the findings reported in this chapter is currently under preparation for submission to *Journal of Nanomaterials*.

A detailed comparative study of the thermal, rheological and pressure-volume-temperature (PVT) properties of the monomodal and bimodal SiC and AlN feedstocks is presented in **Chapter 5**. Additionally, simulation studies based on the above properties on the mold filling behavior were conducted. The research work presented in **Chapter 5** has been published as a research article in the journal *PIM International* and distributed to the attendees of the Powder Metallurgy World Congress in Florence, Italy by the publisher.

A series of injection molding experiments was performed with monomodal and bimodal AlN and SiC powder-polymer mixtures. Following injection molding, the polymer phase is removed (debinding) prior to the sintering stage. In the current research, a multi-step debinding process consists of solvent debinding followed by the thermal degradation was used. This initial binder removal leaves interpenetrating pore channels through which the decomposed gas escapes during the subsequent thermal debinding step. The effect of nanoparticle addition over the solvent debinding kinetics of injection molded AlN and SiC is presented in **Chapter 6**. It was observed that the bimodal powder mixtures demonstrated reduced rates of binder removal from the injection molded SiC and AlN parts, most likely due to the reduced pore size and porosity. The work was also extended to studying the variations in the residual binder content due to nanoparticle addition during the thermal debinding cycle. The results in **Chapter 6** were published in the conference proceedings, ‘*Advances in Powder Metallurgy and Particulate Materials*’. A research article based on the findings reported in this chapter is currently under preparation for submission to *Journal of American Ceramic Society*.

Thermally debound SiC and AlN samples were sintered at different time-temperature combinations. The sintering experiments were designed based on the conditions shortlisted from the literature review (presented in **Chapter 2**). The advantage of using nanoscale sintering additives was demonstrated with a decrease in the temperature for liquid phase formation for both SiC and AlN systems relative to larger particle size sintering additives, present in the literature. In addition to the above observation, **Chapter 7** compares the densification, shrinkage, and weight loss during sintering of monomodal and bimodal SiC samples. The nanoparticle addition was found to increase relative density yet reduce the shrinkage. The sintered samples were also characterized for their mechanical and thermal properties. A research article based on the findings reported in this chapter is currently under preparation for submission to *Science of Sintering*.

Yttrium oxide (Y_2O_3) is the pre-dominantly reported sintering additive for the AlN densification. Changes in density, shrinkage, and weight loss for the bimodal AlN samples with nanosized Y_2O_3 as the additive are reported in **Chapter 8**. Results from the sintering experiments and ensuing properties were compared with the previously reported values and the effect of nanoparticle addition on the AlN system is discussed. A research article based on the findings reported in this chapter is currently under preparation for submission to *Science of Sintering*.

To conclude, all the findings from **Chapters 4-8** are summarized in the **Chapter 9** and directions for future research are presented. The experimental data discussed in the **Chapters 4 -8** are presented in the **Appendices A - I**.

CHAPTER 2

Review of Net Shape Fabrication Techniques for Silicon Carbide and Aluminum Nitride

Abstract

Silicon carbide (SiC) and aluminum nitride (AlN) have a combination of thermal and mechanical properties that are useful for applications in electronics, automotives, defense, and aerospace industries. However, successful conversion of these properties into final applications lies in the fabrication of these ceramics into fully dense microstructures. The current article reviews near-net-shape fabrication processes that have been developed to produce SiC and AlN components. In addition, prior studies on the densification of SiC and AlN are reviewed to understand the effect of materials and process parameters on the sintered microstructure and properties.

2.1. Introduction

Silicon carbide (SiC) has found many applications since the original development by Acheson in the late 19th century [1]. However, recent improvements in SiC fabrication along with property improvements such as hardness (22 GPa) have extended applications in many sectors including wear, ballistics, and automobiles [2-4]. SiC also displays high thermal conductivity (120 W/m.K) and high temperature stability (1600 °C) making it useful for linings in the foundry and glass industries [5-6]. Another emerging application of SiC is in the semiconductor industry where its wide band gap (3.2 eV) has been utilized in MOSFETs and Schottky diodes [7-8]. The semiconducting behavior of SiC has also been used in power monitors in the nuclear reactors [9].

SiC exhibits polymorphism and is reported to have more than 200 polytypes [10-11]. **Table 2.1** lists the characteristic features of the most commonly available SiC polytypes, 3-C, 4-H and 6-H [12]. The stacking sequences of Si and C in these polytypes are discussed elsewhere [11, 12]. From **Table 2.1** it can be inferred that the polytype of the starting materials affect the final properties and thus applications.

Similar to SiC, aluminum nitride (AlN) is another widely studied non-oxide ceramic. AlN has a high thermal conductivity (170 W/m.K) equivalent to Al and a low CTE ($10^{-6}/^{\circ}\text{C}$) equivalent to Si, making it useful for thermal management in electronics [13-15] and automotive industries [16-17]. Unlike SiC, AlN is reported to have only one crystal structure (Wurtzite, Hexagonal). **Table 2.2** confirms the superiority of AlN and SiC in the properties including thermal conductivity, CTE matching that of Si, electrical insulation and mechanical strength relative to other options [18-20]. Additionally, SiC and AlN do not pose health hazards compared to beryllia (BeO) in the RoHS directed global market for the electronic devices [21-22].

A key barrier for translating the tabulated properties of SiC and AlN into final applications lies in their net shaping into fully dense microstructures [23]. Extensive research has been done on fabricating SiC and AlN by slip casting [24-25], tape casting [26-27], hot pressing (HP) [28-29], hot isostatic pressing (HIP) [30-31] and cold isostatic pressing (CIP) [32-33]. Methodologies of these techniques are detailed elsewhere [34]. In addition, techniques including ceramic injection molding (CIM), plasma pressure compaction and pyrolysis of cast pre-ceramic polymers have been recently explored for the net-shaping SiC and AlN. The present review focuses on these recent methods since few reports have comparatively discussed these methods. The characteristic features of fabrication techniques along with their pros and cons from production perspectives are tabulated at the end of the section.

Achieving a high sintered density with controlled microstructure is crucial to improving the thermal and mechanical properties in SiC and AlN. Ceramic densification during net-shaping is achieved by a thermal process called sintering. During sintering, ceramic particles bond into a coherent, predominantly solid structure by mass transport [35]. This process takes place by reduction of particle surface area followed by mass transport by diffusion. The latter is enhanced by raising the temperature whereas the former depends upon surface and grain boundary energies, ϵ_s and ϵ_b respectively [36]. The ratio ϵ_b/ϵ_s for SiC and AlN is around 0.97 [37] due to covalent bonds. As ϵ_b/ϵ_s approaches unity, achieving full densification becomes difficult. Consequently, several alternative techniques have been developed to improve the densification of SiC and AlN. Fully dense SiC and AlN can be produced by the addition of sintering additives/additives. These sintering additives reduce the ϵ_b/ϵ_s ratio to below 0.7 [37] and drive densification.

Initially, the sintering of SiC was achieved by adding boron (B) and carbon (C) as sintering additives [38-40]. B reduces ϵ_b , thus providing a driving force for sintering similar to an external isostatic pressure. C increases ϵ_s by reacting with impurities such as elemental Si and SiO₂ and prevents them from impeding densification [38]. As sintering occurs by the solid-state diffusion of atoms, this mechanism is called as solid state sintering. Typical temperatures for sintering SiC using B and C as additives are around 2100 °C [38-40]. The solid-state sintering route offered the advantage of superior creep resistance at high temperatures, through retention of intrinsic properties of SiC, as dictated by its high degree of covalency (up to 85%) [38]. However, the major drawbacks of this processing method are the sintering temperatures greater than 2000°C and grain growth. These limitations were overcome by using a liquid phase sintering, a technique widely used for the past two decades.

In liquid phase sintering, sintering additives forms a liquid phase, which penetrates between the solid grains, dissolves the sinter bonds, and induces grain rearrangement. Further, because of solid solubility in the liquid, the liquid improves transport rates responsible for grain coarsening and densification. The surface energy associated with pores leads to their annihilation, while there is progressive microstructure coarsening and bonding to increase rigidity [41-42]. Liquid phase sintering of SiC and AlN has been explored in detail in the past by varying material and process parameters. The second section of the review involves a detailed tabulated literature review on the liquid phase sintering of SiC and AlN. The effects of material parameters and process conditions on the densification of these ceramics are summarized in this section. In this manner, the current work fills an important void in the literature, owing to the absence of any such prior reviews on these thermally conducting ceramics.

In addition to the density, microstructure controls the properties of sintered materials. However, the microstructure of SiC and AlN tends to evolve throughout the sintering stage. In practice, a “final” microstructure is never noticed in liquid-phase sintered materials, so what is observed is a glimpse of a slowly evolving structure [42]. With prolonged sintering, the terminal condition would consist of a single grain with an associated liquid. However, years are required to transform micrometer-sized SiC and AlN into a single grain. Thus, similar to the sintered density, microstructures of SiC and AlN can be varied depending on material parameters and process conditions. Substantial performance differences are exhibited by a ceramic with varied microstructures, especially in properties such as hardness, toughness and thermal conductivity. The current review compares the role of process conditions and methods on the microstructures and properties of sintered AlN and SiC reported in the literature.

2.2. Net-shaping of thermally conducting ceramics

Near net-shaping generally involves few/no post-sintering machining, surface preparation or cleaning prior to final application. However, there has been a great challenge to economically net-shape SiC and AlN components with closer dimensional tolerance and defect-free microstructures. As mentioned earlier, slip and tape casting and pressing are the most explored net shaping techniques on SiC and AlN until date. The current section briefs the recently investigated net-shaping techniques including ceramic injection molding (CIM) and plasma assisted powder compaction.

2.2.1. Ceramic Injection Molding (CIM)

The injection molding of ceramics is similar to metal injection molding and normally consists of five steps as follows: i) material selection ii) powder-binder compounding, iii) injection molding, iv) debinding and v) densification by sintering [43-46]. The control of each of these process steps and appropriate selection of the starting material (powder and binder) are critically important for the overall process success [18].

An initial powder-binder mixture with a high powder content (solids loading) is preferred to avoid defects and obtain parts with a low dimensional scatter [47]. A smaller particle size provides better sinterability however, the solids loading could be less due to agglomeration. On the other hand, a larger particle size exhibits lower inter-particle friction leading to slumping and shape distortion during debinding [48]. Therefore, powder selection during the materials design phase involves a careful consideration of conflicting requirements. Once the powder of suitable

size is selected, it is mixed with the binder to determine the appropriate feedstock composition. The binder is usually of multi-components – a backbone polymer that provides strength (e.g. polypropylene), a filler phase that is easily extracted in the first phase of debinding (e.g. paraffin wax) and a lubricant (e.g. stearic acid) [49-52].

Prior to powder- binder compounding, it is necessary to determine the critical solids loading (Φ_c) where the powder particles are tightly packed and all the space between particles is filled with the binder. In practice, a solids loading (Φ) (less than Φ_c) is generally selected to facilitate successful injection molding of the feedstock to minimize large fluctuations in viscosity due to small changes in powder content in highly concentrated suspensions. Following the molding stage, the binder is removed (referred to as debinding) from the part prior to sinter densification. There are various debinding routes reported until date, primarily falling under three categories: solvent [49-52], thermal [53-55] and catalytic debinding [56-57]. One or more debinding techniques are selected and their conditions are optimized, to retain the part shape without the formation of defects [23]. These debound samples are then sintered under controlled time, temperature and atmospheric conditions to get the final part of desired dimensions, density, microstructure and properties. Controlling the sintering atmosphere is also vital to avoid any oxidation at high temperature [35].

2.2.2. Field assisted sintering (FAS)

This technique covers several related processes such as plasma pressure compaction and spark plasma sintering. In this technique, the ceramic powder to be compacted is filled in a graphite die and placed between two electrodes as shown in the **Figure 2.1**. When pulsed electrical power is applied, the current does not flow freely through the powder compact since an effective current path has not yet been established due to the voids inside the powder. The oxide layer on the surface of the powder particle acts as an insulator at the particle contact. This causes a charge buildup at the inter-particle gaps between powder particles [58-61].

As charge builds up, the voltage difference becomes sufficiently large to generate sparks that trigger an ionization process [58-61]. It has been hypothesized that an inter-particle plasma is generated that activates the surface of the powder particles by removing the oxide and other contaminants. At this stage, the powder compact is heated to higher temperatures so that any adsorbed gas and/or moisture is released. This is usually indicated by a drop in the initial vacuum level [62-66]. At this stage, uniaxial pressure is applied to facilitate sufficient current path through the powder compact. The pulse current is applied until the vacuum has reached its initial

value. In the following stage, a constant current is applied to achieve the sintering temperature by Joule heating.

Direct application of the current and external uniaxial pressure accelerates densification of the material by inducing resistance heating and causing plastic deformation at the inter-particle contact surfaces [63]. The resistance heat serves to concentrate the heat at inter-particle points of contact and the concurrent application of light pressure results in densification of the compact [66]. The amount of pressure applied and direct current required to reach the sintering temperature are determined by various factors such as the conductivity of the powder, particle size and dimensions of the graphite dies used [64-66].

2.2.3. Pyrolysis of cast pre-ceramic polymers

Since the last 2 decades, organometallic compounds have been developed as precursors to ceramics. For example, non-crosslinked polysilazanes have been widely explored pre-ceramic polymers for fabricating SiC and/or Si₃N₄ ceramics [67-72]. These pre-ceramic polymers have been used in the ceramic fabrication in two modes, directly cast [67-70] or as a replacement for organic binders [71-72].

Irrespective of the modes mentioned above, it has been prescribed by prior reports to crosslink the oligomeric polysilazane to an infusible solid [68-69]. Compounds such as dicumyl peroxide, potassium hydride, platinum and lithium based organo-metallic compounds have been used as initiators for cross-linking at various concentrations [71-73]. The crosslinking of polysilazane occur by vinyl polymerization, dehydro-coupling or desilylization, which are detailed elsewhere [73-74]. The cross-linked samples are then pyrolyzed to form the ceramics, a step similar to that of thermal debinding in CIM. The pyrolyzed sample is then sintered at different conditions to form the final SiC part. An important advantage of this technique is the ability to cast pre-ceramic polymers of relatively low viscosity into complex shapes. However, the inability to retard the formation of Si₃N₄/SiC composite constitutes an important limitation of the technique [70]. **Table 2.3** lists the pros and cons of using polysilazane as the replacement for the organic binders in the SiC fabrication.

With the capability of CIM and FAS as production level methods, it is necessary to compare their pros and cons with already existing pressing and slip/tape casting techniques. **Table 2.4** lists the characteristics features of various fabrication techniques to net-shape SiC and AlN. From the table, CIM can be the method of choice for economically fabricating complex geometries at a high production rate. For relatively simple shapes and smaller production throughputs, FAS and

HIP can be chosen to fabricate SiC ceramics to provide enhanced densification and greater control over grain size. Additional research on pre-ceramic polymers is required in order to develop niche applications.

2.3. Literature review on the densification of SiC and AlN

Irrespective of the net-shaping techniques discussed in the previous section, achieving a high sintered density is crucial to realizing the property benefits of SiC and AlN. Thus, in addition to the fabrication techniques, prior investigations explored the densification behavior of SiC and AlN. The literature review presented in the **Tables 2.5** and **2.6**, summarizes the effects of several material and process parameters on the densification of SiC and AlN [75-128].

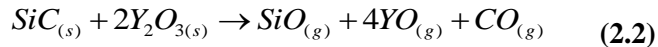
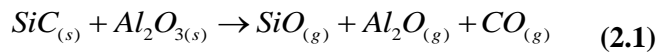
2.3.1. Material Parameters:

Variations in the materials used for SiC and AlN sintering can be broadly classified as starting ceramic powders and sintering additives. Starting particle size and polytype (in SiC) are two important powder variations that have been studied in the past. For example, Y.W. Kim et al [87] (**Figure 2.2**) studied the effect of starting particle size on SiC densification and inferred that the smaller particles provide higher sintered density. Under similar sintering conditions, the smaller SiC particles led to a finer microstructure as final grain growth during hot-pressing was reduced. As shown in the **Figure 2.3**, the grain size tends to increase with increasing particle size and has a positive impact on fracture toughness (**Figure 2.5**). These results can also be extended to the speculation that involvement of smaller SiC particles might achieve higher hardness due to higher grain boundaries.

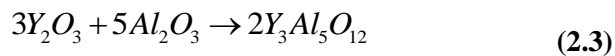
The effect of using different SiC polytypes on the final microstructure and properties was studied by Nader et al [102]. For a given sintering temperature-hold time combination, an Ar atmosphere was found to support the transformation of β -SiC into elongated α -SiC grains (**Figure 2.4b**). Additionally, increasing the β -SiC content in the initial powder mixture resulted in α -SiC grains of high aspect ratio (**Figure 2.4c**). For comparison, samples prepared with pure α -SiC reveals a globular microstructure as shown in the **Figure 2.4a**. Similar to the results observed by Y.W. Kim et al [87], a higher aspect ratio of SiC grains (lesser grain boundaries) leads to higher fracture toughness and flexural strength as shown in the **Figure 2.5**. In summary, smaller size α -SiC when sintered under Ar atmosphere leads to finer microstructures with larger grain boundaries and thus can be utilized for higher hardness applications. On contrary, applications

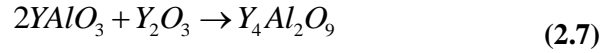
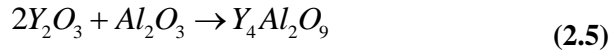
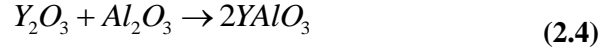
involving higher fracture toughness and flexural strength can be achieved by transforming β -SiC into long aspect ratio α -SiC grains under Ar atmosphere.

As mentioned earlier, sintering additives are generally used to drive the densification of SiC and AlN. The effects of varying the composition and amount of sintering additives on the densification, microstructure and properties of SiC and AlN have been analyzed in detail in the past. For example, Y. Zhou et al compared the efficiency of different rare earth additives as the sintering aid for SiC [86]. Zhou et al concluded that Y_2O_3 when combined with Al_2O_3 forms a better sintering aid for SiC compared to other alternatives including La_2O_3 , Yb_2O_3 and Nd_2O_3 . However, the other rare earths also yielded relative density $> 98\%$ for SiC. It was concluded that the densification of the SiC powder with all Al_2O_3 - RE_2O_3 (RE - La, Nd, Y, Yb) additives proceeded by the same solution-precipitation mechanism (Ostwald ripening). During heating, Al_2O_3 - RE_2O_3 mixtures and the surface SiO_2 react and form rare earth alumino-silicate glass melt. Subsequently, with the dissolution of the small SiC particles, the resulting liquid could be regarded as RE-Si-Al-O-C glass melt. On cooling, the RE-Si-Al-O-C constituted the intergranular phases in the SiC ceramics. Even though widely used for SiC densification, Al_2O_3 - Y_2O_3 has been reported to have a few limitations. She and Ueno [89], Grande et al [92], Guo et al [93], Suzuki and Sasaki [96] report the secondary reactions (*Equations 2.1-2.2*) of Al_2O_3 with SiC at sintering temperatures to form gaseous species leading to weight loss and formation of new pores. Using AlN- Y_2O_3 as a sintering aid has been suggested as a partial solution to the weight loss problem by Biswas et al [75] and Rixecker et al [101], where the presence of excess Al_2O_3 is avoided.



Yoshioka et al [24], Surnev et al [26] and Du et al [27] conducted a similar research on the AlN densification. **Table 2.6** lists several sintering additives that have been studied in the literature. In particular, Y_2O_3 and CaO have been widely studied sintering additives for the AlN system and have been compared by Molisani et al [119]. The common sintering mechanism involves the reaction of Y_2O_3 or CaO with the Al_2O_3 layer on the surface of the AlN particles forming secondary phases that promote the densification at lower temperatures than AlN without additive. *Equations 2.3-2.7* explain the formation of major liquid phase, yttrium aluminum garnet (YAG) ($Y_3Al_5O_{12}$) and other secondary phases by reacting Y_2O_3 and Al_2O_3 .





The lowest reported eutectic temperatures in Y_2O_3 - Al_2O_3 and CaO - Al_2O_3 systems are around 1760 °C and 1390 °C, respectively [119]. Considering that the sintering temperature decreases with diminishing liquid-phase formation temperature, it is expected that AlN with CaO may achieve full density at significantly lower temperatures than AlN with Y_2O_3 . However, it has been observed that both AlN with Y_2O_3 and CaO reach full density around 1800°C. These results have shown that the densification of AlN with CaO additive is slow, even though its liquid phase formation temperature is low. Additional research by Molisani et al [121] indicated that CaO tends to exhibit weight loss forming new pores at sintering temperatures. These pores are detrimental to the sintered density and thus final properties. For example, Surnev et al compared the effect of different sintering additives on the density and thermal conductivity of AlN [26]. From **Figure 2.6**, it can be seen that Y_2O_3 promotes nearly full AlN densification with a thermal conductivity > 110 W/m.K.

The densification of SiC and AlN is affected by not only the chemistry but also the amount of sintering additive. Panchula and Ying [124] and Olhero et al [128] studied the effect of varying the sintering aid content on the densification of AlN. Both reports suggested that while increasing sintering additive amounts increase densification, they can be detrimental to properties due to a higher secondary phase content. This observation was confirmed by Lopez et al where the presence of excessive inter-granular glassy phase reduced the thermal conductivity, hardness and fracture toughness of the sintered SiC samples [91]. A similar behavior was noticed in the Al_2O_3 - Y_2O_3 system by L.S.Sigl (104), She and Ueno [89], and Surnev et al [26] (**Figure 2.7**). From the prior reports, it can be concluded that 4-5 wt. % of Y_2O_3 and 10 wt. % of AlN- Y_2O_3 are preferred amounts of sintering additives for the AlN and SiC densification, respectively [75-128].

2.3.2. Process Parameters:

Liquid phase sintering has typically been reported to be initiated with the formation of eutectic, yttrium aluminum garnet (YAG) at 1720-1760 °C for both SiC and AlN. The eutectic formation is followed by microstructural coarsening primarily by solution-precipitation (Ostwald ripening), where larger grains grow at the expense of the smaller ones [129]. H. Xu et al proposed

a model for coarsening in liquid phase sintered SiC [97]. The relatively high positive curvature of the smaller grains is thought to provide the driving force for their preferential dissolution, setting up a concentration gradient in the liquid phase. This results in the diffusion of the dissolved species towards the larger grains, and their reprecipitation onto those larger grains. Thus, the grain growth/sintering kinetics is controlled by two factors, temperature and time making them the most studied process parameters in SiC and AlN densification.

From prior reports, processing windows were constructed for short-listing the sintering conditions for SiC (**Figure 2.8a**) and AlN (**Figure 2.8b**). The sintering temperatures are in the range of 1800-2000 °C for SiC and 1700-1900 °C for AlN with upto 4 hrs hold time each. For example, Magnani et al [95] (**Figure 2.9**) reported an increase in the grain size of SiC with sintering temperature. Liquid phase formation and the grain growth also accompany the elimination of pores leading to dimensional shrinkage. Such a mechanism was confirmed by an increase in the AlN density with the increase in the sintering temperature as reported by Li et al [115] and Zhou et al [123]. In contrast, She and Ueno [89] reported a reduction in the sintered density by increasing the sintering temperature above a certain temperature. The side reactions of sintering additives (along with their amount) explained in Equations 2.1 and 2.2 leading to new pore formation at sintering temperatures might thus be detrimental for the densification. Such a negative impact of elevating the sintering temperature over the densities of SiC have also been reported by Izhevskiy et al [88], Grande et al [92] and Rixecker et al [101] (**Figure 2.10**).

As mentioned in the introduction section, the microstructure tends to evolve throughout the sintering stage, because of which, Xu et al [120] (**Figure 2.11**), Nakano et al [126] for AlN and Ye et al [85], Rodriguez et al [109] for SiC, reported the positive impact of sintering time over the grain growth. For example, Rodriguez et al (**Figure 2.12**) reported that the SiC grain size has nearly tripled with the hold time of 7 hrs [109]. Additionally, Kume et al noticed an increase in the AlN density with hold time at the sintering temperature [122].

Another parameter studied from the processing perspective for the SiC and AlN densification is the role of pressure during sintering. Pressing (HP, HIP), fielded assisted sintering (FAS) and pressureless sintering are the widely investigated sintering techniques. **Table 2.7** reviews the pros and cons of these techniques. For components with geometric intricacies such as those produced by CIM, pressureless sintering is the best-suited sintering technique. In addition, even though application of external pressure reduces the influence of hold time, it limits the grain growth. The retarded grain growth with pressure reported by Bothara (**Figure 2.13**) [105] in plasma pressure compacted SiC can thus be used for high hardness applications. On the other hand, grain growth

reported in pressureless sintered AlN (**Figure 2.11**) and SiC (**Figure 2.12**) can be preferred for thermal management applications.

Argon and nitrogen atmospheres have generally been used in the past for sintering SiC and AlN, respectively [75-128]. However, when sintering β -SiC in an N₂ atmosphere, nitrogen dissolves into the liquid-stage intergranular phase as well as into the SiC grains. The dissolved N₂ helps to stabilize the β -SiC, thereby suppressing the $\beta \rightarrow \alpha$ phase transformation responsible for the anisotropic grain growth. Thus, as reported by Ortiz et al in the **Figure 2.14**, N₂ atmosphere can be used to retard the grain growth of the β -SiC [98].

2.4. Conclusions

The net-shaping of SiC and AlN to fully dense microstructures will ensure maximum sintered property levels and facilitate a wide range of applications. Processing techniques including ceramic injection molding and field-assisted sintering have been reviewed for the fabrication of SiC and AlN parts. In addition, a review on the effects of material parameters on the densification of SiC and AlN examined the chemistry and amount of sintering additives. Processing windows were constructed to shortlist the sintering conditions for SiC and AlN. This review is expected to facilitate the selection of fabrication routes for achieving final properties by tuning the microstructure with the variations in the process parameters.

2.5. References

1. S. Raman, S.C. Agbaraji, *International Journal of Advanced Manufacturing Technology*, 2009, vol. 44(3-4), pp. 293-305
2. M. Flinders, D. Ray, A. Anderson, R.A. Cutler, *Journal of the American Ceramic Society*, 2005, vol. 88(8), pp. 2217-2226
3. A. Rendtel, B. Moessner, K.A. Schwetz, *29th International Conference on Advanced Ceramics and Composites*, Florida, USA, 2005
4. R. White, *Automotive Industries*, Dec. 2006, pp. -NA-
5. A.N. Pick, *Journal of British of Ceramic Society*, 1979, vol. 78(4), pp.13-15
6. K. Pelissier, T. Chartier, J.M. Laurent, *Ceramics International*, 1998, vol. 24(5), pp. 371–377
7. T. McNutt, S. VanCampen, A. Walker, K. Ha, C. Kirby, M. Sherwin, R. Singh, H. Hearne, *Materials Science Forum*, 2009, vol. 600, pp. 951-954
8. M. O'Neill, *Power Electronics Technology*, 2008, vol. 34 (9), pp. 14-19
9. F.H. Ruddy, J.U. Patel, J.G. Williams, *Proceedings of the Space Nuclear Conference*, California, USA, 2005
10. R. Verma, P. Krishna, *P. Polymorphism and Polytypism in Crystals*; John Wiley: New York, USA, 1966
11. W.F. Knippenberg, *Philips Research Reports*, 1963, vol.18, pp.161-174

12. Y.S. Park, *SiC Materials and Devices*; Academic Press: San Diego, USA, 1998
13. K.H. Lin, Y.C. Lin, S.T. Lin, *Journal of Materials Processing Technology*, 2008, vol. 201, pp. 701-705
14. A.F. Junior, D. Shanafield, *Journal of Materials Science: Materials in Electronics*, 2005, vol. 16, pp. 139-144
15. E.S. Lee, S.M. Lee, D. J. Shanefield, W.R. Cannon, *Journal of American Ceramic Society*, 2008, vol. 91, pp.1169-1174
16. A. Okada, *Journal of the European Ceramic Society*, 2008, vol.28(5), pp. 1097-1104
17. N. Kuramoto, K. Takada, *Key Engineering Materials*, 2003, vol.247, pp. 467-472
18. M.H. Bocanegra-Bernal, B. Matovic, *Materials Science and Engineering A*, 2009, vol. 500, pp. 130–149
19. M. Mazaheri, A.M. Zahedi, M.M. Hejazi, *Materials Science and Engineering A*, 2008, vol. 492(1-2), pp. 261-267
20. A.Z.A., Azhar, M.M. Ratnam, Z.A. Ahmad, *Materials Science and Technology*, 2010, vol. 26(1), pp. 95-103
21. A. Profumo, G. Spini, L. Cucca, M. Pesavento, *Talanta*, 2002, vol. 57, pp. 929–934
22. A.B. Stefaniak, M.D. Hoover, G.A. Day, A.A. Ekechukwu, G.E. Whitney, C.A. Brink, R.C. Scripsick, *Journal of ASTM International*, 2005, vol. 2(10), pp. 325-339
23. R.M. German, A. Bose, *Injection Molding of Metal and Ceramics*; MPIF Publ: New Jersey, USA, 1997
24. T. Yoshioka, Y. Makino, S. Miyake, H. Mori, *Journal of Alloys and Compounds*, 2006, vol. 408, pp. 563–567
25. T.S., Suzuki, Y. Sakka, *Scripta Materialia* 2005, vol.52, pp. 583-586
26. S. Surnev, D. Lepkova, A. Yoleva, *Materials Science and Engineering B*, 1991, vol.10(3) pp. 5-40
27. S. Du, Z. Liu, L.. Li, Z. Gui, *Materials Letters*, 1995, vol. 25, pp. 105-109
28. X. Luo, J. Li, B. Zhang, W. Li, H. Zhuang, *Journal of American Ceramic Society*, 2006, vol. 89(3), pp. 836-841
29. Y. Wu, Y. Liu, H. Zhou, *Materials Chemistry and Physics*, 1998, vol. 56, pp. 271-274
30. X.L., Li, H.A. Ma, Y.J. Zheng, Y. Liu, G.H. Zuo, W.Q., Liu, J.G. Li, X. Jia, *Journal of Alloys and Compounds*, 2008, vol.463, pp. 412–416
31. J.K. Lee, H. Tanaka, H. Kim, D.J. Kim, *Materials Letters*, 1996, vol. 29, pp. 135-142
32. M. Medraj, Y. Baik, W.T. Thompson, R.A.L. Drew, *Journal of Materials Processing Technology*, 2005, vol.161, pp. 415–422
33. M. Fukushima, Y. Zhou, Y. Yoshizawa, *Journal of Membrane Science*, 1999, vol. 339, pp. 78–84
34. G. Dowson, *Powder Metallurgy-The process and its products*; Adam Hilger: New York, USA, 1990
35. R.M. German, *Sintering Theory and Practice*; John Wiley and Sons, Inc.: New York, USA, 1996.
36. Y. Inomata, *Proceeding of International Symposium on Ceramic Components for Engine*, pp. 253, S. Somiy, Eds., KTK Scientific Publishers: Tokyo, 1984
37. Y. Uemura, Y. Inomata, Z. Inoue, *Journal of Materials Science*, 1981, vol. 95(9), pp. 2333-2335
38. S. Prochazka, *Ceramics for High-Performance Applications*, Proc.2nd Army Materials Technology Conference, Hyannis, MS, 1973, pp. 239–52
39. W. Bocker, H. Hausner, *Powder Metallurgy International*, 1978, vol.10(2), pp. 87-89
40. L. Stobierski, A. Gubernat, *Ceramics International*, 2003, vol.29, pp. 287-292
41. R.M. German, *Liquid Phase Sintering*; Plenum Publication: New York, USA, 1985
42. R.M. German, P. Suri, S.J. Park, *Journal of Materials Science*, 2009, vol. 44, pp. 1–39

43. T.P. Vielma, A. Cervera, B. Levenfeld, A. Varez, *Journal of the European Ceramic Society*, 2008, vol. 28(4), pp. 763-771
44. I. Krindges, R. Andreola, C.A. Perottoni, J.E. Zorzi, *International Journal of Applied Ceramic Technology*, 2008, vol. 5(3), pp. 243-248
45. J.E. Zorzi, C.A. Perottoni, J.A.H. Da Jornada, *Industrial Ceramics*, 2003, vol. 23(1), 47-49
46. S.E. Lin, *Ceramics International*, 2001, vol. 27(2), pp. 205-214
47. D.M.O. Liu, W.J. Tseng, *Journal of Materials Science*, 2000, vol. 35(4), pp. 1009-1016
48. R.M. German, *Reviews in Particulate Materials*, 1993, vol.1, pp. 109-60
49. R.V.B. Oliveira, V. Soldi, M.C. Fredel, A.T.N Pires, *Journal of Materials Processing Technology*, 2005, vol.160, pp. 213–220
50. M.T. Zaky, *Journal of materials science*, 2004, vol. 39(10), pp. 3397-3402
51. B. Zhu, X. Qu, Y. Tao, *Journal of Materials Processing Technology*, 2003, vol.142, pp. 487–492
52. M.A. Omar, R. Ibrahim, M.I. Sidik, M. Mustapha, M. Mohamad, *Journal of Materials Processing Technology*, 2003, vol. 140, pp. 397–400
53. A. Bandyopadhyay, S.C. Danforth, A. Safari, *Journal of Materials Science*, 2000, vol. 35, pp. 3983-3988
54. S. Ying, Y.C. Lam, S.C.M. Yu, K.C. Tam, *Metallurgical and Materials Transactions B*, 2002, vol. 33(3), pp. 477-488
55. M. Trunec, J. Cihlar, *Journal of European Ceramic Society*, 2002, vol. 22 (13), pp. 2231-2241
56. J. Ebenhoch, J.T. Maat, *Advances in Powder Metallurgy and Particulate Materials*, 1993, no.5, pp. 45-56
57. G. Fu, N.H. Loh, S.B. Tor, B.Y. Tay, Y. Murakoshi, R. Maeda, *Applied Physics A: Materials Science and Processing*, 2005, vol. 81(3), pp. 495-500
58. X. Xiong, Z.Y. Fu, H. Wang, F. Quan, *Journal of Material Science*, 2006, vol. 41, pp. 2537-2539
59. K.A. Khor, K.H. Cheng, L.G. Yu, F. Boey, *Materials Science and Engineering A*, 2003, vol. 347, pp. 300-305
60. X. He, F. Ye, H. Zhang, L. Liu, *Journal of Alloys and Compounds* 2009, vol. 482, pp. 345-348
61. K.A. Khor, L.G. Yu, Y. Murakoshi, *Journal of the European Ceramic Society*, 2005, vol. 25, pp. 1057–1065
62. T.S. Srivatsan, A.S. Naruka, B.G. Ravi, T.S. Sudarshan, M. Petraroli, L. Riester, *Powder Metallurgy*, 2002, vol. 45(3), pp. 255-260
63. M. Bothara, S.V. Atre, S.J. Park, R.M. German, T.S. Sudarshan, R. Radhakrishnan, *NSTI Nanotech 2007*, vol.4, pp. 494-497
64. B.G. Ravi, O.A. Omotaye, T.S. Srivatsan, M., Petraroli, T.S. Sudarshan, *Journal of Alloys and Compounds*, 2000, vol.299, pp. 292-296
65. T.S. Srivatsan, B.G. Ravi, A.S. Naruka, M. Petraroli, L. Riester, T.S. Sudarshan, *Powder Technology*, 2001, vol.114(1-3), pp. 136-144
66. T.S. Srivatsan, R. Woods, M. Petraroli, T.S. Sudarshan, *Powder Technology*, 2002, vol. 122(1), pp. 54-60
67. L.A. Liew, Y. Liu, R. Luo, T. Cross, L. An, V.M. Bright, M.L. Dunn, J.W. Daily, R. Raj, *Sensors and Actuators, A: Physical*, 2002, vol. 95(2-3), pp. 120-134
68. C. Haluschka, H.J. Kleebe, R. Franke, R. Riedel, *Journal of European Ceramic Society*, 2000, vol. 20 (9), pp. 1355-1364
69. C. Haluschka, C. Engel, R. Riedel, *Journal of European Ceramic Society*, 2000, vol. 20 (9), pp. 1365-1374

70. Zemanová, M., Lecomte, E., Sajgalík, P., Riedel, R. *Journal of European Ceramic Society*, 2002, vol. 22 (16), pp. 2963-2968
71. M.F. Gonon, G. Fantozzi, M. Murat, J. P. Disson, *Journal of European Ceramic Society*, 1995, vol. 15(6), pp. 185-190
72. M.F. Gonon, S. Hampshire, *Journal of European Ceramic Society*, 1999, vol. 19(3), pp. 285-291
73. G. Ziegler, H.J. Kleebe, G. Motz, H. Müller, S. Traül, W. Weibelzahl, *Materials Chemistry and Physics*, 1999, vol. 61, pp. 55-63
74. M.F. Gonon, S. Hampshire, J. P. Disson, G.A. Fantozzi, *Journal of European Ceramic Society*, 1995, vol.15(7), pp. 683-688
75. K. Biswas, J. Schneider, G. Rixecker, F. Aldinger, *Scripta Materialia*, 2005, vol. 53, 591-596
76. Y. Zhou, K. Hirao, K. Watari, Y. Yamauchi, S. Kanzaki, *Journal of the European Ceramic Society*, 2004, vol. 24, pp. 265-270
77. D. Sciti, D., A. Bellosi, *Journal of Materials Science*, 2000, vol. 35, pp. 3849-3855
78. S.G. Lee, W.H. Shim, J.Y. Kim, Y.W. Kim, W.T. Kwon, *Journal of Material Science Letters*, 2001, vol. 20, pp. 143-146
79. Y.W. Kim, Y.S. Chun, T. Nishimura, M. Mitomo, Y.H. Lee, *Acta Materialia*, 2007, vol. 55, pp. 727-736
80. B.V. Manoj Kumar, M.H. Roh, Y.W. Kim, W. Kim, S.W. Park, W.S. Seo, *Journal of Materials Science*, 2009, vol. 44, pp. 5939-5943
81. M. Balog, K. Sedlackova, P. Zifcak, J. Janega, *Ceramics Silikáty*, 2005, vol. 49, pp. 259-262
82. Y. Lee, Y.W. Kim, M. Mitomo, *Journal of American Ceramic Society*, 2003, vol. 86(10), pp. 1803-1805
83. Y.W. Kim, M. Mitomo, T. Nishimura, *Journal of American Ceramic Society*, 2002, vol. 85(4), pp. 1007-1009
84. X. He, Y. Guo, Z. Yu, Y. Zhou, D. Jia, *Materials Science and Engineering A*, 2009, vol. 527, pp. 334-338
85. H. Ye, V.V. Pujar, N.P. Padture, *Acta Materialia*, 1999, vol. 47(2), pp. 481-487
86. Y. Zhou, K. Hirao, M. Toriyama, Y. Yamauchi, S. Kanzaki, *Journal of American Ceramic Society*, 2001, vol. 84(7), pp. 1642-1644
87. Y.W. Kim, J.Y. Kim, S.H. Rhee, D.Y. Kim, *Journal of the European Ceramic Society*, 2000, vol. 20, pp. 945-949
88. V.A. Izhevskiy, A.H.A. Bressiani, J.C. Bressiani, *Journal of American Ceramic Society*, 2005, vol. 88, pp. 1115-1121
89. J.H. She, K. Ueno, *Materials Research Bulletin*, 1999, vol. 34, pp. 1629-1636
90. J. Gao, H. Xiao, H. Du, *Journal of Materials Science Letters*, 2002, vol.21, pp. 1835-1837
91. O.B. Lopez, A.L. Ortiz, F. Guiberteau, *Journal of American Ceramic Society*, 2005, vol.88(8), pp. 2159-2163
92. T. H. Grande, H. Sommerset, E. Hagen, K. Wiik, M.A. Einarsrud, *Journal of American Ceramic Society*, 1997, vol.80(4), pp. 1047-1052.
93. X.Z. Guo, H. Yang, *Journal of Zhejiang University Science*, 2005, vol.6B(3), pp. 213-218
94. V.V. Pujar, R.P., Jensen, N.P. Padture, *Journal of Materials Science Letters*, 2000, vol.19, pp. 1011-1014
95. G. Magnani, L. Beaulardi, L. Pilotti, *Journal of the European Ceramic Society*, 2005, vol.25, pp. 1619-1627
96. K. Suzuki, M. Sasaki, *Journal of the European Ceramic Society*, 2005, vol.25, pp. 1611-1618
97. H. Xu, T. Bhatia, S.A. Deshpande, N.P. Padture, *Journal of American Ceramic Society*, 2001, vol.84(7), pp. 1578-1584

98. A.L. Ortiz, A.M. Bernabe, O.B. Lopez, A.D. Rodriguez, F. Guiberteau, N.P. Padture, *Journal of the European Ceramic Society*, 2004, vol.24, pp. 3245-3249
99. M.F. Zawrah, M.F., L. Shaw, *Ceramics International*, 2004, vol.30, pp. 721–725
100. X. Guo, H. Yang, L. Zhang, X. Zhu, *Ceramics International*, 2010, vol.36, pp. 161–165
101. G. Rixecker, K. Biswas, I. Wiedmann, F. Aldinger, *Journal of Ceramic Processing Research*, 2009, vol.1(1), pp. 12-19
102. M. Nader, F. Aldinger, M.J. Hoffmann, *Journal of Materials Science*, 1999, vol. 34, pp. 1197-1204
103. J.K. Lee, H. Tanaka, H. Kim, *Materials Letters*, 1996, vol. 29, pp.1-6
104. L.S. Sigl, *Journal of the European Ceramic Society*, 2003, vol.23, pp. 1115–1122
105. M. Bothara, *Sintering of nanocrystalline silicon carbide in plasma pressure compaction system*; PhD Thesis, Oregon State University: USA 2007
106. K. Wetzel, G. Rixecker, G. Kaiser, F. Aldinger, *Advanced Engineering Materials*, 2005, vol. 7(6), pp. 520-524
107. A. Can, M. Herrmann, D.S. McLachlan, I. Sigalas, J. Adler, *Journal of the European Ceramic Society*, 2006, vol.26, pp.1707–1712
108. M. Herrmann, R. Neher, K. Brandt, S. Hoehn, *Journal of the European Ceramic Society*, 2010, vol. 30, pp.1495-1501
109. M.C. Rodriguez, A. Munoz, A.D. Rodriguez, *Journal of the European Ceramic Society*, 2006, vol. 26, pp. 2397–2405
110. F.J. Clemens, V. Wallquist, W. Buchser, M. Wegmann, T. Graule, *Ceramics International*, 2007, vol.33, pp. 491–496
111. V. Onbattuvelli, G. Purdy, G. Kim, P. Rogers, S. Laddha, S. Atre, *Advances in Powder Metallurgy and Particulate Systems*, 2010, no.01, pp. 64-72
112. Y. Zhang, J. Han, L. Hu, *Materials Science & Engineering A*, 2008, vol.480, pp. 62-67
113. Y. Liu, H. Zhou, L. Qiao, Y. Wu, *Journal of Materials Letters*, 1999, vol. 18, pp. 703-704
114. Y. Liu, H. Zhou, Y. Wu, L. Qiao, *Materials Letters*, 2000, vol. 43(3), pp. 114-117
115. X.L. Li, H.A. Ma, G.H. Zuo, W.Q. Liu, Y.J. Zheng, J.G. Li, S.S. Li, X. Jia, *Scripta Materialia*, 2007, vol.56, pp. 1015-1018
116. H. Zhao, W. Wang, H. Wang, Z. Fu, *Journal of Wuhan University of Technology-Material Science Edition*, 2008, vol.23(6), pp. 866-869
117. J. Cheng, D. Agrawal, Y. Zhang, R. Roy, *Journal of Electroceramics*, 2002, vol.9, pp.67–71
118. J.Y. Qiu, Y. Hotta, K. Watari, *Journal of American Ceramic Society*, 2006, vol.89, pp. 377-380
119. L. Molisani, H.N. Yoshimura, H. Goldenstein, *Journal of Material Science: Material Electronics*, 2009, vol. 20, pp. 1–8
120. X. Xu, H. Zhuang, W. Li, S. Xu, B. Zhang, X. Fu, *Materials Science and Engineering A*, 2003, vol.342, pp. 104-108
121. A. L. Molisani, H.N. Yoshimura, H. Goldenstein, K. Watari, *Journal of the European Ceramic Society*, 2006, vol.26, pp. 3431–3440
122. S. Kume, M. Yasuoka, N. Omura, K. Watari, *Journal of American Ceramic Society*, 2005, vol.88, pp. 3229-3231
123. H. Zhou, Y. Liu, W. Miao, Y. Wu, *Journal of Materials Science*, 1999, vol.34, pp. 6165-6168
124. M.L. Panchula, J.Y. Ying, *Journal of American Ceramic Society*, 2003, vol. 86, pp. 1121-1127
125. C.F. Chen, M.E. Perisse, A.F. Ramirez, N.P. Padture, H.M. Chan, *Journal of Material Science*, 1994, vol. 29, pp. 1595-1600
126. H. Nakano, K. Watari, H. Hayashi, K. Urabe, *Journal of American Ceramic Society*, 2002, vol. 85(12), pp. 3093-3095.

127. L. Qiao, H. Zhou, K. Chen, K., R. Fu, *Journal of the European Ceramic Society*, 2003, vol. 23, pp. 1517–1524.
128. S.M. Olhero, P. Miranzo, J.M.F. Ferreira, *Journal of the European Ceramic Society*, 2006, vol. 26, pp. 2475–2483.
129. L.S. Sigl, H.J. Kleebe, *Journal of the American Ceramic Society*, 1993, vol. 76(3), pp. 773–776.

List of Figures

Figure 2.1: Schematic of a plasma pressure compaction apparatus

Figure 2.2: Effect of initial particle size on the densification and fracture toughness of SiC

Figure 2.3: Densification of SiC with an initial particle size, a. 0.4 μm (sintered grain size: 0.7 μm), b. 0.5 μm (sintered grain size: 1.1 μm) and c. 0.7 μm (sintered grain size: 1.5 μm), indicating that a smaller particle size leads to finer microstructures

Figure 2.4: The effect of using different SiC polytypes on the microstructure indicating that the aspect ratio of the grains increases with increase in β -SiC content

Figure 2.5: The effect of initial β -SiC content (wt.%) on fracture toughness and flexural strength

Figure 2.6: The effect of different sintering additives on the density and thermal conductivity of AlN

Figure 2.7: The effect of sintering additive concentration on the thermal conductivity of SiC and AlN

Figure 2.8a: Processing window for sintering conditions for SiC

Figure 2.8b: Processing window for sintering conditions for AlN

Figure 2.9: Growth of SiC grains with increase in the sintering temperature; a. 1850 $^{\circ}\text{C}$, b. 1875 $^{\circ}\text{C}$, c. 1900 $^{\circ}\text{C}$, d. 1950 $^{\circ}\text{C}$

Figure 2.10: The effect of sintering temperature on the weight loss experienced during SiC sintering

Figure 2.11: Growth of AlN grains with increment in the hold time at sintering temperature (1830 $^{\circ}\text{C}$); a. 25 min, b. 100 min, c. 240 min, d. 720 min

Figure 2.12: Effect of hold time over the size and aspect ratio of SiC grains pressureless sintered at 1950 $^{\circ}\text{C}$

Figure 2.13: SiC sintering at 1700 $^{\circ}\text{C}$ for 60 minutes by plasma pressure compaction with an external pressure of a. 10MPa, b. 30 MPa, c. 50 MPa'

Figure 2.14: β -SiC sintered at 1950 $^{\circ}\text{C}$ for 60 minutes in, a. Ar atmosphere, b. N_2 atmosphere

List of Tables

Table 2.1: Characteristics of SiC polytypes

Table 2.2: Quantitative comparison of the properties of ceramics

Table 2.3: Comparison of processes for organic binders and pre-ceramic polymers

Table 2.4: Comparison of ceramic net-shaping processes

Table 2.5: Prior reports on the additive-assisted sintering of SiC

Table 2.6: Prior reports on the additive-assisted sintering of AlN

Table 2.7: Pros and cons of applying external pressure to densify SiC and AlN

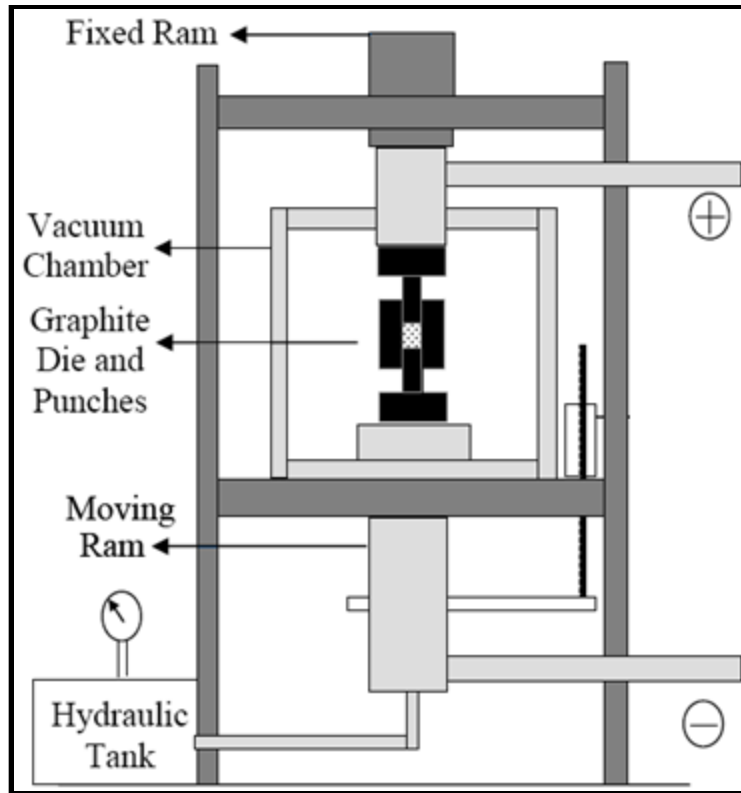


Figure 2.1: Schematic of a plasma-pressure compaction apparatus [63]

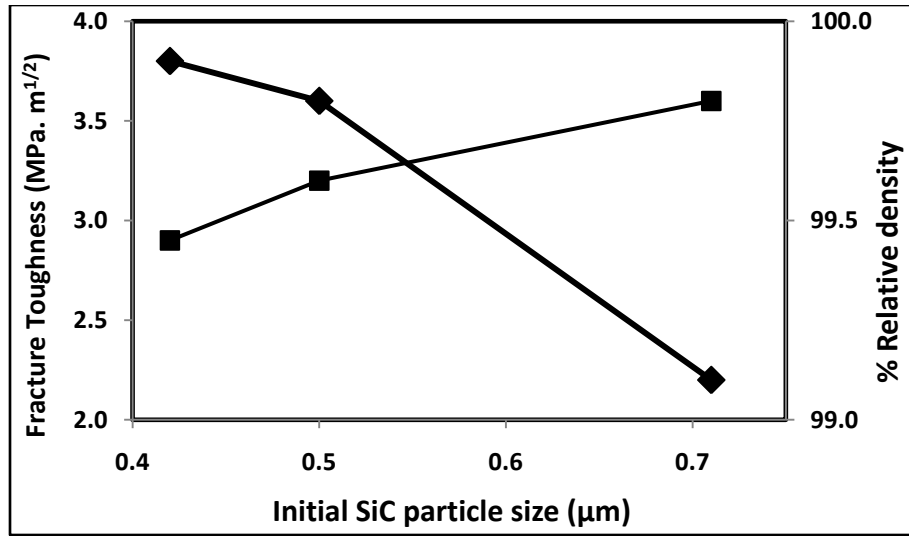


Figure 2.2: The effect of initial particle size on the densification and fracture toughness of SiC (Courtesy: Y.W. Kim et al, 2000, [87])

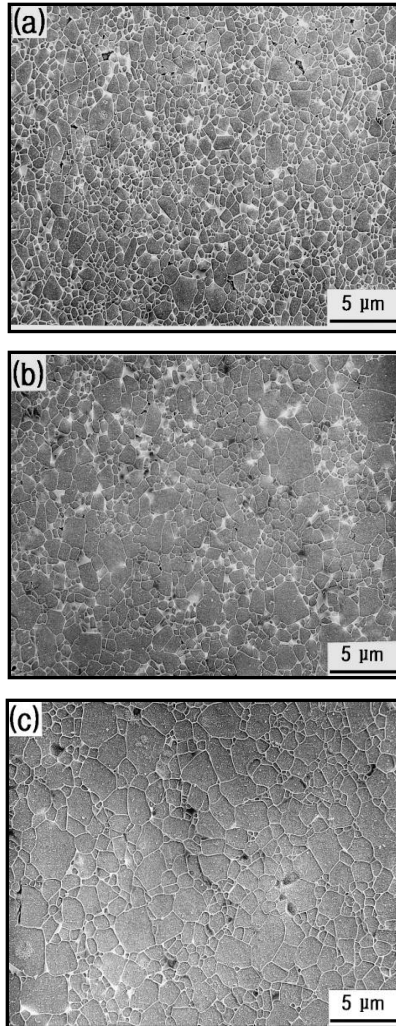


Figure 2.3: Densification of SiC with an initial particle size, a. 0.4 μm (sintered grain size: 0.7 μm), b. 0.5 μm (sintered grain size: 1.1 μm) and c. 0.7 μm (sintered grain size: 1.5 μm), indicating that a smaller particle size leads to finer microstructures (Courtesy: Y.W. Kim et al, 2000, [87]).

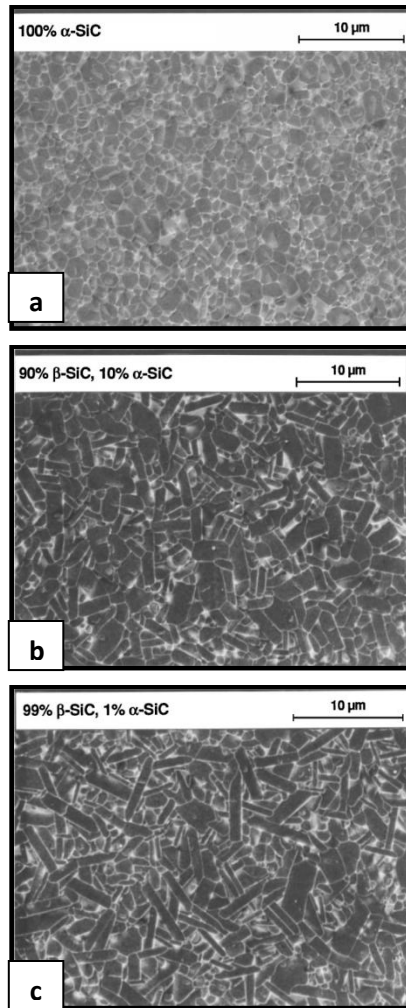


Figure 2.4: The effect of using different SiC polytypes on the microstructure indicating that the aspect ratio of the grains increases with increase in β -SiC content. (Courtesy: Nader et al, 1999, [102]).

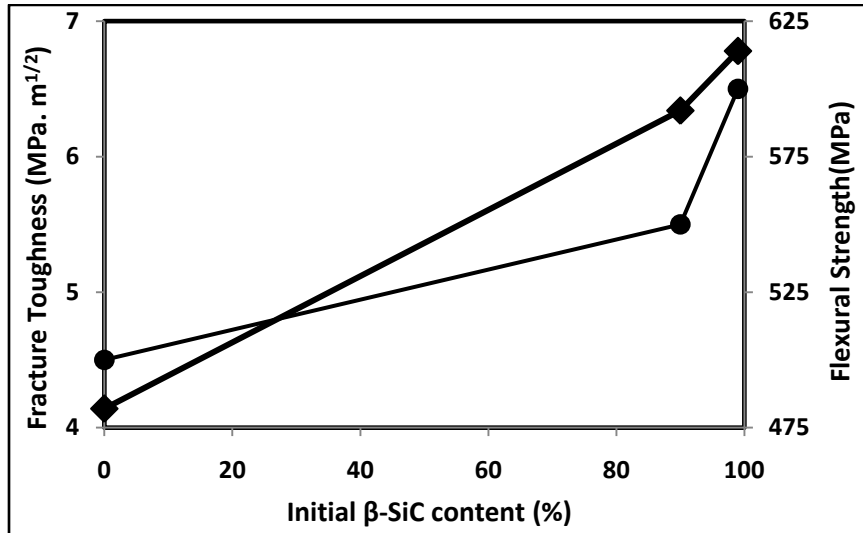


Figure 2.5: The effect of initial β -SiC content (wt.%) on fracture toughness and flexural strength (Courtesy: Nader et al, 1999, [102]).

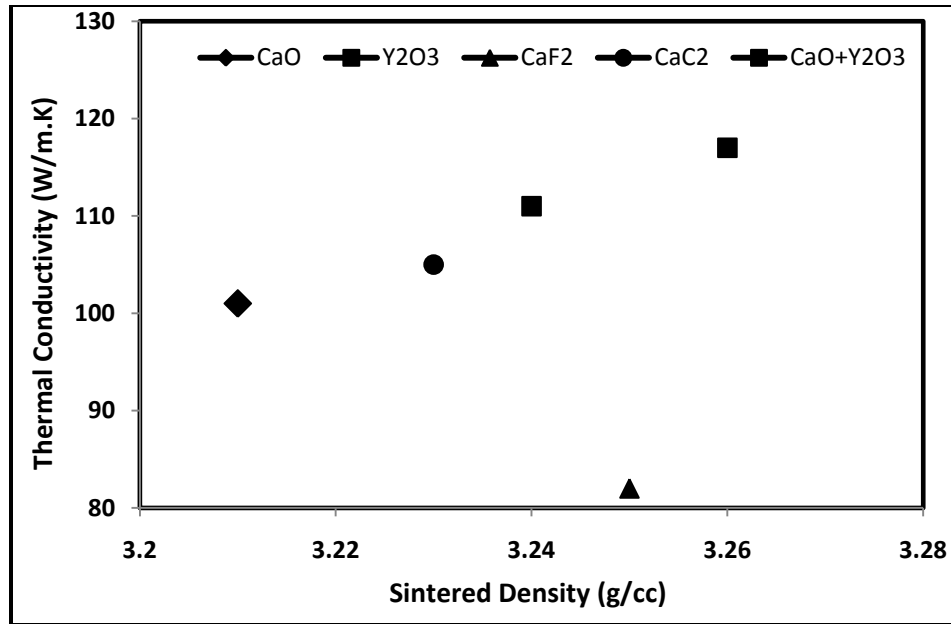


Figure 2.6: The effect of different sintering additives on the density and thermal conductivity of AlN (Courtesy: Surnev et al, 1991, [26])

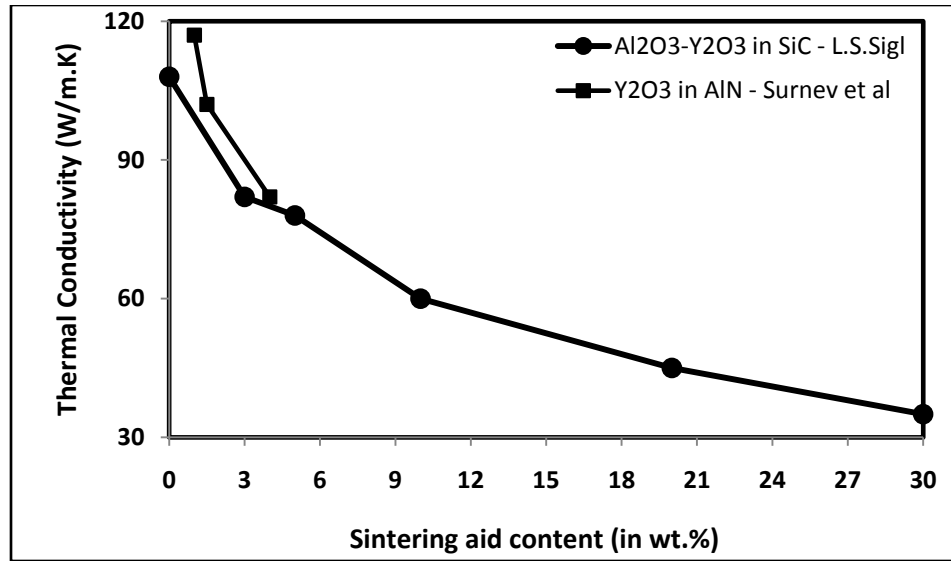


Figure 2.7: The effect of sintering additive concentration on the thermal conductivity of SiC and AlN

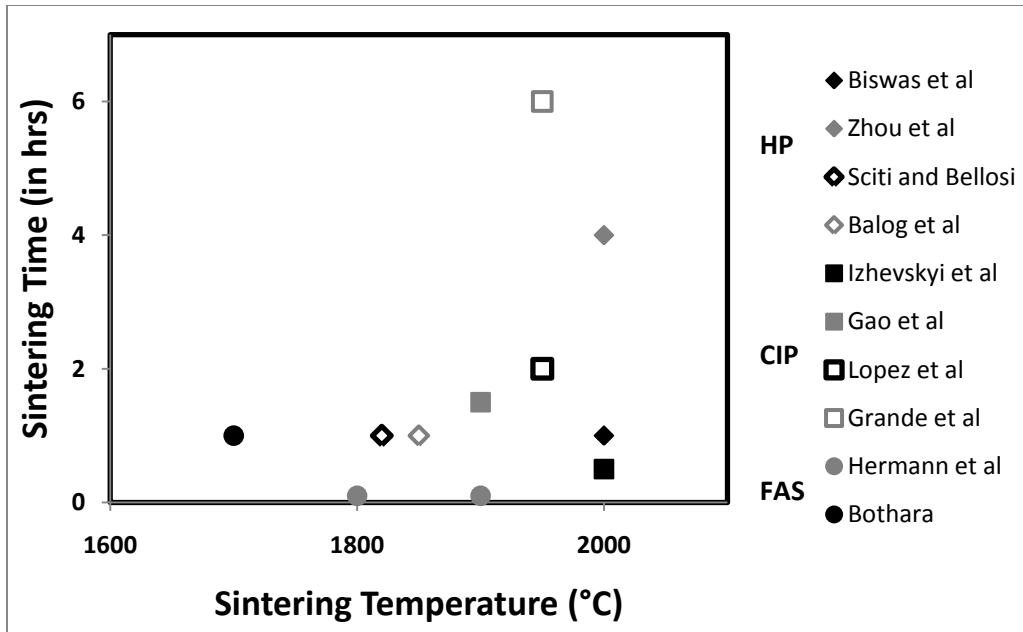


Figure 2.8a: Processing window for sintering conditions for SiC

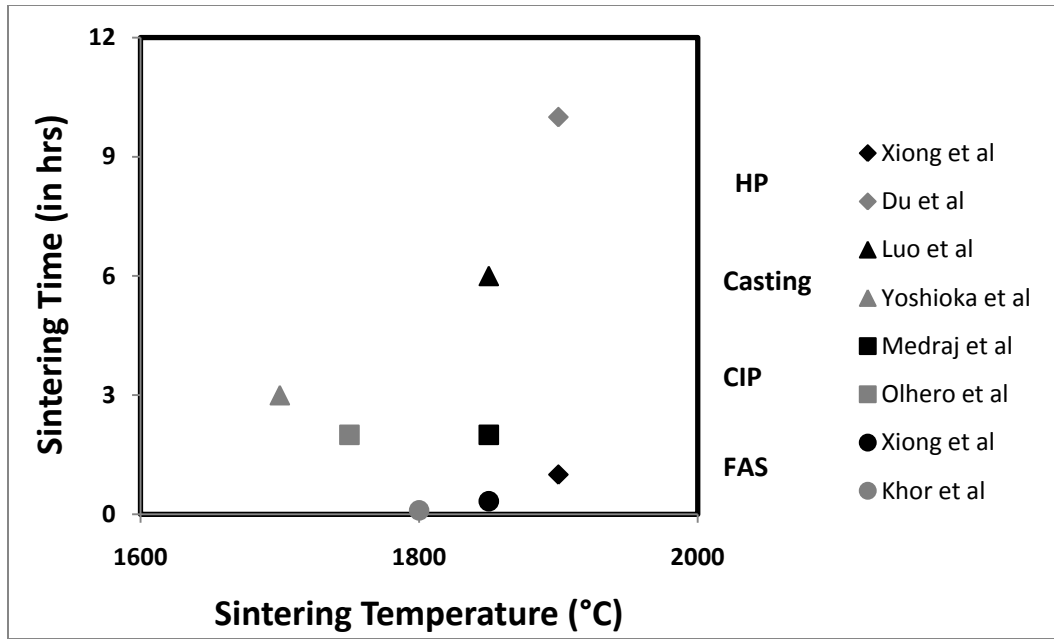


Figure 2.8b: Processing window for sintering conditions for AlN

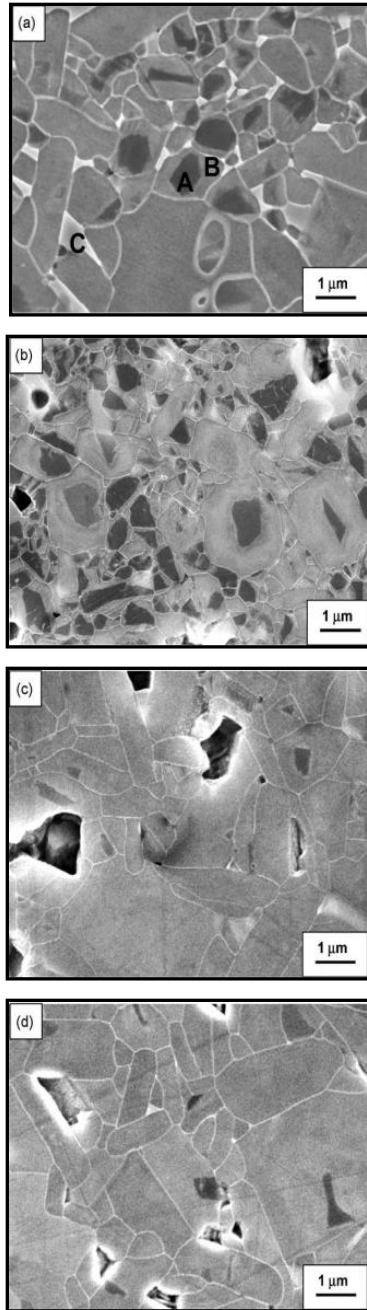


Figure 2.9: Growth of SiC grains with the increase in sintering temperature; a. 1850 °C, b. 1875 °C, c. 1900 °C, d. 1950 °C (Courtesy: G. Magnani et al, 2005, [95])

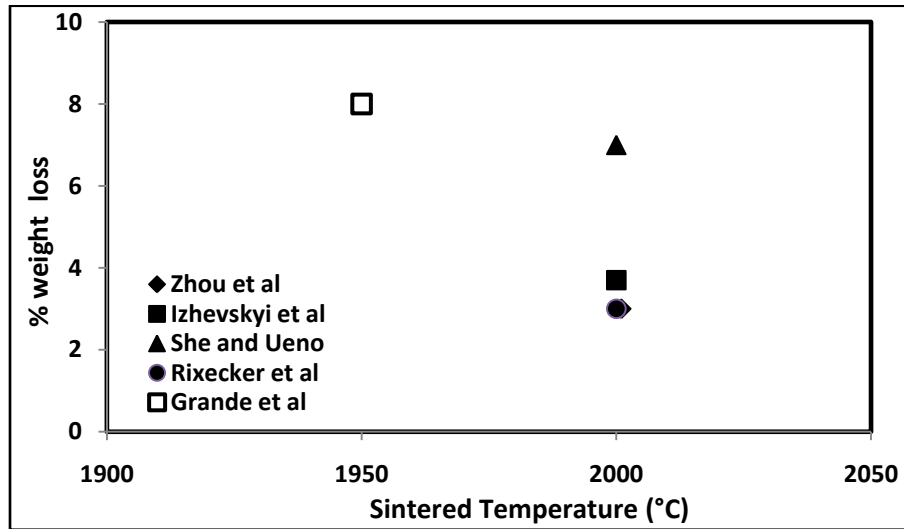


Figure 2.10: The effect of sintering temperature on the weight loss experienced during SiC sintering

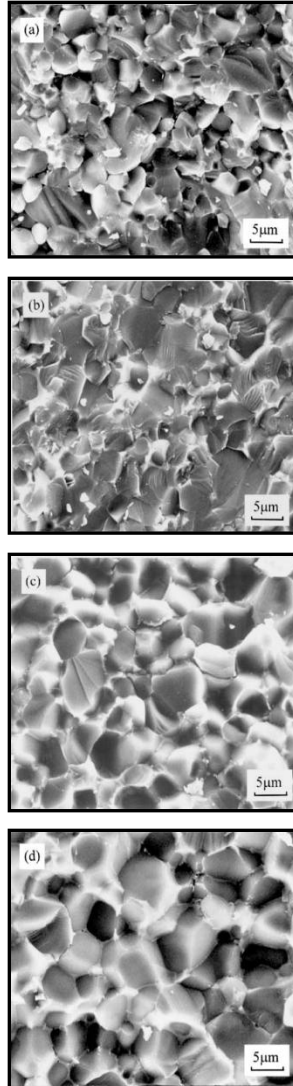


Figure 2.11: Growth of AlN grains with an increase in the hold time (1830 °C); a. 25 min, b. 100 min, c. 240 min, d. 720 min (Courtesy: X.Xu et al, 2003, [120])

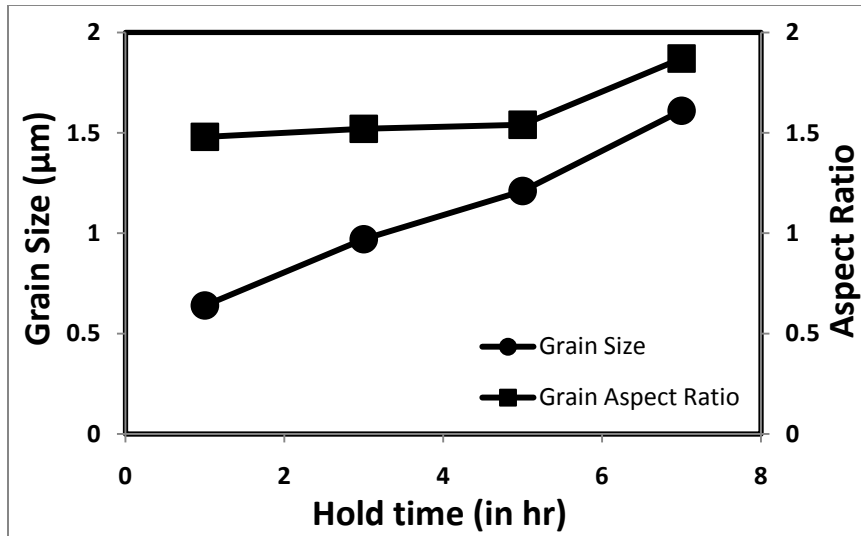


Figure 2.12: The effect of hold time on the size and aspect ratio of SiC grains pressureless sintered at 1950 °C (Courtesy: et al, Rodriguez et al, 2006, [109])

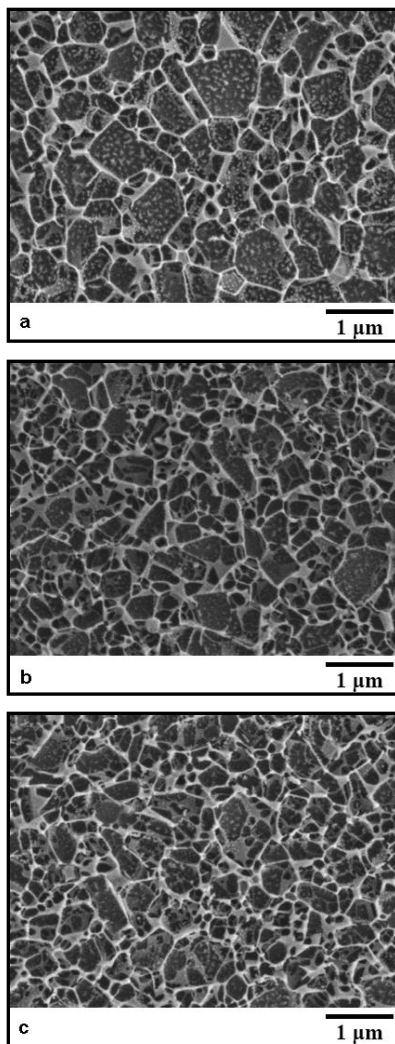


Figure 2.13: SiC sintering at 1700 °C for 60 minutes by plasma pressure compaction with an external pressure of a. 10MPa, b. 30 MPa, c. 50 MPa (Courtesy: Manish Bothara, 2007, [105])

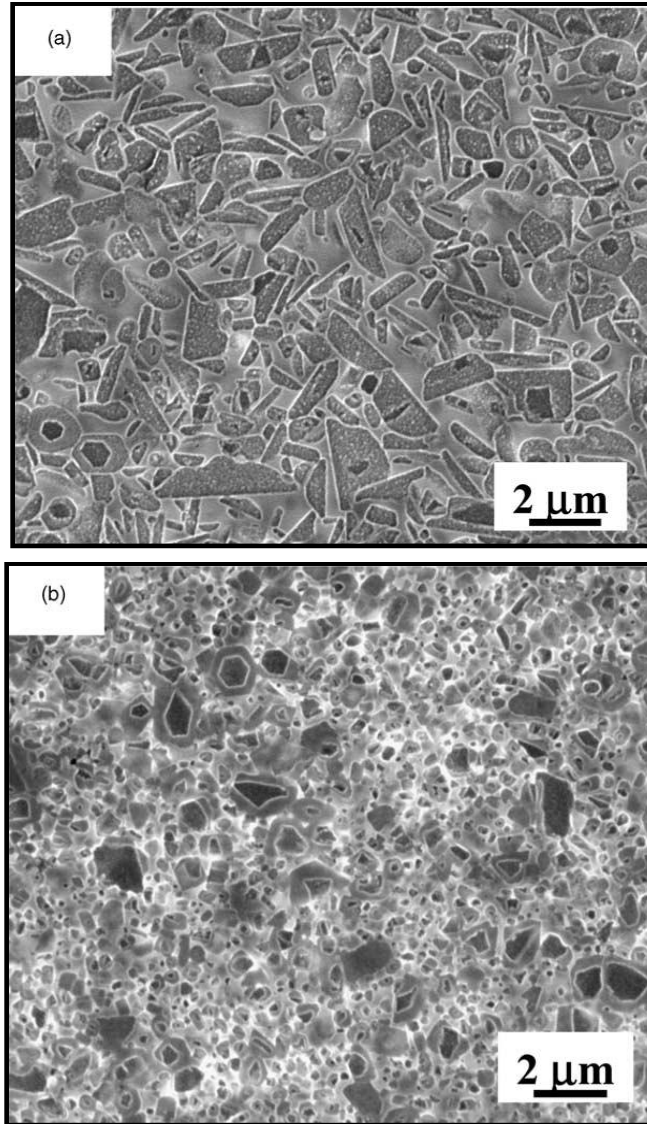


Figure 2.14: β -SiC sintered at 1950 °C for 60 minutes in, a. Ar atmosphere, b. N_2 atmosphere (Courtesy: Ortiz et al, 2004, [98])

Table 2.1: Characteristics of SiC polytypes

Property	3C-SiC (β)	4H-SiC	6H-SiC (α)
Crystal Structure	Zinc Blende (Cubic)	Hexagonal	Wurtzite (Hexagonal)
Density(g/cc)	3.21	3.21	3.21
Bandgap (eV)	2.36	3.23	3.06
Breakdown electric field (10^6 V/cm)	-	2.22	2.5
Bulk Modulus(GPa)	250	220	220
Thermal Conductivity (W/m.K) (@ 25°C)	360	370	490
Coefficient of thermal expansion ($10^{-6}/^\circ\text{C}$) (@ 25°C)	2.9	4.2	4.68

Table 2.2: Quantitative comparison of the properties of thermally conducting ceramics

Property	Al₂O₃	ZrO₂	Si₃N₄	BeO	SiC	AlN
Density (g/cc)	3.96	6	3.29	2.86	3.2	3.26
Thermal Conductivity (W/m.K)	35	2	30	260	120	170
Thermal Diffusivity (mm ² /s)	6	1	12	80	56	64
Heat Capacity (J/g. K)	0.88	0.45	0.75	1.12	0.67	0.72
CTE (10 ⁻⁶ /°C)	8.1	10.3	3.3	8.7	4	4.5
Vicker's Hardness (GPa)	14	12.8	15	12	22	10.4
Fracture Toughness (MPa.m ^{0.5})	4	13	6.1	-	4.5	2.6
Flexural Strength (MPa)	379	900	830	240	450	320
Poisson's Ratio	0.22	-	0.27	0.26	0.17	0.24
Volume Resistivity (Ω.cm)	>10 ¹⁴	>10 ¹⁴	>10 ¹⁴	>10 ³	10 ⁴	>10 ¹⁴

Table 2.3: Comparison of the processing of organic binders and pre-ceramic polymers

Organic Binder	Pre-ceramic Polymer	Comment
Hot Mix/Cold Mold	Cold Mix/Hot Mold	
Less green density	More green density	Pros with polysilazane usage
High shrinkage after sintering	Lower shrinkage after Sintering	
Completely removed before sintering	Binder pyrolyzed to ceramic	
	Sinters into Si ₃ N ₄ /SiC composite	Cons with polysilazane usage
Overall process is quick	Slow ramping rate to sintering temperature makes the process comparatively slower	

Table 2.4: Comparison of ceramic net-shaping processes

Characteristics	Hot Pressing	Slip/Tape Casting	Machining	CIM	Field Assisted Sintering	Pyrolysis of Polysilazanes
Density	95-100%	95-99%	100%	90-100%	> 99%	>95%
Surface Finish	< 2 μm	3 μm	0.4-2 μm	0.4 -0.8 μm	< 2 μm	-
Secondary Machining	Required	Required	-	Nil	Required	Nil
Wall Thickness	>2mm	>5mm	>2mm	10 μm	>0.5 mm	>0.5 mm
Dimensional Tolerance	Poor	Poor	Poor	Close	Close	Close
Shape Complexity	Medium	Medium	High	High	Low	High
Production Rate	Medium	Low	Low	High	High	Low

Table 2.5: Prior reports on additive-assisted sintering of SiC

Ref. #	Author	SiC Particle Size (μm)	Sintering aid			Net shaping and densification by (with pressure in MPa)	Sintering Conditions				% relative density
			Nature	% content	Size (μm)		Atm.	Temp ($^{\circ}\text{C}$)	Hold time (hrs)	Pressure (MPa)	
31	J.K. Lee et al	α - 0.45	YAG	10	-	HIP	Ar	1850	0.5	200	99%
75	Biswas et al	α - 0.51	AlN-Y ₂ O ₃	5.3-7.3	4.48-0.92	HP	Ar	2000	1	10	100%
76	Y. Zhou et al	β -0.3	Y ₂ O ₃ - La ₂ O ₃	1-1	-	HP	Ar	2000	4	40	97.1%
77	Sciti and Bellosi	-	Al ₂ O ₃ -Y ₂ O ₃	6-4	-	HP	-	1780	0.5	30	98.5%
			Y ₂ O ₃ - La ₂ O ₃	3-3	-			1820	1		94.2%
78	S.G. Lee et al	β -0.27	Oxynitride- Al ₂ O ₃	10-5	-	HP	N ₂	1800	1	25	99.2%
79	Y-W. Kim et al	α - 0.9%; β - 85.6%, Size: -	AlN-Y ₂ O ₃	2.9-10.6	-	HP	N ₂	1900	1	25	98.1%
80	Manojkumar et al	β -0.27	AlN-Y ₂ O ₃	1.26-1.74	-	HP	N ₂	2050	6	25	98%
81	Balog et al	-	Al ₂ O ₃ -Y ₂ O ₃ -Yb ₂ O ₃	13	-	HP	Ar	1850	1	30	96.5%
85	Ye et al	α - 0.7	Al ₂ O ₃ -Y ₂ O ₃	5-5	-	HP	Ar	1900	0.5	25	98.5%
86	Y. Zhou et al	β -0.3	Al ₂ O ₃ -La ₂ O ₃	3.19-1.81	-	HP	Ar	1780	1	40	98.1%
			Al ₂ O ₃ -Nd ₂ O ₃	3.25-1.75				1720			98.3%
			Al ₂ O ₃ -Y ₂ O ₃	3.28-1.72				1760			98.5%
			Al ₂ O ₃ -Yb ₂ O ₃	3.49-1.51				1750			98.2%
87	Y-W. Kim et al	α -0.42	YAG-SiO ₂	7.2-4.8	-	HP	Ar	1850	1	25	99.8%
		α -0.5									99.9%
		α -0.71									99.1%

Table 2.5: Prior reports on additive-assisted sintering of SiC (continued)

Ref. #	Author	SiC Particle Size (μm)	Sintering aid			Net shaping and densification by (with pressure in MPa)	Sintering Conditions				% relative density
			Nature	% content	Size (μm)		Atm.	Temp ($^{\circ}\text{C}$)	Hold time (hrs)	Pressure (MPa)	
82	Y. Lee et al	0.02	$\text{Al}_2\text{O}_3\text{-Y}_2\text{O}_3\text{-CaO}$	7-2-1	-	HP	-	1750	0.5	20	98%
83	Y-W. Kim et al	α ; Size: -	$\text{AlN-Y}_2\text{O}_3$	-	-	HP	Ar	1900	1	25	97%
84	He et al	β -0.8	$\text{MgO-Al}_2\text{O}_3\text{-Y}_2\text{O}_3$	6-1-1	-	HP	Ar	1800	1	20	97%
88	Izhevskiy et al	α - 10%; β - 90%, Size: -	$\text{AlN-Yb}_2\text{O}_3$	5-5	-	UP (50) + CIP (200)	N_2	2000	16	0	99.8%
89	She and Ueno	α - 0.6	$\text{Al}_2\text{O}_3\text{-Y}_2\text{O}_3$	6.25-3.75	0.5	UP (3) + CIP (200)	Ar	2000	1	0	98%
90	Gao et al	-	$\text{Al}_2\text{O}_3\text{-Y}_2\text{O}_3$	5-5	-	UP (25) + CIP (200)	N_2	1900	1.5	0	98%
91	Lopez et al	-	$\text{Al}_2\text{O}_3\text{-Y}_2\text{O}_3$	-	-	UP (50) + CIP (350)	Ar	1950	2	0	100%
92	Grande et al	α - 0.6	$\text{Al}_2\text{O}_3\text{-Y}_2\text{O}_3$	4.72-2.73	0.45-0.25	UP (312) + CIP (350)	Ar	1950	6	0	100%
93	Guo et al	α - 0.75	$\text{Al}_2\text{O}_3\text{-Y}_2\text{O}_3$	6.25-3.75	-	UP (100) + CIP (250)	Vac.	1860	0.75	0	96.1%
94	Pujar et al	α ; Size: -	$\text{Al}_2\text{O}_3\text{-Y}_2\text{O}_3$	12.5-7.5	-	UP (50) + CIP (350)	Ar	1900	0.5	0	96%
33	Fukushima et al	β -0.3	$\text{Al}_2\text{O}_3\text{-Y}_2\text{O}_3$	2.4-1.6	-	UP (40) + CIP (100)	Ar	1800	2	0	70%
95	Magnani et al	β -0.72	$\text{Al}_2\text{O}_3\text{-Y}_2\text{O}_3$	6--4	0.3-3.9	UP (67) + CIP (250)	Ar	1875	0.5	0	97.1%
96	Suzuki & Sasaki	β ; Size: -	Al_2O_3	15	-	UP (20) + CIP (200)	N_2	1950	5	0	97%
97	H. Xu et al	α - 0.6	$\text{Al}_2\text{O}_3\text{-Y}_2\text{O}_3$	14.92-11.22	-	UP (50) + CIP (350)	Ar	1950	0.5	0	-
		β -0.5									-
98	Ortiz et al	β ; Size: -	$\text{Al}_2\text{O}_3\text{-Y}_2\text{O}_3$	14.92-11.22	-	UP (50) + CIP (350)	Ar	1950	1	0	98%
99	Zawrah and Shaw	α -0.75	$\text{Al}_2\text{O}_3\text{-Y}_2\text{O}_3\text{-CaO}$	7-2-1	-	UP (50) + CIP (350)	Ar	1800	-	0	97%
100	X. Guo et al	α -0.75	$\text{TiN-Al}_2\text{O}_3\text{-Y}_2\text{O}_3$	5-4.3-5.7	-	UP (100) + CIP(250)	Vac.	1950	0.25	0	98%

Table 2.5: Prior reports on additive-assisted sintering of SiC (continued)

Ref. #	Author	SiC Particle Size (μm)	Sintering aid			Net shaping and densification by (with pressure in MPa)	Sintering Conditions				% relative density
			Nature	% content	Size (μm)		Atm.	Temp ($^{\circ}\text{C}$)	Hold time (hrs)	Pressure (MPa)	
101	Rixecker et al	α - 0.51; β -0.89	AlN-Y ₂ O ₃	0.92-4.48	0.92 -4.48	CIP (240)	N ₂	2000	0.5	0	99.6%
102	Nader et al	α ; Size: -	AlN-Y ₂ O ₃	2.95-10.34	-	CIP (630)	N ₂	1925	14	0	-
103	J.K. Lee et al	α - 80%; β - 80%, Size: α -0.42; β - 0.44	YAG	10	-	CIP (200)	Ar	1850	0.5	0	98%
104	L.S.Sigl	α ; Size: -	Al ₂ O ₃ -Y ₂ O ₃ -AlN	-	-	CIP (200)	Ar	1930	0.5	0	-
105	Manish Bothara	α - 0.75	AlN-Y ₂ O ₃	5--5	.035 - .020	PAC	Ar	1700	1	50	99.5%
106	Wetzel et al	β -0.05	Al ₂ O ₃ -Y ₂ O ₃	5-5	0.02-0.05	UP (90) + CIP (210)+ Sinter Forging	Ar	1850	1	40	99%
						HP	Ar	1660	1	40	97%
						UP (90) + CIP (210)+ GPS	N ₂	1900	1	10	100%
107	Can et al	α ; Size: -	Al ₂ O ₃ -Y ₂ O ₃	3.25-6.75	-	HP	Ar	1975	0.5	30	100%
				5-5	-	CIP (250) + GPS		1925	1	8	98.8%
108	Hermann et al	α - 0.55	Al ₂ O ₃ -Y ₂ O ₃	3-7	- 0.9	PAC	-	1900	0.1	50	97%
			Al ₂ O ₃ -Y ₂ O ₃ -TiC	3-7-1	-0.9-			1800			97.5%
			Al ₂ O ₃ -Yb ₂ O ₃	3-7	-			1800			96.5%
109	Rodriguez et al	α ; Size: -	Al ₂ O ₃ -Y ₂ O ₃	5--5	-	UP	Ar	1950	Pressureless	1	98.8%
										3	97.3%
										5	96.7%
										7	94.9%
110	Clemens et al	α -0.6	C-B ₄ C	-	-	Extrusion (Powder: 52 vol.%)	Ar	2180	0.5	Pressureless	92.4%
111	Onbattuvelli et al	α -0.75	AlN-Y ₂ O ₃	5--5	-	PIM (Powder: 53 vol.%)	Ar	1950	0	Pressureless	94%
112	Zhang et al	α - 0.5	Al ₂ O ₃ -Y ₂ O ₃	4.5-4.5	1.5 -0.5	-	N ₂	2000	1	-	98%

Table 2.6: Prior reports on additive-assisted sintering of AlN

Ref. #	Author	AlN Particle Size (μm)	Sintering aid			Net shaping and densification by (with pressure in MPa)	Sintering Conditions				% relative density
			Nature	% content	Size (μm)		Atm.	Temp ($^{\circ}\text{C}$)	Hold time (hrs)	Pressure (MPa)	
28	Surnev et al	-	CaO	3	-	HP	N_2	-	0.5	40	98%
			Y_2O_3	4							
			CaF_2	3							
			CaC_2	1							
29	Du et al	-	Y_2O_3 -CaO	1-0.5	-	HP	N_2	2000	5	-	98.5%
			Yb_2O_3 -CaO	1-0.5				1950	10		96%
			Er_2O_3 -CaO	1-0.5							97%
30	Li et al	2	La_2O_3	5	-	HIP	N_2	1700	0.83	5000	99%
113	Liu et al	2.04	YF_3 - CaF_2	4--2	-	UP	N_2	1650	6 hr	-	99%
114	Y. Liu et al	2.04	Dy_2O_3 -CaO- Li_2O	7-0.5-0.5	-	UP	N_2	1600	1.75	-	98%
115	X. Li et al	0.5	-	-	-	UP(150)+HP	N_2	1700	1.25	4750	99.8%
116	Zhao et al	-	CaF_2	4	-	SPS	N_2	1650	0.08	30	98.14%
117	Cheng et al	1.5	-	-	-	UP (30)+CIP (280) + Microwave (2.45 GHz - 6 kW)	N_2	1850	1	-	99.5%
58	Xiong et al	-	-	-	-	PAC	N_2	1850	0.03	30	99%
			CaF_2	3							99%
			-	-							HP
59	Khor et al	3.5	CaF_2	1	-	PAC	Vac.	1900	0.08	45	96%
60	He et al	1	Sm_2O_3	2%	-	PAC	N_2	1700	0.16	40	99%
61	Khor et al	2.77	Sm_2O_3	3	-	PAC	Vac.	1500	0.05	-	98%

Table 2.6: Prior reports on additive-assisted sintering of AlN (continued)

Ref. #	Author	AlN Particle Size (μm)	Sintering aid			Net shaping and densification by (with pressure in MPa)	Sintering Conditions				% relative density
			Nature	% content	Size (μm)		Atm.	Temp ($^{\circ}\text{C}$)	Hold time (hrs)	Pressure (MPa)	
24	Wu et al	1.99	Dy ₂ O ₃ -CaO	5--1	-	Tape Casting	N ₂	1850	4	Pressureless	99%
25	Luo et al	1.7	Y ₂ O ₃ -Dy ₂ O ₃	10.2-1.53	-	Tape Casting	N ₂	1800	6	Pressureless	-
27	Suzuki & Sakka	0.7	Y ₂ O ₃	5		Slip Casting	N ₂	1900	2	Pressureless	-
13	Lin et al	1.5	Y ₂ O ₃	3%	44	PIM - 78.35 wt.% powder	N ₂	1800	2	Pressureless	-
14	Junior & Shanafield	1.35	(C ₃ H ₇ O)-Y	10	-	UP (30)+CIP (300)	N ₂	1850	2	Pressureless	99%
32	Medraj et al	0.3	Y ₂ O ₃	5	1.8	UP+CIP	N ₂	1850	1	Pressureless	100%
118	Qiu et al	0.9	Y ₂ O ₃ -CaO	3.53-2	-	UP (10)+CIP (140)	N ₂	1600	6	Pressureless	100%
119	Molisani et al	-	Y ₂ O ₃	4	5.3	UP(10)+CIP(150)	N ₂	1850	1	Pressureless	99%
			CaO	4	5.7						97%
120	X. Xu et al	1.67	1.67	Sm ₂ O ₃	8	-	CIP(200)	N ₂	1830	12	Pressureless
121	Molisani et al	0.92	0.92	CaCO ₃	1.8	5.6	UP (10)+CIP (150)	N ₂	1700	1	Pressureless
122	Kume et al	-	-	Y ₂ O ₃	5	-	UP+CIP(100)	N ₂	1900	2	Pressureless
123	Zhou et al	2.7	B ₂ O ₃ -Y ₂ O ₃	2.4-1.6	-	-	N ₂	1850	4	Pressureless	98%
61	Khor et al	2.77	Sm ₂ O ₃	3	-	PAC	Vac.	1500	0.05	-	98%
127	L. Qiao et al	1.46	Y ₂ O ₃ -CaF ₂ -Li ₂ CO ₃	2-2-2	-	UP	N ₂	1650	8	Pressureless	-

Table 2.6: Prior reports on additive-assisted sintering of AlN (continued)

Ref. #	Author	AlN Particle Size (μm)	Sintering aid			Net shaping and densification by (with pressure in MPa)	Sintering Conditions				% relative density
			Nature	% content	Size (μm)		Atm.	Temp ($^{\circ}\text{C}$)	Hold time (hrs)	Pressure (MPa)	
124	Panchula & Ying	-	Y_2O_3	4	-	UP(7)+CIP(400)	N_2	1900	2	Pressureless	98%
				5		HP				100	98%
125	Chen et al	1.22	Y_2O_3	2	-	UP (170)	N_2	1810	2	Pressureless	98.8%
									8		99.6%
126	Nakano et al	-	Y_2O_3	4	-	UP (10)+CIP (150)	N_2	1800	1	Pressureless	-
								1900	100		
128	Olhero et al	0.33	$\text{YF}_3\text{-CaF}_2$	3-2	-	UP (90)+CIP (200)	N_2	1750	2	Pressureless	100%
				4-2	-						
				4-3	-						

Table 2.7: Pros and cons of applying external pressure to densify SiC and AlN

Method	Principle	Pros	Cons
Hot Pressing	Simultaneous application of heat and pressure		
Hot Isostatic Pressing	Application of heat over the sample placed inside a fluid pressurized vessel	Fast, 100% densification possible	Minimal grain growth, not for intricate geometries, poor production rate
Plasma Pressure Compaction	Resistive heating of the powder compact by passing electric current through it in the presence of pressure		
Pressureless sintering	Heating to sintering temperature with or without hold time	Increased grain size, product shape independence, high production rate	Additional hold time, incomplete densification

CHAPTER 3

Sintered Nanoscale Powders

Abstract

The property benefits of nanoscale powders are well recognized. However, translation of properties into final applications lies in net-shaping of the nanoscale powders into fully dense structures. The current article reviews near-net-shape fabrication processes that have been recently developed to produce components via sintering nanopowders. In addition, prior studies on the densification of nanoscale powders are reviewed to understand the effect of materials and process parameters on the sintered microstructure and properties.

3.1. Introduction

The role of sintering technologies for the net shape production of complex engineering components from powdered materials that are difficult to machine or cast – ceramics, intermetallics, refractory metals, thermosetting plastics, and composites continues to grow. Hence it is of great interest to extend the concept of sinter manufacturing to nanoscale particles, especially for microminiature components where the particle size has to be at least an order of magnitude less than the minimum feature size [1]. The application of sintered materials to microminiature components is widespread. Some of the devices are used in lighting systems, semiconductor assembly tools, optical transmission networks, digital light projectors, telecommunication systems, minimally invasive surgical tools, circuit board micro drills, radio isotope containers, and automotive sensors [2,3]. A good example for the use of tungsten powder as tungsten collimators (current submicrometer sized powders limit the hole diameter to 10 μm) is in PET (positron emission tomography) where image resolution is strictly limited by the feature size in the tungsten collimators. Likewise, in other miniature devices, refractory materials (such as Ta, Mo, Ti) or their compounds (carbides, nitrides, borides, oxides) would be the material of choice because of density, wear resistance, radio opacity, arc resistance, inertia, stiffness, hardness, biocompatibility, strength, thermal expansion coefficient, or vapor pressure are favorable factors in making such devices.

Table 3.1 lists the literature available on synthesizing ceramic nanoparticles. Curiously, the availability of nanoscale powders have been reported since the 1960s [2-7], yet advantages are poorly realized from these powders. Small particles are required for both geometric and performance attributes. However, besides printed circuit drills [8], where 200 nm WC-Co powders are used to fabricate 70 μm diameter drills, the fabrication of microminiature devices by traditional press-sinter cycles has lead to disappointing properties.

Thus, in spite of nanoscale powder availability, sintered nanomaterials have not yet seen widespread application. A major difficulty is from rapid microstructure coarsening during processing. To overcome grain growth in sintering, novel consolidation processes have been used to lower the densification temperatures [9-15]. Even so there is difficulty in attaining dense products from nanoscale systems with grain sizes below 200 nm [15-18]. This has led to recent suggestions that nanoscale microstructures will be inaccessible in some cases [19], but those calculations assume standard processing cycles, a route not useful with nanoscale powders. The present review examines the work to date and provides insight to accelerate manufacturing

research in nanoscale processing by predicting the routes that will lead to new property combinations, new product performance levels, and new designs.

3.2. Nanoscale Powder Consolidation Processes

The attributes of common shaping techniques used in the net-shaping of ceramics are listed in **Table 3.2**. Following shaping, sintering is an important step common to all processes. Maintaining the grain size to <100 nm while attaining complete densification are important goals for sintering nanoscale powders. Prior investigations explored the densification and grain growth behavior of ceramic nanoscale powders by varying the process and material parameters. Densification of ceramics can be broadly classified as pressurized and pressureless sintering.

Hot pressing, hot isostatic pressing and sinter forging have been extensively studied over the years. The applied pressure acts as an external sintering driving force accelerating densification and retarding grain growth [39]. As a result, densification might be complete faster and at relatively lowers sintering temperatures. Thus, in addition to the grain boundary diffusion and volumetric diffusion one should consider the inclusion of creep/plastic deformation as the rate-controlling factor [40]. A summary of data from the literature on the densification of nanoscale powders using these conventional methods is listed in the **Table 3.3**.

Recently, techniques that involve other dominant sintering driving forces in addition to the external pressure were developed. These include, plasma assisted compaction, microwave sintering and dynamic compaction. **Table 3.4** summarizes selected data from the literature on the densification of nanoscale powders by these methods. Some salient features of these recent methods are summarized below:

3.2.1. Field-assisted compaction (FAC)

In this technique, the ceramic powder to be compacted is filled in a graphite die and placed between two electrodes. When pulsed electrical power is applied, the current does not flow freely through the powder compact since an effective current path has not yet been established due to the voids inside the powder. The oxide layer on the surface of the powder particle acts as an insulator at the particle contact. This causes a charge buildup at the inter-particle gaps between the powder particles, with one particle to be negatively charged with respect to the other particles that are in contact with it [41-44]. As the charge builds up, the voltage difference becomes sufficiently large to generate sparks that trigger an ionization process [41-44]. The resultant inter-particle plasma serves to activate the surface of the powder particles by removing the oxide and

other contaminants. At this stage, the powder compact is heated to higher temperatures so that any adsorbed gas and/or moisture is released. This is usually indicated by drop in the initial vacuum level [45-48]. At this stage, uniaxial pressure is applied to facilitate sufficient current path through the powder compact. The pulse current is applied until the vacuum has reached its initial value. In the following stage, a constant current is applied to achieve the sintering temperature. Direct application of the current and external uniaxial pressure accelerates densification of the material by inducing resistance heating and causing plastic deformation at the inter-particle contact surfaces [46]. The resistance heat serves to concentrate the heat at inter-particle points of contact and the concurrent application of light pressure results in densification of the compact [47]. The amount of pressure applied and direct current required to reach the sintering temperature are determined by various factors such as the conductivity of the powder, particle size and dimensions of the graphite dies used [47,48].

3.2.2. Microwave sintering

Unlike FAC, in microwave sintering the heat is generated in the bulk of the material through electromagnetic radiation absorption [49]. Thus, the microwave sinterability of a given nanoscale powders depends on its absorption rate of microwave energy, which is proportional to the microwave frequency and dielectric electric factor. In simpler terms, higher the microwave frequency, better is the sinterability. With grain boundaries being the primary location for electric dipoles, a rapid heating of nanoscale powders with higher surface area is possible. Possibility of heating rate > 1000 °C/min with nearly no hold time suppresses the surface diffusion thereby retarding the grain growth. In summary, microwave sintering can be 10 times faster than the conventional sintering while consuming only 5% of the energy required [50-52]. As an additional note, for the nanoscale powders such as Al_2O_3 or TiO_2 , which does not couple with microwaves, susceptor plates (generally SiC) are embedded for microwave heating [51,52]. One major limitation of microwave sintering is the difficulty experienced in controlling the grain growth when aiming for full densification [50-54]. A proposed solution to this issue involves a microwave sintering of nanostructures to 90% densification followed by prolonged hold at relatively lower temperature to achieve full density yet with limited grain growth. Additional limitations including poor temperature control and inability to sinter complex geometries are mentioned in the prior reports. Further fundamental understanding of the interactions between the microwave and nanoscale powders are still needed to further advance this technique.

3.2.3. Explosion/shock wave compaction

The explosion compaction method consisting of a ceramic powder surrounded by a proper type and amount of explosive is an inexpensive method to achieve high densities close to theoretical density¹⁰³. The explosive's parameters have to be adjusted to the type of the powder to be compacted. Detonation of these explosive creates a shock wave that travels downward. This shockwave rearranges particles to denser packing and brings them into contact at high pressures to bond at contact surfaces [55-57]. The explosive's pressure required for packing is linearly related to the Vickers hardness of the ceramic particles. Under these high pressure and heat, the ceramic nanoscale powders undergo plastic deformation. The pores in the green compacts thus collapse leading to inter-particle friction and point defects. Prior investigations have reported a successful shock wave compaction of Al₂O₃ nanoscale powders and particulate composite materials [55-57]. Further research on this technique can be possible with overcoming the current issues including heat dissipation, cracking and non-uniform microstructures.

3.3. Attributes of Nanoscale Powder Sintering

Prior sintering studies on nanoscale powders have generated several relevant observations [8,12,14,17-19,77-101]:

- a smaller final grain size gives a higher strength and hardness, and other metals, no breakdown in the Hall-Petch strengthening has been reported for the W, Mo, Ta, ZrO₂, or WC materials
- nanoscale powders exhibit high sintering rates, but faster sintering has failed to directly deliver property gains because of poor grain size control
- grain growth inhibitors are effective, but they must be dispersed homogeneously in the powder prior to the press-sinter cycle
- sintering temperatures below 1100°C may give densification, but the properties often are unattractive due to residual impurities that do not evaporate at lower temperatures
- densification at temperatures below approximately 1000°C require high compaction pressures or pressure-assisted sintering

There is much difficulty in converting nanoscale powders into 3D bulk engineering products with minimized grain coarsening. The scientific challenge is how to consolidate these powders, especially for use in microminiature devices where classic press-sinter processing cycles are inappropriate. There is a need to explore nanoscale powder processing over a broad range of consolidation conditions to derive and validate robust processing models. For nanoscale powders,

grain growth in sintering is so rapid that pores become stranded in the microstructure, resulting in incomplete densification. Even if the product is dense, then the grain size is large, denying access to the property gains from small grain sizes. An additional dilemma arises with sintering many metals since historically refractory metal processing relied on high sintering temperatures to evaporate contaminants, yet these same cycles induce microstructure coarsening.

The surface area of a nanoscale powder increases the impurity burden, while the high sintering activity traps contaminants prior to evaporation. We need to know what combinations of process parameters lead to real property gains from nanoscale powders; what are the basic processing rules? Early on, this research will conduct a broad study designed to generate a spectrum of density-microstructure responses as required to model the processing. Several processing models have been postulated [102-114], but some of these are invalid. Further research is needed to couple modeling to experimentation (shown in flow chart below) to predict properties from simple input parameters such as material composition, powder characteristics, and pressure-time-temperature parameters.

For nanoscale powders, traditional press-sinter processes inherently circumvent important material reactivity issues [115]. Consolidation of nanoscale powders involves both size-dependent and temperature-dependent parameters. For example, the cemented carbide composition WC-10Co-0.5VC (wt. %) relies on several temperature-dependent reactions during heating. Vanadium carbide is an effective grain-growth inhibitor [77] that segregates to the WC interface at high temperatures [78]. But the low concentration of VC (0.5 wt. %) creates heterogeneity in the initial microstructure since it is mostly added as an admixed powder. Regions far from the VC particles coarsen 3- to 5-times faster than those in proximity to the VC [78,79]. Consequently, substantial nonuniform grain growth is detected prior to densification, starting as low as 1150°C [8]. At high temperatures the VC is homogenized, but the initial local imbalances have already induced exaggerated grain growth.

Several important thermochemical reactions require high temperatures, independent of the microstructure scale [116-118]. Hot isostatic pressing and hot pressing give densification at lower temperatures with reduced grain growth, but with a high cost and loss of impurity evaporation, so the nanoscale product is not successful [12,14,15,18]. These conflicts between size-dependent events and temperature-dependent events create processing imbalances that result in lackluster properties, as seen in several refractory systems such as W [18,119], W-Cu [120-126], W-Ni-Fe [127], W-Y and W-Y₂O₃ [128]. Relevant to the proposed research, 20 nm W sinters to near full density at temperatures below 830°C [129], but oxide reduction is delayed to higher temperatures.

3.3.1. Material parameters

Variations in materials parameters can be broadly classified as starting nanoscale powders and sintering aids. Nanoscale powder size has been a major material parameter studied in the past. As an example, Kim et al [58] studied the effect of starting nanoparticle size on SiC densification and concluded that smaller particles provide a higher sintered density. Under similar sintering conditions, the smaller SiC particles led to the finer microstructure as the grain growth during hot-pressing was minimal. Additionally, the grain size tends to increase with increasing particle size [130]. As discussed earlier, agglomeration is a fundamental problem in the compaction and sintering of nanoscale powders. Compacting such aggregated powders leads to inhomogeneous ceramic green bodies containing large inter-agglomerate pores. Trunec and Maca investigated the role of nanoscale powders size in controlling the pore formation in the cold isostatic pressed ZrO₂ green bodies [68]. It was found that under similar compaction conditions, smaller the starting nanoscale powders, lower is the pore size. The shifting of T_{max} (temperature at which maximum densification occurs) towards lower values confirms enhanced sinterability with reduced particle and pore sizes.

The successful densification of a given nanopowder is dependent on its packing characteristics which in turn relies on the pore size and % porosity. In addition, prior reports by Kim et al [58] and Trunec and Maka [68] studied the effects of initial particle size and specific surface area on the green density (**Table 3.5**). The total number of inter-particle contacts tends to increase with specific surface area thus extending their frictional resistance to compaction. Thus, smaller particle size leads to lower green density (or higher % porosity). In summary, smaller particle size tends to decrease the pore size in the green compact, which together increases the sinterability of the nanoscale powders at relatively lower temperatures. However, their higher surface area reduces the green density, paving path to prolonged sintering and thus possibly grain coarsening. Controlling the particle size distribution may solve the above trade-off between the % porosity and pore size. Unfortunately, very few reports have addressed this issue till date. Recently, Qiu et al [131] and Onbattuvelli et al [132] suggested a bimodal μ -n powder mixture to reduce the pore size yet achieve higher green density in AlN ceramics. Further research is required to extend the above idea into multimodal nanoscale powder mixtures.

As mentioned earlier, sintering aids are generally used to drive the densification of covalently bonded ceramic oxides (ZrO₂, BaTiO₃), nitrides (AlN, Si₃N₄) and carbides (SiC, B₄C). For example, Y₂O₃ reacts with the Al₂O₃ layer on the surface of the AlN particles forming a eutectic, yttrium aluminum garnet (Y₃Al₅O₁₂) which in turn densifies AlN [132]. However, its retention as

an intergranular glassy phase proved detrimental to all the sintered properties. Thus, prior reports focused on studying the effect of the composition and amount of the sintering aid(s) over the densification of difficult to sinter ceramics. Prior reports by G. Skandan [64] on n- ZrO₂ and Kim et al on n-SiC [58] discussed the faster dissolution of nanoscale powders into the liquid phase due to their higher surface area. On contrary, Qiu et al [131] confirmed that the mechanism involved in the eutectic formation is independent of the initial particle size. However, there is an absence of any literature on employing nanosized sintering aids, making it an area worthy of future research.

3.3.2. Process parameters

Sintering is accompanied by the reduction of surface area as result of mass transport via diffusion. Surface diffusion is often dominant at lower sintering temperatures. However, at elevated temperatures, inter-particle bonds grow larger, impinging on each other forming a network of pores connected by grain boundaries along which atoms are transported. Such impingements are expedited when the nanoscale powders with higher surface area are used [68]. In simple words, smaller particle size and higher temperatures speeds the particle bonding process. The above discussion can also be correlated to the substantial difference witnessed in the densification of SiC nanoscale powders [58]. These particle bonds generally result in the reduction of particle surface energy, which in turn reduces the grain boundary energy. Thus in addition to the elimination of pores, higher sintering temperatures also accompanies grain growth [63]. Employing higher heating rate and/or application of external pressure (for sintering via creep) are generally suggested for complete densification yet retard the grain growth¹³². During sintering, loss of grain boundaries near the pores generally slows the densification. Slower heating rate and/or isothermal heating at sintering temperatures for extended time are suggested as the solutions to the above-mentioned issue. For example, the sintered density of nano-ZrO₂ tends to increase when held at 1100 °C for 4 hr [68]. However, the grain growth is found inevitable with both the solutions even though their effect of densification is promising. For example, Rodriguez et al [133] demonstrated the growth of SiC grains with increase in the hold time at sintering temperature. As evident from the **Table 3.4**, the recent research work combat the grain growing issue by involving additional densification sources such as external pressures, plasma and microwaves. Additionally, two-step sintering was suggested for retarded grain growth during pressureless sintering. The reheating of a partially sintered sample during the second step is found to suppress the grain-boundary migration while promoting grain-boundary diffusion [63].

This in turn reduces the grain size of sintered ceramics. Additionally, higher heating rates are also made possible with the two-step sintering.

With techniques including HP, HIP, FAC being used for sintering nanoscale powders, the role of external pressure over densification and grain growth should be understood. Application of pressure during the sintering leads to various mass transport mechanisms such as plastic yield, diffusion controlled creep and grain boundary sliding. Thus, the near elimination of volumetric diffusion during pressurized sintering diminishes the requisite for higher temperature or hold time. Higher pressures are proved beneficial during initial and intermediate stages of sintering through nanoscale powders rearrangement, plastic deformation and pore shrinkage [134, 135]. As a case in point, a reduction of grain size from 700 to 500 nm was observed with increased pressure during the FAC of n-SiC ceramics [136].

3.4. Sintering Models

Several models have been proposed and extended into the nanoscale size range. From a manufacturing viewpoint, the critical need is to predict the final dimensions and performance. In turn, this requires analysis of the powder densification and microstructure development using input parameters such as the particle size, agglomeration level, compaction pressure, heating rate, peak sintering temperature, and sintering time. Some of the models are based on classic material data [137,138], yet several parameters must be extracted via experimentation; for example, the grain growth exponent and anisotropic shrinkage during sintering. Other unknown factors include the agglomeration size effect, change in grain boundary diffusion due to impurities, and agglomerate strength. Assumptions are made on how the material parameters change with temperature, density, and grain size. However, actual data are required to accurately handle these problems if we are to predict component size, density, and properties. This is the area not well explored and denies solving relevant manufacturing problems. Many of these issues are simply handled by broad assumptions. For example, Iyer and Sastry [106] have a model that requires approximately 70 input parameters, a critical one being the assumption of faster grain boundary diffusion (and faster sintering) in nanoscale powders due to higher impurity levels. However, often oxides have the opposite effect [139]. Other unrealistic assumptions are problems, such as an assumed lack of particle size effect on compaction; which is contrary to experimental observations, since at 160 MPa a 46 nm tungsten powder presses to 41% green density, a 110 nm powder presses to 47%, and a 490 nm powder presses to 50% [140].

Modeling the sintering behavior of nanoscale powders has a strong foundation in press-sinter simulations to predict component size, shape, as well as density, and properties. Prior efforts [102-113,141-143] have formulated constitutive equations for powder packing, compaction, sintering densification, sintering distortion, microstructure coarsening, and properties. These are coupled into finite element packages to predict component size, shape, warpage, density, or properties for three-dimensional shapes [141-144]. Input parameters for the models are a large barrier, so a need is to generate algorithms or to recognize patterns that help estimate the required parameters with reduced experimentation.

The major challenge for understanding the sintering behavior of nanoscale powders will be to adapt and integrate the models into a form that handles the special densification, coarsening, agglomeration, and other features associated with the press-sinter processing of nanoscale powders. This requires a critical assessment of options to isolate the appropriate models based on the experimental data. As several materials are processed, an understanding will emerge to integrate and generalize the models, allowing first guesses on processing parameters as new nanoscale powders emerge.

When a powder is loaded into compaction tooling it packs at the apparent density. A small quantity of polymer is coated on the tooling for lubrication. During pressurization the powder exhibits a declining rate of densification. Typical compaction models rely on the apparent density as the zero-pressure density, and include a means to account for particle rearrangement, porous body plastic deformation, and work hardening [145,146]. These factors give the pressed density as a function of the compaction pressure based on a model that requires at four to six independent parameters. Plotted below (a) is the Shima and Oyane [147] model as compared to the compaction curves for four tungsten powders. This model has been verified for a wide range of nanoscale powders with typically 1 % error.

Green strength is critical to handling pressed powders. Compact handling requires a green strength of 20 MPa range, but values as low as 3 MPa can be accommodated in special situations. Green strength arises from the inter-particle locking, deformation, and cold welding during compaction [113,141,146]. For nanoscale particles pressed at low pressures, the green strength is unacceptable, so manufacturing viability depends on exceeding a minimum green strength. This is a particular difficulty with nanoscale powders, requiring high green densities from high compaction pressures to obtain handling strength, as treated in a recent model [113].

Sintering has been the subject of considerable study; more than 10% of the sintering literature dealing with refractory powder sintering at peak temperatures up to 2800°C [2-4,148-159]. Sinter

bonding and shrinkage is determined by a combination of temperature, grain size, and time [148,149]. For the refractory metals, sintering is by a combination of surface diffusion and grain boundary diffusion [148,156,160]; but only the latter contributes to dimensional change via shrinkage. Further, sintering shrinkage is sustained only as long as the pores remain coupled with the grain boundaries, although there is a separation of grain boundaries from pores [161], leading to decaying shrinkage versus time [148]. Treatments of this coupled problem often link grain size to sintered density [161-165]. For low starting densities, as is typical of nanoscale powders, the separation of pores from grain boundaries is not coupled to density, and nanoscale powders follow different trajectories [114]. During sintering the microstructure converges to a constant grain size distribution [166].

In isostatic pressing, the sintering shrinkage is uniform and can be treated using isotropic concepts. This is not true for agglomerated powders [114]. If a compact starts with a low green density, as is typical of nanoscale powders, then the asymptotic sintered density is low, reflecting the combined roles of surface diffusion, grain boundary diffusion, grain growth, and pore separation from the grain boundaries. The implication with respect to sintered nanoscale powders is that only limited densification is possible. Low green densities result in low sintered densities.

Grain size and sintered density determine hardness, strength, and other properties, so accurate models for grain size in the sintered product are needed to predict properties. Like densification, grain growth is thermally activated, and further influenced by the porosity, pore size, and time at temperature. The inhibitions to grain growth disappear as the density increases [113,162-168]. The models link grain size to the thermal work and sintered density, giving accurate predictions of density and grain size for nonisothermal cycles [102-113].

From this base, component size and shape are predicted in finite element models using constitutive compaction and shrinkage equations. Further, since microstructure is quantified in the models, properties can be predicted where microstructure-property links are established. The intent is to formalize the models, integrate the pieces into a single platform, train the model with experimental data, and verify the model for the four materials. In turn, the study has the potential to generalize the findings to other material systems via basic material data. For example, modeling and simulations data for some of the systems we developed are shown below.

Continuum modeling of the sintering process is the most relevant approach to modeling grain growth, densification, and deformation. Key contributions have been made by Ashby [138,169,170], McMeeking and Kuhn [171], Olevsky et al.[172-175] Riedel et al. [176,177], McHugh and Riedel [178], Bouvard and Meister [179], Cocks [180], Kwon et al. [181,182], and

Bordia and Scherer [183-185] based on sintering mechanisms such as surface diffusion, grain-boundary diffusion, volume diffusion, viscous flow (amorphous materials), plastic flow (crystalline materials), evaporation–condensation, and rearrangement. For industrial applications, the phenomenological models are used for sintering simulations with the following key physical parameters:

- Sintering stress [137] is the driving force for sintering due to the interfacial energy of pores and grain boundaries. The sintering stress depends on surface energy, density, and geometric parameters such as grain size when all the pores are closed in the final process.
- Effective bulk viscosity is the resistance to densification during sintering and is a function of the material, porosity, grain size, and temperature. Models for the effective bulk viscosity display various forms, depending on the assumed dominant sintering mechanism.
- Effective shear viscosity is the resistance to deformation during sintering and is also a function of the material, porosity, grain size, and temperature. Several rheological models for the effective bulk viscosity are available. The cited parameters are functions of grain size. Therefore, a grain-growth model is needed for the accurate prediction of densification and deformation during sintering. Typical initial and boundary conditions for the sintering simulations include the following:
 - Initial condition: mean particle size and grain size of the green compact for grain growth and initial green-density distribution for densification obtained from compaction simulations.
 - Boundary conditions: surface energy condition imposed on the free surface and friction condition of the component depending on its size, shape, and contact with the substrate support.

The initial green-density distribution within the shaped body imposes the necessity to start the sintering simulation with the output from an accurate compaction simulation, since die compaction induces green-density gradients that depend on the material, pressure, rate of pressurization, tool motions, and lubrication. The initial and boundary conditions help to determine the shape distortion during sintering from gravity, nonuniform heating, and from density gradients in the green body. **Table 3.7** summarized some applications of sintering models.

Even though many numerical methods have been developed, FEM is most popular for continuum models of the pressing and sintering processes. Many powerful commercial software packages are available for calculating two-dimensional (2D) and 3D thermo-mechanical processes operative during sintering. To increase accuracy and convergence speed for sintering simulations, developers of simulation tools have selected explicit and implicit algorithms for time

advancement, as well as numerical contact algorithms for problems such as surface separation, and remeshing algorithms that are required for large deformations such as those seen in some sintered materials in which up to 25% dimensional contraction is possible.

As a result of efforts in developing models and simulation tools, it is now possible to simulate numerically most of the individual processes in PIM, not only in academe, but also by means of commercial software. One advantage of this integration is that the powder concentration prediction during injection molding can be considered as the initial condition for debinding and sintering. As a consequence of this integration, a sensitivity analysis and optimization during the entire PIM process may be possible. The measurement of material properties and their database are critical in this integration and a material informatics concept can be used, as will be discussed.

Numerical methods have been developed not only on a continuum scale but also on other scales such as electronic, atomistic, and meso. In addition, as the need for miniaturization of components increases, simulations on smaller scales become more significant in light of their narrow process window, which requires an understanding of the attendant scientific fundamentals. In this manner multiscale simulations have been developed including:

- Atomistic simulation using the modified embedded atom method (MEAM) originally proposed by Baskes et al [194,195] and development of a two-particle model from the atomistic simulation results [196]
- Electronic scale quantum mechanical simulation based on density functional theory (DFT) [197,198] and development of an activator/inhibitor model from electronic simulation results [199]
- Mesoscale simulation using the discrete element method (DEM) by calculating the inter- actions between contacting grains modeled by atomistic simulation and development of a continuum-based model from DEM simulation results
- Continuum-based macroscale simulation

The smaller-scale simulation can be considered as a virtual experiment for obtaining material parameters for higher-scale simulations. Some-times a lower-scale experiment is impossible, but can be replaced by a lower-scale simulation. In atomistic simulations, the Monte-Carlo (MC) method is frequently used. The fluid-particle interaction can be simulated numerically by DEM. Furthermore, multiscale sensitivity analysis and optimization can be introduced.

If the compacted body density predictions are in error, then sintering response, dimensional change in sintering, final size and shape, and even property predictions are wrong. Thus, most of the models focus on density predictions [102-113], and some treat microstructure [109-111], but only a few address property predictions [112]. Although microstructure evolution trajectories are often assumed during sintering, they tend to be unverified. Hence, predictions of final size, shape, and properties are either avoided or are inaccurate. Yet from a manufacturing viewpoint these are critical needs. In the end, the component size, shape, and properties are the key determinants of technical success. Then knowing the processing details helps establish the economic viability. Thus, existing models need to be critically reviewed and updated to enable manufacturing from nanoscale powders.

3.5. Structure –Property Relationships for Sintered Nanoscale Powders

When complete densification along with controlled grain growth can be achieved, sintered nanoscale powders with unusual mechanical properties such as extreme hardness, strength, super plasticity and creep have been reported in the literature. The current sections focus on the variations noticed in the mechanical and thermal properties of sintered nanoscale powders due to the grain size refinement.

3.5.1. Hardness and yield strength

In several sintered nanoscale powders an increase of microhardness H_v and yield strength is noticed with decreasing grain size according to the Hall-Petch relationship. When the grain size decreases, the grain boundary area tends to increase. These grain boundaries act as the pinning points impeding crack propagation. Since the lattice structure of the grains differs in orientation, it requires more energy for a crack to change directions and move into the adjacent grain. Impeding the crack propagation also hinders the onset of plasticity and hence increases the yield strength of the material. However, despite the fact that nanoscale materials are inherently stronger/harder than their microscale counterparts, the increment in strength falls below the theoretical prediction [59,63,136]. Below a certain grain size, a softening mechanism has been suggested to take over, resulting in lowering of hardness/strength and is referred to as the inverse Hall–Petch relationship. For example, Ehre and Chaim claim 130 nm as the critical grain size below which an inverse Hall–Petch relationship was noticed for nanophase MgO [200]. Some studies have suggested the possible role of grain boundary thickness over the strength and hardness of the nanophase ceramics. Theoretical models including Hill effect, Reuss effect and

Voigt effect have been proposed that indicate that the volume fraction and hardness of the grain boundary material could control microhardness values [200]. Experimental verifications are yet to be reported to support the predictions.

3.5.2. Creep resistance

The presence of intergranular refractory particles has been found to improve the creep resistance. For example, Ohji et al reports a proportional relation between the threshold stress and n-SiC content in the Al₂O₃-SiC nanocomposites [201]. Possible mechanisms including diffusion hindrance at intergranular glassy phase and increased refractoriness of grain boundary amorphous phase have been credited for the enhanced creep resistance.

3.5.3. Superplasticity

The primary mechanism involved in superplastic deformation is grain-boundary sliding. Thus, a small grain size is useful for attaining high-strain-rate superplasticity. For example, Kim et al reported 1050% deformation in 210 nm ZrO₂ - spinel - Al₂O₃ nanocomposites when a strain rate of 0.4 s⁻¹ is applied at 1650 °C [202]. It has been suggested that superplastic deformation can be beneficial in lowering the sintering temperatures and net shaping of nanoscale powders. Superplasticity has also been observed for other nanophase ceramics such as Si₃N₄ [203], Y-TZP [204], at intermediate temperatures with a relatively low strain rate of 10⁻⁴s⁻¹.

3.5.4. Thermal diffusivity

Reduced grain size is found to drastically change the thermal properties of nanophase non-oxide ceramics [205]. Thermal diffusivity has been suggested to be limited by intrinsic phonon scattering of the microstructure [206]. For most solid materials with a perfect crystal lattice, the transfer of thermal elastic waves, otherwise known as phonons, primarily controls the thermal diffusion behavior. In real solid materials, imperfections such as grain boundaries, pores, impurities (secondary phases in liquid phase sintering) and dislocations are unavoidably present. Phonons collide with these imperfections, causing phonon scattering, which reduces the mean free path [206]. Thus, smaller grains lead to an increase in the mean free path of the phonons and contribute to the decrease in thermal diffusivity. For example, Liu et al correlate retarded grain growth (during isothermal hold at sintering temperature) on the thermal diffusivity of the nano-YSZ [207].

3.6. Potential Applications of Sintered Nanoscale powders

Recent improvements in the net shaping and sintering of nanophase ceramics provide a promise for various applications. For example, a plasma pressure compacted n-SiC plate exhibited a Vickers hardness of 2 GPa with a fracture toughness of $4.6 \text{ MPa}\cdot\text{m}^{1/2}$ extending its possibility in body armor application [136]. Additionally, a high wear resistance makes nanograined ceramics potential candidates for heavy-duty wear/ tribological applications. Other than sintered structures, n- Al_2O_3 powders have drastically improved the wear resistance when incorporated as filler (5 wt.%) in the PTFE matrix [208]. Additionally, thermal insulation applications of nanosized oxide ceramics were made possible due to their lower thermal conductivity, higher thermal shock resistance and superior mechanical properties. Recently, synergistic effects of improved mechanical properties and biocompatibility render nanostructured ceramics including hydroxyapatite, Al_2O_3 - ZrO_2 nanocomposites as potential candidates for load bearing biomedical applications [209,210].

Sintered nanoscale powders are also likely to greatly impact the production of microdevices. Microdevices are envisioned for many aspects of life with estimated growth rates of 20 to 30% per year [211,212]. Demands on nanoscale powder processing arise from two sources – 1) the demands for small features on 3D microminiature devices and 2) the generation of novel properties possible via nanoscale microstructures. Several applications will benefit from this basic manufacturing and modeling research, such as –

- optical mirrors for digital light processing units, with features in the $1 \mu\text{m}$ range
- eye implants to relieve glaucoma intraocular fluid pressure, with pore features down to $1 \mu\text{m}$
- collimators for PET medical imaging with holes smaller than $10 \mu\text{m}$
- micro-fluid reactors with features in the $1 \mu\text{m}$ range
- wire bonding tools for semiconductor packages, with tip features below $1 \mu\text{m}$
- robotic surgical manipulators with features in smaller than $10 \mu\text{m}$
- high-speed carbide drills with flute and tip features in the $2 \mu\text{m}$ range
- drive motors for surgical robots, with features in the $10 \mu\text{m}$ range.

Shrinking component sizes tax our fabrication abilities. In powder systems, the rule of thumb is that the powder size must be smaller than 5% of the feature dimension to reduce wall effects [213]. Features of $1 \mu\text{m}$ size require particles below 50 nm. Besides feature sizes, many engineering properties will improve with a small grain size, including strength, hardness, arc and

wear resistance [3]. For example, abrasive wear rates fall exponentially as the hardness increases while fracture toughness increases [214]. Thus, significant gains are anticipated in dense nanoscale structures. Today, such gains require special and expensive consolidation techniques such as spark sintering [215]. From the above examples, it is clear that research and technological advances in sintered nanoscale powders systems will assist in the manufacturing of dense, small grain size microminiature devices for broad human benefit.

3.7. Future Trends

3.7.1. Material informatics

Informatics is a science in which a new knowledge system is developed by collecting, storing, processing, retrieving, indexing, extracting, exchanging, transmitting, analyzing, studying, and classifying data. Some examples of current activities in powder informatics include:

- Establishing a database of terminology, models and equations, figures, and experimental data
- A graphic capability to make plots and curve fitting capability to obtain material parameters
- A simulation capability based on a material parameter database

The concept of the “computational thinking” algorithm from material informatics provides useful information such as the prediction of missing data points, a reduction in the number of experiments for material properties, validation and verification, and generation of material–process–property mapping.

3.7.2. Integration of bulk synthesis with nanoscale powder processing

Integrating the synthesis of nanoscale powders with downstream processing is important from the perspective of facilitating the handling of bulk quantities of nanoscale powders and limiting their exposure to the environment. In this regard, microchannel reactors used for nanoscale powders synthesis provide the attribute of portability in addition to the ability to generate specific particle attributes (size, shape, purity) and scalable throughput [216]. A potential area of integration of bulk synthesis to nanoscale powders production involves directing the reaction product from the microchannels directly into a compaction press for fabricating metal and ceramic components. The concept for integrating the microchannel reactor to a compaction press using a sliding feed shoe is shown in **Figure 3.1**. It allows for creating components from nanoscale powders directly after synthesis. The feed shoe will have 2 inlets. The first inlet will be to the microreactor. The

second inlet will be to a lubricant delivery system that tribostatically applies an organic lubricant on the inside of the die to reduce friction at the die-wall. The lubricant will also provide protection of the compacted nanoscale powders prior to sintering. The press will be placed in an inert air / moisture-free chamber to avoid exposure to the ambient. Issues pertaining to flowability of the nanoscale powders will have to be resolved using this approach using a combination of fluidization, tribostatic and electrostatic principles. As another example of process integration, variations of this feed shoe technique could be developed to introduce the nanoscale powders into a high intensity mixer. Here the nanoscale powders could be combined with surfactant and binder additives in an inert atmosphere before being further processed by conventional powder processing techniques such as injection molding, extrusion, slip casting and tape casting. A third example is to direct the production of nanoscale powders with polymer mixing into a molding operation similar to reaction injection molding or gas-pressure assisted molding that is currently prevalent in the world of plastics. The commercial implications from success of integrating production and use of nanoscale powders are enormous as they range from automotive and energy generation to petrochemical processing and aerospace.

3.8. Concluding Remarks

Nanoscale powders have been available recently for many materials. The submicron and microscale powders of these material chemistries have historically been net-shape processed via various manufacturing routes followed by sintering. The property benefits of sintered nanoscale powders are well recognized and can be potentially used in a diversity of applications. However, enhanced properties require new thinking on how to balance size-dependent gains from nanoscale powders against temperature-dependent processing barriers. The present review establishes the need to develop processing methods and design tools for powders at the nanoscale range. These developments will allow evaluation of alternative processing cycles to determine realistic property gains, over variations in component size and shape. The developments will eventually lead to lower cost (time, effort, equipment, dollars, and false expectations) in experimentation, optimization, and assessing performance goals when compared to current approaches with submicron and microscale powders.

3.9. References

1. C. P. Poole, F. J. Owens, *Introduction to Nanotechnology*, Wiley-Interscience, Hoboken, NJ, 2003, pp. 133-137.
2. S. W. H. Yih, C. T. Wang, *Tungsten: Sources, Metallurgy, Properties, and Applications*, Plenum Press, New York, NY, 1979.
3. E. Lassner, W. D. Schubert, *Tungsten: Properties, Chemistry, Technology of the Element, Alloys and Chemical Compounds*, Kluwer Academic / Plenum Publishers, New York, NY, 1999.
4. W. E. Kuhn, H. Lamprey, C. Sheer (eds.), *Ultrafine Powders*, John Wiley and Sons, New York, NY, 1963; see R. L. Ripley and H. Lamprey, "Preparation and Properties of Ultrafine Tungsten Powder," pp. 262-270 and H. Lamprey, "Coated Fine Powders," pp. 514-529.
5. E. R. Buckle, P. Tsakirooulos, K. C. Pointon, *International Metals Reviews*, 1986, vol. 31, pp. 258-288.
6. H. Ishikawa, K. I. Otsuka, M. Nitta, Y. Yonehana, *Kawasaki Steel Technical Report*, 1990, no. 23, pp. 41-47.
7. L. E. McCandlish, B. H. Kear, B. K. Kim, *Nanostructured Materials*, 1992, vol. 1, pp. 119-124.
8. G. Gille, B. Szesny, K. Dreyer, H. Van Den Berg, J. Schmidt, T. Gestrich, G. Leitner, *International Journal of Refractory Metals and Hard Materials*, 2002, vol. 20, pp. 3-22.
9. P. M. Pettersson and M. Nygren, *Proceedings Sintering 2003*, R. G. Cornwall, R. M. German, G. L. Messing (eds), Materials Research Institute, Pennsylvania State University, University Park, PA, 2003, see web site www.mri.psu.edu/conferencs/sint03 for paper.
10. A. Sampath, B. G. Ravi, H. Nguyen, T. S. Sudarshan, *Powder Metallurgy*, 2001, vol. 44, pp. 313-316.
11. S. Kangwantrakool, K. Shinohara, *International Journal of Refractory Metals and Hard Materials*, 2003, vol. 21, pp. 171-182.
12. I. Azcona, A. Ordonez, L. Dominguez, J. M. Sanchez, F. Castro, *Proceedings Fifteenth International Plansee Seminar*, vol. 2, P. Rodhammer and H. Wildner (eds.), Plansee Holding, Reutte, Austria, 2001, pp. 35-49.
13. E. Ivanov, C. E. Wickersham, *Proceedings of the Fourteenth Plansee Seminar*, vol. 1, G. Kneringer, P. Rodhammer and P. Wilhartitz (eds.), Plansee AG, Reutte, Austria, 1997, pp. 207-216.
14. L. Bartha, P. Atato, A. L. Toth, R. Porat, S. Berger, A. Rosen, *Journal of Advanced Materials*, 2000, vol. 32, no. 3, pp. 23-26.
15. D. Agrawal, J. Cheng, P. Seegopaul, L. Gao, *Powder Metallurgy*, 2000, vol. 43, no. 1, pp. 15-16.
16. R. K. Sadangi, L. E. McCandlish, B. H. Kear, P. Seegopaul, *Advances in Powder Metallurgy and Particulate Materials - 1998*, Metal Powder Industries Federation, Princeton, NJ, 1998, pp. 1.51-1.60.
17. L. E. McCandlish, P. Seegopaul, R. K. Sadangi, *Advances in Powder Metallurgy and Particulate Materials - 1995*, Metal Powder Industries Federation, Princeton, NJ, pp. 13.17-13.23.

18. O. Seo, S. Kang, E. J. Lavernia, *Materials Transactions*, 2003, vol. 44, pp. 2339-2345.
19. K. Hayashi, N. Matsuika, *Journal of Advanced Materials*, 2002, vol. 34, pp. 38-48.
20. J. Shi, H. Verweij, *Langmuir*, 2005, vol. 21, pp. 5570-5575
21. H. Yang, X. Song, X. Zhang, W. Ao, G. Qiu, *Materials Letters*, 2003, vol.57, pp. 3124-3127
22. E. R.Trejo, A. B. Rico, S. G. Reynoso, M. A. Rosas, *Journal of The Electrochemical Society*, 2007, vol.154 (4), pp. A258-A262
23. L. Li, X. Hao, N. Yu, D. Cui, X. Xu, M. Jiang, *Journal of Crystal Growth*, 2003, vol. 258, pp. 268–271
24. V.M. Boddu, D.S. Viswanath, S.W. Maloney, *Journal of American Ceramic Society*, 2008, vol. 91(5), pp. 1718-1720.
25. S.L. Isley, R.L. Penn, *Journal of Physical Chemistry C*, 2008, vol. 112, pp. 4469-4474
26. H.B. Zhang , K.C. Zhou, Z.Y. Li, S.P. Huang, *Journal of Physics and Chemistry of Solids*, 2009, vol. 70, pp. 243–248
27. H. Yin, Y. Wada, T. Kitamura, S. Kambe, S. Murasawa, H. Mori, T. Sakata, S. Yanagida, *Journal of Materials Chemistry*, 2001, vol. 11, pp. 1694–1703
28. S.K. Lee, T.J. Park, G.J. Choi, K.K. Koo, S.W. Kim, *Materials Chemistry and Physics*, 2003, vol. 82, pp. 742–749
29. G.W. Meng, Z. Cui, L.D. Zhang, F. Phillipp, *Journal of Crystal Growth*, 2000, vol. 209, pp. 801-806
30. D. Sarkar, M. Chu, S.J. Cho, Y.I. Kim, *Journal of American Ceramic Society*, 2009, vol.92(12), pp. 2877-2882
31. P.V. Umnuay, MS Thesis, Flow Characterization of Multiple-tube Reactors for Synthesis of Nano-Sized Silicon Nitride Powder via Silicon Monoxide Ammonolysis, Oregon State University, 2008
32. H.U. Joo, S.A. Chae, W.S. Jung, *Diamond & Related Materials*, 2008, vol. 17, pp. 352–355
33. J.C. Kuang, C.R. Zhang, X.G. Zhou, Q.C. Liu, C. Ye, *Materials Letters*, 2005, vol.59, pp. 2006– 2010
34. M. Lei, H. Yang, P.G. Li, W.H. Tang, *Journal of Alloys and Compounds* , 2008, vol. 459, pp.338–342
35. M. Radwan, M. Bahgat, *Journal of Materials Processing Technology*, 2007, vol. 181, pp. 99–105
36. H. Imamura, T. Imahashi, M. Zaimi, Y. Sakata, *Journal of Alloys and Compounds*, 2008, vol. 451, pp. 636–639
37. K.K Akurati, S. S. Bhattacharya, M. Winterer, H. Hahn, *Journal of Physics, D: Applied Physics*, 2006, vol. 39, pp. 2248–2254
38. Y. Azuma, M. Shimada, K. Okuyama, *Chemical Vapor Deposition*, 2004, vol.10 (1), pp. 11-13.
39. M.H.B. Berna, B. Matovic, *Materials Science and Engineering A*, 2009, vol. 500, pp. 130–149
40. K. Lu, *International Materials Reviews*, 2008, vol.53 (1), pp. 21-37

41. X. Xiong, Z. Y. Fu, H. Wang, F. Quan, *Journal of Material Science*, 2006, vol.41, pp. 2537-2539
42. K.A. Khor, K.H. Cheng, L.G. Yu, F. Boey, *Materials Science and Engineering A*, 2003, vol.347, pp. 300-305
43. X. He, F. Ye, H. Zhang, L. Liu, *Journal of Alloys & Compounds*, 2009, vol. 482, pp. 345-348
44. K. A. Khor, L. G. Yu, Y. Murakoshi, *Journal of the European Ceramic Society*, 2005, vol.25, pp. 1057–1065
45. T.S. Srivatsan, A.S. Naruka, B.G. Ravi, T.S. Sudarshan, M. Petraroli, L. Riester, *Powder Metallurgy*, 2002, vol. 45(3), pp. 255-260
46. M. Bothara, S.V. Atre, S.J. Park, R.M. German, T.S. Sudarshan, R. Radhakrishnan, , *NSTI Nanotech 2007*, vol. 4, pp. 494-497
47. B.G. Ravi, O.A. Omotaye, T.S. Srivatsan, M. Petraroli, T.S. Sudarshan, *Journal of Alloys and Compounds*, 2000, vol. 299, pp. 292-296
48. T.S. Srivatsan, B.G. Ravi, A.S. Naruka, M. Petraroli, L. Riester, T.S. Sudarshan, *Powder Technology*, 2001, vol. 114 (1-3), pp. 136-144
49. D. E. Clark, D. C. Folz, C. E. Folgar, M. M. Mahmoud, *Microwave Solutions for Ceramic Engineers*, 2005, American Ceramic Society, OH
50. V.P. Paranosenkov, I.Y. Kelina, L.A. Plyasunkova, Y.V. Bykov, *Refractories and Industrial Ceramics*, 2003, vol.44 (4), pp.223-226.
51. S .Vijayan, H. Verma, *Materials Letters*, 2002, vol. 56, pp. 827– 831
52. Z. Xie, C. Wang, X. Fan, Y. Huang, *Materials Letters*, 1999, vol. 38, pp. 190–196
53. S.T. Oh, K. Tajima, M. Ando, T. Ohji, *Materials Letters*, 2001, vol. 48, pp. 215–218
54. Y. Bykov, A. Eremeev, S. Egorov, V. Ivanov, Y. Kotov, V. Khurstov, A. Sorokin, *Nanostructured Materials*, 1999, vol.12, pp. 115-118
55. Z. Zhao, X.J. Li, G. Tao, *Journal of Alloys and Compounds*, 2009, vol.478, pp. 237–239
56. I. Song, L. Wang, M. Wixom, M.T. Thompson, *Journal of Materials Science*, 2000, vol.35, pp. 2611-2617
57. A.A. Bukaemskii, E.N. Fedorova, *Combustion, Explosion, and Shock Waves*, 2008, vol. 44(6), pp. 717–728
58. Y.W. Kim, Y. I. Lee, M. Mitomo, *Journal of Ceramic Society of Japan*, 2006, vol.114(8), pp. 681-685
59. S. Chang, R.H. Doremus, L.S. Schadler, R.W. Siegel, *International Journal of Applied Ceramic Technology*, 2004, vol.1(2), pp. 172-179
60. M.L. Panchula, J.Y. Ying, *Journal of American Ceramic Society*, 2003, vol.86, pp 1121-1127
61. S. Dong, D. Jiang, S. Tan, J. Guo, *Journal of Materials Science Letters*, 1997, vol.16, pp. 1080-1083
62. H. Xu, L. Guo, *Materials Letters*, 2004, vol.58, pp. 1582– 1586

63. M. Mazaheri, A.M. Zahedi, M.M. Hejazi, *Materials Science and Engineering A*, 2008, vol. 492 pp. 261–267.
64. G. Skandan, *Nanostructured Materials*, 1995, vol.5, pp.111–126.
65. M. Trunec, K. Maca, *Journal of American Ceramic Society*, 2007, vol. 90(9), pp. 2735–2740
66. J.G. Li, Y. Wang, T. Ikegami, T. Mori, T. Ishigaki, *Materials Science and Engineering B*, 2005, vol.121 pp. 54–59
67. G. Suárez, Y. Sakka, T.S. Suzuki, T. Uchikoshi, X. Zhu, E.F. Aglietti, *Science and Technology of Advanced Materials*, 2009, vol.10, pp.1-8
68. M. Trunec, K. Maca, Z. Shen, *Scripta Materialia*, 2008, vol.59, pp. 23-26
69. M. Nygren, Z. Shen, *Solid State Sciences*, 2003, vol. 5, pp. 125-131
70. M.S.E.Eskandarany, *Journal of Alloys and Compounds*, 2000, vol. 296, pp. 175–182
71. Y.I. Lee, J.H. Lee, S.H. Hong, D.Y. Kim, *Materials Research Bulletin*, 2003, vol. 38, pp. 925–930
72. B.N. Kim, K. Hiraga, K. Morita, H. Yoshida, T. Miyazaki, Y. Kagawa, *Acta Materialia*, 2009, vol. 57, pp. 1319–1326
73. H. Yoshida, K. Morita, B.N. Kim, K. Hiraga, M. Kodo, K. Soga, T. Yamamoto, *Journal of American Ceramic Society*, 2008, vol.91 (5), pp.1707–1710
74. X. Guo, P. Xiao, J. Liu, Z. Shen, *Journal of American Ceramic Society*, 2005, vol.88 (4), pp. 1026–1029
75. X. Xu, T. Nishimura, N. Hirosaki, R.J. Xie, Y. Zhu, Y. Yamamoto, H. Tanaka, *Journal of American Ceramic Society*, 2005, vol.88 (4), pp. 934–937
76. L. Feher, M. Thumm, K. Ritzhaupt, J. Hans, R. Boehme, A. Weisenburger, *IEEE Transactions on Plasma Science*, 1999, vol. 27(2), pp. 547-554
77. B. H. Kear and L. E. McCandlish, *Nanostructured Materials*, 1993, vol. 3, pp. 19-30.
78. S. Lay, S. Hamar-Thibault, A. Lackner, *International Journal of Refractory Metals and Hard Materials*, 2002, vol. 20, pp. 61-69.
79. M. Sommer, W. D. Schubert, E. Zobetz, P. Warbichler, *International Journal of Refractory Metals and Hard Materials*, 2002, vol. 20, pp. 41-50.
80. K. Hayashi, N. Matsuika, *Journal of Advanced Materials*, 2002, vol. 34, pp. 38-48.
81. P. Seegopaul, L. E. McCandlish, L. Gao, *Proceedings of the Fourteenth Plansee Seminar*, vol. 4, G. Kneringer, P. Rodhammer and P. Wilhartitz (eds.), Plansee AG, Reutte, Austria, 1997, pp. 304-316.
82. J. Hojo, R. Oono, A. Kato, *Journal of Materials Science*, 1980, vol. 15, pp. 2335-2344.
83. L. Zhang, T. E. Madey, *Nanostructured Materials*, 1993, vol. 2, pp. 487-493.
84. H. Suzuki, O. Terada, H. Ike, *Journal of the Japan Society of Powder and Powder Metallurgy*, 1995, vol. 42, pp. 1345-1349.
85. K. Mohan, P. R. Strutt, *Nanostructured Materials*, 1996, vol. 7, pp. 547-555.
86. R. Porat, S. Berger, A. Rosen, *Nanostructured Materials*, 1996, vol. 7, pp. 429-436.

87. D. F. Carroll, *Proceedings of the Fourteenth Plansee Seminar*, vol. 2, G. Kneringer, P. Rodhammer and P. Wilhartitz (eds.), Plansee AG, Reutte, Austria, 1997, pp. 168-182.
88. R. Porat, S. Berger, A. Rosen, *Proceedings of the Fourteenth Plansee Seminar*, vol. 2, G. Kneringer, P. Rodhammer and P. Wilhartitz (eds.), Plansee AG, Reutte, Austria, 1997, pp. 183-196.
89. B. K. Kim, G. H. Ha, G. G. Lee, D. W. Lee, *Nanostructured Materials*, 1997, vol. 9, pp. 233-236.
90. P. Seegopaul, L. E. McCandlish, F. M. Shinneman, *International Journal of Refractory Metals and Hard Materials*, 1997, vol. 15, pp. 133-138.
91. P. Arato, L. Bartha, A. L. Toth, R. Porat, S. Berger, A. Rosen, *Proceedings of the Fourteenth Plansee Seminar*, 1997, vol.2, pp. 658-664.
92. M. J. Yang, R. M. German, *International Journal of Refractory Metals and Hard Materials*, 1998, vol. 16, pp. 107-117.
93. J. M. Doh, J. R. Groza, J. Oakes, *Advances in Powder Metallurgy and Particulate Materials - 1998*, Metal Powder Industries Federation, Princeton, NJ, 1998, pp. 1.105-1.114
94. D. F. Carroll, *International Journal of Refractory Metals and Hard Materials*, 1999, vol. 17, pp. 123-132.
95. R. K. Sadangi, L. E. McCandlish, B. H. Kear, P. Seegopaul, *International Journal of Powder Metallurgy*, 1999, vol. 35, no. 1, pp. 27-33.
96. V. Richter, M. V. Ruthendorf, *International Journal of Refractory Metals and Hard Materials*, 1999, vol. 17, pp. 141-152.
97. C. Carry, J. M. Chaix, J. M. Missiaen, D. Bouvard, *Sintering Science and Technology*, R. M. German, G. L. Messing, and R. G. Cornwall (eds.), Pennsylvania State University, State College, PA, 2000, pp. 283-288.
98. B. K. Kim, G. H. Ha, D. H. Kwon, *Materials Transactions*, 2003, vol. 44, pp. 111-114.
99. T. Lin, L. Zhang, Z. Guo, W. Li, C. Wu, Q. Wu, *Journal of the Japan Society of Powder and Powder Metallurgy*, 2003, vol. 50, pp. 828-831.
100. B. Basu, J. H. Lee, D. Y. Kim, *Journal of the American Ceramic Society*, 2004, vol. 87, pp. 317-319.
101. H. C. Kim, D. Y. Oh, I. J. Shon, *International Journal of Refractory Metals and Hard Materials*, 2004, vol. 22, pp. 197-203.
102. M. I. Alymov, E. I. Maltina, Y. N. Stepanov, *Nanostructured Materials*, 1994, vol. 4, pp. 737-742.
103. G. R. Shaik, W. W. Milligan, *Metallurgical and Materials Transactions*, 1997, vol. 28A, pp. 895-904.
104. J. Freim, J. McKittrick, *Journal of the American Ceramic Society*, 1998, vol. 81, pp. 1773-1780.
105. M. R. Zachariah, M. J. Carrier, *Journal of Aerosol Science*, 1999, vol. 30, pp. 1139-1151.
106. R. S. Iyer, S. M. L. Sastry, *Acta Materialia*, 1999, vol. 47, pp. 3079-3098.
107. T. Moritz, H. Riedel, G. Werner, G. Tomandl, *Journal of Materials Science*, 2000, vol. 35, pp. 2235-2240.

108. H. S. Kim, *Journal of Korean Powder Metallurgy Institute*, 2001, vol. 8, pp. 168-173.
109. D. E. Rosner, S. Yu, *American Institute of Chemical Engineers Journal*, 2001, vol. 47, pp. 545-561.
110. S. H. Park, S. N. Rogak, *Aerosol Science and Technology*, 2003, vol. 37, pp. 947-960.
111. P. Redanz, R. M. McMeeking, *Philosophical Magazine*, 2003, vol. 83, pp. 2693-2714.
112. H. J. Schmid, S. Tejwani, C. Artelt, W. Peukert, *Journal of Nanoscale powders Research*, 2004, vol. 6, pp. 613-626.
113. R. M. German, E. Olevsky, *International Journal of Refractory Metals and Hard Materials*, 2005, vol. 23, pp. 294-300.
114. E. A. Olevsky, B. Kushnarev, A. Maximenko, V. Tikare, M. Braginsky, *Philosophical Magazine*, 2005, vol. 85, pp. 2123-2146.
115. Y. S. Kwon, A. A. Gromov, A. P. Ilyin, A. A. Ditts, J. S. Kim, S. H. Park, M. H. Hong, *International Journal of Refractory Metals and Hard Materials*, 2004, vol. 22, pp. 235-241.
116. G. K. Schwenke, *Proceedings of Fifteenth International Plansee Seminar*, vol. 2, P. Rodhammer and H. Wildner (eds.), Plansee Holding, Reutte, Austria, 2001, pp. 647-661.
117. P. Seegopaul, L. E. McCandlish, *Advances in Powder Metallurgy and Particulate Materials - 1995*, pp. 13.3-13.15.
118. C. H. Allibert, *International Journal of Refractory Metals and Hard Materials*, 2001, vol. 19, pp. 53-61.
119. Y. Hashimasa, M. Okita, S. Mino, N. Ishigaki, *Journal of the Japan Society of Powder and Powder Metallurgy*, 1997, vol. 44, pp. 807-811.
120. E. S. Yoon, J. S. Lee, S. T. Oh, B. K. Kim, *International Journal of Refractory Metals and Hard Materials*, 2002, vol. 20, pp. 201-206.
121. G. G. Lee, G. H. Ha, B. K. Kim, *Powder Metallurgy*, 2000, vol. 43, no. 1, pp. 79-82.
122. J. S. Lee, E. S. Yoon, J. H. Yu, *Proceedings 1998 PM World Congress, Granada Spain*, published on CD by European Powder Metallurgy Association, Shrewsbury, UK, December 1998, no page number.
123. S. S. Ryu, Y. D. Kim, I. H. Moon, *Journal of Alloys and Compounds*, 2002, vol. 335, pp. 233-240.
124. E. S. Yoon, J. H. Yu, J. S. Lee, *Journal of the Japan Society of Powder and Powder Metallurgy*, 1999, vol. 46, pp. 898-903.
125. B. K. Kim and S. H. Hong, *Powder Metallurgy World Congress*, 2000, pp. 682-685.
126. I. H. Moon, S. S. Ryu, J. C. Kim, *Sintering Science and Technology*, R. M. German, G. L. Messing, and R. G. Cornwall (eds.), Pennsylvania State University, State College, PA, 2000, pp. 45-48.
127. J. Fan, B. Huang, X. Qu, K. A. Khalil, *International Journal of Powder Metallurgy*, 2002, vol. 38, no. 2, pp. 56-61.
128. M. N. Avettand-Fenoel, R. Taillard, J. Dhers, J. Foct, *International Journal of Refractory Metals and Hard Materials*, 2003, vol. 21, pp. 205-213.
129. L. P. Dorfman, D. L. Houck, M. J. Scheithauer, *Consolidation of Tungsten-Coated Copper Composite Powder*, internal report, Osram Sylvania, Towanda, PA, 2002.

130. Y.W. Kim, J.Y. Kim, S.H. Rhee, D.Y. Kim, *Journal of the European Ceramic Society*, 2000, vol. 20, pp. 945-949
131. T. Yoshioka, Y. Makino, S. Miyake, H. Mori, *Journal of Alloys and Compounds*, 2006, vol. 408-412, pp. 563-567.
132. V.P. Onbattuvelli, G. Purdy, G. Kim, S. Laddha, S. Atre, Nanotech 2010, Pasadena , CA
133. C.L. Huang, J.J. Wang, C.Y. Huang, *Materials Letters*, 2005, vol.59 (28), pp. 3746-3749.
134. M.C. Rodriguez, A. Munoz, A.D. Rodriguez, *Journal of the European Ceramic Society*, 2006, vol. 26, pp. 2397-2405.
135. R. Chaim, M. Levin, A. Shlayer, C. Estournes, *Advances in Applied Ceramics*, 2008, vol.107(3), pp. 159-169
136. M. Bothara, Sintering of nanocrystalline silicon carbide in plasma pressure compaction system, PhD Thesis, 2007, Oregon State University
137. R. M. German, *Sintering Theory and Practice*, John Wiley and Sons, New York, NY, 1996, pp. 67-141.
138. M. F. Ashby, "A First Report on Sintering Diagrams," *Acta Metallurgica*, 1974, vol. 22, pp. 275-289.
139. S. G. Dubois, *Sintering High Surface Area Tantalum Powder: Simulation and Experimental Verification*, MS Thesis, Pennsylvania State University, University Park, PA, 1995.
140. S. J. Park (Mississippi State University), "Mapping the Densification and Grain Growth of Nanoscale Tungsten Carbide," unpublished research report to Kennametal, Latrobe, PA, September 2005.
141. S. H. Chung, Y. S. Kwon, C. M. Hyun, K. T. Kim, M. J. Kim, R. M. German, *Advances in Powder Metallurgy and Particulate Materials - 2004*, no. 8, pp. 26-39.
142. R. M. German, S. H. Chung, D. Blaine, *Materials Processing and Design: Modeling, Simulation and Applications*, Proceedings NUMIFORM 2004, S. Ghosh, J. C. Castro, and J. K. Lee (eds.), Springer Verlag, New York, NY, 2004, pp. 1320-1325.
143. C. Binet, K. L. Lencoski, D. F. Heaney, R. M. German, *Metallurgical and Materials Transactions*, 2004, vol. 35A, pp. 3833-3841.
144. M. J. Yang, *Binder System Chemistry Analysis and Defect Control of Cemented Carbides in Powder Injection Molding Processing*, PhD Thesis, Pennsylvania State University, University Park, PA, 1995.
145. R. M. German, *Particle Packing Characteristics*, Metal Powder Industries Federation, Princeton, NJ, 1989, pp. 68-73.
146. R. M. German, *Powder Metallurgy Science*, second edition, Metal Powder Industries Federation, Princeton, NJ, 1994, pp. 205-227.
147. S. Shima and M. Oyane, "Plasticity Theory for Porous Metals," *International Journal of Mechanical Sciences*, 1976, vol. 18, pp. 285-291.
148. N. C. Kothari, *Powder Metallurgy*, 1964, vol. 7, pp. 251-260.
149. N. C. Kothari, *Journal of the Less-Common Metals*, 1963, vol. 5, pp. 140-150.
150. I. H. Moon, Y. S. Kwon, *Powder Metallurgy*, 1974, vol. 17, pp. 363-369.
151. R. M. German, Z. A. Munir, *Metallurgical Transactions*, 1976, vol. 7A, pp. 1873-1877.

152. V. V. Panichkina, V. V. Skorohod, N. P. Pavlenko, *Soviet Powder Metallurgy and Metal Ceramics*, 1977, vol. 16, pp. 950-951.
153. R. D. McIntyre, *Transactions of the American Society for Metals*, 1963, vol. 56, pp. 468-476.
154. T. Vasilos, J. T. Smith, *Journal of Applied Physics*, 1964, vol. 35, pp. 215-217.
155. S. Gowri, J. A. Lund, *Tungsten and Tungsten Alloys - 1992*, A. Bose and R. J. Dowding (eds.), Metal Powder Industries Federation, Princeton, NJ, 1993, pp. 183-194.
156. L. C. Chen, *International Journal of Refractory Metals and Hard Materials*, 1994, vol. 12, pp. 41-51.
157. C. Selcuk, R. Bentham, N. Morley, J. V. Wood, *International Journal of Powder Metallurgy*, 2003, vol. 39, no. 6, pp. 45-51.
158. A. Frisch, W. A. Kaysser, G. Petzow, *Advances in Powder Metallurgy*, 1989, vol. 2, pp. 431-444.
159. T. E. M. Staab, R. Krause-Rehberg, B. Vetter, B. Kieback, G. Lange, and P. Klimanek, *Journal of Physics: Condensed Matter*, 1999, vol. 11, pp. 1787-1806.
160. R. M. German, *Powder Metallurgy*, 1979, vol. 22, pp. 29-30.
161. B. R. Patterson, Y. Liu, J. A. Griffin, *Metallurgical Transactions*, 1990, vol. 21A, pp. 2137-2139.
162. J. H. Rosolowski, C. Greskovich, *Journal of the American Ceramic Society*, 1975, vol. 58, pp. 177-182.
163. C. Greskovich, K. W. Lay, *Journal of the American Ceramic Society*, 1972, vol. 55, pp. 142-146.
164. T. K. Gupta, *Journal of the American Ceramic Society*, 1972, vol. 55, pp. 276-277.
165. T. K. Gupta, R. L. Coble, *Journal of the American Ceramic Society*, 1968, vol. 51, pp. 521-525.
166. I. Nettleship, R. J. McAfee, W. S. Slaughter, *Journal of the American Ceramic Society*, 2002, vol. 85, pp. 1954-1960.
167. T. S. Yeh, M. D. Sacks, *Journal of the American Ceramic Society*, 1988, vol. 71, pp. C484
168. T. A. Dorling, R. L. Moss, *Journal of Catalysis*, 1966, vol. 5, pp. 111-115.
169. F. B. Swinkels, M. F. Ashby, *Acta Metallurgica*, 1981, vol. 29, pp. 259
170. A. S. Helle, K. E. Easterling, M. F. Ashby, *Acta Metallurgica*, 1985, vol. 33, pp. 2163
171. R. M. McMeeking, L. Kuhn, *Acta Metallurgica Materialia*, 1992, vol. 40, pp. 961
172. E. Olevsky, V. Skorohod, M. Bohsmann, G. Petzow, *Sintering and Materials*, International Academic Publishers, Wuhan, China, pp. 9-14, 1995.
173. E. A. Olevsky, *Materials Science and Engineering*, 1998, vol. 23, pp. 41
174. V. Tikare, M. V. Braginsky, E. A. Olevsky, R. T. Dehoff, *Sintering Science and Technology*, R. M. German, G. L. Messing, and R. G. Cornwall (ed.), Pennsylvania State University, State College, PA, pp. 405-409, 2000

175. V. Tikare, E. A. Olevsky, M. V. Braginsky, Recent Developments in Computer Modeling of Powder Metallurgy Processes, A. Zavaliangos and A. Laptev (eds.), ISO Press, Ohmsha, Sweden, pp. 94-104, 2001
176. H. Riedel, D. Meyer, J. Svoboda, H. Zipse, *International Journal of Refractory Metals and Hard Materials*, 1994, vol. 12, pp. 55
177. T. Kraft, H. Riedel, *Powder Metallurgy*, 2002, vol. 45, pp. 227
178. P. E. McHugh, H. Riedel, *Acta Metallurgica Materialia*, 1997, vol. 45, pp. 2995
179. D. Bouvard, T. Meister, *Modeling and Simulations in Material Science and Engineering*, 2000, vol. 8, pp. 377
180. A. C. F. Cocks, *Acta Metallurgica Materialia*, 1994, vol. 45, pp. 2191
181. Y. S. Kwon, K. T. Kim, *Journal of Engineering Materials and Technology*, 1996, vol. 118, pp. 448
182. Y. S. Kwon, Y. Wu, P. Suri, R. M. German, *Metallurgical and Materials Transactions A*, 2004, vol. 35, pp. 257
183. R. K. Bordia, G. W. Scherer, *Acta Metallurgica*, 1998, vol. 36, pp. 2393
184. R. K. Bordia, G. W. Scherer, *Acta Metallurgica*, 1998, vol. 36, pp. 2399
185. R. K. Bordia, G. W. Scherer, *Acta Metallurgica*, 1998, vol. 36, pp. 2411
186. R. M. German, S. J. Park, S. H. Chung, J. L. Johnson, Proceedings of the 2006 International Conference on Tungsten, Refractory and Hardmetals IV, A. Bose and R. Dowding (eds.), Metal Powder Industries Federation, Princeton, NJ, 2006, pp. 71-82.
187. S.J. Park, S. H. Chung, J. L. Johnson, R. M. German, Accepted for publication to *Materials Transactions*, 2006.
188. G. Aggarwal, S. J. Park, I. Smid, R. M. German, Accepted for publication to *International Journal of Refractory Metals & Hard Materials*, 2006.
189. J. L. Johnson, J. J. Brezovsky, R. M. German, *Metallurgical and Materials Transactions*, 2005, vol. 36A, pp. 2807-2814.
190. D. C. Blaine, P. Garg, R. M. German, "Modeling of Fine Molybdenum Powder for Press and Sinter Processing," *Proceedings of the 4th International Conference on Science, Technology and Applications of Sintering*, D. Bouvard (ed.), Institut National Polytechnique de Grenoble, Grenoble, France, 2005, pp. 268-271.
191. S. J. Park, S. H. Chung, J. L. Johnson, R. M. German, *International Conference on Powder Metallurgy*, Metal Powder Industries Federation, San Diego, USA, 2006.
192. S. Kim, S.J. Park, S.G. Kim, R. M. German, *MS&T '06*, Cincinnati, OH, 2006.
193. S.J. Park, K. Cowan, J.L. Johnson, R. M. German, *International Conference on Powder Metallurgy*, Metal Powder Industries Federation, San Diego, USA, 2006.
194. M. I. Baskes, J. S. Nelson, and A. F. Wright, *Physical Review B*, 1989, vol. 40, pp. 6085
195. M. I. Baskes, *Physical Review B*, 1992, vol. 46, pp. 2727
196. A. Moitra, S. Kim, J. Houze, B. Jelinek, S.J. Park, R. M. German, Seong-Gon Kim, *Journal of Physics D: Applied Physics*, 2008, vol. 41, 185406
197. W. Kohn, L. J. Sham, *Physical Review*, 1965, vol. 140, A1133

198. G. Kresse, J. Furthmüller, *Physical Review B*, 1996, vol. 54 (16), pp. 11169
199. J. Houze, Sungho Kim, Seong-Jin Park, R. M. German, M. F. Horstemeyer, S-G. Kim, *Journal of Applied Physics*, 2008, vol. 103, pp. 106-103
200. D. Ehre, R. Chaim, *Journal of Materials Science*, 2008, vol. 43, pp. 6139–6143
201. T. Ohji, *Scripta Materialia*, 2001, vol. 44, pp. 2083–2086
202. B.N. Kim, K. Hiraga, K. Morita and Y. Sakka, *Nature*, 2001, vol. 413, pp. 288-291
203. X. Xu, T. Nishimura, N. Hirosaki, R.J. Xie, Y. Zhu, Y. Yamamoto, H. Tanaka, *Acta Materialia*, 2006, vol. 54, pp. 255–262
204. M.J. Mayo, *Nanostructured Materials*, 1997, vol.9, pp. 717-726
205. R. Vaben, D. StoËver, *Philosophical Magazine B*, 1997, vol. 76(4), pp. 585-591
206. F. Cernuschi, P.G. Bison, S. Marinetti, P. Scardi, *Acta Materialia*, 2008, vol 56, pg. 4477-88
207. Y. Liu, Y.F. Gao, S.Y. Tao, X.M. Zhou, H.J. Luo, *Surface and Coatings Technology*, 2009, vol. 203, pp. 1014-1019
208. D.L. Burris, W.G. Sawyer, *Wear*, 2006, vol.260, pp. 915–918
209. M. Uota, H. Arakawa, N. Kitamura, T. Yoshimura, J. Tanaka, T. Kijima, *Langmuir*, 2005, vol. 21, pp. 4724-4728
210. J. F. Bartolome, A.H.D. Aza, A. Marti´n, J.Y. Pastor, J. Llorca, R. Torrecillas, G. Bruno, *Journal of American Ceramic Society*, 2007, vol.90 (10), pp. 3177-3184
211. R. Thomas, *Micromachining Technology Map*, SRI Consulting Business Intelligence, Palo Alto, CA, 2001.
212. M. Ritter, *Ceramic Bulletin*, 2002, vol. 81, no. 3, pp. 33-36.
213. B. Wittmann, W. D. Schubert, B. Lux, *International Journal of Refractory Metals and Hard Materials*, 2002, vol. 20, pp. 51-60.
214. B. Roebuck, M. G. Gee, R. Morrell, *Proceedings Fifteenth International Plansee Seminar*, 2001, vol. 4, pp. 245-266.
215. H. C. Kim, I. J. Shon, J. E. Garay, Z. A. Munir, *International Journal of Refractory Metals and Hard Materials*, 2004, vol. 22, pp. 257-264.
216. C.H. Chang, B.K.Paul, V. Remcho, S.V. Atre, and J.E. Hutchison, *Journal of Nanoparticle Research*, 2008, vol. 10, pp. 965-975.

List of Figures

Figure 3.1: An example of integrating bulk synthesis with nanoscale powders consolidation

List of Tables

Table 3.1: Chemical methods for synthesizing ceramic nanoparticles

Table 3.2: Comparison of the ceramic net-shaping processes

Table 3.3: Effects of material and process parameters on densification and grain growth for conventional processes

Table 3.4: Effect of materials and process parameters on densification and grain growth for recent processes

Table 3.5: The effect of particle size and specific area on green density

Table 3.6: Example of Nanoscale Sintering Models

Table 3.7: Applications of sintering models

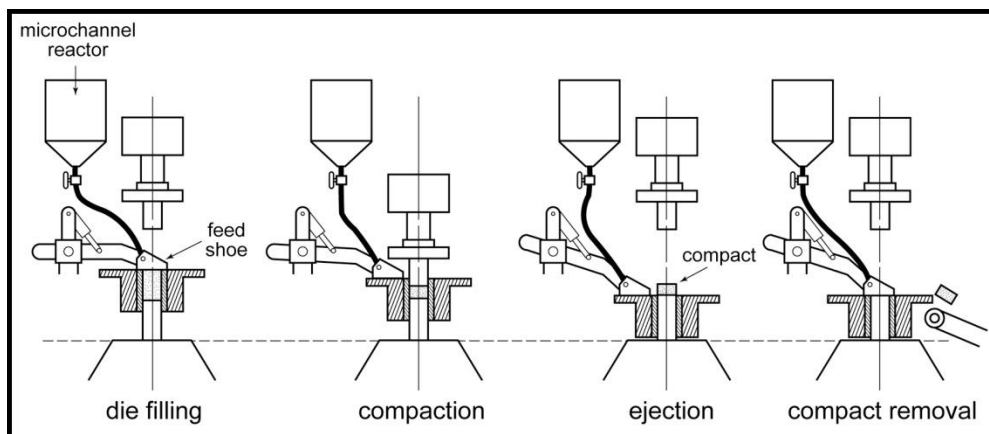


Figure 3.1: An example of integrating bulk synthesis with nanoscale powders consolidation

Table 3.1: Chemical methods for synthesizing ceramic nanoparticles

Method	Reference		Starting material	Resultant Material	Atm.	Particle Size (nm)	Particle Shape
	#	Author					
Precipitation	20	Shi and Verweij	Zirconium chloride	Zirconia	-NA-	10	-
	21	Yang et al	Vanadium chloride and tin chloride	Vanadium doped tin dioxide	Air	7.7	-
Spray pyrolysis	22	Trejo et al	Cerium nitrate and yttrium nitrate	Yttrium doped ceria	Air	200	Spherical
	23	Li et al	Aluminum chloride and sodium nitride	Aluminum nitride	-	5	Cubic
Sol-gel Method	24	Boddu et al	Magnesium hydroxide	Magnesium oxide	NA	200	Corraline
	25	Isley and Penn	Titanium isopropoxide	Titanium dioxide	NA	27.6	-
Hydrothermal synthesis	26	Zhang et al	Calcium nitrate and disodium hydrogen phosphate	Hydroxyapatite	Air	5	Platelet
	27	Yin et al	Titanium chloride	Titanium dioxide		11	Spherical
	28	Lee et al	Titanium acylate and barium hydroxide	Barium Titanate		100	Agglomerate
Carbothermal reduction	29	Meng et al	Silica	Silicon carbide	Ar	15	Nanowires
	30	Sarkar et al	Titanium dioxide	Titanium carbide		5	Oval

Table 3.1: Chemical methods for synthesizing ceramic nanoparticles (contd.)

Method	Reference		Starting material	Resultant Material	Atm.	Particle Size (nm)	Particle Shape
	#	Author					
CRN	31	P.V. Umnuay	Silicon monoxide	Silicon nitride	NH ₃	47	Spherical
	32	Joo et al	Alumina	Aluminum nitride	N ₂	-	-
	33	Kuang et al					Cubic
Direct nitridation	34	Lei et al	Aluminum	Aluminum nitride	N ₂	80	Nanowires
	35	Radwan and Bahgat					-
	36	Imamura et al	Cerium hydride	Cerium nitride	NH ₃	-	-
CVD	37	Akurati et al	Tetraisopropyl orthotitanate	Titanium dioxide	-	4.5	Spherical
	38	Azuma et al	Trimethyl gallium	Gallium nitride	NH ₃	30	Hexagonal

Table 3.2: Comparison of the ceramic net-shaping processes

Characteristics	Hot Pressing	Slip Casting	Machining	Injection Molding	Pyrolysis of Pre-Ceramic Polymers	Robocasting
Density	95-100%	95-99%	100%	90-100%	>95%	95-99%
Surface Finish	< 2 μm	3 μm	0.4-2 μm	0.4 -0.8 μm	-	<1 μm
Secondary Machining	Required	Required	-	Nil	Nil	Nil
Wall Thickness	>2mm	>5mm	>2mm	10 μm	>0.5 mm	<100 μm
Dimensional Tolerance	Poor	Poor	Poor	Close	Close	Close
Shape Complexity	Medium	Medium	High	High	High	-
Production Rate	Medium	Low	Low	High	Low	High

Table 3.3: Effects of material and process parameters on densification and grain growth for conventional processes

#	Author	System	Initial Particle Size (nm)	Sintering aid		Net shaping and/or densification via (with pressure in MPa)	Sintering Conditions			% relative density	Final grain size (nm)
				Nature	% content		Atm.	Temp (°C)	Hold time (hrs)		
58	Kim et al	SiC	30	Al ₂ O ₃ -Y ₂ O ₃ -CaO	7-2-1	HP (25)	Ar	1750	0.5	95.6	100
								1800			170
								1850			300
59	Chang et al	Al ₂ O ₃	23	-		HP (40)	Ar	1345	1	58	65
				MgO	0.1	HP (60)				99	65
60	Panchula and Ying	AlN	100	Additive Free		HP (100)	He/NH ₃	1900	2	100	-
				Y ₂ O ₃	4	CIP (400)				99.3	
				Additive Free						98	
62	Xu and Gao	BaTiO ₃	80	-		CIP (130)		1250	5	96.5	80
			150							94.7	150
63	Mazaheri et al	8 mol.% YTZ	25	-		CIP (600)		1500	5	97	2000
64	Skandan	3 mol.% YTZ	9	-		CIP (400)		1125	1.33	100	70
65	Trunec and Maca	ZrO ₂	10	Y ₂ O ₃	3	CIP (300)		1100	4	99.7	85
66	Li et al	CeO ₂	12.6	-		CIP (300)		1000	4	99	262
		Sm doped CeO ₂	6								132
		Gd doped CeO ₂	6.6								117
67	Suarez et al	ZrO ₂	75	Y ₂ O ₃	3	Slip cast and CIP (392)		1250	5	99.5	113
		3 mol.% YTZ	65	-							175
50	Paranosenkov et al	Si ₃ N ₄	25	Al ₂ O ₃ -Y ₂ O ₃		1-9	HP(500)	N ₂	1850	3	93
61	Dong et al	SiC	60	-		HIP (200)	Ar	1850	1	-	100

Table 3.4: Effect of materials and process parameters on densification and grain growth for recent processes

#	Author	System	Initial Particle Size (nm)	Sintering aid		Net shaping and/or densification via (with pressure in MPa)	Sintering Conditions			% relative density	Final grain size (nm)
				Nature	% content		Atm.	Temp (°C)	Hold time (hrs)		
67	Suarez et al	ZrO ₂	75	Y ₂ O ₃	3	FAC (150)	-	1150	0.5	90	115
		3 mol.% YTZ	65	-							
94	Bothara	SiC	750	AlN-Y ₂ O ₃	5-5	FAC (50)	Ar	1700	1	99.5	
68	Trunec et al	ZrO ₂	12	Y ₂ O ₃	1.5	FAC (500)	-	1000	0.05	99.4	70
69	Nygren and Shen	ZnO	-	-		FAC (50)	Vac	850	0.05	100	-
		ZrO ₂	60	Y ₂ O ₃	5			1100			<100
		Al ₂ O ₃	400	-				1250			500
		Si ₃ N ₄	-	Al ₂ O ₃ -Y ₂ O ₃	2.5-7.5			1500	0.05		-
70	Eskandarany	WC	7	MgO	18	FAC (38.2)	Vac	1690	0.05	99.7	25
71	Lee et al	TiO ₂	20	-		FAC (62)		800	1	99	200
72	Kim et al	Al ₂ O ₃	150			FAC (80)		1150	0.33	-	290
73	Yoshida et al	Y ₂ O ₃	20			FAC (83)		1050	1	97.3	500
74	Guo et al	Hydroxyapatite	84			FAC (50)		825	3	98.6	130
75	Xu et al	Si ₃ N ₄	500			Al ₂ O ₃ -Y ₂ O ₃	3-5	FAC (30)	N ₂	1600	0.08
50	Paranosenkov et al	Si ₃ N ₄	25	Al ₂ O ₃ -Y ₂ O ₃	1-9	UP(500); Microwave (-)	-	1750	-	93	Non-uniform
76	Feher et al	Si ₃ N ₄	-	Y-ZrO ₂	20	mm-wave (30 GHz)	N ₂	1575	Nil	100	<100
53	Oh et al	Al ₂ O ₃	150	ZrO ₂	10	CIP (200); Microwave (28 GHz)	Air	1200	-	62.2	-
51	Vijayan and Varma	Hydroxyapatite	35	-		Microwave (2.45 GHz)	-	1200	0.08	95	200
52	Xie et al	Ce-Y-ZrO ₂	100	-		CIP (220); Microwave (2.45 GHz)	-	1400	0.25	99.5	650

Table 3.5: The effect of particle size and specific area on green density

n-SiC (Kim et al, 2006, [58])			n-ZrO₂ (Trunec and Maka, 2007, [68])		
Particle size (nm)	Specific surface area (m²/g)	Green density (UP at 25MPa)	Particle size (nm)	Specific surface area (m²/g)	Green density (CIP at 300 MPa)
20	94	39	8	123	42
25	71	48	23	46	55
30	48	50	44	23	53
			62	16	58

Table 3.6: Example of Nanoscale Sintering Models

Alymov et al. (1994) [102]	W, Mo, Ag, Cu	time-dependent initial stage sintering neck growth for loose nm powders
Shaik & Milligan (1997) [103]	mechanically alloyed steel	density, grain size, properties for nm scale powders consolidated using forging or hot isostatic pressing
Freim & McKittrick (1998) [104]	Al ₂ O ₃ -ZrO ₂	density and microstructure predictions for mixed nm powder composites
Zachariah & Carrier (1999) [105]	Si	grain coalescence as a function of time assuming mixtures of diffusion and viscous flow for nm spheres
Iyer and Sastry (1999) [106]	MoSi ₂ , Cu	density predictions versus time applied to nm powders with different pressures, temperatures, and impurity levels
Moritz et al. (2000) [107]	TiO ₂	drying, sinter density, and shape predictions for viscous nm solids with particle packing gradients as formed by centrifugal compaction
Kim (2001) [108]	Cu	strength and ductility predictions for creep deformation of nm particles based on grain boundary diffusion and assumed grain size distribution behavior
Rosner & Yu (2001) [109]	not applied to any material	predictions of agglomerate size distribution based on nm particle coagulation and sintering as driven by surface area reduction
Park & Rogak (2003) [110]	TiO ₂	agglomerate size predictions based on sintering, grain growth, and coagulation for assumed nm particle distributions and sintering rates
Redanz & McMeeking (2003) [111]	not applied to any material	pressure-assisted sintering densification for ideal spheres in ideal green body, adjustable solid-vapor dihedral angle,
Schmid et al. (2004) [112]	not applied to any material	grain growth and agglomerate size predictions for diffusion controlled sintering of nm spheres with fractal behavior,
German & Olevsky (2005) [113]	W	density, grain size, strength predictions for various particle sizes and green densities assuming traditional press-sinter processing cycles
Olevsky et al. (2005) [114]	not applied to any material	anisotropic shrinkage and microstructure predictions using multiple scale sintering model for anisotropic particles,

Table 3.7: Applications of sintering models

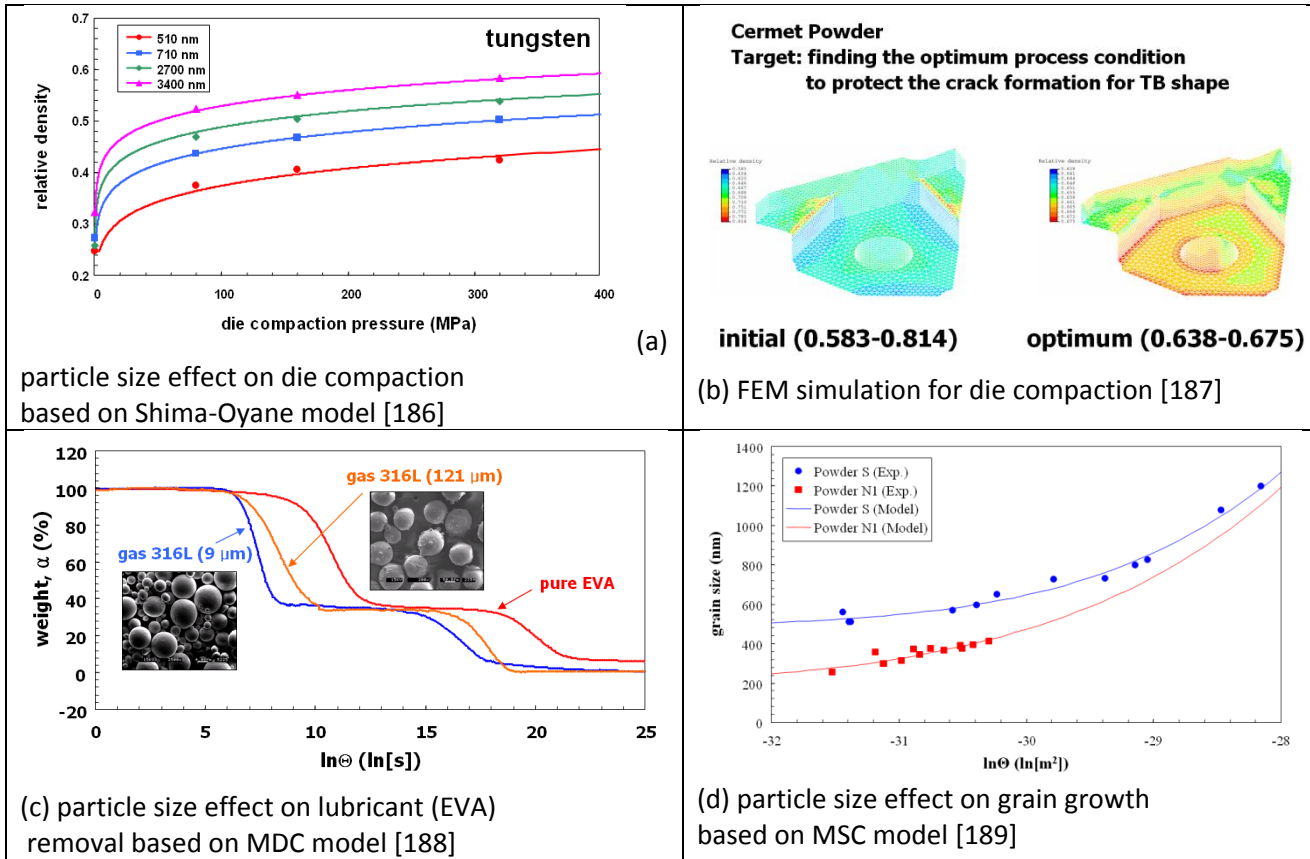
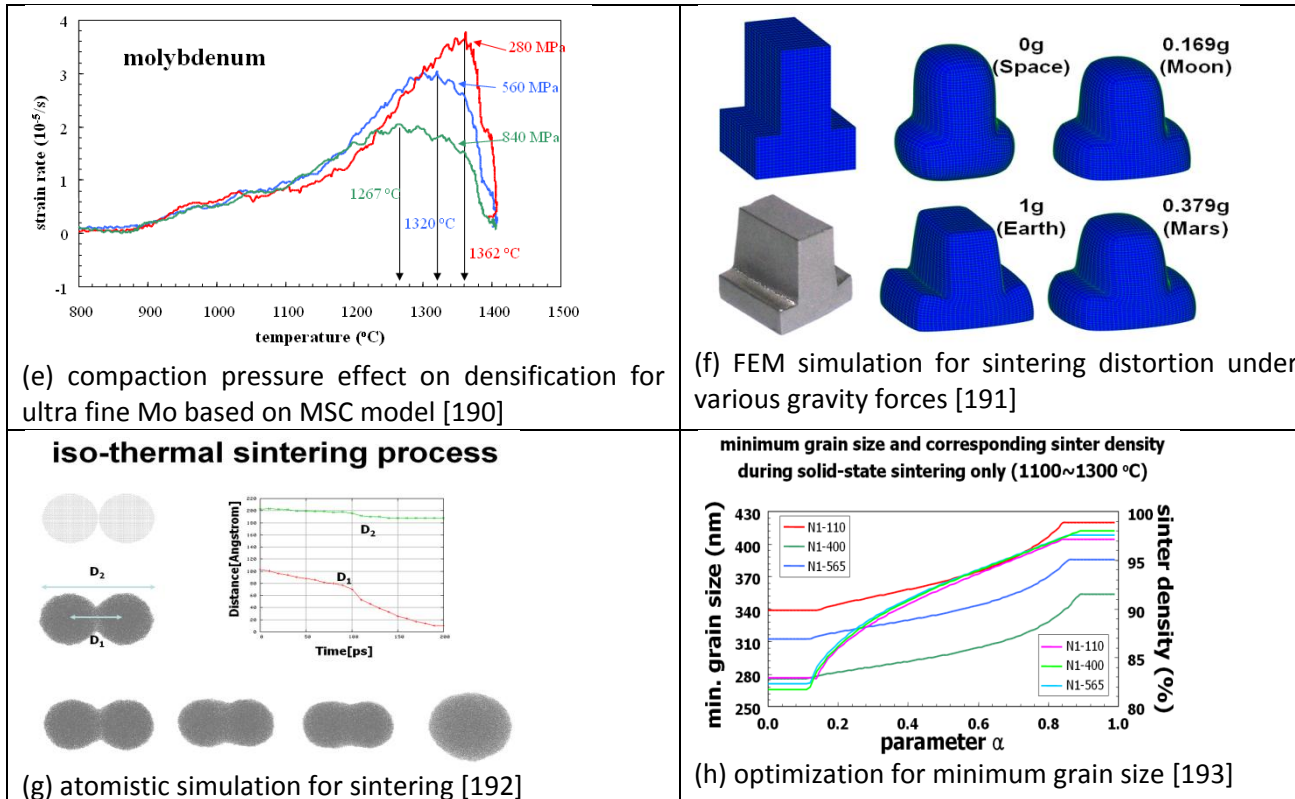


Table 3.7: Applications of sintering models (contd.)



(e) compaction pressure effect on densification for ultra fine Mo based on MSC model [190]

(f) FEM simulation for sintering distortion under various gravity forces [191]

(g) atomistic simulation for sintering [192]

(h) optimization for minimum grain size [193]

CHAPTER 4

The Effect of Nanoparticle Addition on the Solids Loading of SiC and AlN Powder-Polymer Mixtures

Abstract

The development of methods to increase sintered density and improve dimensional tolerances is a crucial issue in powder metallurgy and ceramic processing. Increasing the packing density of starting powders is one effective route to achieve high sintered density and dimensional precision. The current paper presents an in-depth study on the effect of nanoparticle addition on the powder content of SiC and AlN powder-polymer mixtures. In particular, bimodal mixtures of nanoscale and sub-micrometer particles was found to have significantly increased powder volume fraction (solids loading) in the mixtures for injection molding. The implication of nanoparticle additions on the powder injection molding cycle is discussed by studying the effect of nanoparticle addition on the powder-polymer mixtures' rheological properties.

4.1. Introduction

Higher green density and homogeneity of powder packing in powder-polymer mixtures are important for improving the sintered density and ensuing properties [1-3]. Prior studies have focused on the role of organic additives to increase packing and homogeneity in suspensions by steric or electrostatic stabilization [2-5]. Fine powders are desirable in a suspension since they exhibit enhanced densification behavior during with their high surface area [6-9]. For example, Trunec and Makka showed an increase in sintered density by reducing the particle size of zirconia [6]. However, smaller particles also agglomerate, increase the mixture viscosity, reduce the solids loading and display slower debinding rates compared to larger particles [10-12]. Prior studies have also examined the merits of using a wide particle size distribution where small particles fit into the interstitial spaces between large particles [13-16]. However, size segregation is possible with such particle distribution which in turn can lead to inhomogeneous microstructure [17]. Different bimodal mixture models have been proposed in the past by to predict particle packing behavior [18-21]. However, their applicability to nanoscale particle sizes where agglomeration dominates has not received much attention, especially from the perspective of powder processing into net-shaped architectures.

In the current work, bimodal microscale (μ) and nanoscale (n) powder mixtures of AlN were mixed in different ratios with a polymer phase. The effect of the n-AlN content on powder packing was studied and the bimodal μ -n powder mixture providing the maximum powder-binder mixture density was determined. Additionally, a comparative study between monomodal and bimodal powder-binder mixtures was performed to understand the effect of nanoparticle addition on rheological properties. A similar set of experiments was also conducted to extend this study to bimodal μ -n SiC powder mixtures. These experiments show a surprising result that mixtures of fine particles with poor packing characteristics display vastly increased solids loading (volume fraction) in the powder-polymer mixtures. The rheological behavior of such mixtures and the implications for processing by powder injection molding (PIM), extrusion, slip casting and tape casting are discussed.

4.2. Experimental Section

4.2.1. Materials:

The starting powder materials contain as-received., commercially available AlN, with Y_2O_3 and α -SiC with AlN- Y_2O_3 as the sintering additives. The commercially available nanosized SiC and

AlN were used as received. Similar to the earlier reports on PIM, a multicomponent polymer system based on paraffin wax, polypropylene is chosen as the binder to facilitate a multi-step debinding process [22, 23].

4.2.2. Instrumentation:

Torque rheometry on different ratios of particle sizes was performed in the Intelli-Torque Plasticorder (Brabender) with a maximum chamber volume of 46 cc. The monomodal and bimodal powder-polymer mixture formulations thus determined were then scaled-up in production on a 27 mm co-rotating twin-screw extruder (Entek Extruders) with a L/D ratio of 40. The density for all the extruded mixtures was measured with a lab-built Archimedes apparatus. Rheological characteristics of the extruded mixtures were examined on a Goettfert Rheograph 6000 capillary rheometer at different temperatures (140-180°C). A Rabinowitsch correction was applied to the viscosity data. Micrographs of the thermally debound powder samples were taken with a QuantaTM –FEG (FEI) dual beam scanning electron microscope (SEM) coupled with an energy dispersive X-ray spectrometer (EDS).

4.2.3. Torque Rheometry - Experimental Procedure:

A homogeneous powder-polymer mixture is required for consistent part fabrication using the PIM process [22, 23]. The maximum volumetric powder-polymer ratio at which the suspension viscosity is still finite and the powder particles are tightly packed and molten polymer fills all the voids between the particles is called the critical solids loading (Φ_C) [23]. Φ_C was measured by torque rheometry with a starting batch of 70 wt% powder content mixed at 160 °C. The polymer mixture was initially added to the chamber and allowed to melt while being mixed at a programmed speed of 50 rpm. The bimodal μ -n powder mixtures were roll-milled for 30 minutes prior to mixing with the polymer mixture. The roll milled powder mixtures were then slowly added and allowed to blend with the polymers until the mixing torque stabilized. Additional doses of premixed powders were incrementally added to raise the solids loading and the torque was again allowed to stabilize. This procedure was repeated until the mixing torque either did not stabilize or rapidly decreased, both indicating an excess amount of powder. A similar procedure was performed for all bimodal μ -n powder ratios and repeated thrice to check for the reproducibility. A solids loading ($\Phi < \Phi_C$) was scaled up by twin screw extrusion and pelletized for further characterization. For scale up, a solids loading less than the critical solids loading was chosen for processing flexibility to minimize the impact of large viscosity changes for minor variations in particle content that is typically observed for concentrated suspensions [24].

4.3. Results and Discussion

Figure 1 represents the mixing torque as a function of time for incremental powder additions for 100% μ -AlN (a) and μ -SiC (b) powders. It can be seen that for any addition, there is an initial increase in mixing torque followed by a stabilization to a lower value when the mixture attains a maximum homogeneity level possible at the shear rate. Further, the mixing torque increases with increasing powder content until a critical point following which the mixing torque falls indicating an excess of powder in the mixture.

There is an upper limit to powder content that is possible in a powder-polymer mixture for any particle size distribution. The particle size distribution was varied by adding nanoparticles to the μ -sized powders. The fraction of n-sized particles in the bimodal μ -n powder mixture was plotted against the maximum powder content in the resulting powder-polymer mixtures as shown in the **Figure 4.2**. Thus, a maximum powder content of 90 wt. % (\sim critical solids loading (Φ_c) of 71 vol.%) in the powder-polymer mixture was achieved for the bimodal AlN mixture containing 82 wt.% μ - AlN and 18 wt.% n-AlN (**Figure 4.2a**). Similarly, a maximum powder content of 87 wt. % (Φ_c - 65 vol.%) in the powder-polymer mixture was achieved with a particular bimodal mixture containing 90 wt.% μ - SiC and 10 wt.% n-SiC (**Figure 4.2b**). Comparative experiments for monomodal 100 wt.% μ -SiC and μ -AlN systems, resulted in a maximum powder content of only 81 wt. % (53 vol.% - SiC and 54 vol.% - AlN) in the powder-polymer mixture. Further, the monomodal 100 wt.% n-SiC and n-AlN systems showed a maximum powder content below 75 wt. %. Thus, a synergistically improved packing tendency can be observed for the mixtures of microscale and nanoscale powders.

SEM was performed on the monomodal and bimodal samples to examine the increase in the powder content with the nanoparticle addition for AlN and SiC systems (**Figures 4.3** and **4.4**). It can be noticed that in the bimodal powder-polymer mixtures (**Figures 4.3b** and **4.4b**), the nanoparticles fit into the interstitial spaces between the microparticles for the AlN and SiC systems, respectively.

The mixing torque is plotted as a function of solids loading in **Figures 4.5a** and **4.5b** for the monomodal and bimodal AlN and SiC systems . From the figure, it can be noticed mixing torque increases as a function of solids loading for all four material systems. In addition, the mixing torque was found to generally decrease by the addition of nanoparticles in both AlN and SiC mixtures, as shown in the **Figure 4.5a** and **4.5b** respectively. This behavior can be attributed to a

lower suspension viscosity in bimodal mixtures, possibly due to the higher packing capability observed in the bimodal mixtures leading to lesser hydrodynamic friction between the powder and polymer phases. Such observations can be extended to predict and compare the rheological behavior of the monomodal and bimodal mixtures. For example, Suri et al (**Equation 4.1**) that the viscosity of the powder-polymer mixture is dependent to the hydrodynamic stress (σ_H), mixer's gap thickness (H), screw speed (U_0) and geometric factor (S)[15]:

$$\eta_{mixture} = \frac{3}{10} \left(\frac{(1+S)*H}{U_0} \right) * \sigma_H \quad (4.1)$$

Additionally, higher mixing torque values were observed for SiC mixtures compared to AlN mixtures at a comparable solids loading. This observation is likely be due to the shape irregularity in the SiC particles relative to the AlN particles as seen in **Figures 4.3** and **4.4**. Further studies on this behavior could provide reason for the fluctuations in the torque values for lower solids loading SiC mixtures. From the above findings, formulations with optimal solids loading (Φ) of 65 and 58 vol.% for bimodal SiC and AlN respectively, were compounded using twin screw extrusion. The conditions used for the scale-up are listed in the **Table 4.1**. Similarly, powder-polymer mixtures of monomodal μ -sized SiC and AlN powders with Φ of 51 and 52 vol.%, were also compounded for comparison purposes.

Nanoparticles are well known to exhibit poor packing density owing to their tendency to agglomerate. Hence, the current finding of using nanoparticles to increase the solids loading appears to be rather interesting. However, successful processing of these bimodal mixtures (with higher powder content) is contingent upon the in-depth understanding of the rheological behavior of such mixtures. Thus, the apparent viscosity - shear rate curves of the extruded AlN and SiC powder-polymer mixtures were measured at different temperatures, as shown in the **Figures 4.6** and **4.7**, respectively. In addition, the viscosity of the binder mixture (**Figure 4.8**) was also measured to model the rheological behavior of bimodal suspensions.

Irrespective of the powder composition, the viscosity of all the powder-polymer mixtures decreased with an increase in shear rate, indicating pseudoplastic behavior. This was confirmed by evaluating the slope of such viscosity plots which represent (n-1), where “n” is the power law coefficient. The plots in our current case hold a negative slope with value of (1-n) [25]. **Table 4.2** lists the “n” values of the powder-polymer mixtures and the binder mixtures. These values once again confirm the absence of dilatant behavior, indicating no powder-binder separation. The reduced “n” values with the addition of nanoparticles indicate a possible increase in the shear-

thinning behavior. An elaborate analysis is however required to evaluate the role of nanoparticles addition on such pseudoplastic behavior by fitting the rheological data into a detailed modified Cross-WLF equation. The higher coefficient values of monomodal SiC mixture compared to that of AlN mixture necessitates future studies on the effect that particle shape has on the flow behavior. Additionally, the viscosity of all the powder-polymer mixtures tends to decrease with increasing temperature. This may be attributed to powder volume reduction arising from binder expansion and increased disentanglement of the molecular chains under shear during heating [4].

The viscosity of both AlN (**Figure 4.6b**) and SiC bimodal powder-polymer mixtures (**Figure 4.7b**) was found to be higher than that of the monomodal powder-polymer mixtures (**Figure 4.6a and 4.7a**) at any given shear rate - temperature conditions. This could be due to the increased solids loading as well as the presence of nanoparticles in the mixtures. An attempt was made to analytically separate the contributions of reduced particle size from the increased solids loading by computing viscosity values at comparable solids loadings. A number of theoretical as well as empirical equations have been developed to predict the rheological behavior of suspensions with and without using the Φ_c values [26-31]. However, several of these equations are derived for dilute suspensions of spheres in Newtonian liquids. For the current study, it was necessary to consider models that take into account the maximum powder content Φ_c , for predicting the viscosity of concentrated suspensions.

For our current work on powder-polymer mixtures with higher powder content, three such models were utilized for a detailed comparison of the mixture rheology. Firstly, the *Krieger-Dougherty* model was used [18, 22] as shown in **Equation 4.2**:

$$\eta_{mixture} = \eta_{binder} * \left[1 - \frac{\phi}{\phi_c} \right]^{-\phi_c[\eta]} \quad (4.2)$$

Secondly, a simplified version of the above model [32] was used as shown in **Equation 4.3**:

$$\eta_{mixture} = \frac{\eta_{binder}}{\left[1 - \frac{\phi}{\phi_c} \right]^2} \quad (4.3)$$

Thirdly, the *Modified Eiler's* model [33-36] was used as shown in **Equation 4.4**:

$$\eta_{mixture} = \eta_{binder} \left[1 + \frac{[\eta]\phi\phi_c}{2(\phi_c - \phi)} \right]^m \quad (4.4)$$

The variants used in the equation have the same physical meaning; $[\eta]$ is the intrinsic viscosity, Φ is the optimal solids loading, Φ_c is the critical solids loading and “m” generally assumes the value of 2 [36].

In our current work, the $[\eta]$ corresponding to the particular powder mixtures was determined by rewriting **Equations 4.2** and **4.4** as,

$$[\eta] = \frac{(\ln[\eta_{mixture}] - \ln[\eta_{binder}])}{-\phi_c * \ln\left[1 - \frac{\phi}{\phi_c}\right]} \quad (5)$$

$$[\eta] = \left(\left[\frac{\eta_{mixture}}{\eta_{binder}} \right]^{0.5} - 1 \right) * \frac{2(\phi_c - \phi)}{\phi\phi_c} \quad (6)$$

$[\eta]$ was calculated using **Equation 4.5** to be 2.57 (± 0.22) and 1.94 (± 0.14) for monomodal SiC and AlN powder-polymer mixtures, respectively. These values however increased to 3.58 (± 0.32) and 3.19 (± 0.26) for bimodal SiC and AlN mixtures, respectively. These results are supported by similar findings by Liu et al in zirconia-wax systems [26] and by Dabak and Yucel in metal/metal-oxide- organic solvent suspensions [36]. A similar trend was also noticed for $[\eta]$ calculated using **Equation 4.6** as 1.25 (± 0.27) and 0.66 (± 0.1) for monomodal and 4.7 (± 1.16) and 4.07 (± 1.01) for bimodal SiC and AlN mixtures, respectively. The rheological data was also evaluated by the above method to compute Φ_c which showed similar trends to experimentally determined values of Φ_c by torque rheometry (**Table 4.3**).

Equations 4.2-4.4 were used to compute $\eta_{mixture}$ for various volumetric fractions of powder-polymer mixtures with the calculated values of $[\eta]$ and experimental values of Φ_c . The trends are compared in **Figures 4.9-4.11** for AlN (a) and SiC (b) powder-polymer mixtures, for a melt temperature of 160 °C at shear rates of 160 - 800/s. Irrespective of the models, the bimodal powder-polymer mixtures tend to show more fluidity than the respective monomodal systems. The lower viscosity in bimodal mixtures can be attributed to the effect of better powder packing and reduced critical solids loading. Similar trend computations are reported in the past by Ferrini et al who compared the shear viscosity of glass-beads (of various sizes) suspended in mineral oil [35]. Due to their dependence on η_{binder} , the current calculations evolve to have similar trends with the shear rate variations. These results have important implications for processing of particulate suspensions by powder injection molding (PIM), extrusion, slip casting and tape casting. These implications are a part of on-going studies that will be reported elsewhere in the future.

4.4. Conclusions

The current work successfully reported the technical feasibility of increasing the powder content in powder-polymer mixtures by nanoparticle addition using torque rheometry and SEM. This novel principle of bimodal μ -n powder mixtures can also be applied to other material systems and applications through the use of the approach reported in this work. Rheological studies indicated that for comparable solids loading, the bimodal mixtures with nanoscale particles have lower viscosity than corresponding monomodal suspensions.

4.5. References

1. Y. Inomata, *International Symposium on Ceramic Components for Engine*, ed. S. Somiyai et al, KTK Scientific Publishers, Tokyo, 1984, Pages: 253-261.
2. V. Vinothini, P. Singh, M. Balasubramanian, *Journal of Materials Science*, 2006, vol.41, pp. 7082-7087.
3. S.B. Reddy, P.P. Singh, N. Raghu, V. Kumar, *Journal of Materials Science*, 2007, vol.37, pp. 929-934.
4. L. Liu, N.H. Loh, B.Y. Tay, S.B. Tor, Y. Murakoshi, R. Maeda, , *Materials Characterization*, 2005, vol. 54, pp. 230-238.
5. V.P. Onbattuvelli, S. Vallury, T. McCabe, S-J. Park, S.V. Atre, *PIM International*, 2010, vol. 4(3), pp. 64-70.
6. M. Trunec, K. Maca, *Journal of American Ceramic Society*, 2007, vol. 90(9), pp. 2735–2740
7. M. Trunec, K. Maca, Z. Shen, *Scripta Materialia*, 2008, vol.59, pp. 23-26
8. R.M.German, *Sintering theory and practice*, 1st edition, 1996, John Wiley and Sons, NY
9. M. Bothara, *Sintering of nanocrystalline silicon carbide in plasma pressure compaction system*, PhD Thesis, 2007, Oregon State University
10. W.Wagner, R.S. Averbach, H. Hahn, W.Petry, A. Wiedmann, *Journal of Materials Research*, 1991, vol.6, pp. 2193-2198
11. K. Wetzel, G. Rixecker, G. Kaiser, F. Aldinger, *Advanced Engineering Materials*, 2005, vol.7 (6), pp. 520-524.
12. C.L. Huang, J.J. Wang, C.Y. Huang, *Materials Letters*, 2005, vol.59(28), pp. 3746-3749
13. J. Hashim, L. Looney, M.S.J. Hashmi, *Journal of Materials Processing Technology*, 2002, vol.123, pp. 251-257
14. G. Skandan, *Nanostructured Materials*, 1995, vol.5, pp.111–126
15. P. Suri, S.V. Atre, R.M. German, J.P. DeSouza, *Materials Science and Engineering A*, 2003, vol. 356, pp. 337-344.
16. L. Qiu, X. Li, Y. Peng, W. Ma, G. Qiu, Y. Sun, *Journal of Rare Earths*, 2007, vol.25 (2), pp. 322-326
17. S.M. Olhero, J.M.F. Ferreira, *Powder Technology*, 2004, vol.139, pp. 69-75

18. R.M. German, *Advances in Powder Metallurgy and Particulate Materials*, 1992, vol. 3, pp. 1-15
19. J. Zheng, W.B. Carlson, J.S. Reed, *Journal of the European Ceramic Society*, 1995, vol.15, pp. 479- 483
20. J-L.Shi, J.D. Zhang, *Journal of American Ceramic Society*, 2000, vol.83 (4), pp. 737-742
21. C.L. Martin, D. Bouvard, *International Journal of Mechanical Sciences*, 2004, vol. 46, pp. 907–927
22. G. Aggarwal, S.J. Park, I. Smid, *International Journal of Refractory Metals and Hard Materials*, 2006, vol. 24, 253–262
23. S.J. Park, Y. Wu, D.F. Heaney, X. Zou, G. Gai, R.M. German, *Metallurgical and Materials Transactions A*, 2009, vol. 40 A, pp. 215-222
24. R.M. German, A. Bose, *Injection Molding of Metal and Ceramics*, 305-337, MPIF Publication, New Jersey, USA, 1997.
25. R. S. Lib, B.R. Patterson, H.A. Heflin, *Progress in Powder Metallurgy*, 1986, vol. 42, pp. 95-104
26. D-M. Liu, W.J. Tseng, *Journal of Materials Science*, 2000, vol. 35, pp. 1009-1016
27. T. Honek, B. Hausnerova, P. Saha, *T. Bata, Polymer Composites*, 2004, vol. 26(1), pp.29-36.
28. C. Atzeni, L. Massidda, U. Sanna, Comparison between rheological models for Portland cement pastes, *Cement and Concrete Research*, 1985, vol. 15(3), pp. 511-519.
29. A. Grants, A. Irbītis, G. Kronkalns, M.M. Maiorov, *Journal of Magnetism and Magnetic Materials*, 1990, vol. 85(1-3), pp. 129-132.
30. H.J.H. Brouwers, *Physical Review E*, 2010, vol. 81(5), pp. 051402-1-11.
31. D.L. Faulkner, LL.R. Schmidt, *Polymer Science and Engineering*, 1977, vol.17(9), pp. 657-665.
32. P. C. Hiemenz and R. Rjagopalan, “Principles of Colloid and Surface Science,” 169, 3rd ed., Merce Dekker Inc., New York, USA, 1997.
33. R. Lapasin, S.Pricl, *The Canadian Journal of Chemical Engineering*, 1992, vol. 70(1), pp. 20-27.
34. P.S. Leung, E.D. Goddard, *Langmuir*, 1990, vol. 6(1), pp. 3-6.
35. F. Ferrini, D. Ercolani, B. de Cindio, L. Nicodemo, L. Nicolias, S. Ranaudo, *Rheologica Acta*, 1979, vol. 18(2), pp. 289-296.
36. T. Dabak, O. Yucel, *Rheologica Acta*, 1986, vol. 25(5), pp. 527-533.

List of Figures

Figure 4.1: Torque rheometry plot for 100% μ -AlN (a) and 100% μ -SiC (b) with the insets showing the resulting mixtures

Figure 4.2a: Effect of n-AlN addition to μ -AlN on the maximum powder fraction in the powder-polymer mixture

Figure 4.2b: Effect of n-SiC addition to μ -SiC on the maximum powder fraction in the powder-polymer mixture

Figure 4.3: Comparison of powder packing behavior in monomodal (a) and bimodal (b) AlN powder-polymer mixtures

Figure 4.4: Comparison of powder packing behavior in monomodal (a) and bimodal (b) SiC powder-polymer mixtures

Figure 4.5a: Effect of nanoparticle addition on the mixing torque of AlN powder-polymer mixtures

Figure 4.5b: Effect of nanoparticle addition on the mixing torque of SiC powder-polymer mixtures

Figure 4.6: Viscosity of extruded monomodal (a) and bimodal (b) AlN powder-polymer mixtures at different shear rate and temperature combinations, exhibiting pseudo-plastic behavior

Figure 4.7: Viscosity of extruded monomodal (a) and bimodal (b) SiC powder-polymer mixtures at different shear rate and temperature combinations, exhibiting pseudo-plastic behavior

Figure 4.8: Viscosity of the binder mixture at different shear rate and temperature combinations

Figure 4.9a: Comparison of viscosity (calculated by the Krieger-Dougherty model) as a function of solids loading for monomodal and bimodal AlN *powder-polymer mixtures* at 160 °C for the shear rates of (i) 800/s, (ii) 400/s and (iii) 160/s.

Figure 4.9b: Comparison of viscosity (calculated by the Krieger-Dougherty model) as a function of solids loading for monomodal and bimodal SiC *powder-polymer mixtures* at 160 °C for the shear rates of (i) 800/s, (ii) 400/s and (iii) 160/s.

Figure 4.10a: Comparison of viscosity (calculated by the simplified Krieger-Dougherty model) as a function of solids loading for monomodal and bimodal AlN *powder-polymer mixtures* at 160 °C for the shear rates of (i) 800/s, (ii) 400/s and (iii) 160/s.

Figure 4.10b: Comparison of (calculated by the simplified Krieger-Dougherty model) as a function of solids loading for monomodal and bimodal SiC *powder-polymer mixtures* at 160 °C for the shear rates of (i) 800/s, (ii) 400/s and (iii) 160/s.

Figure 4.11a: Comparison of viscosity (calculated by the modified Eiler's model) as a function of solids loading for monomodal and bimodal AlN *powder-polymer mixtures* at 160 °C for the shear rates of (i) 800/s, (ii) 400/s and (iii) 160/s.

Figure 4.11b: Comparison of viscosity (calculated by the modified Eiler's model) as a function of solids loading for monomodal and bimodal SiC *powder-polymer mixtures* at 160 °C for the shear rates of (i) 800/s, (ii) 400/s and (iii) 160/s.

List of Tables

Table 4.1: Conditions used for scaling up of SiC and AlN powder-polymer mixtures

Table 4.2: Slopes of the viscosity plots of *powder-polymer mixtures* and binders representing the power law coefficient “n” values

Table 4.3: Comparison of experimental and theoretical Φ_c values for SiC and AlN powder-polymer mixtures

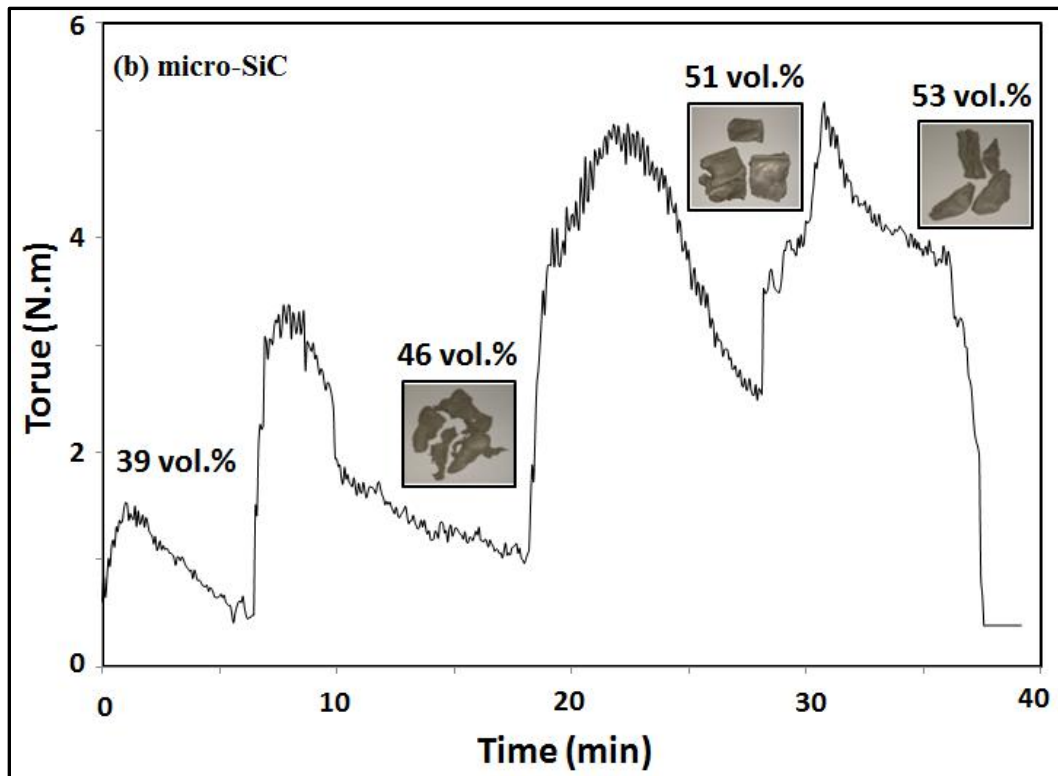
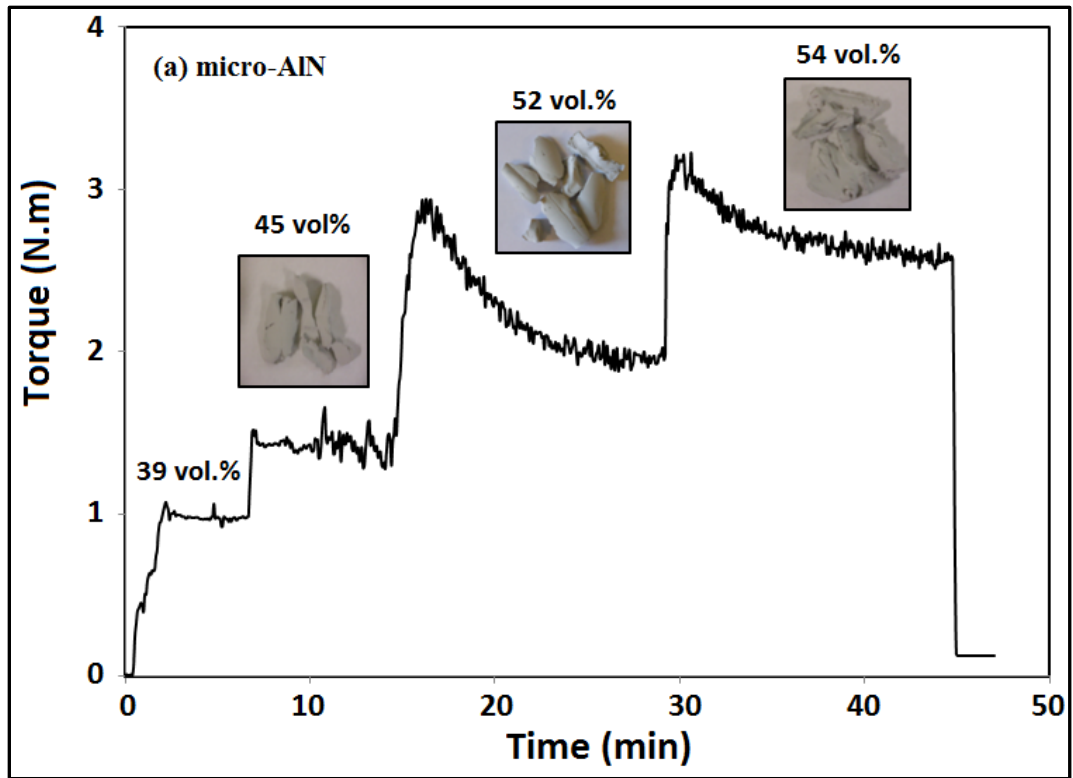


Figure 4.1: Torque rheometry plot for 100% μ -AlN (a) and μ -SiC (b) with the insets showing the resulting mixtures

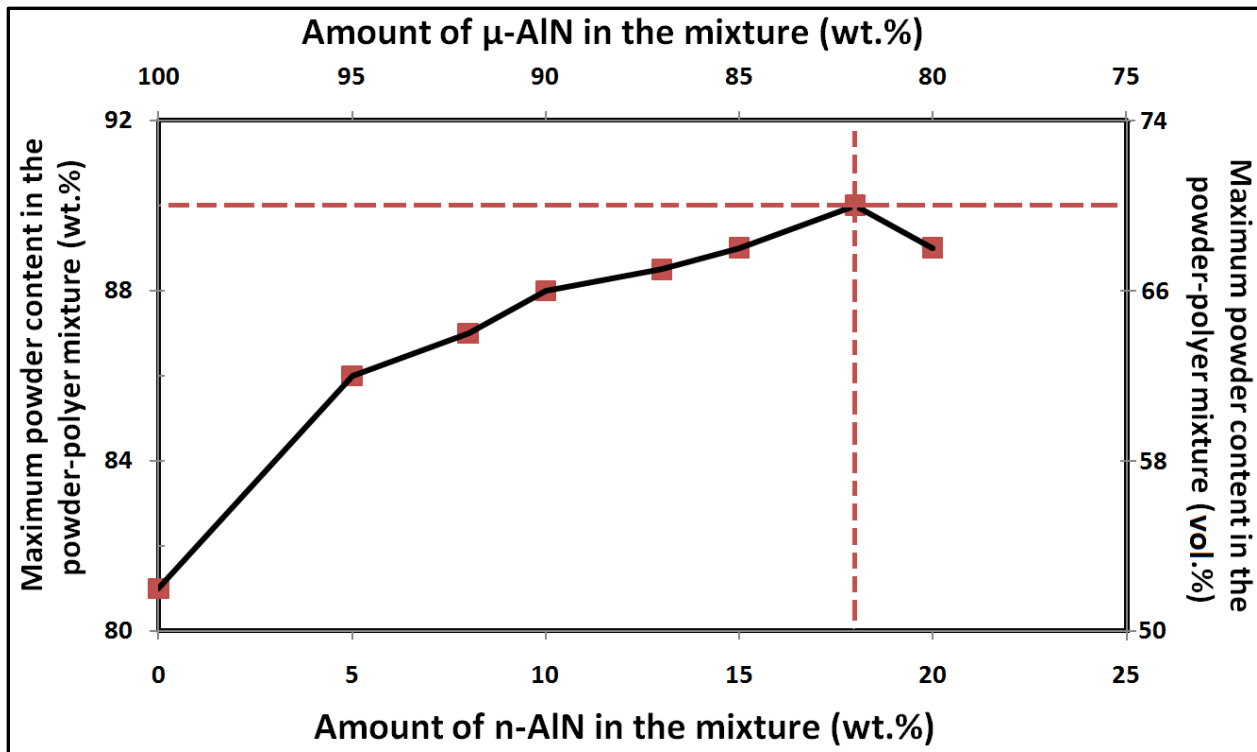


Figure 4.2a: Effect of n-AlN addition to μ -AlN on the maximum powder fraction in the powder-polymer mixture

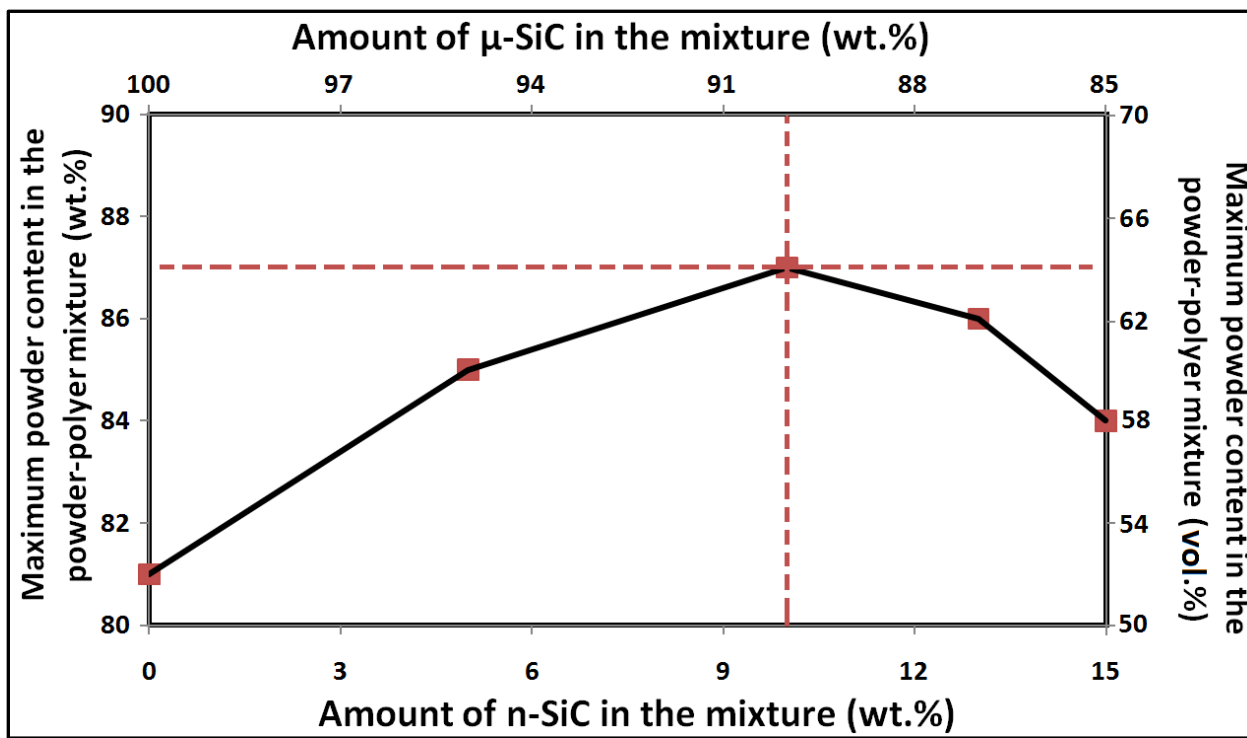


Figure 4.2b: Effect of n-SiC addition to μ -SiC on the maximum powder fraction in the powder-polymer mixture

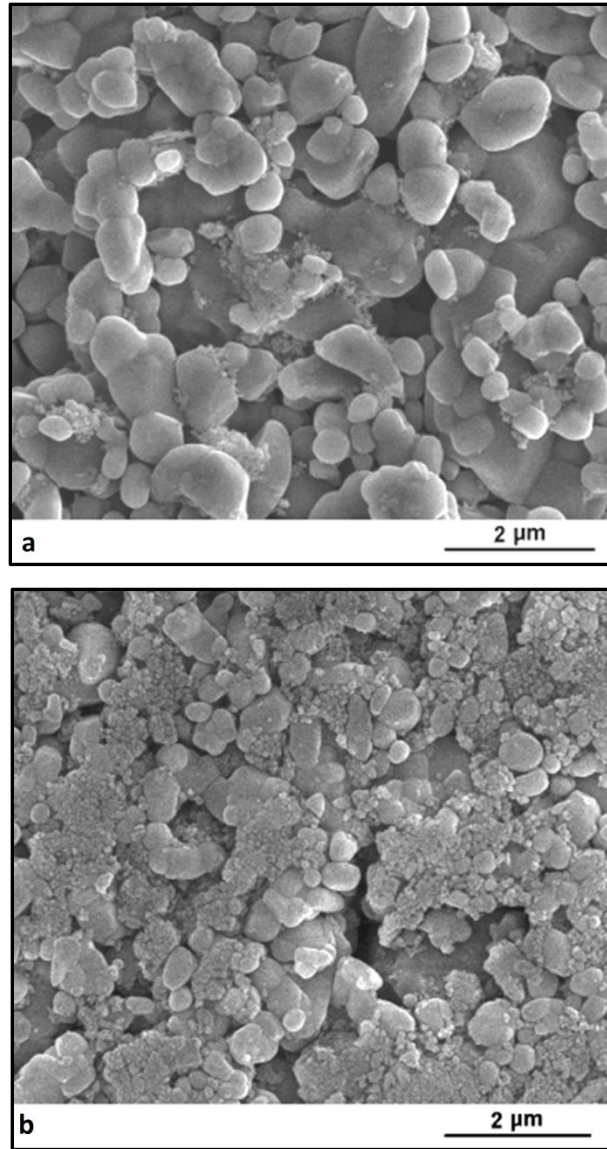


Figure 4.3: Comparison of powder packing behavior in monomodal (a) and bimodal (b) AlN powder-polymer mixtures

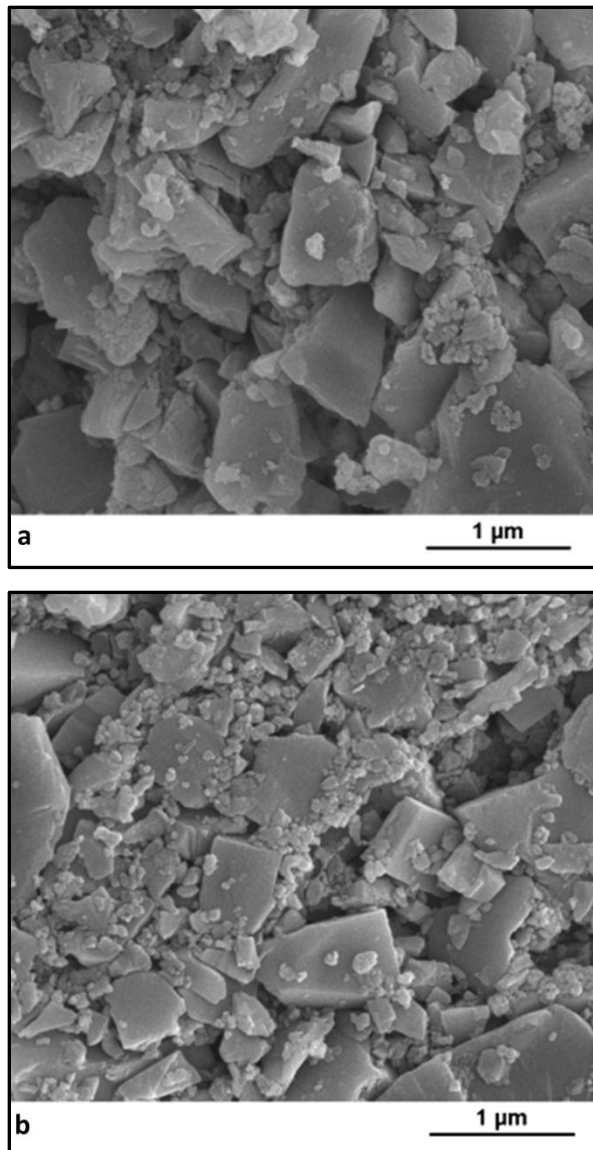


Figure 4.4: Comparison of powder packing behavior in monomodal (a) and bimodal (b) SiC powder-polymer mixtures

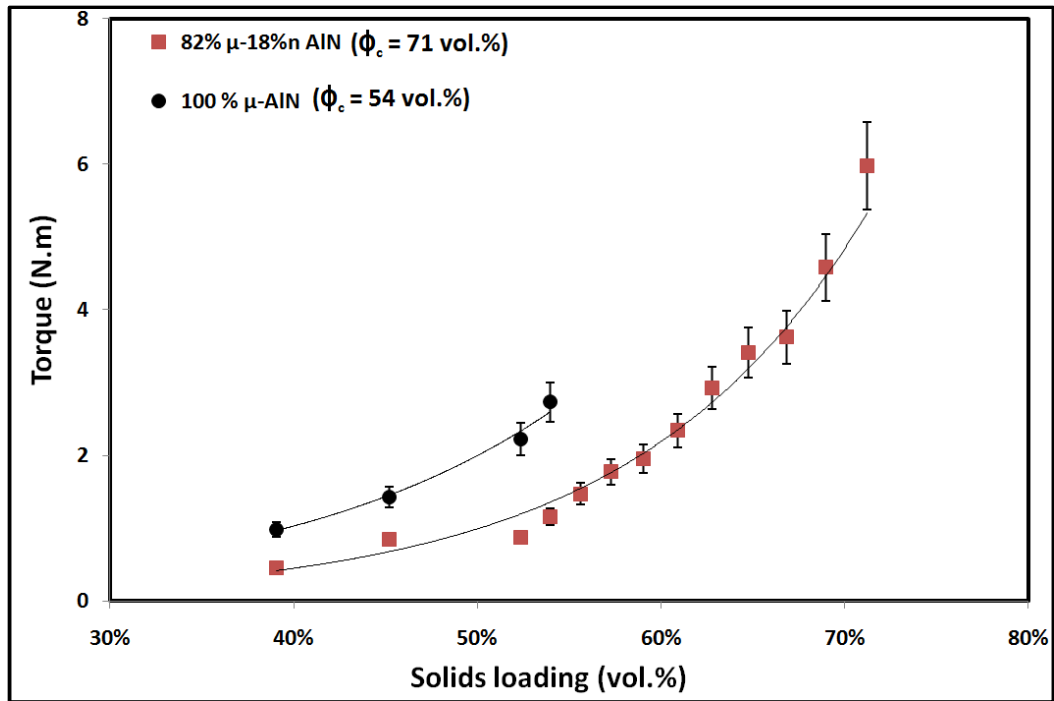


Figure 4.5a: Effect of nanoparticle addition on the mixing torque of the AlN powder-polymer mixtures

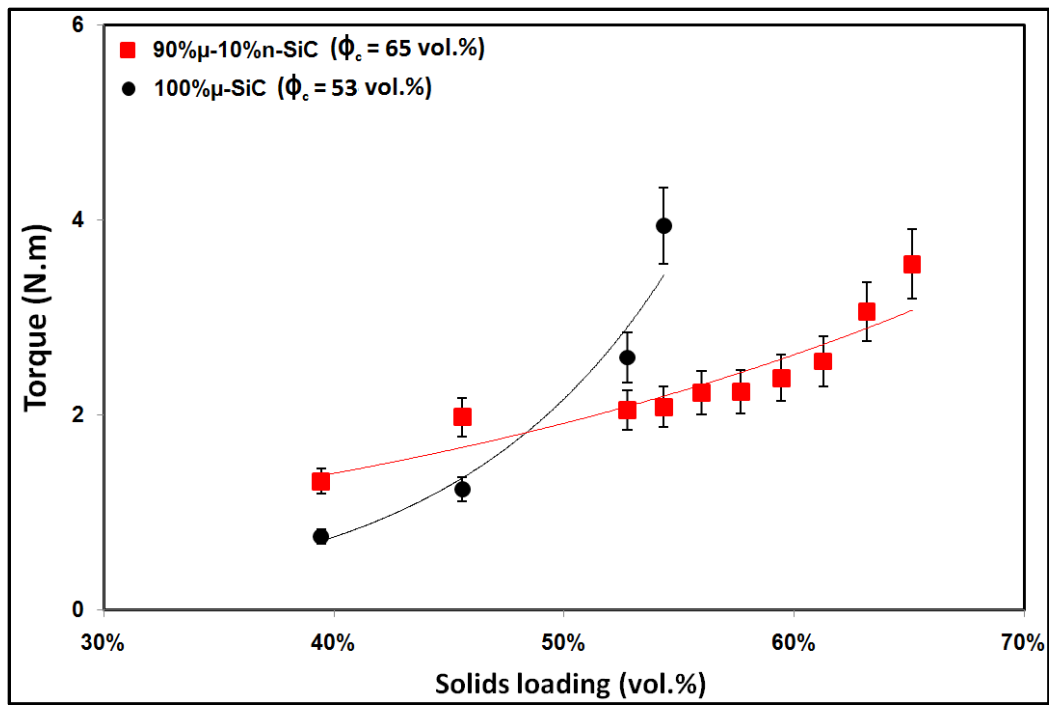


Figure 4.5b: Effect of nanoparticle addition on the mixing torque of the SiC powder-polymer mixtures

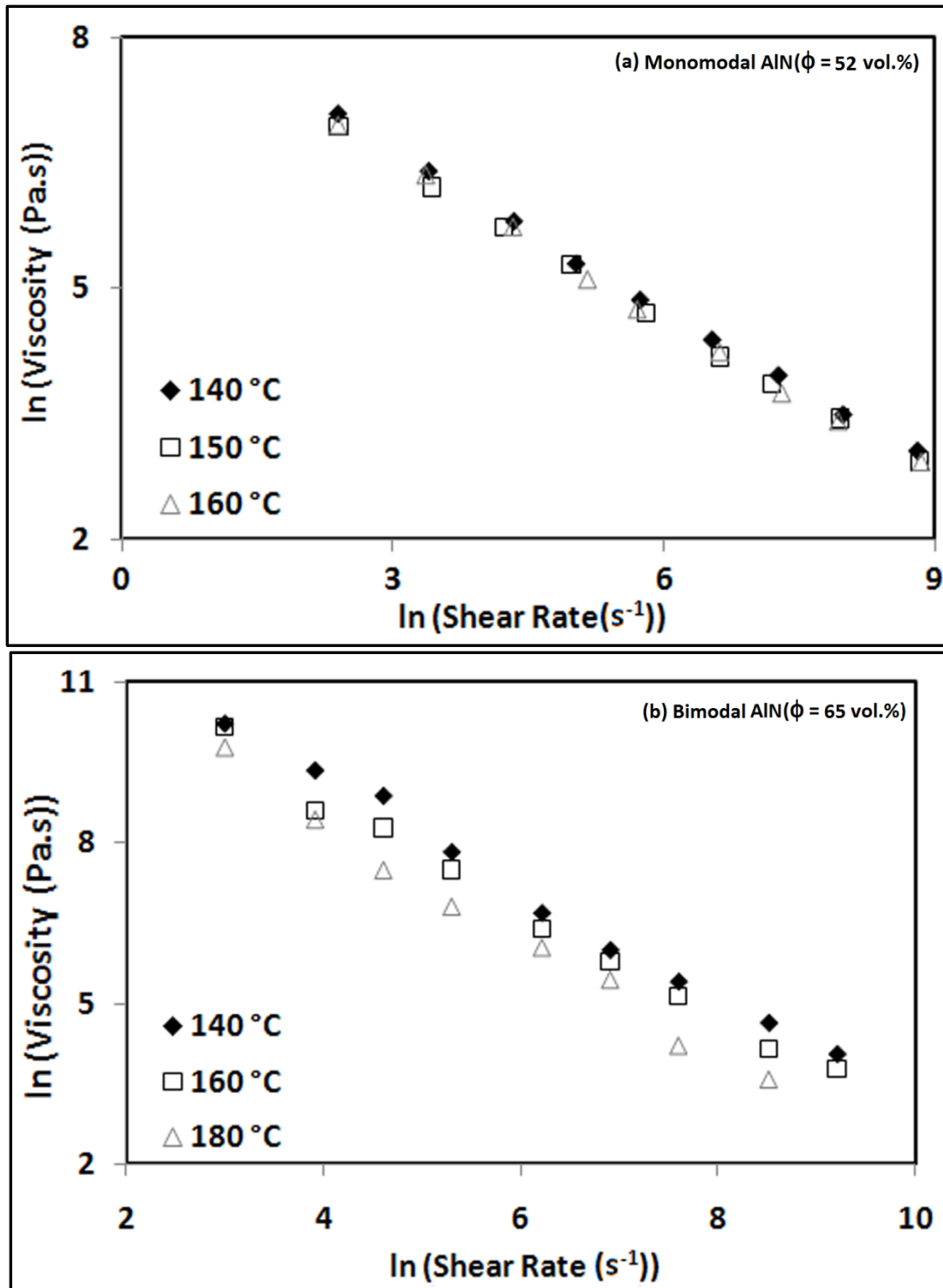


Figure 4.6: Viscosity of monomodal (a) and bimodal (b) AlN powder-polymer mixtures at different shear rate and temperature combinations, exhibiting pseudo-plastic behavior

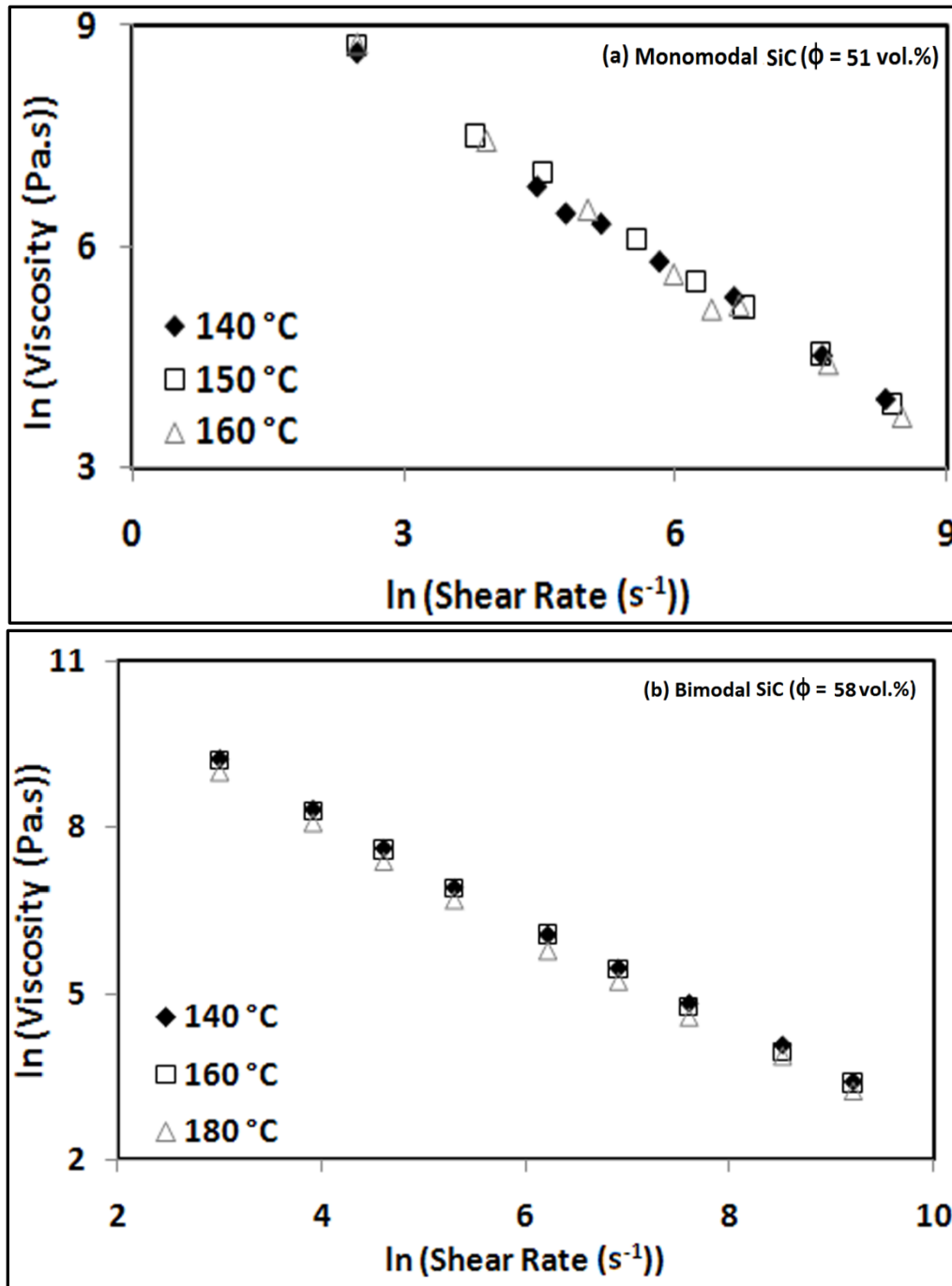


Figure 4.7: Viscosity of monomodal (a) and bimodal (b) SiC powder-polymer mixtures at different shear rate and temperature combinations, exhibiting pseudo-plastic behavior

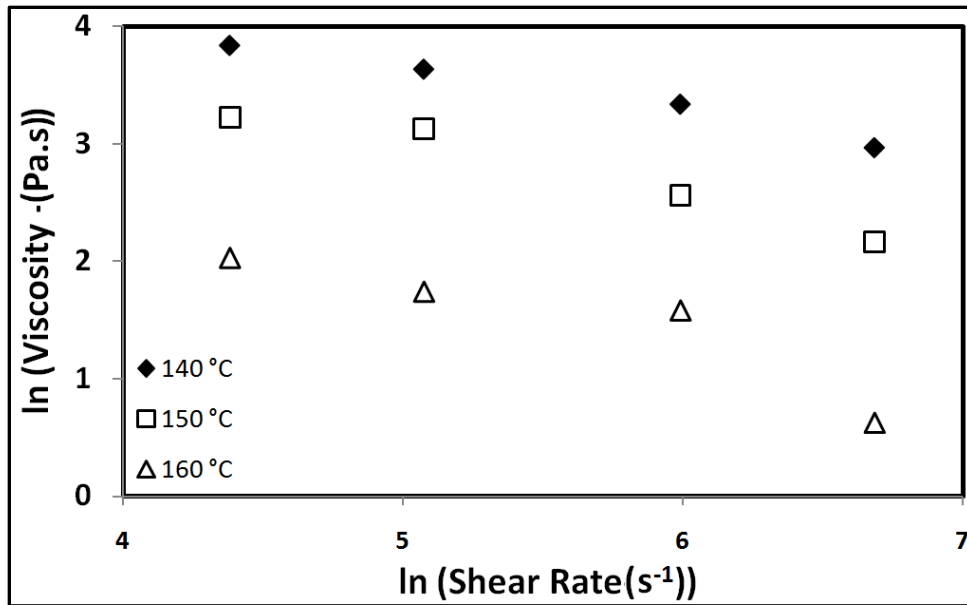


Figure 4.8: Viscosity of the binder mixture at different shear rate and temperature combinations

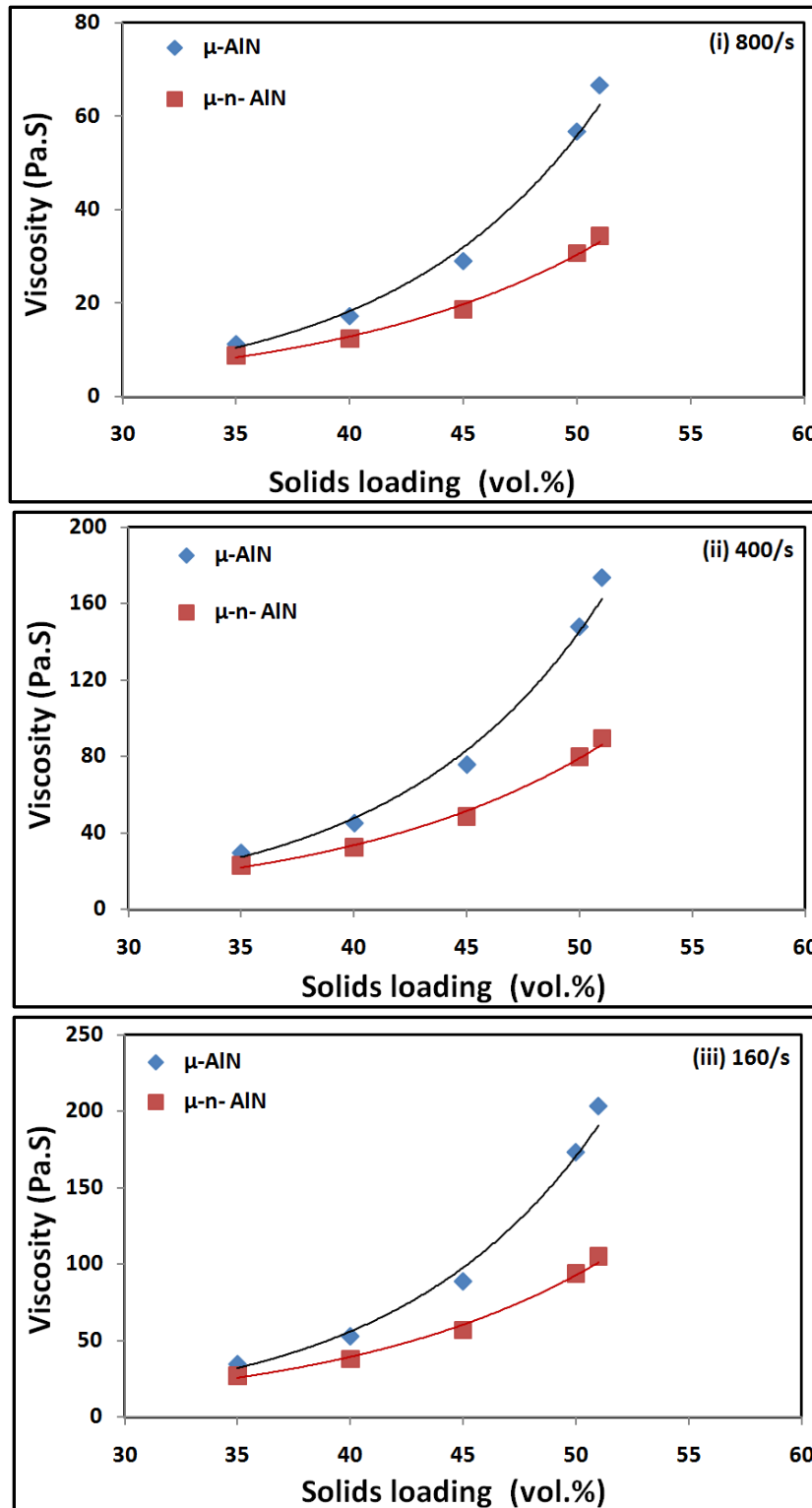


Figure 4.9a: Comparison of viscosity (calculated by the Krieger-Dougherty model) as a function of solids loading for monomodal and bimodal AlN powder-polymer mixtures at 160 °C for shear rates of (i) 800/s, (ii) 400/s and (iii) 160/s.

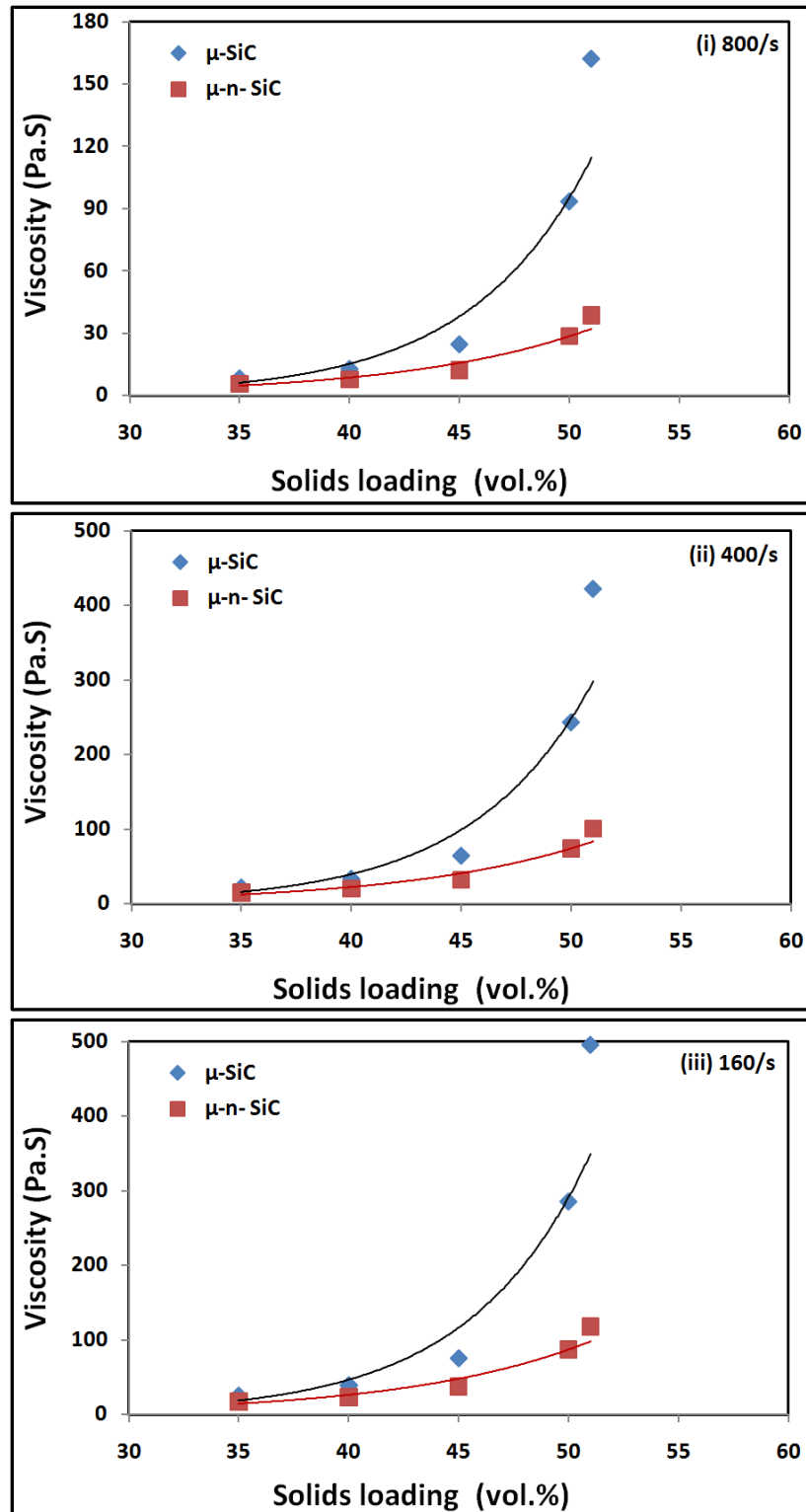


Figure 4.9b: Comparison of viscosity (calculated by the Krieger-Dougherty model) as a function of solids loading for monomodal and bimodal SiC powder-polymer mixtures at 160 °C for shear rates of (i) 800/s, (ii) 400/s and (iii) 160/s.

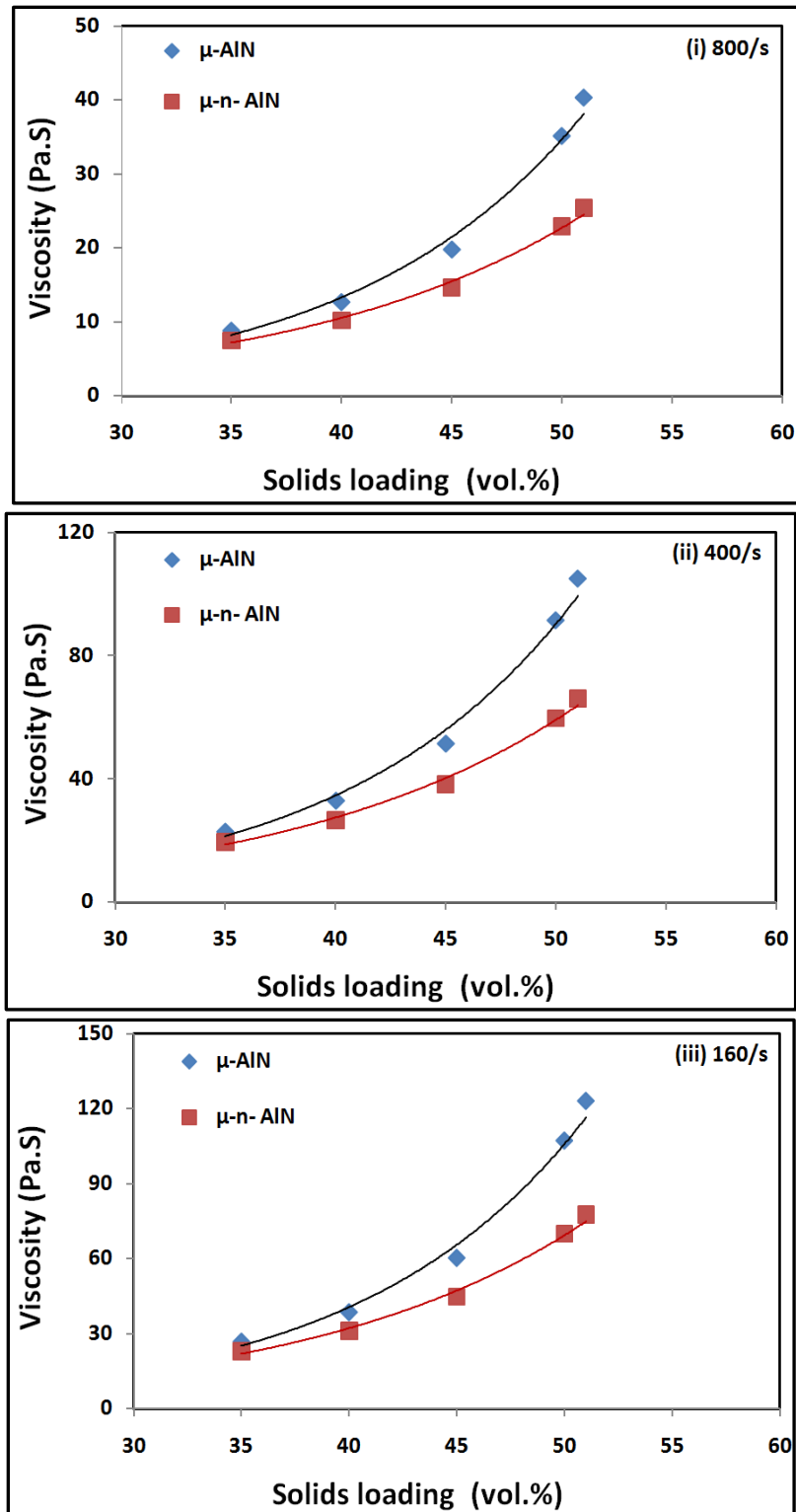


Figure 4.10a: Comparison of viscosity (calculated by the simplified Krieger-Dougherty model) as a function of solids loading for monomodal and bimodal AlN powder-polymer mixtures at 160 °C for shear rates of (i) 800/s, (ii) 400/s and (iii) 160/s.

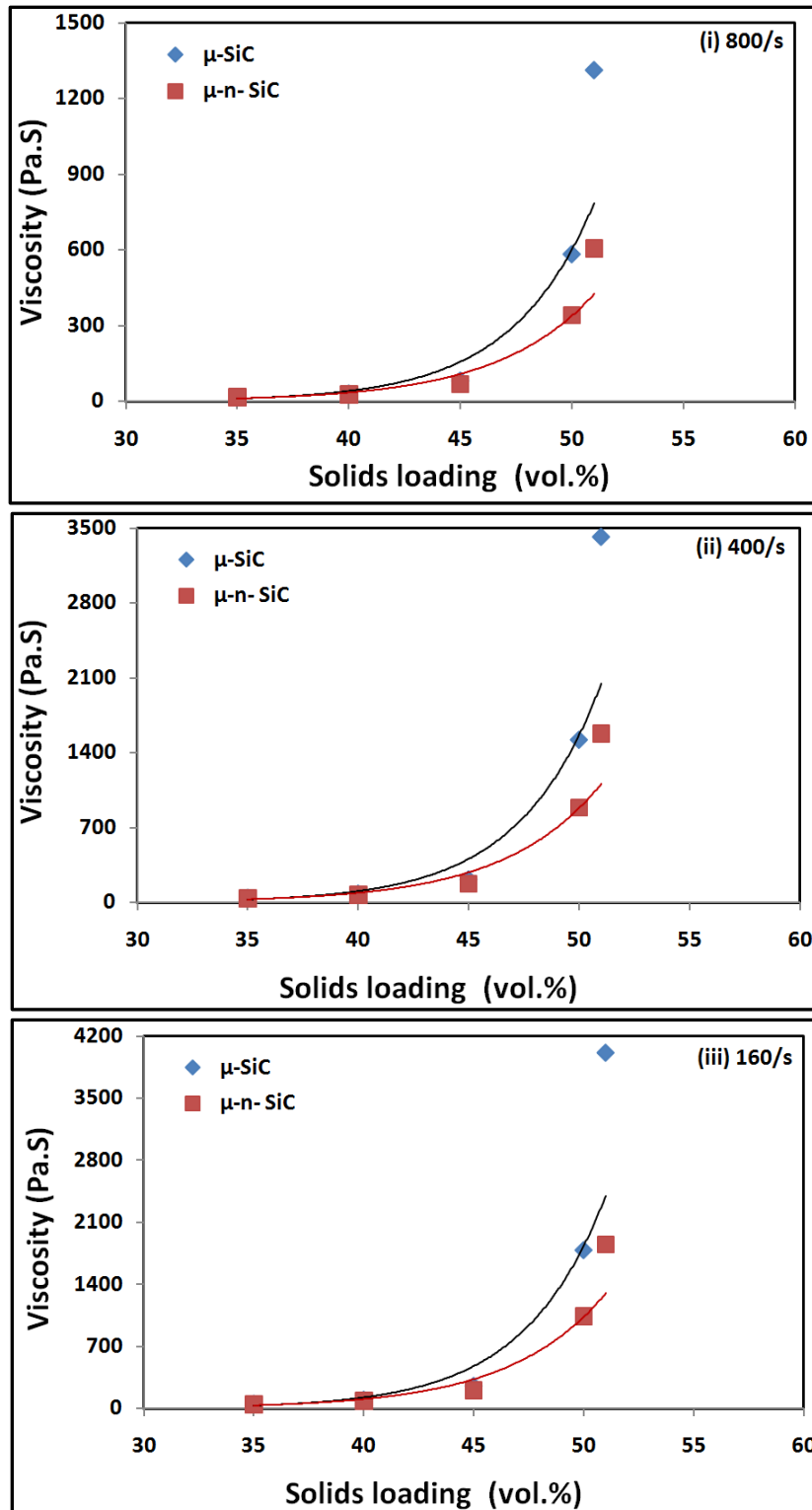


Figure 4.10b: Comparison of viscosity (calculated by the simplified Krieger-Dougherty model) as a function of solids loading for monomodal and bimodal SiC powder-polymer mixtures at 160 °C for shear rates of (i) 800/s, (ii) 400/s and (iii) 160/s.

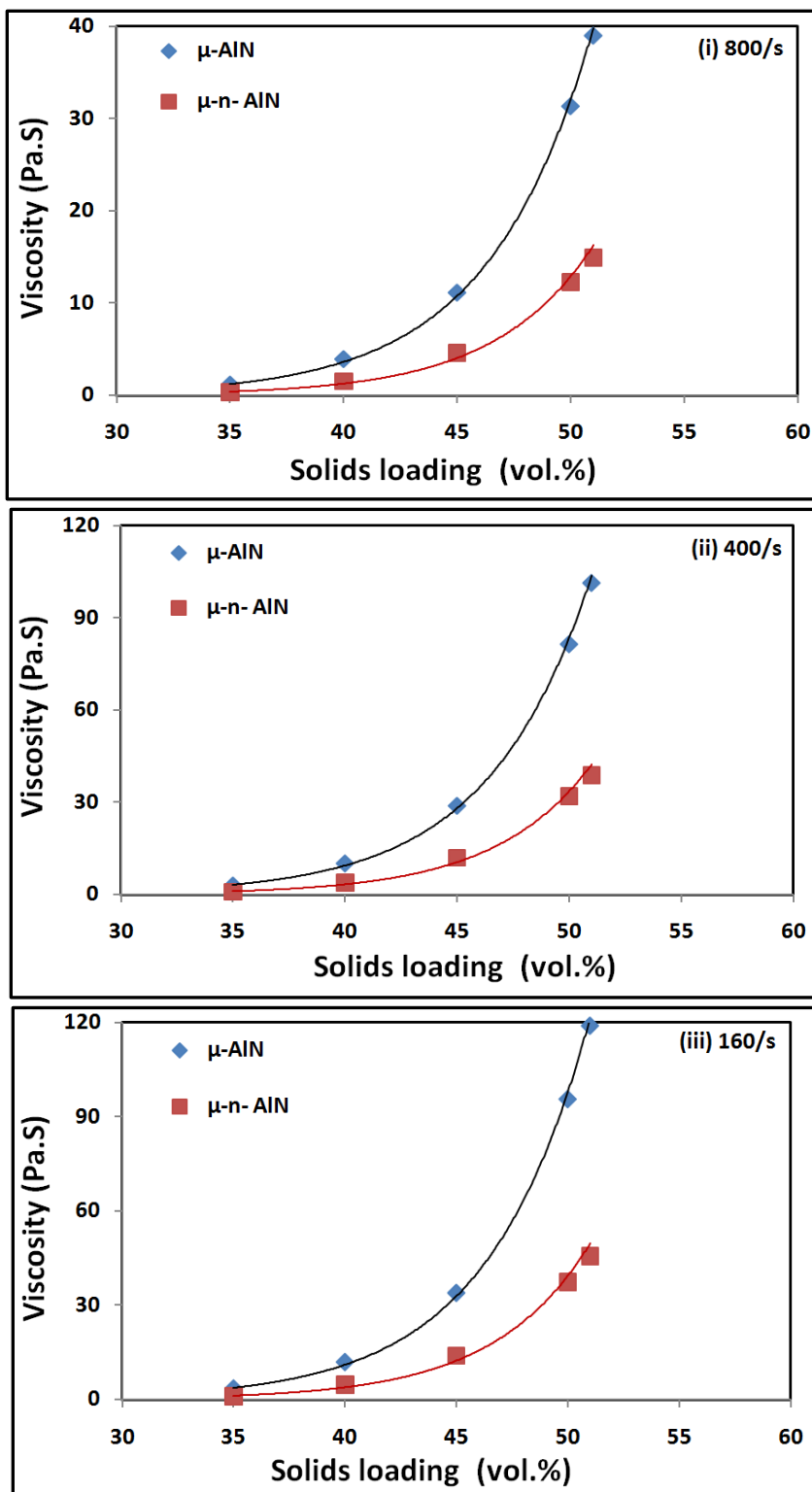


Figure 4.11a: Comparison of viscosity (calculated by the modified Euler's model) as a function of solids loading for monomodal and bimodal AlN powder-polymer mixtures at 160 °C for shear rates of (i) 800/s, (ii) 400/s and (iii) 160/s.

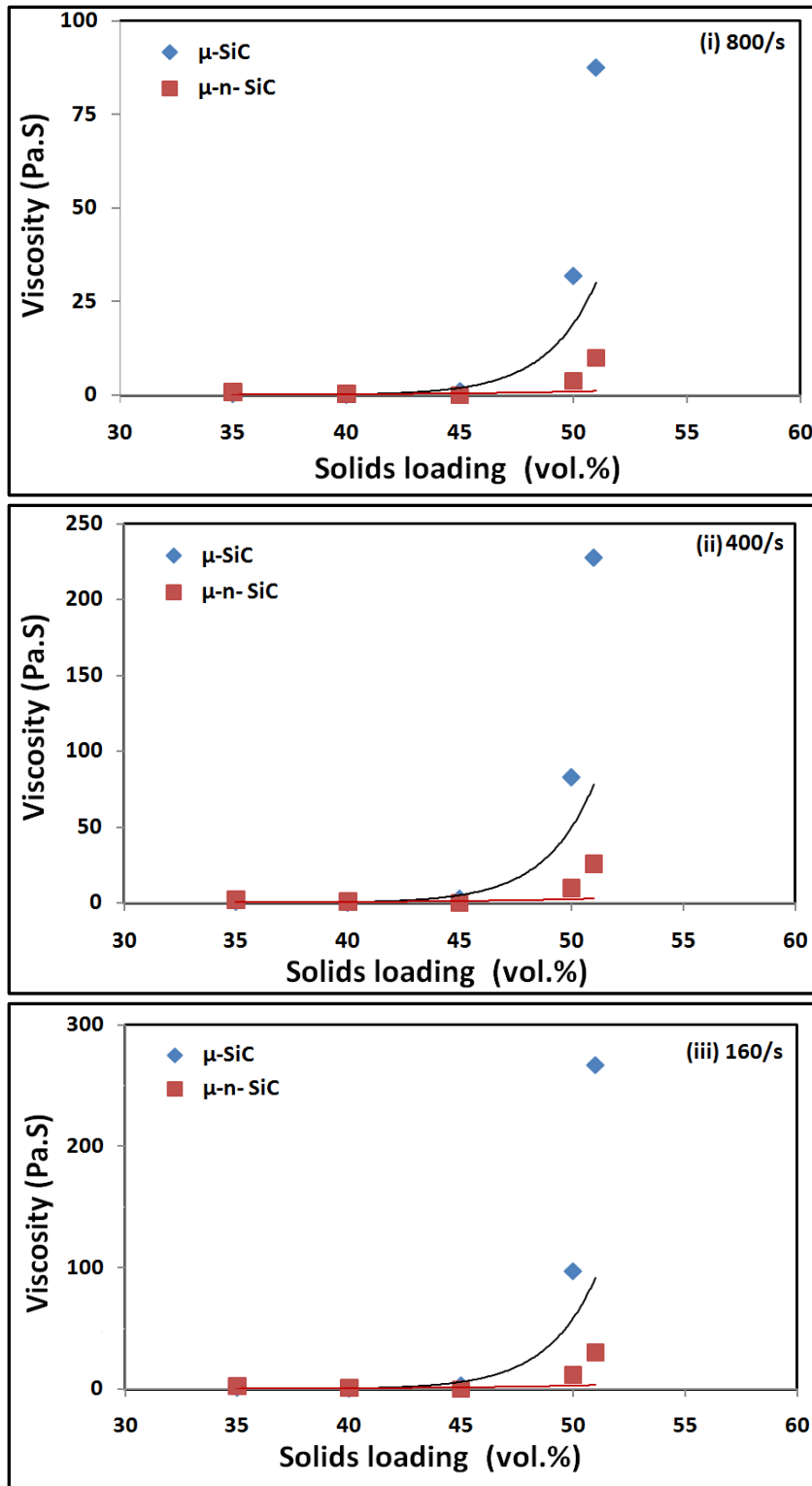


Figure 4.11b: Comparison of viscosity (calculated by the modified Euler's model) as a function of solids loading for monomodal and bimodal SiC powder-polymer mixtures at 160 °C for shear rates of (i) 800/s, (ii) 400/s and (iii) 160/s.

Table 4.1: Conditions used for scaling up of SiC and AlN powder-polymer mixtures

Extruder Specifications	Values
Screw Diameter (Co-Rotating)	27 mm
L/D	40
Flight Depth	4.3
Barrels/Zones involved	10
Zone Temperature	160 °C
Screw Speed	260 rpm
Extrusion Rate	30 lb/hr
Cooling System	Air-cooled conveyor belt system

Table 4.2: Slopes of the viscosity plots of powder-polymer mixtures and binders representing the power law coefficient “n” values

Material	(1-n)	R²
Binder Mixture	0.61	0.98
Monomodal μ -SiC (51 vol.%)	0.84	0.99
Bimodal μ -n SiC (58 vol.%)	0.93	0.98
Monomodal μ -AlN (52 vol.%)	0.66	1
Bimodal μ -n AlN (65 vol.%)	0.95	0.99

Table 4.3: Comparison of experimental and theoretical Φ_c values for SiC and AlN powder-polymer mixtures

Powder-polymer mixture	Φ_c (vol.%)	
	Experimental	Calculated by simplified Krieger-Dougherty model
Monomodal μ -SiC	52%	58 \pm 1.4%
Bimodal μ -n SiC	65%	63 \pm 1.2%
Monomodal μ -AlN	54%	63 \pm 1.9%
Bimodal μ -n AlN	71%	69 \pm 0.9%

CHAPTER 5

The Effects of Nanoparticle Addition on the Properties of SiC and AlN Feedstocks for Powder Injection Molding

Abstract

Aluminum nitride (AlN) and silicon carbide (SiC) were chosen for the fabrication of thermal management devices due to their high thermal conductivity and coefficient of thermal expansion values equivalent to that of silicon and silicon carbide dies. Additionally, powder injection molding (PIM) was selected for net-shaping these ceramics in order to harness its production and geometric advantages. This paper presents an in-depth study on the effects of nanoparticle addition on the thermal and rheological properties of the SiC and AlN feedstocks. Specifically, bimodal mixtures of nanoscale and sub-microscale particles addition were found to significantly improve the powder content (solids loading) in the powder-polymer mixtures (feedstocks) for injection molding. The implications of the variation in feedstock properties with nanoparticle addition are discussed in the context of the mold-filling behavior of these material systems.

5.1. Introduction

Silicon carbide (SiC) and aluminum nitride (AlN) exhibit a combination of thermal and mechanical properties (**Table 5.1**) that are relevant to applications in electronics, aerospace, defense and automotive industries [1-4]. However, the successful translation of these properties into final applications lies in the net-shaping of these ceramics into fully dense microstructures. Extensive research has been done on net-shaping SiC and AlN via slip casting [5-6], tape casting [7-8], hot pressing [9-10], hot isostatic pressing [11-12] and cold isostatic pressing [13-14]. Additional methods including pyrolysis of pre-ceramic polymers have also explored [15-16]. However, few studies involving powder injection molding (PIM) of SiC and AlN have been reported to date [17-19]. It is evident from a comparative study presented in the **Table 5.2** that PIM has many advantages over competing net-shaping techniques to mass produce complex geometric parts for thermal management with closer dimensional tolerances.

Achieving a high final density is crucial for obtaining useful thermal and mechanical properties for sintered materials [20-21]. Prior studies investigated this issue by exploring the material and process parameters. For example, the effect of nature and content of the sintering additives on the densification of SiC and AlN have been widely studied material parameters [22-23]. Similarly, process parameters including sintering temperature, hold time and pressure have been varied to study the pattern of densification and/or grain growth [24-26].

Improving the green density of the feedstock provides an important parameter to increase the final density during sintering. This can typically be achieved by increasing the solids loading of the feedstock by blending two different particle sizes [27-28]. Our prior research work successfully demonstrated an increase in the solids loading with the addition of nanoparticles, forming a bimodal μ -n powder mixture [29-30]. For example, the critical solids loading is found to increase from 54 to 71 vol.% when AlN nanoparticles are added to the monomodal μ -sized AlN powders. Similarly, the SiC powder mixture exhibited an increase from 53 to 65 vol.% with the nanoparticles addition. The current work provides a comparative study on the thermal and rheological properties of the monomodal and bimodal SiC and AlN feedstocks. The primary objective of the study is to study the effect of nanoparticles on the thermal, rheological and PVT properties of the bimodal feedstocks. Additionally, simulation studies on the mold-filling behavior were conducted based on these feedstock properties.

5.2. Experimental Methods

5.2.1. Materials

Commercially available α -SiC, AlN, and Y_2O_3 were used as the starting materials as received. Similar to the earlier reports on PIM, a multi-component polymer system based on paraffin wax, polypropylene, was chosen as the binder to facilitate a multi-step debinding process [31-32].

5.2.2. Feedstock Formulation and Scale-Up

As mentioned in the introduction section, our prior findings involve an increased critical solids loading (Φ_m) of 71 and 65 vol.% for the bimodal μ -n SiC and AlN powder mixtures [29-30]. To facilitate a consistent part fabrication by the PIM process, a homogeneous feedstock (~ 2 -5 vol.% $< \Phi_m$) was designed. Thus, formulations with solids loading (Φ) of 65 and 58 vol.% for SiC and AlN respectively, were compounded using twin screw extrusion. The conditions used for the scale-up are listed in the **Table 5.3**. Similarly, feedstocks of monomodal μ -sized SiC and AlN powders with Φ of 52 and 51 vol.% respectively, were also compounded for comparison purposes.

5.2.3. Instrumentation

Thermogravimetric analysis (TGA) was performed on the extruded feedstocks using a TA- 2950 (TA Instruments) thermal system operated under nitrogen flow in the temperature range of 50-600°C with a heating rate of 20°C/min. The calorimetric measurements were carried out using a TA- 2920 unit (TA Instruments) over a temperature range of 20-200°C. The samples were heated at the rate of 20°C/min under a nitrogen atmosphere. The rheological characteristics of the feedstock were examined on a Gottfert Rheograph 2003 capillary rheometer at different shear rates and temperatures. The rheology tests were carried out in accordance with ASTM D 3835. The temperatures were between the highest melting temperature and the lowest degradation temperature of the binder system. A barrel of inner diameter 1 mm and a die length of 20 mm was used. The preheating time was kept at 6 minutes. The micrographs of the thermally debound feedstock samples were taken with a QuantaTM –FEG (FEI) dual beam scanning electron microscope (SEM) coupled with an energy dispersive X-ray spectrometer (EDAX). A Gnomix PVT apparatus was used to find the PVT relationships of the feedstock materials. The PVT tests were carried out in accordance with ASTM D 792. The pellets were dried for 4 hours at 70°C under vacuum. The measurement type used was an isothermal heating scan with a heating rate of approximately 3°C/minute. Moldflow software was used for simulating the injection behavior using the measured properties.

5.3. Results and Discussions

5.3.1. Thermal Properties

The thermal properties of the extruded feedstocks provide basic guidelines for the subsequent PIM steps. **Figures 5.1a and 5.1b** show the DSC curves of all the feedstocks where two endothermic peaks at $62 \pm 2^\circ\text{C}$ and $130 \pm 3^\circ\text{C}$ are observed during heating. These peaks indicate the melting of filler phase (paraffin wax) at 62°C and backbone polymers (polypropylene) at 130°C . Similar results were observed by Aggarwal *et al* for niobium injection molding [33] and Liu *et al* for stainless steel injection molding [34]. With the composition of the binder being constant, minor/no shifts are noticed in the melt peaks with the nanoparticle addition. However, an increase in the heat flow is well pronounced in both SiC and AlN bimodal feedstocks. The corresponding reduction in the specific heat values could be explained as the possible outcome of increased powder content with the nanoparticle addition.

From the TGA plots (**Figures 5.2a and 5.2b**), the powder content in the SiC and AlN monomodal feedstocks can be finalized 79.5 ± 0.2 wt.% and 80.5 ± 0.2 wt.%, respectively. The advantage of nanoparticle addition is once again confirmed from the plots of bimodal SiC and AlN feedstocks revealing the powder content as 82 ± 0.4 wt.% and 85 ± 0.2 wt.%, respectively. The two stage degradation exhibited by all the feedstocks correspond to the degradation of the filler phase from 175 - 400°C and backbone polymers from 400 - 550°C . This pyrolysis data can be used for establishing the upper limit for the injection molding temperatures and thermal debinding profiles [28]. **Figures 5.2a and 5.2b** also reveal a shift in the degradation peaks for the SiC and AlN bimodal feedstocks. This expedited degradation might be due to the presence of additional nanoparticles whose inclusion is found to increase the heat flow in the feedstocks. Contribution to such behavior might also be extended to the higher surface area of the nanoparticles. This finding in bimodal mixtures rejects the expected delay in the binder removal due to reduced porosity. However, further research is required in studying the effect of nanoparticle addition on the percentage of residual carbon during the thermal debinding stage. In addition to the above discussion, the DSC and TGA results can also be utilized to set a lower and upper limit for the injection molding temperatures. In our present work, the injection temperature for all feedstocks can be conducted in the range between 135°C and 180°C .

5.3.2. Rheological Properties

To evaluate the dependence of feedstock viscosity on temperature, the apparent viscosity (η) - shear rate ($\dot{\gamma}$) curves of the extruded SiC and AlN feedstocks were measured at different

temperatures, as shown in the **Figure 5.3 and Figure 5.4**, respectively. The temperatures were between the highest melting temperature (135°C) and lowest degradation temperature (180°C) of the feedstocks. Irrespective of the content, the viscosity of all the feedstocks decreased with an increase in shear rate, indicating pseudoplastic behavior. The results also indicate the absence of dilatant behavior, indicating no powder-binder separation. Normally, a feedstock exhibiting pseudoplastic flow during molding eases mold filling and minimizes jetting [35]. Additionally, the viscosity of the feedstocks decreases with increasing temperature. This can be attributed to powder volume reduction arising from larger binder expansion and disentanglement of the molecular chain during heating [33].

The viscosity of both SiC (**Figure 5.3b**) and AlN bimodal feedstocks (**Figure 5.4b**) were found to be higher than that of the monomodal feedstocks (**Figures 5.3a and 5.4a**) at any given shear rate - temperature conditions. This can be attributed to the increased powder content in the feedstocks with the nanoparticle addition. As shown in the SEM micrographs (**Figures 5.5 and 5.6**) of the bimodal feedstocks, nanoparticles appear to fit into the interstitial spaces between the microparticles. Nanoparticle inclusion will also greatly increase the overall interfacial area between the powder and binder phases. The extent to which the increased hydrodynamic resistance affects the feedstock fluidity will be examined in a separate study.

The role of nanoparticle addition on the pseudoplastic behavior was examined by fitting the rheological data into a modified Cross-WLF equation as shown in **Equation 5.1**:

$$\eta(T, \gamma, P) = \frac{\eta_0(T, P)}{1 + \left[\frac{\eta_0(T) \times \gamma}{\tau^*} \right]^{(1-n)}}$$

$$T \geq T^*, \eta_0(T, P) = D1 \times e^{\left\{ \frac{-[A1(T - T^*)]}{[A2 + (T - T^*)]} \right\}} \dots\dots (5.1)$$

$$T < T^*, \eta_0(T, P) = \infty$$

where, $T^* = D_2 + D_3 P$, and $A = A_2^* + D_3 P$

with $D_3 = 0$ (in this paper); $A = A_2^*$ and $T^* = D_2$

η_0 is the zero-shear rate viscosity, γ is the shear rate, T is the temperature, p is the pressure, n , τ^* , D_1 , D_2 , D_3 , A_1 and A_2 are model constants. Along with their definitions, the values of these parameters are listed in the **Table 5.4**.

Most PIM feedstocks demonstrate two patterns of fluidity: Newtonian and shear thinning. While Newtonian behavior exhibits a linear shear stress - shear rate relationship, the latter involves more

fluidity at higher shear rates [36]. The onset of such transition in the feedstock's fluidity pattern is represented by a shear stress parameter, τ^* , in the above equation. The slope of the shear-thinning curves in **Figures 5.3 and 5.4** is represented by the value (1-n) where n is the power law coefficient. From the (1-n) and D1 values, given in **Table 5.4**, it is evident that the nanoparticle addition increases the shear-thinning behavior of the feedstock. However, the increased τ^* values for the bimodal feedstocks suggest that an additional shear stress is required to begin the shear-thinning regime. Further comparative studies on the feedstocks containing equal powder content can give an improved understanding about the effect of nanoparticles on the shear–thinning behavior. Additionally, the higher coefficient values of monomodal SiC feedstock compared to that of AlN feedstock necessitate future studies on the effect that particle shape has on the flow behavior.

5.3.3. PVT Measurements

The pressure - volume - temperature (PVT) behavior of the SiC (**Figure 5.7**) and AlN feedstocks (**Figure 5.8**), gives the specific volume of the melt in the cavity as a function of the cavity pressure and temperature. These plots help in understand the compressibility and temperature effects during a typical injection molding cycle. The hold pressure should be chosen after appropriately referring to the PVT diagram so that the residual cavity pressure is near atmospheric pressure before mold opening [36]. This in turn ensures avoidance of any part ejection and/or relaxation issue. From the **Figures 5.7 and 5.8**, it is clear that monomodal feedstocks have higher slope values implying more thermal expansion than those of bimodal feedstocks. Thus, the increased powder content using nanoparticles addition reduces the thermal expansion of the feedstock indicating a lower tendency for shrinkage in the final part which is inversely proportional to packing density. The reduced specific volume indicates a positive impact of nanoparticle addition on the feedstock density.

Additional analysis was done by fitting the PVT data into a modified Tait two-domain empirical model that defines two domains below and above a transition temperature T_t as shown in **Equation 5.2**:

$$v(T, P) = \left[v_0(T) \times \left(1 - C \times \ln \left(1 + \frac{P}{B(T)} \right) \right) + v_f(T, P) \right]^{-1} \dots\dots (5.2)$$

Where v is the specific volume (cc/g), T is the temperature ($^{\circ}$ C), P is the pressure (MPa), C is a dimensionless constant, $B(T)$ is a temperature dependent parameter with the same dimension as pressure, v_0 and v_f are the specific volumes at room temperature and at temperatures above the

transition temperature respectively. Specific volume at temperatures higher than the transition temperature is given by **Equation 5.3**.

$$T \geq T_f, \upsilon_0(T) = b1_m + b2_m \times T^* \dots\dots (5.3)$$

where T* is any specific temperature above the transition temperature. B(T) can be expressed as shown in **Equation 5.4**.

$$B(T) = b3_m \times e(-b4_m \times T^*) \dots\dots (5.4)$$

However, the specific volume at transition temperature is considered to be zero while heating the feedstock. It is represented with **Equation 5.5**.

$$\upsilon_f(T, P) = 0 \dots\dots\dots (5.5)$$

The specific volume at temperatures lower than the transition temperature is given by **Equation 5.6**, where the feedstock is in solid and semi-solid state.

$$T < T_f, \upsilon_0(T) = b1_s + b2_s \times T^* \dots\dots (5.6)$$

Here, B (T) can be expressed as shown in **Equation 5.7**.

$$B(T) = b3_s \times e(-b4_s \times T^*) \dots\dots (5.7)$$

Here, T* is any specific temperature below the transition temperature. The specific volume while cooling is given as shown in **Equation 5.8**.

$$\upsilon_f(T, P) = b7^* \exp(b8 \times T^* - b9 \times P) \dots\dots (5.8)$$

The subscripts, m and s refer to the melt and solid states. **Table 5.5** gives the values and definition of different PVT coefficients for the SiC and AlN feedstocks.

From **Table 5.5**, it is evident that nanoparticle addition brings in none or minor changes in the crystallization temperature and the specific volume transition. This might be due to the fact that the binder composition is kept constant for both the monomodal and bimodal feedstocks. Thus, similar to prior work by Wu *et al* on alumina feedstocks, a future PVT analysis with varied binder composition is required [37].

5.3.4. Injection Molding Simulations

Figures 5.9a-d depicts the progressive filling pattern during injection molding of the monomodal SiC feedstocks. Similar patterns were noticed for other feedstocks as well. Simulations were performed to evaluate the effect of melt temperature on the mold fill time. From **Figure 5.10**, it

can be seen that the fill time decreases with an increase in the melt temperature, as expected with the shear thinning behavior of the feedstocks. Irrespective of the melt temperatures, the bimodal feedstocks showed prolonged fill time compared to that of the monomodal feedstocks. This can be attributed to the increased bimodal feedstock viscosity due to nanoparticle addition, as discussed in the previous sections.

Additional simulations were performed to further understand the effect of feedstock viscosity on the mold filling behavior. From these simulations, an average melt velocity was calculated and plotted against the melt temperature (**Figure 5.11**). The lower melt velocity values can be attributed to the reduced fluidity of the bimodal feedstocks due to nanoparticles addition. These reduced velocity values can be directly correlated to the increased mold filling time. Such prolongation in the mold filling generally leads to heat transfer through the mold wall, resulting in the formation of a thick frozen layer narrowing the actual flow channel [34, 38]. This in turn results in the increased shear stress at the walls for bimodal feedstocks as plotted in the **Figure 5.12**.

In addition to the above discussions, it is necessary to understand the differences in the simulated values of monomodal SiC and AlN feedstocks in spite of their similar powder content. The orientation of irregularly shaped micro-sized SiC particles along the cavity walls could be suggested as the reason for its lower melt velocity and higher shear stress values compared to that of monomodal AlN feedstock. Similar orientation issues were explained in the past by Krug *et al* [38] and Gietzelt *et al* [39] in the injection molding of irregularly shaped Al₂O₃ particles. Based on the above discussion, a series of injection molding cycles were performed with the feedstocks to mold a multi-slotted part as shown in the **Figure 5.13**. Our on-going work focuses on a detailed analysis of process simulations and molding experiments to further understand the effects of nanoparticle additions on mold filling behavior of these feedstocks.

5.4. Conclusions

This research emphasizes the effects of nanoparticle addition on the thermal and rheological properties of SiC and AlN feedstocks. Rheological measurements concluded a reduced fluidity for the bimodal feedstocks due to their increased powder content via nanoparticle addition. Coefficient values obtained from the viscosity models indicated that additional shear stress is required to initiate the pseudo-plastic behavior in bimodal μ -n feedstocks. Even though the nanoparticles addition was found to hold positive impact on feedstock properties, the mold filling

simulation studies indicated that bimodal mixtures posed challenges. The higher viscosity of the bimodal feedstocks led to slower melt velocity which in turn increased the fill time and shear stress along the mold walls. Further studies are on-going to determine whether additional benefits can be gained during the sintering stage from using the bimodal μ -n feedstocks.

5.5. References

1. M. Flinders, D. Ray, A. Anderson, R.A. Cutler, *Journal of American Ceramic Society*, 2005, vol.88, pp. 2217-2226.
2. K. Pelissier, T. Chartier and J.M. Laurent, *Ceramics International*, 1998, vol. 24, pp. 371-377.
3. A. Okada, *Journal of European Ceramic Society*, 2008, vol. 28, pp. 1097-1104.
4. A.F. Junior, D. Shanafield, *Journal of Materials Science: Materials in Electronics*, 2005, vol. 16, pp. 139-144.
5. T. Yoshioka, Y. Makino, S. Miyake, H. Mori, *Journal of Alloys and Compounds*, 2006, vol. 408-412, pp. 563-567.
6. T.S. Suzuki, Y. Sakka, *Scripta Materialia*, 2005, vol. 52, pp. 583-586.
7. X. Luo, J. Li, B. Zhang, W. Li, H. Zhuang, *Journal of American Ceramic Society*, 2006, vol.89, pp. 836-841.
8. Y. Wu, Y. Liu, H. Zhou, *Materials Chemistry and Physics*, 1998, vol.56, pp. 271-274.
9. S. Surnev, D. Lepkova, A. Yoleva, *Materials Science and Engineering B*, 1991, vol. 10, pp. 35-40.
10. S. Du, Z. Liu, L. Li, Z. Gui, *Materials Letters*, 1995, vol. 25, pp. 105-109.
11. X.L. Li, H.A. Ma, Y.J. Zheng, Y. Liu, G.H. Zuo, W.Q. Liu, J.G. Li, X. Jia, *Journal of Alloys and Compounds*, 2008, vol. 463, pp. 412-416.
12. J.K. Lee, H. Tanaka, H. Kim, D.J. Kim, *Materials Letters*, 1996, vol. 29, pp. 135-142.
13. M. Medraj, Y. Baik, W.T. Thompson, R.A.L. Drew, *Journal of Materials Processing Technology*, 2005, vol. 161, pp. 415-422.
14. M. Fukushima, Y. Zhou, Y. Yoshizawa, *Journal of Membrane Science*, 2009, vol. 339, pp. 78-84.
15. H. Hassanin, K. Jiang, *Advanced Engineering Materials*, 2009, vol. 11, pp. 101-105.
16. Y.C. Song, Y. Zhao, C.X. Feng, Y. Lu, *Journal of Materials Science*, 2002, vol. 29, pp. 5745-5756.
17. K.H. Lin, Y.C. Lin, S.T. Lin, *Journal of Materials Processing Technology*, 2008, vol. 201, pp. 701-705.
18. D. Xueli, M. Qin, H. Islam, P. Feng, X. Qu, *Key Engineering Materials*, 2007, vol. 336-338, pp. 1028-1030.
19. X. Qu, D. Huang, M. Qin, D. Li, J. Lin, *Rare Metal Materials and Engineering*, 2001, vol. 30, pp. 212-215.
20. Y. Inomata, *Proceeding of International Symposium on Ceramic Components for Engine*, ed. S. Somiyai et al, KTK Scientific Publishers, Tokyo, 1984, pp. 253-261.
21. Y. Uemura, Y. Inomata, Z. Inoue, *Journal of Materials Science*, 1981, vol. 95, pp. 2333-2335.

22. J. H. She, K.Ueno, *Materials Research Bulletin*, 1999, vol. 34, pp. 1629–1636.
23. D. Sciti, A. Bellosi, *Journal of Materials Science*, 2000, vol.35, pp. 3849-3855.
24. M.C. Rodriguez, A. Munoz, A.D. Rodriguez, *Journal of the European Ceramic Society*, 2006, vol. 26, pp. 2397–2405.
25. V.A. Izhevskiy, A.H.A. Bressiani, J.C. Bressiani, *Journal of American Ceramic Society*, 2005, vol.88, pp. 1115-1121.
26. M. Bothara, S. V. Atre, S-J. Park, R.M. German, T.S. Sudarshan, R. Radhakrishnan, *NSTI Nanotech 2007*, vol.4, pp. 494-497.
27. J.Y. Qiu, Y. Hotta, K. Watari, K. Mitsuishi, *Journal of American Ceramic Society*, 2006, vol.89, pp. 377-380.
28. P. Suri, S. Atre, R. German, J. D'Souza, *Materials Science and Engineering A*, 2003, vol.356, pp. 337-344.
29. V. Onbattuvelli, G. Purdy, G. Kim, S. Laddha, S. Atre, *Advances in Powder Metallurgy and Particulate Materials*, 2010, no.1, pp. 64-72.
30. V. Onbattuvelli, G. Purdy, G. Kim, S. Laddha, S. Atre, *NSTI Nanotech 2010*, vol.1, pp. 800-803.
31. S.J. Park, Y. Wu, D.F. Heaney, X. Zou, G. Gai and R.M. German, *Metallurgical and Materials Transactions A*, 2009, vol. 40 A, pp. 215-222.
32. Y. Ahn, S.T. Chung, S.V. Atre, S.J. Park, R.M. German, *Powder Metallurgy*, 2008, vol.51, pp. 318-326.
33. L. Liu, N.H. Loh, B.Y. Tay, S.B. Tor, Y. Murakoshi, R. Maeda, *Materials Characterization*, 2005, vol. 54, pp. 230-238.
34. G. Aggarwal, S.J. Park, I. Smid, *International Journal of Refractory Metals & Hard Materials*, 2006, vol.24, pp. 253–262.
35. R. S. Lib, B.R. Patterson, H.A. Heflin, *Progress in Powder Metallurgy*, 1986, vol. 42, pp. 95-104.
36. S.G. Laddha, C. Wu, S-J Park, S. Lee, S. Ahn, R. M. German, S.V. Atre, *International Journal of Powder Metallurgy*, 2010, vol.46, pp. 49-58.
37. C. Wu, S.V. Atre, S. Laddha, S. Lee, K. Simmons, S-J. Park, R. German, *PIM International*, 2008, vol. 2, pp. 68-73.
38. **S. Krug, J. R. G. Evans, J. H. H. TerMaat**, *Journal of the European Ceramic Society*, 2002, vol.22, pp. 173-181.
39. T. Gietzelt, O. Jacobi, V. Piotter, R. Rupercht, J. Hausselet, *Journal of Materials Science*, 2004, vol.39, pp. 2113-2119.

List of Figures

Figure 5.1: DSC of monomodal and bimodal SiC (a) and AlN (b) feedstocks

Figure 5.2: TGA of monomodal and bimodal SiC (a) and AlN (b) feedstocks

Figure 5.3: Viscosity of monomodal (a) and bimodal (b) SiC feedstocks at different shear rate and temperature combinations, displaying pseudo-plastic behavior

Figure 5.4: Viscosity of the monomodal (a) and bimodal (b) AlN feedstocks at different shear rate and temperature combinations, displaying pseudo-plastic behavior

Figure 5.5: Comparison of powder packing behavior in monomodal (a) and bimodal (b) SiC feedstocks

Figure 5.6: Comparison of powder packing behavior in monomodal (a) and bimodal (b) AlN feedstocks

Figure 5.7: PVT relationships for monomodal (a) and bimodal (b) SiC feedstocks

Figure 5.8: PVT relationships for monomodal (a) and bimodal (b) AlN feedstocks

Figure 5.9: Progressive filling pattern during the injection molding of monomodal SiC feedstock at 170°C, (a) 25% fill, (b) 50% fill, (c): 75% fill and (d) 100% fill

Figure 5.10: Fill time vs. injection temperature for all feedstocks, revealing that nanoparticle addition slows the mold filling process

Figure 5.11: Melt velocity vs. injection temperature for all feedstocks indicating that nanoparticle addition slows down the melt's fluidity thereby increasing the mold fill time

Figure 5.12: Shear stress at the wall vs. injection temperature for all feedstocks, indicating that nanoparticle addition increases the shear stress on the walls

Figure 5.13: Multi-slotted parts injection molded with the monomodal SiC feedstocks

List of Tables

Table 5.1: Properties of sintered SiC and AlN ceramics

Table 5.2: Comparison of the net-shaping processes for SiC and AlN

Table 5.3: Conditions used for scaling up of SiC and AlN feedstocks

Table 5.4: Values of different rheological constants for SiC and AlN feedstocks

Table 5.5: PVT coefficients for SiC and AlN feedstocks

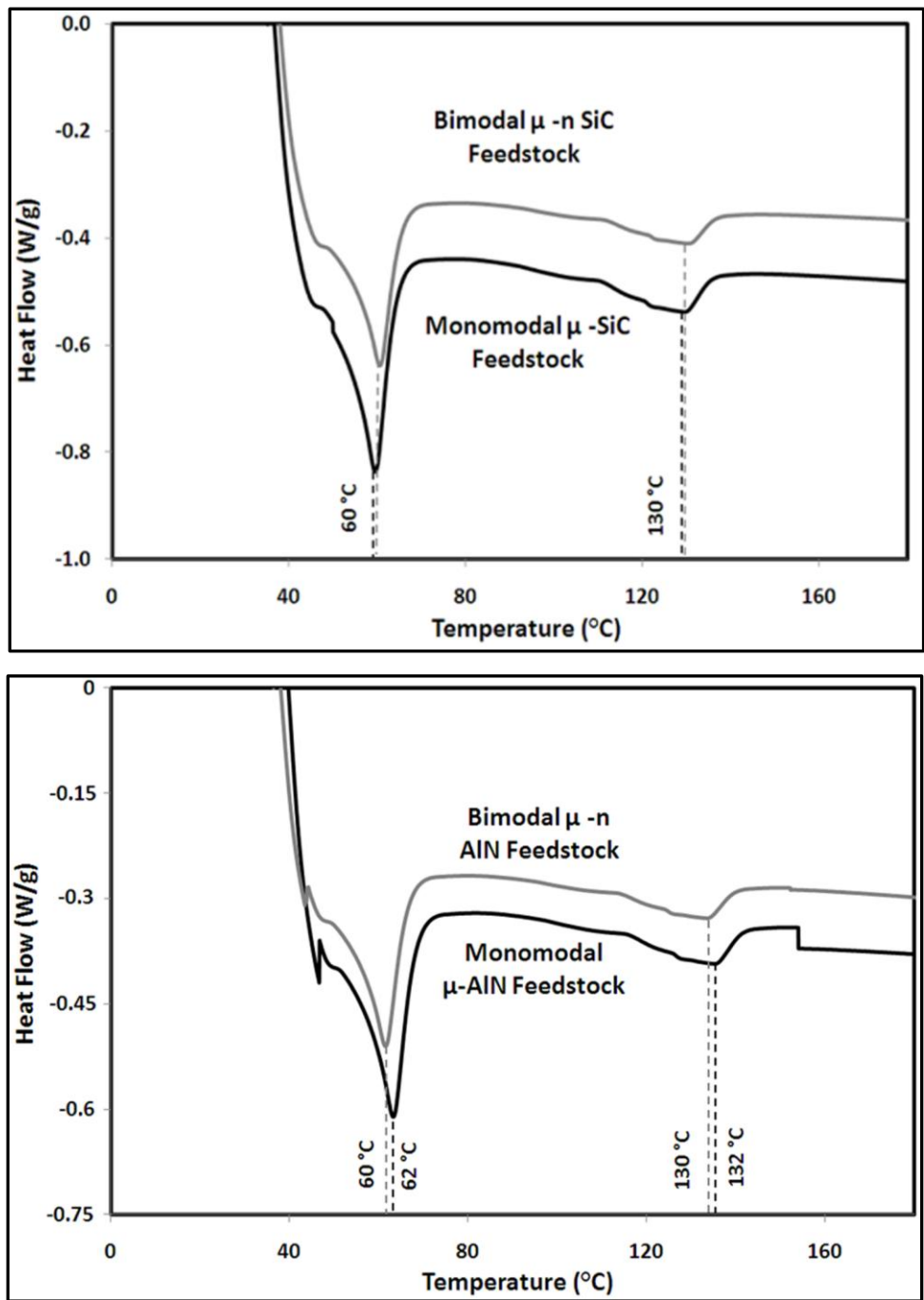


Figure 5.1: DSC of monomodal and bimodal SiC (a) and AlN (b) feedstocks

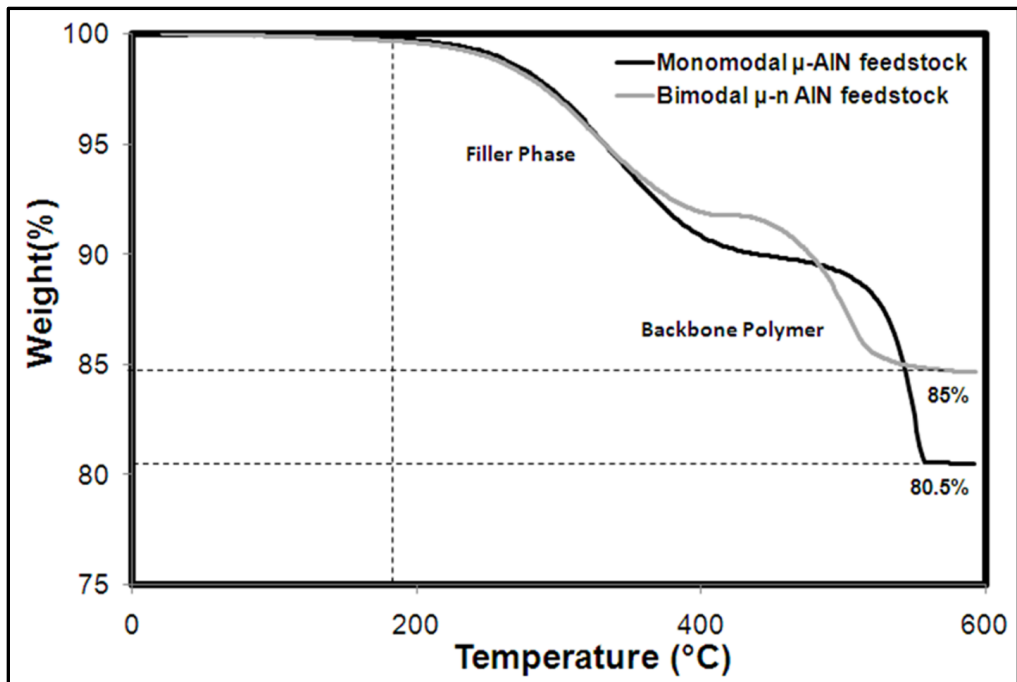
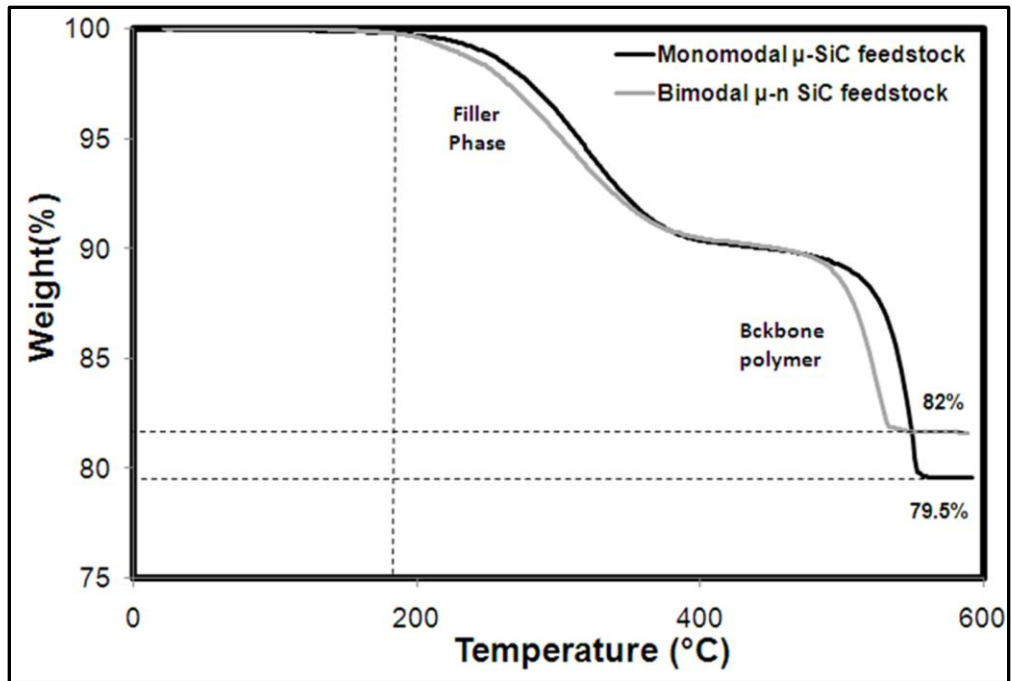


Figure 5.2: TGA of monomodal and bimodal SiC (a) and AlN (b) feedstocks.

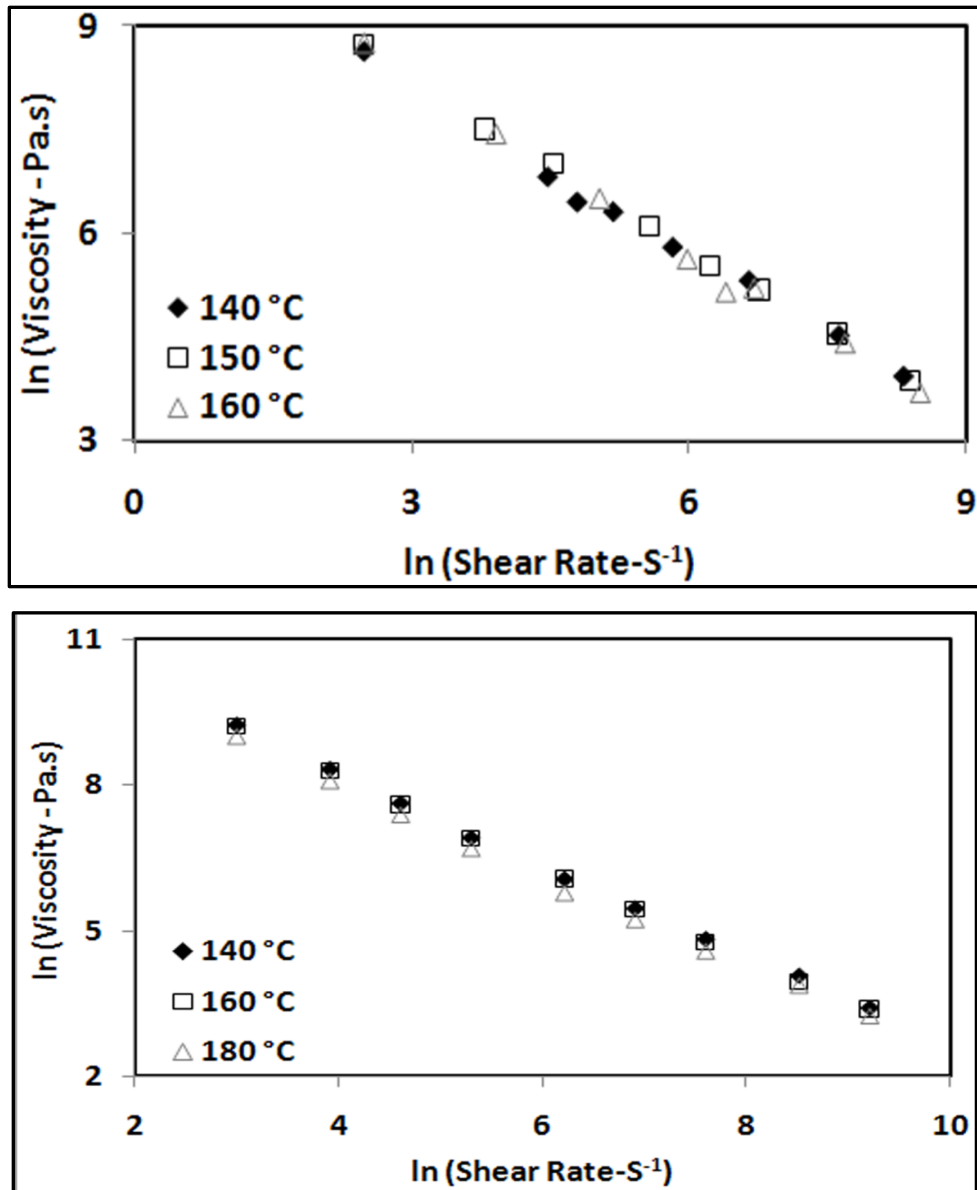


Figure 5.3: Viscosity of monomodal (a) and bimodal (b) SiC feedstocks at different shear rate and temperature combinations, exhibiting pseudo-plastic behavior

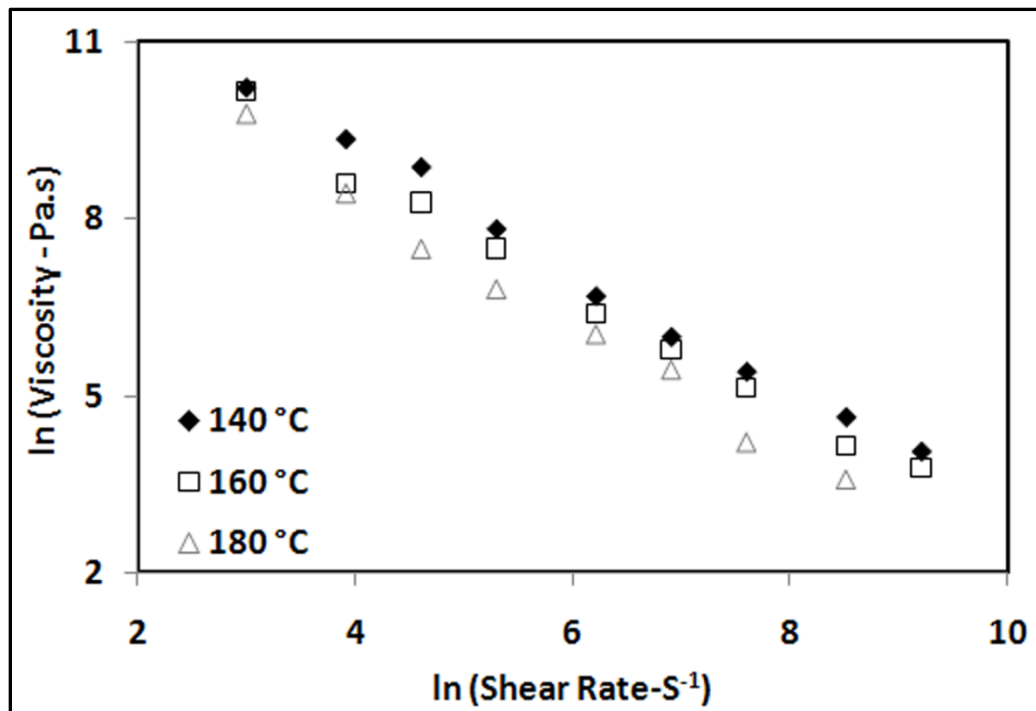
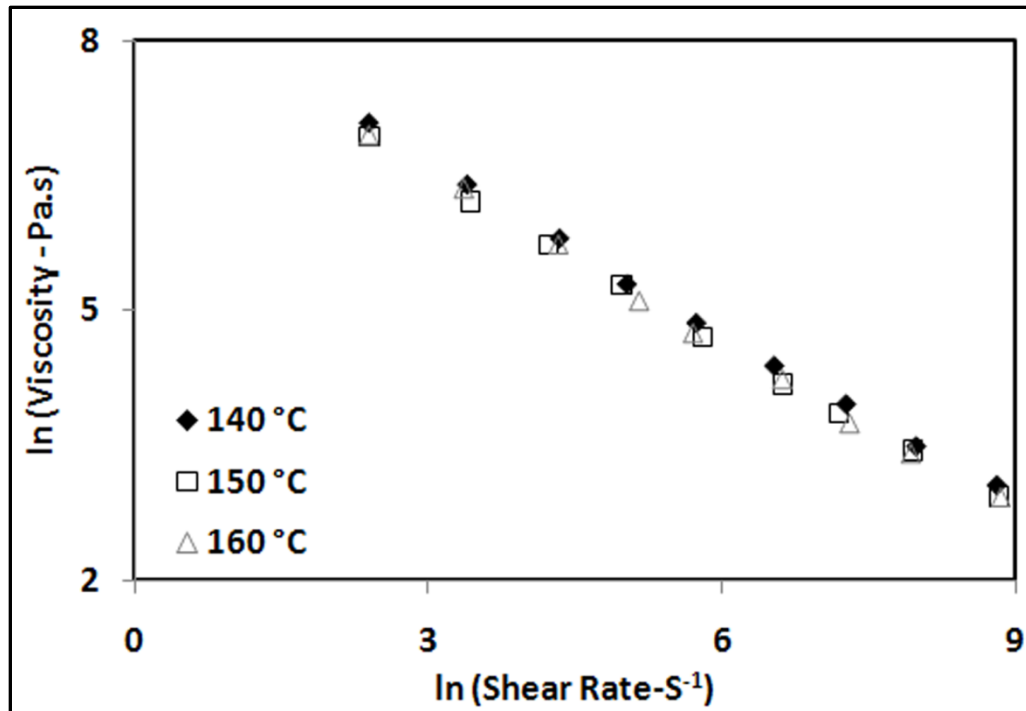


Figure 5.4: Viscosity of monomodal (a) and bimodal (b) AlN feedstocks at different shear rate and temperature combinations, exhibiting pseudo-plastic behavior

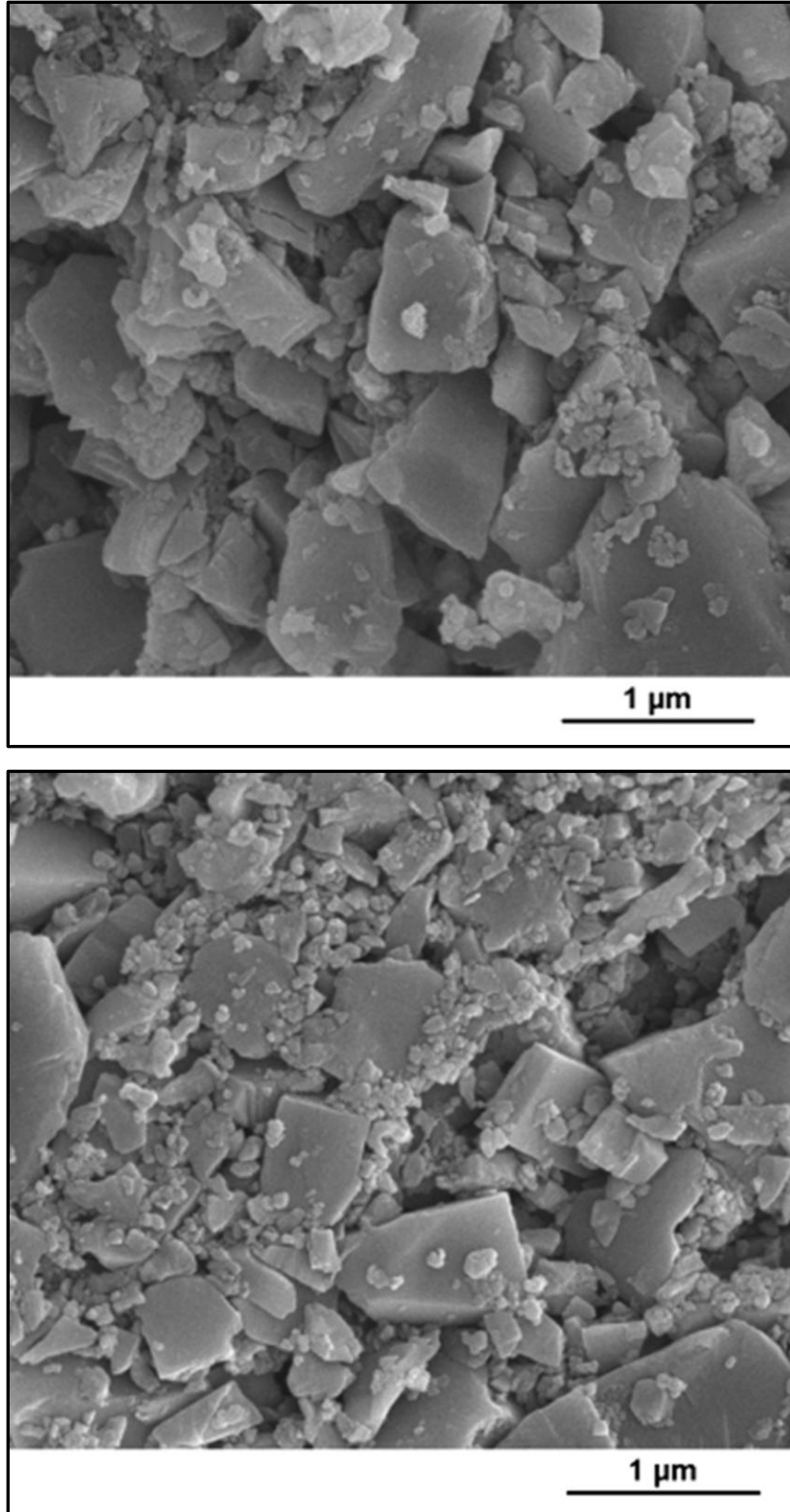


Figure 5.5: Comparison of powder packing behavior in monomodal (a) and bimodal (b) SiC feedstocks

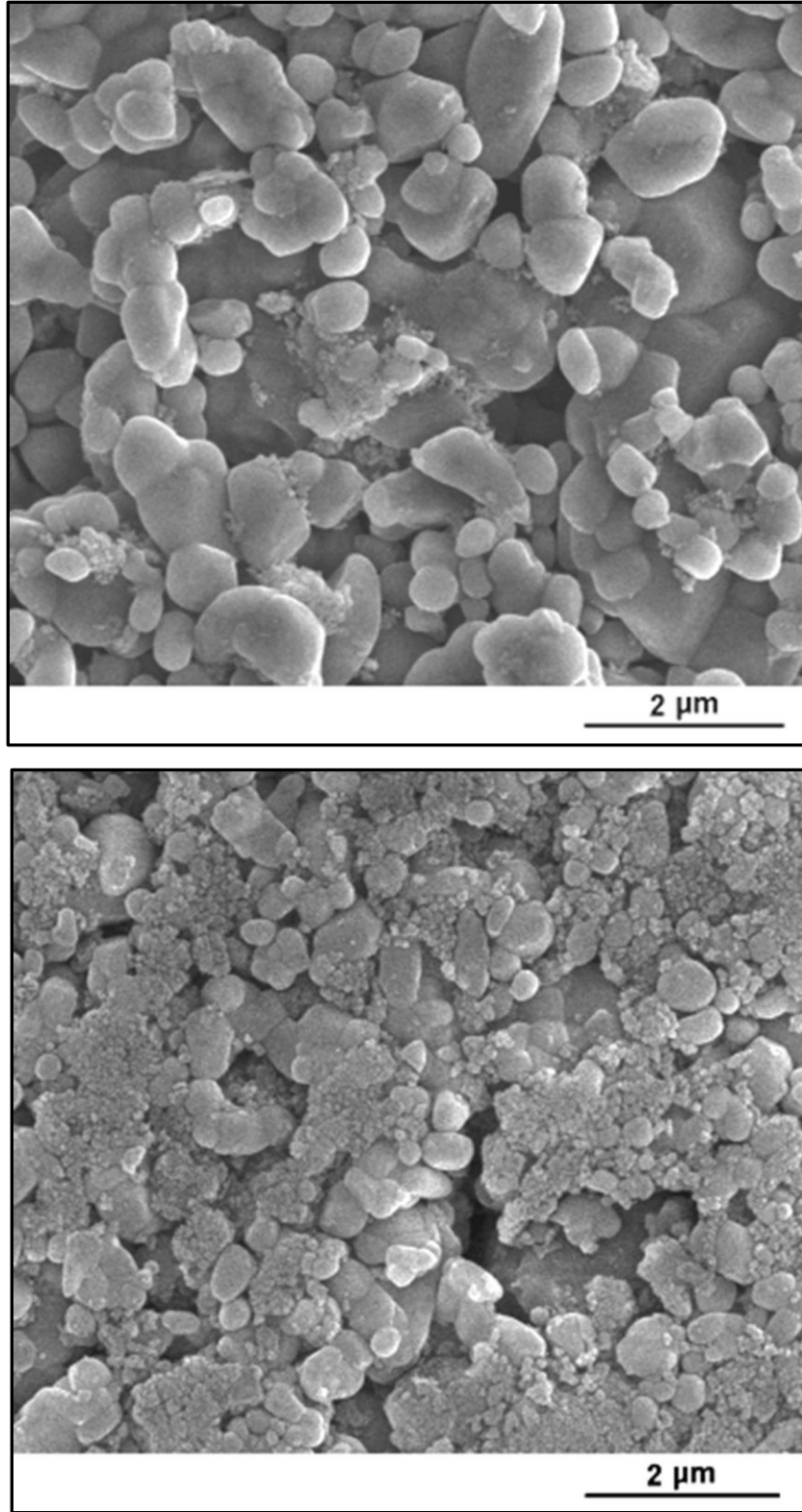


Figure 5.6: Comparison of powder packing behavior in monomodal (a) and bimodal (b) AlN feedstocks

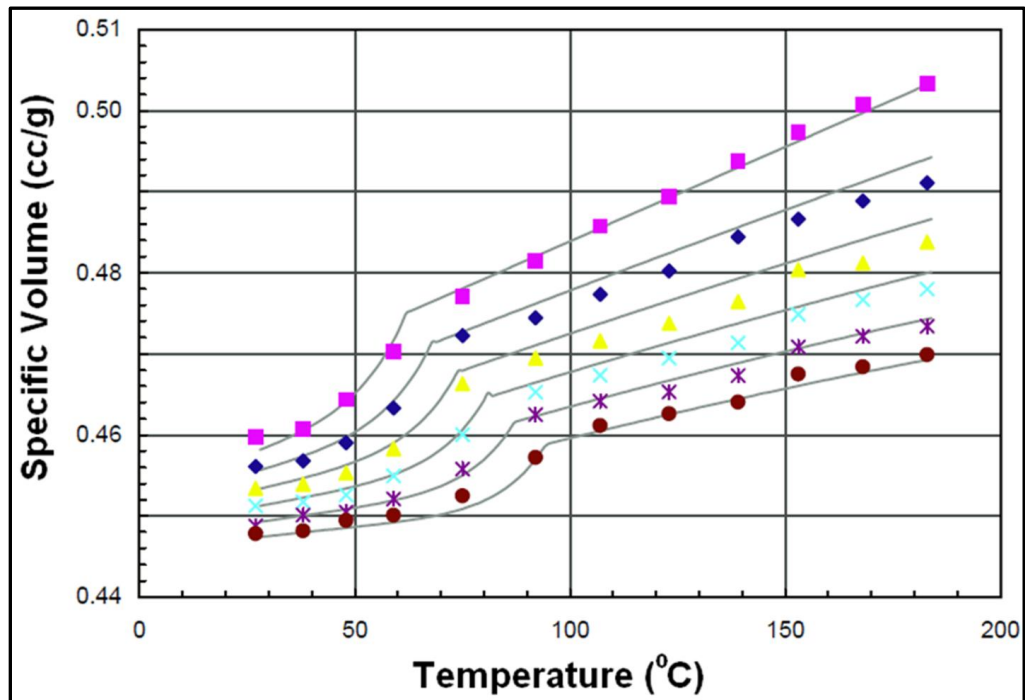
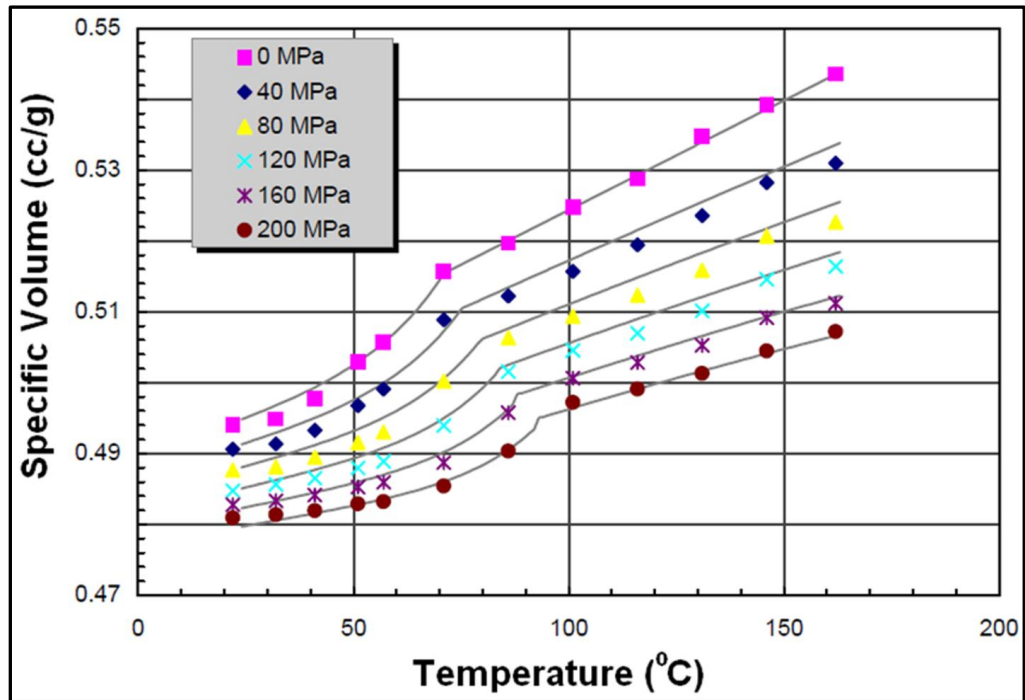


Figure 5.7: PVT relationships for monomodal (a) and bimodal (b) SiC feedstocks

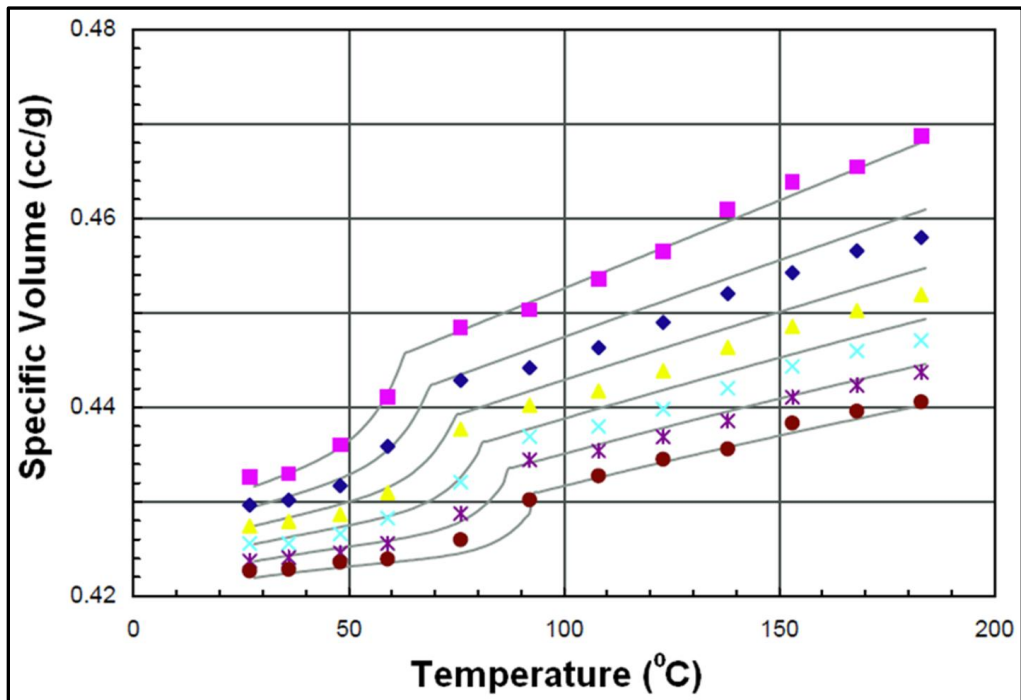
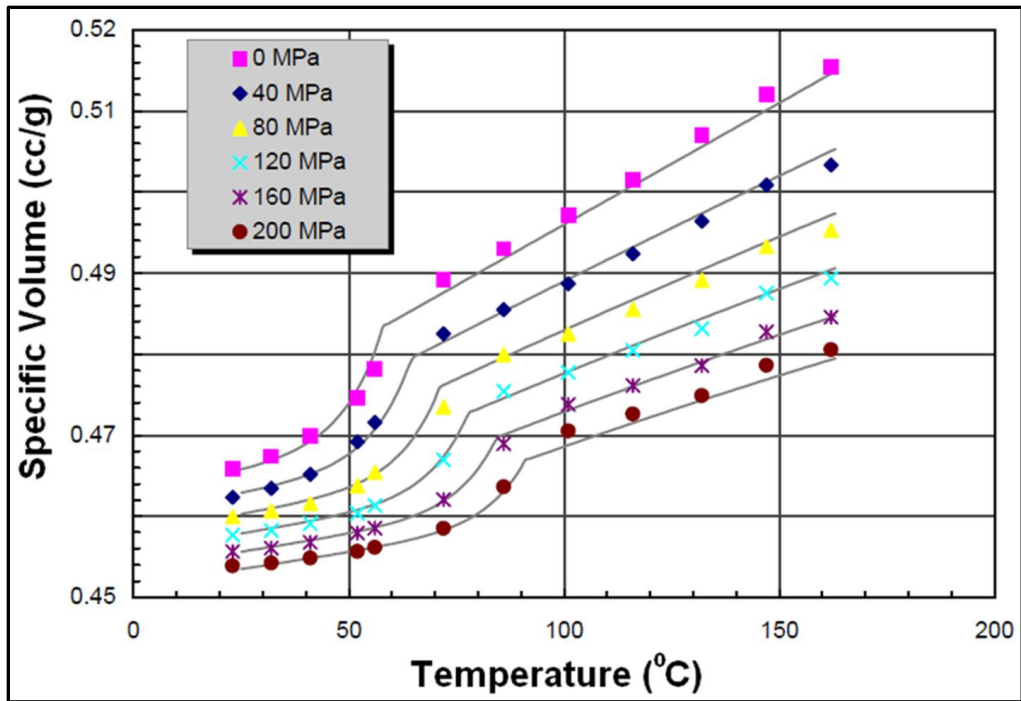


Figure 5.8: PVT relationships for monomodal (a) and bimodal (b) AlN feedstocks

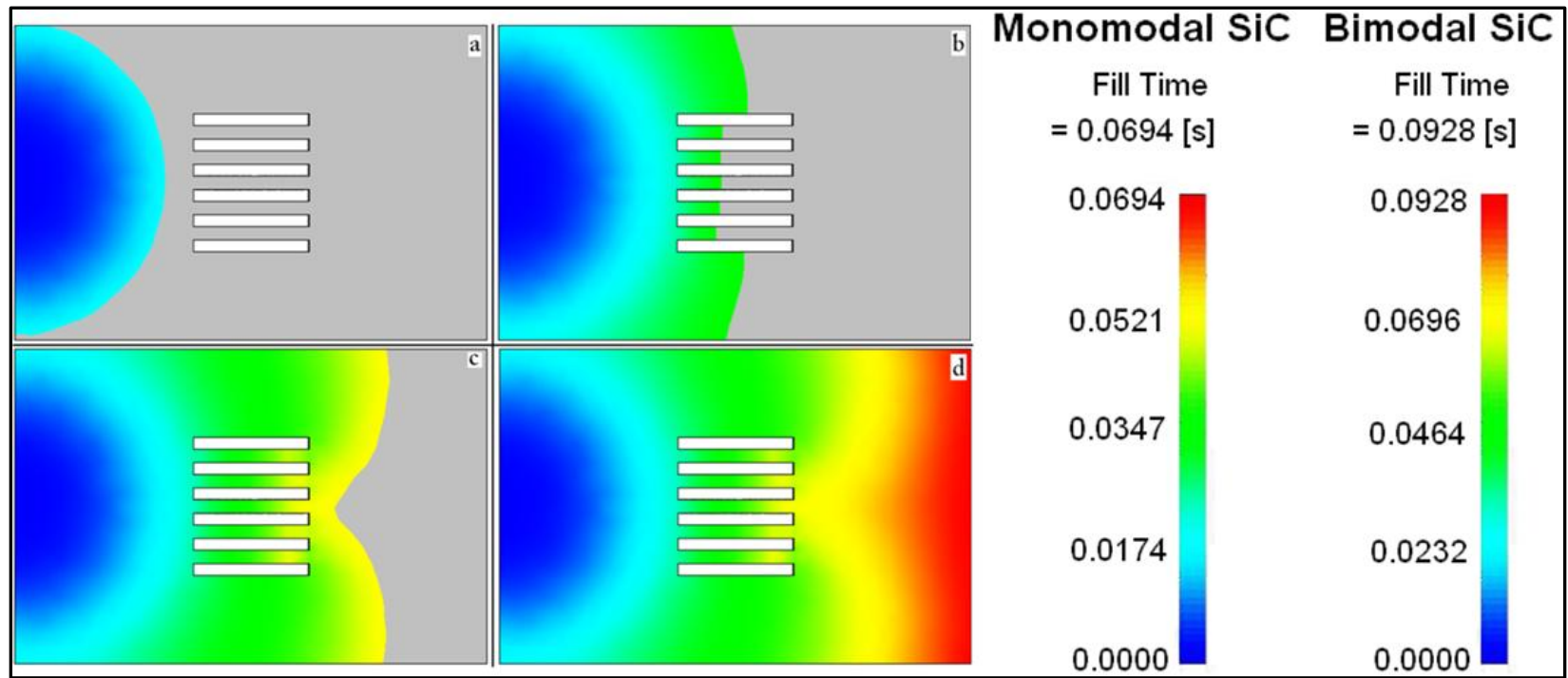


Figure 5.9: Progressive filling pattern during the injection molding of monomodal SiC feedstock at 170°C, (a) 25% fill, (b) 50% fill, (c): 75% fill and (d) 100% fill

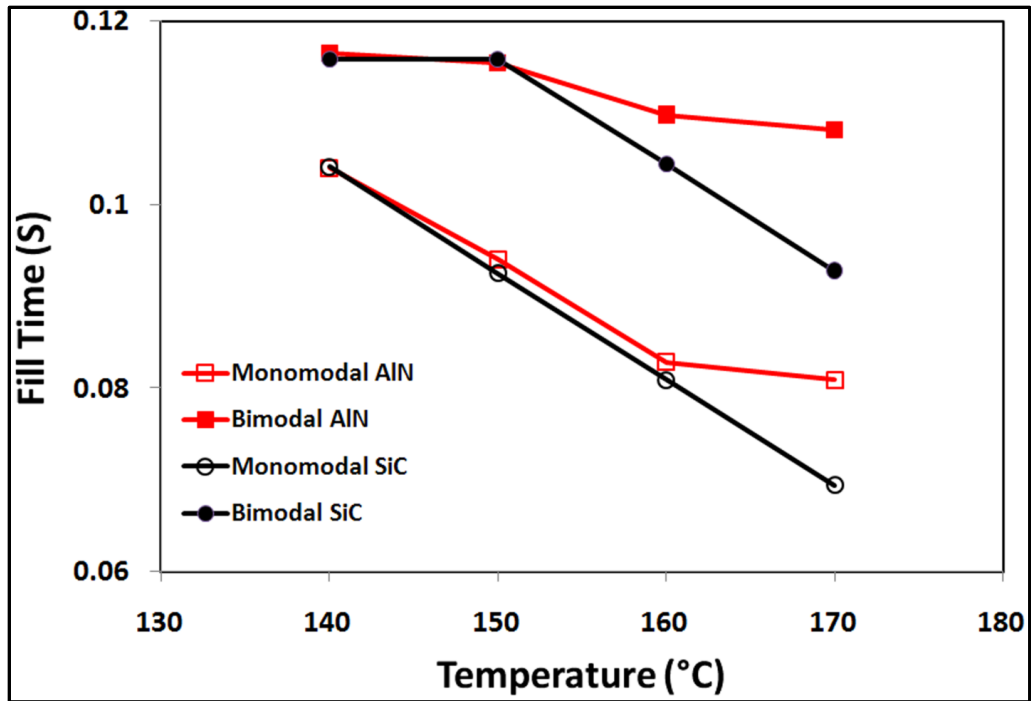


Figure 5.10: Fill time vs. injection temperature for all feedstocks, revealing that nanoparticle addition slows the mold filling process

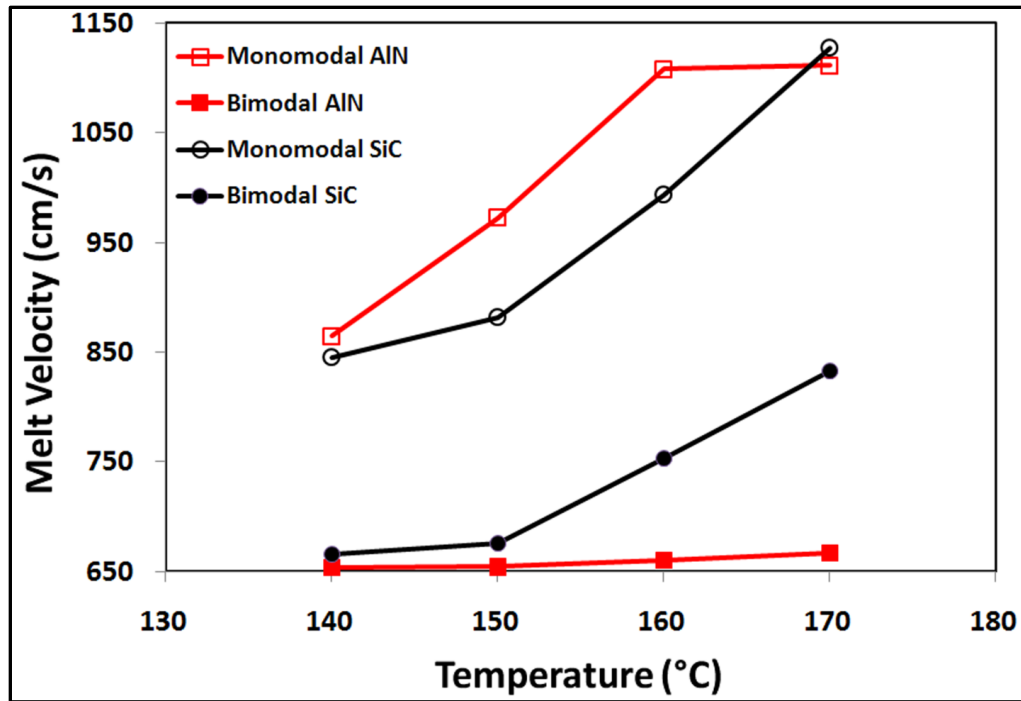


Figure 5.11: Melt velocity vs. injection temperature for all feedstocks indicating that nanoparticle addition slows down the melt's fluidity thereby increasing the mold fill time.

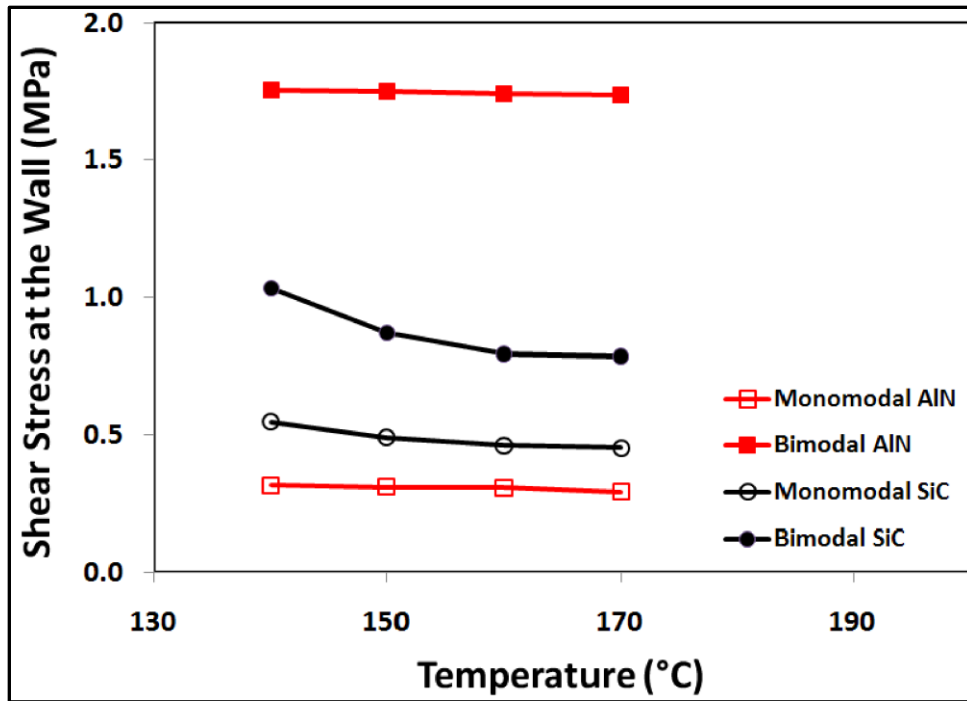


Figure 5.12: Shear stress at the wall vs. injection temperature for all feedstocks, indicating that nanoparticle addition increases the shear stress on the walls

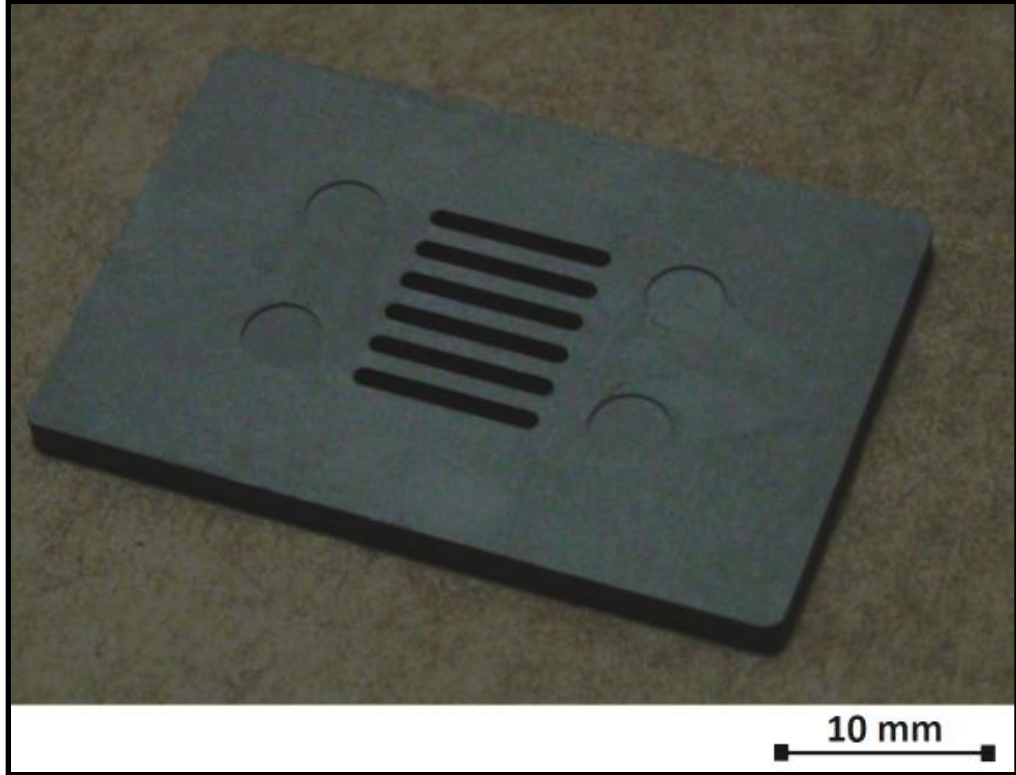


Figure 5.13: Multi-slotted parts injection molded with the monomodal SiC feedstock

Table 5.1: Properties of sintered SiC and AlN ceramics

Property	SiC	AlN
Density (g/cc)	3.2	3.26
Thermal Conductivity (W/m.K)	120	170
CTE ($10^{-6}/^{\circ}\text{C}$)	4	4.5
Vicker's Hardness (GPa)	22	10.4
Fracture Toughness ($\text{MPa}\cdot\text{m}^{0.5}$)	4.5	2.6
Flexural Strength (MPa)	450	320
Volume Resistivity ($\Omega\cdot\text{cm}$)	10^{14}	$>10^{14}$

Table 5.2: Comparison of the net-shaping processes for SiC and AlN

Characteristics	PIM	Pressing	Casting	Machining
Density	90-100%	95-100%	95-99%	100%
Surface Finish	0.4 to 0.8 μm	< 2 μm	3 μm	0.4 to 2 μm
Secondary Machining	Not required	Required	Required	-
Wall Thickness	10 μm	>2mm	>5mm	>2mm
Dimensional Tolerance	Close	Poor	Poor	Poor
Shape Complexity	High	Medium	Medium	High
Production Rate	High	High	Low	Low

Table 5.3: Conditions used for scaling up of SiC and AlN feedstocks

Extruder Specifications	Values
Screw Diameter	27 mm
L/D	40
Flight Depth	5.3
Number of Barrels/Zones	10
Zone Temperatures	160 °C
Screw Speed	260 rpm
Extrusion Rate	30 lb/hr
Cooling System	Air-cooled conveyor belt system

Table 5.4: Values of different rheological constants for SiC and AlN feedstocks

Coefficients	Definitions	SiC Feedstocks		AlN Feedstocks	
		Monomodal	Bimodal	Monomodal	Bimodal
(1-n)	slope of the shear-thinning curve	0.84	0.93	0.63	0.95
τ^* (KPa)	Constant with Weissenberg-Rabinowitsch correction at user's specification during data fit	28	127	12	178
D_1 (Pa-s)	Scale factor for viscosity	0.17E+19	10 E+19	8.77E+10	9.13 E+19
A_1	WLF temperature shift factor	37.73	42.69	15.24	29.54
D_2 (K)	Glass Transition Temperature at zero gauge pressure	263			
A_2 (K)	WLF temperature shift factor	51.6			

Table 5.5: PVT coefficients for SiC and AlN feedstocks

Coefficients	Definition	SiC Feedstocks		AlN Feedstocks	
		Monomodal	Bimodal	Monomodal	Bimodal
b5 (K)	Crystallization temperature	7.1E+01	6.9E+01	5.8E+01	6.3E+01
b6 (K/Pa)	Pressure sensitivity of b5	1.05E-01	1.6E-01	1.65E-01	1.45E-01
b1m (m ³ /kg)	Tait constants for melt	5.15E-01	4.75E-01	4.83E-01	4.46E-01
b2m (m ³ /kg-K)		3.09E-04	2.33E-04	3E-4	1.86E-04
b3m (Pa)		2.83E+02	3.19E+02	2.87E+02	3.43E+02
b4m (1/K)		5.23E-03	4.84E-03	4.82E-03	4.03E-03
b1s (m ³ /kg)	Tait constants for solid	5.03E-01	4.63E-01	4.69E-01	5.37E-01
b2s (m ³ /kg-K)		1.9E-04	1.53E-04	9.7E-05	1.49E-04
b3s (Pa)		3.72E+02	5E+02	5.79E+02	5E+02
b4s (1/K)		6.73E-03	1E-02	1.26E-03	1E-02
b7 (m ³ /kg)	Transition of specific volume from solid to melt	1.23E-02	1.22E-02	1.49E-02	0.9E-02
b8 (1/K)		6.16E-02	9.03E-02	1.1E-01	1.31E-01
b9 (1/Pa)		8.5E-03	1.59E-02	2.12E-02	2.22E-02

CHAPTER 6

The Effect of Nanoparticle Addition on Binder Removal from Injection Molded SiC and AlN

Abstract

The effect of nanoparticle addition on the multi-step debinding of injection molded silicon carbide (SiC) and aluminum nitride (AlN) samples was studied. Variations brought in by the increased powder content and reduced particle size on the solvent debinding kinetics are discussed. A series of experiments was performed by varying the solvent debinding conditions (time, temperature and aspect ratio). The corresponding diffusion coefficients were calculated and were extended to analyze the effect of reduced particle size and solids loading on the solvent debinding kinetics. The thermal debinding behavior of dewaxed samples was also studied and the trends correlated with the solvent debinding behavior.

6.1. Introduction

Binder systems play a vital role in determining the properties of the powder-polymer mixtures and their moldability [1]. Selection of an appropriate binder system is critical for the success of the PIM process [2-3]. Binder systems used in PIM comprise of multi-components with a major filler phase and minor backbone polymer along with little or no surfactants [4-11]. Following injection molding, binder removal (debinding) is required prior to the sintering stage. Various debinding techniques including solvent debinding [4-7], thermal debinding [8, 9] and catalytic debinding [10, 11] have been reported in the past. Irrespective of the techniques, the primary aim is rapid binder removal without any physical distortion of the injection molded green parts.

R.M. German had suggested a multi-step debinding process to expedite binder removal [12]. One common multi-step debinding process consists of solvent debinding followed by the thermal degradation of the remaining polymers. This initial binder removal leaves interpenetrating pore channels, which are used to escape the decomposed gas during subsequent thermal debinding. Thus, the solvent debinding process shortens the debinding cycle significantly and has been widely accepted by the PIM industry [12, 13]. **Table 6.1** lists the prior reports on multi-component binder systems for a two stage debinding process initiating with a solvent debinding.

Lin et al [14] have proposed the existence of three stages of solvent debinding process. First, the solvent molecules penetrate into the binder, producing a swollen gel. When the binder-solvent interactions are strong enough, the gel gradually disintegrate into a true solution. The solution then diffuses toward the surface and thus removed. Rapid binder removal may result in defects such as cracking, distortion, and slumping [13-16]. A successful solvent debinding process thus depends on the diffusion controlling factors including the temperature [17-21], time [17-19, 21], solvent [19] and aspect ratio [17-18, 21] of the samples. Prior efforts have attempted to understand the effect of the above factors on debinding kinetics [1, 17, 22]. However, little research pertaining to the effect of powder particle content and particle size distribution on the debinding kinetics is available till date. Our prior report on SiC and AlN injection molding demonstrated the use of bimodal μ -n powder mixtures as an efficient way to improve the solids loading [23, 24]. Such reduced particle size and increased solids loading corresponds to reduced pore size and % porosity. This in turn will increase the tortuous path, slowing the rate of binder removal from the injection molded “green” parts. Thus, in the current paper, the effect of nanoparticle addition over the solvent debinding kinetics of injection molded AlN and SiC samples was studied. The work was also extended to studying the variations in the residual binder content due to nanoparticle addition during the thermal debinding cycle.

6.2. Experimental section

6.2.1. Materials

Commercially available α -SiC, AlN, Y₂O₃ were used as the starting materials as received. A multi-component binder system comprising of paraffin wax (PW), polypropylene (PP), polyethylene-g-maleic anhydride (LDPE-g-MA) and stearic acid (SA) was used in the current study. The formulations and injection molding conditions for the monomodal and bimodal SiC and AlN powder-binder mixtures were discussed elsewhere [24]. **Table 6.2** lists the composition of the SiC and AlN samples used in the present study. The binder composition was chosen in such a way to facilitate a multi-step (solvent, thermal) debinding. Heptane (Fischer Scientific) was used as the solvent to dissolve the soluble binder components without any further treatment.

6.2.2. Sample preparation:

Injection molded green samples were machined to the dimensions (l×b×h in mm) of 23 × 13.2 × 7.2, 34.5 × 6.6 × 7.2 and 25 × 14 × 2, which correspond to an effective length scale, ψ of volume-to-surface area ratio of 1.92, 1.56, and 82 mm, respectively.

6.2.3. Debinding procedure:

Isothermal solvent debinding experiments utilizing five specimens of each dimension were performed in heptane at 20, 40 and 60 °C under slow and continuous stirring. The continuous solvent recycling at 2ml/min was performed to avoid concentration effect of soluble components [17, 18]. All specimens were placed together into the solvent bath and were removed at each time-point for gravimetric analysis. The solvent debinding was monitored for up to 4 h. The fraction of the soluble binder remaining (f) can be calculated using the following Eq.6.1,

$$f = 1 - \frac{w_0 - w}{f_0 w_0} \quad (1)$$

where f_0 is the initial weight fraction of soluble binder, w_0 is the initial mass of compact, and w is the instantaneous mass of compact.

Thermogravimetric analysis (TGA) was performed (TA instruments - Q 500) under nitrogen atmosphere (50ml/min) with a heating rate of 20 °C/min, in order to verify the specimen weight losses during solvent debinding. Furthermore, scanning electronic microscopy (SEM) (Quanta™ – FEI) images were taken on both the surface and core of the samples to examine pore evolution. Thermal debinding cycles of the solvent debound samples were performed under inert

atmosphere in the CM 1212 FL furnace. TGA was once again performed on the thermally debound (brown) samples to determine the % residual carbon.

6.3. Results and Discussion

During the solvent debinding, heptane diffuses into the sample to dissolve PW and SA. As the molecular weight of the heptane is significantly lower than the molecular weights of the binders, heptane can diffuse into the sample faster than the PW+SA diffuse out of the sample. Consequently, the rate-limiting step is assumed to be the diffusion of the dissolved PW+SA molecules rather than the inward diffusion of the much smaller heptane molecules. A similar hypothesis has been reported by Zaky for PW in hexane [19] and Omar et al for polyethylene glycol in water [7]. Thus, factors including ψ , immersion time and temperature that may affect the diffusion of the binder molecules are to be considered.

Figures 6.1-6.4 shows the soluble binder extracted (%) in heptane at different time-temperature combinations from the SiC and AlN samples with different ψ ratio. As expected, increasing the ψ ratio signifies greater contact areas between solvent and binder and as consequence, lowers the debinding times. Similar results were noticed earlier by Oliviera et al [17] and Krauss et al [18] for alumina molded parts. Irrespective of the ψ ratio, the debinding rate was found to reduce with increase in the time. Such behavior has also been reported earlier by Oliviera et al [17], Krauss et al [18] and Zaky in stainless steel molded parts [19]. With increasing solvent immersion time, the solubilized components inside the samples diffuse through tortuous pathways, from inner regions to the specimen surface, leading to a reduction in the debinding rate. Increasing the solvent temperature is found to exhibit an improvement in debinding process efficiency for all specimen dimensions. This may be due to an increase in solubility of PW and SA in heptane as function of temperature. Similar temperature effects over the solubility were reported earlier by Omar et al [7] and Tsai et al [15].

6.3.1. Confirmation Studies

No dimensional change was noticed with the samples irrespective of the solvent debinding conditions. These findings are in contradiction with those of Zaky [19] and Wang et al [21] where dimensional change/swelling is reported when hexane is used as the solvent under similar conditions. To evaluate the total composition change in the samples during solvent debinding, thermogravimetric analysis (TGA) was performed. **Figures 6.5-6.6** shows the TGA curves for the SiC and AlN samples with the ranges of 200–375 °C and 380–490 °C, respectively. The thermal

analysis results agree with the initial proportion of binder components of the prepared feedstock. As immersion time increases, the composition varies due to a decrease in weight loss in the first degradation step, indicating the decrease in the soluble binder components. Similar TGA results were reported in the past by Oliveira et al for injection molded alumina samples [17]. After 240 minutes, only the weight loss of the backbone polymer was observed, suggesting that nearly all soluble components were removed.

Figures 6.7-6.10 shows the SEM micrographs of SiC and AlN samples after different solvent debinding times. The micrographs of all the green samples show a similar microstructure at regions close to the core and the surface. The surface micrograph of the region close to specimen surface after initial immersion in heptane (**Figures 6.7c, 6.8c, 6.9c, 6.10c**) show porous structure due to the elimination of soluble components, while no appreciable changes were observed in the micrograph of the specimen core (**Figures 6.7d, 6.8d, 6.9d, 6.10d**). By increasing the immersion time, (**Figures 6.7e, 6.8e, 6.9e, 6.10e and 6.7f, 6.8f, 6.9f, 6.10f**), the specimen microstructures at areas near the core and the surface become similar, indicating the removal of soluble components.

6.3.2. Effect of nanoparticle addition on the solvent debinding kinetics

From the **Figures 6.3-6.4**, it can be inferred that the bimodal samples exhibit slower polymer removal than the monomodal ones irrespective of the debinding conditions. This is due to the increase in the tortuous path to be followed by the binder components. Such behavior is an outcome of the combined effect of increased solids loading (lower % porosity) and decreased pore size via nanoparticle addition. In order to analyze the effect of such nanoparticle addition, factors including powder particle content and particle size should be studied separately. For example, Kozeny-Carman relation (Eq. 6.2) can be used to determine the effect of varying the solids loading on the permeability (k) (**Figures 6.11a-b**) [22].

$$k = \frac{2 * d_p^2 (1 - \varepsilon)^3}{75 * \varepsilon^2} \quad (6.2)$$

where, ε is the porosity (=1-solids loading) and d_p is the average particle size. Equal permeability values for the monomodal and bimodal samples at higher solids loading indicates a nullified effect of particle size at higher powder content, for the average particle size considered in the present study. Thus, the debinding variations exhibited by the bimodal samples in the current study are presumed to primarily correspond to the increase in the solids loading.

Solvent debinding is predominantly diffusion-controlled process that can be represented as,

$$\ln\left(\frac{1}{f}\right) = \frac{D_e t \pi^2}{\psi^2} + K \quad (6.3)$$

where, f is the fraction of the remaining soluble polymer, D_e is the interdiffusion coefficient of polymer and solvent, t is time and K represents the change in the mechanism controlling the debinding behavior [1, 22].

D_e can thus be calculated from the slope of the plot $\ln(1/f)$ as a function of immersion time. **Figures 6.12-6.14** plot the variations in the D_e values of monomodal and bimodal samples with respect to the solvent temperature (for a given ψ ratio). At room temperature, the dissolution of the wax in heptane is the likely rate limiting step in the beginning of the debinding process over a leaching time of 120 min. Polymer removal during the dissolution controlled stage is twice as fast as the removal during the diffusion limited stage at later times. **Table 6.3** lists the dissolution and diffusion coefficients exhibited by the samples at room temperature. Similar results of 1.75×10^{-5} and 0.6×10^{-5} cm^2/s were reported in the past as the dissolution and diffusion coefficients at 40°C by Bakan for alumina with water soluble binder system [1]. As the process proceeds, a longer diffusion distance through porous channels formed after initial debinding slows down the process and diffusion becomes the rate determining step. Debinding due to dissolution is less pronounced with the nanoparticle addition.

At higher solvent temperatures, the debinding was seen to be largely controlled only by diffusion for all immersion times studied. Higher D_e values observed for increasing temperatures are possibly due to the increased diffusivity of the paraffin wax in heptane. Irrespective of the sample aspect ratio and solvent temperature, the bimodal samples showed lower D_e values than the corresponding monomodal samples. This may be due to the decreased rate of the binder-solvent interactions due to the nanoparticle inclusion. Additionally, an order of magnitude increase in the D_e values by increasing the aspect ratio of the sample necessitated further examination.

Despite the fact that the monomodal $\mu\text{-SiC}$ and $\mu\text{-AlN}$ samples have similar powder content (~ 51 vol. %), the latter shows expedited debinding. This in turn necessitates a future work on extending the calculated D_e values to study the effect of varying particle size on solvent debinding kinetics. Further research including intrusion porosimetry measurements is required for an in-depth understanding of these findings.

6.3.3. Thermal debinding of solvent debound samples

The solvent debound parts with partially open pores were subjected to thermal debinding to further remove the binders. Keeping the TGA plots discussed earlier as the basis, a thermal

profile for the debinding could be built. An initial heating up to 300 °C at the rate of 2 °C/min and a hold of 2 hrs thus ensure the complete removal of the leftover filler phase from the solvent debinding step. The sample was further heated to 500 °C at the rate of 2 °C/min and kept at different hold times to remove the backbone polymers thus forming “brown” parts. Variations in the hold time are required to minimize the residual weight of the debound parts.

Carbon is believed to be an important impurity, which affects the thermal conductivity of polycrystalline AlN and SiC. It was shown by Tajika et al that a small amount of carbon, ≤ 0.3 wt.% reduces the oxygen impurity level, thus enhancing the thermal conductivity [26]. On the other hand, large amount of carbon ≥ 0.5 wt.%, is extremely detrimental to the thermal conductivity because density of sintered AlN is decreased significantly [27]. As shown in the **Table 6.4**, the residual weight of bimodal μ -n SiC debound sample was reduced to 0.16 wt.% when held at 500 °C for 5 hrs. Similarly, a 7 hr hold at 500 °C provided a residual weight of 0.28% for bimodal μ -n AlN debound samples. The requisite for higher hold time in bimodal samples can be seen as the possible result of nanoparticle addition leading to more tortuous path for the degraded products to follow. Further studies is required in understanding the effect of pore size, % porosity, part geometry, heating rate and hold time on the thermal debinding kinetics.

6.4. Conclusions

The bimodal SiC and AlN samples exhibited slower polymer removal behavior compared to that of the monomodal samples irrespective of the debinding conditions. The combined effect of increased powder content and reduced average particle size via nanoparticle addition is inferred as the reason for such behavior. Theoretical models indicated that the effect of particle size on solvent debinding was minimized at higher powder content, for the samples under consideration. The diffusion coefficients (D_e) values were calculated and discussed as an outcome of varying debinding parameters. The nanoparticle addition in the bimodal samples also exhibited delay in the completion of the thermal debinding cycles.

6.5. References

1. H.I. Bakan, *Materials Science and Technology*, 2007, vol. 23(7), pp. 787-791
2. V.M. Kryachek, *Powder Metallurgy and Metal Ceramics*, 2004, vol.43(11-12), pp. 336-348
3. R.M. German, *Journal of American Ceramic Society*, 1994, vol.77, pp. 283-285
4. K.S. Hwang, G.J. Shu, H.J. Lee, *Metallurgical and Materials Transactions A*, 2005, vol.36 A, pp.161-167

5. L. Moballeggh, J. Morshedean, M. Esfandeh, *Materials Letters*, 2005, vol.59, pp. 2832 – 2837
6. T. Jardiel, M.E. Sotomayor, B. Levenfeld, A. Va´rez, *International Journal of Applied Ceramic Technology*, 2008, vol.5(6), pp. 574–581
7. M.A. Omar, R. Ibrahim, M.I. Sidik, M. Mustapha, M. Mohamad, *Journal of Materials Processing Technology*, 2003, vol.140, pp. 397–400
8. A. Bandyopadhyay, S.C. Danforth and A. Safari, *Journal of Materials Science*, 2000, vol.35, pp.3983-3988
9. S. Ying, Y. C. Lam, S. C. M. Yu, K. C. Tam, *Metallurgical and Materials Transactions B*, 2002, vol.33(3), pp.477-488
10. K. E. Hrdina, J. W. Halloran, *Journal of Materials Science*, 1998, vol.33(11), pp. 2805-2815
11. M. Trunec, J. Cihlar, *Journal of European Ceramic Society*, 2002, vol.22(13), pp. 2231-2241
12. R.M. German, A. Bose, *Injection Molding of Metals and Ceramics*, MPIF, Princeton, New Jersey, 1997, pp. 23
13. S.T. Lin, R.M.German, *Powder Metallurgy International*, 1989, vol.21, pp. 19-24
14. H.K. Lin, K.S.Hwang, *Acta Materialia*, 1998, vol.46(12), pp. 4303-09
15. D.S. Tsai, W.W. Chen, *Ceramics International*, 1995, vol. 21, pp. 257–264
16. H.E. Amaya, Solvent dewaxing. Principles and Application, *Advances in Powder Metallurgy*, edited by E. R. Andreotti and P. J. McGeehan. MPIF, Princeton, NJ, 1990, vol. 1, pp.233-246
17. R.V.B. Oliveira, V. Soldi, M.C. Fredel, A.T.N. Pires, *Journal of Materials Processing Technology*, 2005, vol. 160, pp.213–220
18. V.A. Krauss, A.A.M. Oliveira, A.N. Klein, H.A. AlQureshi, M.C. Fredel, *Journal of Materials Processing Technology*, 2007, vol. 182, pp. 268–273
19. M.T. Zaky, *Journal of materials science*, 2004, vol. 39(10), pp. 3397-3402
20. B. Zhu, X. Qu and Y. Tao, *Journal of Materials Processing Technology*, 2003, vol. 142, pp. 487–492.
21. J.S. Wang, S.P. Lin, M.H. Won, M.C. Wang, *Japanese Journal of Applied Physics*, 2000, vol. 39, pp.616-621
22. T.S. Shivashanar, R.M. German, *Journal of American Ceramic Society*, 1999, vol. 82(5), pp. 1146-1152.
23. V.P. Onbattuvelli, G. Purdy, G. Kim, S. Laddha, S. Atre *Advances in Powder Metallurgy and Particulate Materials*, 2010, no.1, pg. 64-72.
24. V.P. Onbattuvelli, S. Vallury, T. McCabe, S-J. Park, S. Atre, *PIM International*, 2010, vol. 4(3), pp. 64-70
25. I. Nanjo, M. Achikit, S. Matsuda, in *Proceedings of Powder Metallurgy World Congress*, Japan, 1993, pp. 241.
26. M. Tajika, H. Matsubara, W. Rafaniello, *Nanostructured Materials*, 1999, vol.12(1-4), pp. 131-134
27. K.H. Lin, Y.C. Lin, S.T. Lin, *Journal of Materials Processing Technology*, 2008, vol. 201, pp. 701-705

List of Figures

Figure 6.1: The effect of immersion time on the solvent debinding of monomodal μ -SiC samples with different ψ ratios at (a) RT, (b) 40 °C and (c) 60 °C

Figure 6.2: The effect of immersion time on the solvent debinding of monomodal μ -AlN samples with different ψ ratios at (a) RT, (b) 40 °C and (c) 60 °C

Figure 6.3: The effect of immersion time on the solvent debinding of bimodal μ -n SiC samples with different ψ ratios at (a) RT, (b) 40 °C and (c) 60 °C

Figure 6.4: The effect of immersion time on the solvent debinding of bimodal μ -n AlN samples with different ψ ratios at (a) RT, (b) 40 °C and (c) 60 °C

Figure 6.5: TGA runs on solvent-debound monomodal μ - SiC (a) and μ -AlN (b) samples ($\psi = 1.22/\text{mm}$) indicating the increasing removal of soluble binder components with increased immersion time.

Figure 6.6: TGA runs on solvent-debound bimodal μ -n SiC(a) and AlN(b) samples ($\psi = 1.22/\text{mm}$) indicating the increasing removal of soluble binder components with increased immersion time.

Figure 6.7: SEM micrographs of monomodal μ -SiC samples ($\psi = 1.22/\text{mm}$) after debinding in heptane at 60 °C as function of immersion time

Figure 6.8: SEM micrographs of bimodal μ -n SiC samples ($\psi = 1.22/\text{mm}$) after debinding in heptane at 60 °C as function of immersion time

Figure 6. 9: SEM micrographs of μ -AlN samples ($\psi = 1.22/\text{mm}$) after debinding in heptane at 40 °C as function of immersion time.

Figure 6.10: SEM micrographs of μ -n AlN samples ($\psi = 1.22/\text{mm}$) after debinding in heptane at 60 °C as function of immersion time.

Figure 6.11: The effect of solids loading on the permeability of monomodal and bimodal SiC (a) and AlN (b) samples.

Figure 6.12: Diffusion coefficients as a function of solvent temperature for the SiC (a) and AlN (b) samples ($\psi = 1.22/\text{mm}$).

Figure 6.13: Diffusion coefficients as a function of solvent temperature for the SiC (a) and AlN (b) samples ($\psi = 1.22/\text{mm}$)

Figure 6.14: Diffusion coefficients as a function of solvent temperature for the SiC (a) and AlN (b) samples ($\psi = 0.52/\text{mm}$)

List of Tables

Table 6.1: Literature review on the binder formulations used in multi-step debinding process

Table 6.2: Composition of SiC and AlN samples tested in the current study

Table 6.3: Dissolution and diffusion coefficients of monomodal and bimodal SiC and AlN samples at room temperature with different aspect ratios.

Table 6.4: The effect of hold time on the % residual weight in the SiC and AlN samples during the thermal debinding

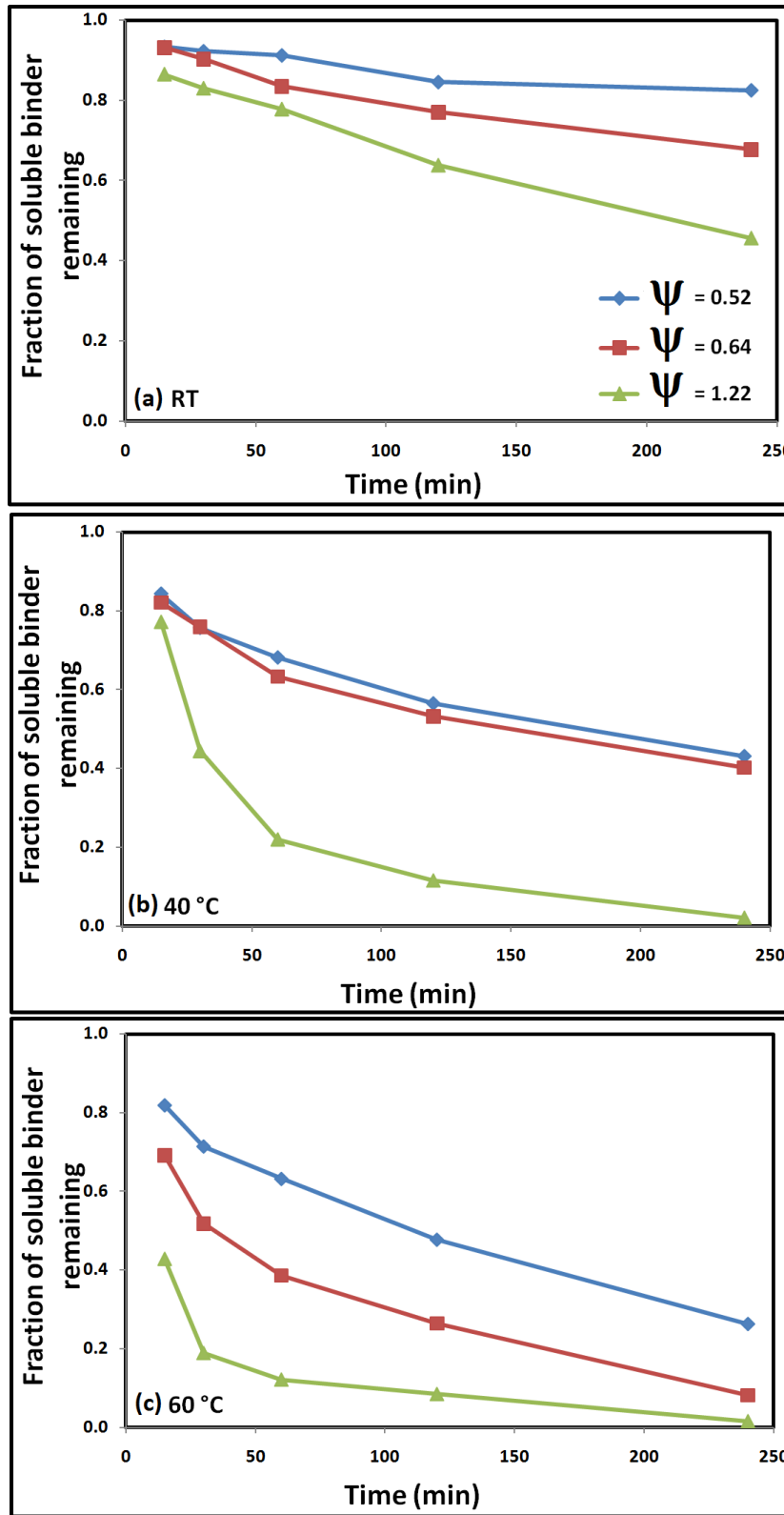


Figure 6.1: The effect of immersion time on the solvent debinding of monomodal μ -SiC samples with different ψ ratios at (a) RT, (b) 40 °C and (c) 60 °C.

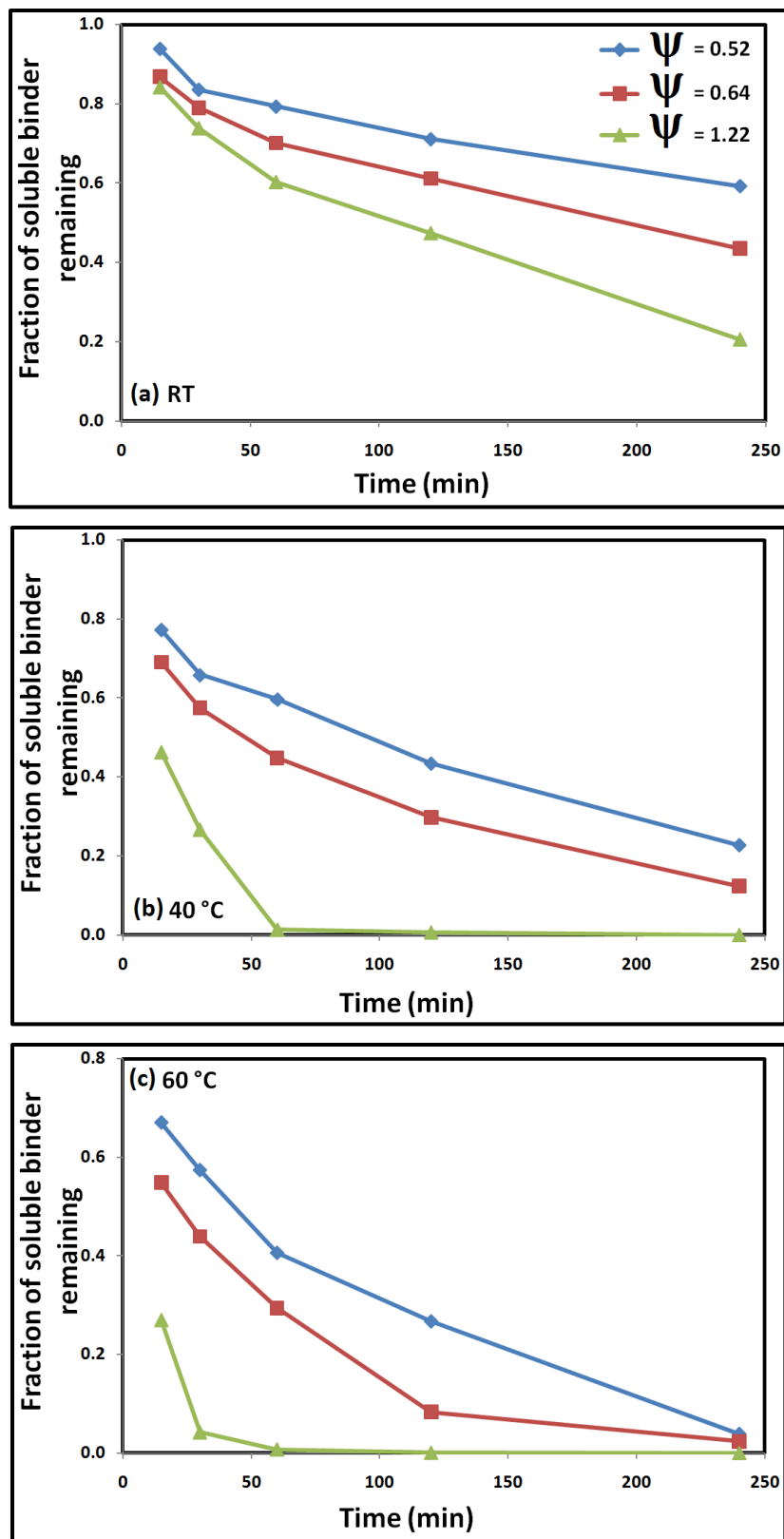


Figure 6.2: The effect of immersion time on the solvent debinding of monomodal μ - AlN samples with different ψ ratios at (a) RT, (b) 40 °C and (c) 60 °C.

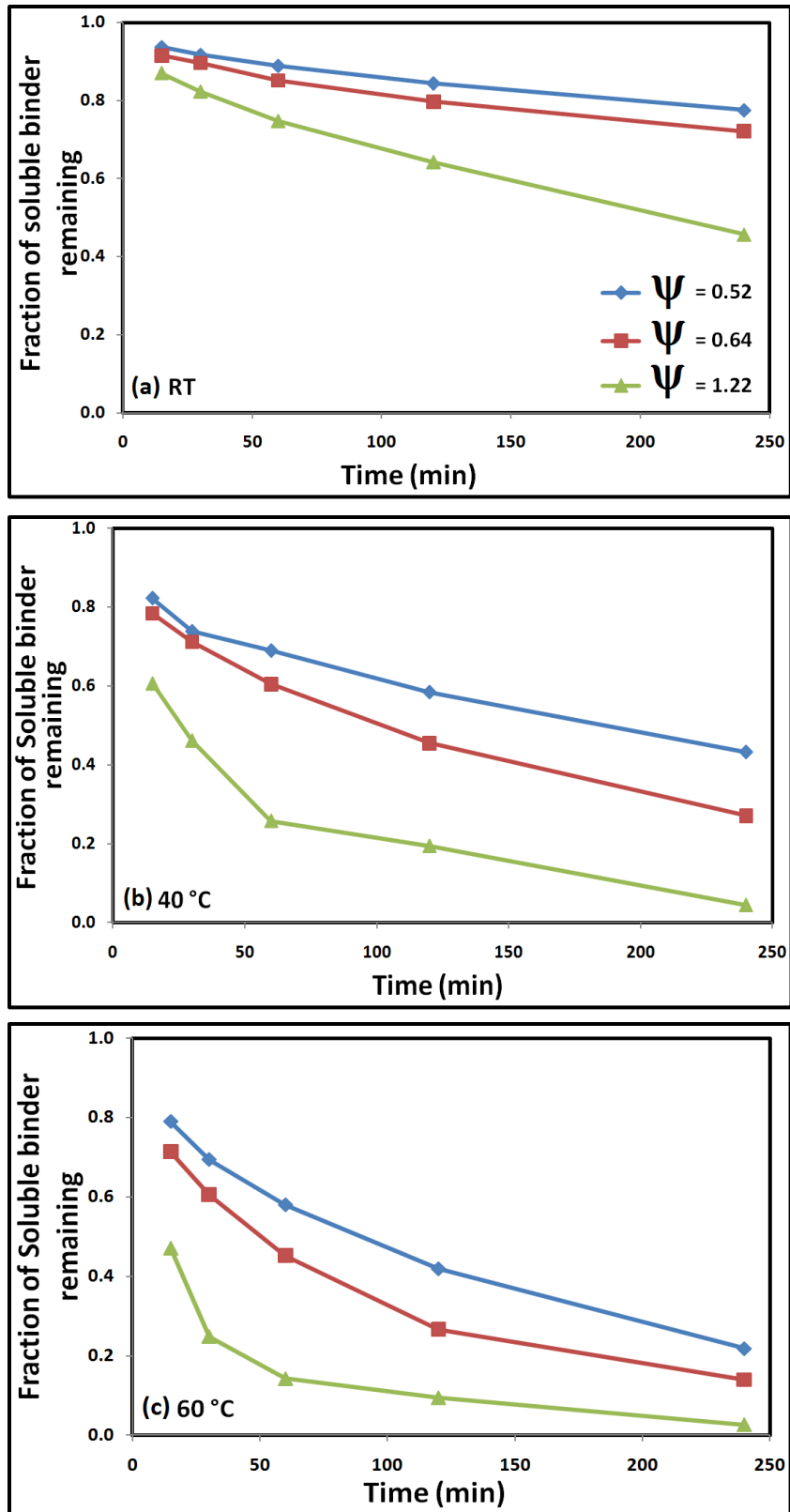


Figure 6.3: The effect of immersion time on the solvent debinding of bimodal μ -n SiC samples with different ψ ratios at (a) RT, (b) 40 °C and (c) 60 °C.

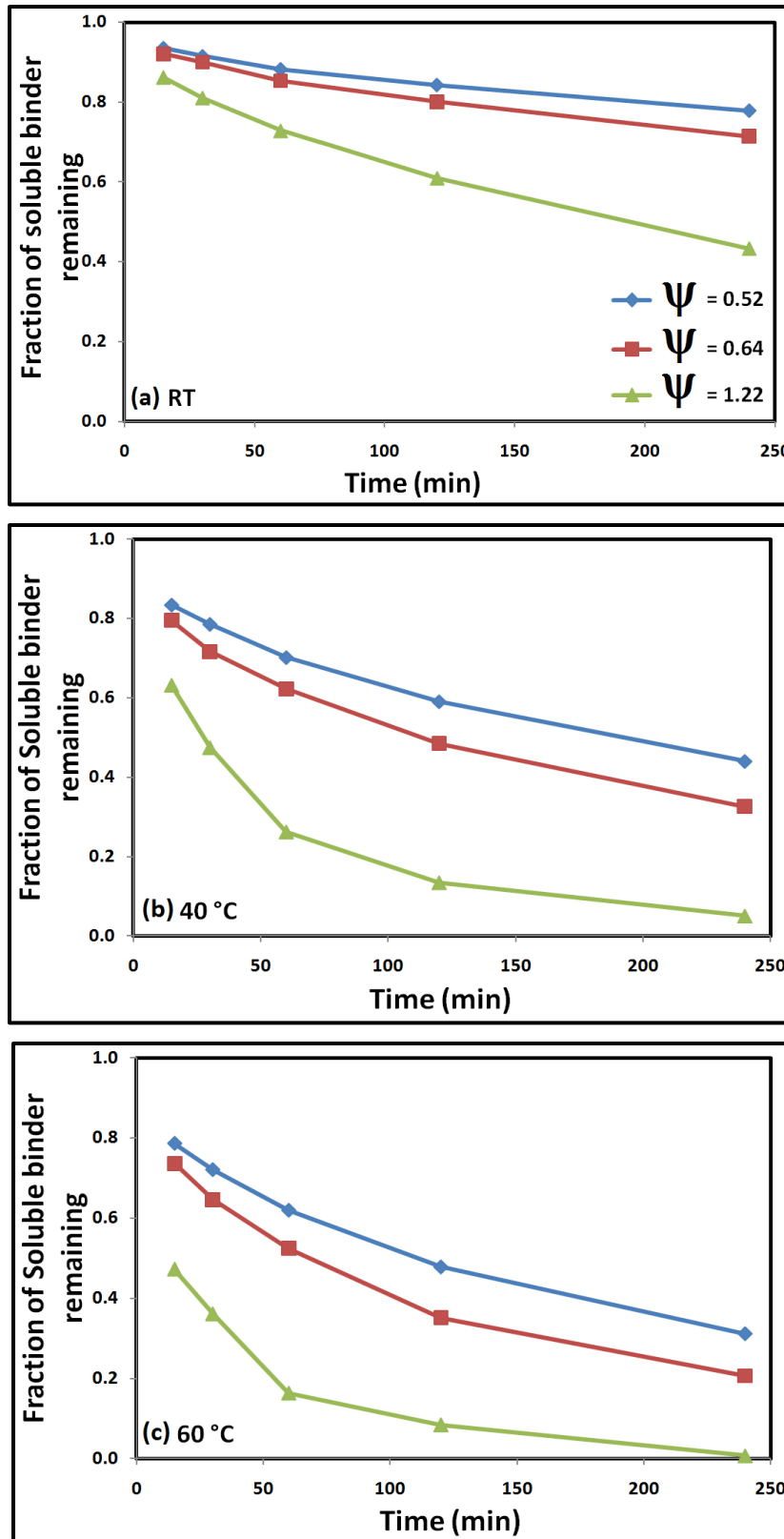


Figure 6.4: The effect of immersion time on the solvent debinding of bimodal μ -n AlN samples with different ψ ratios at (a) RT, (b) 40 °C and (c) 60 °C.

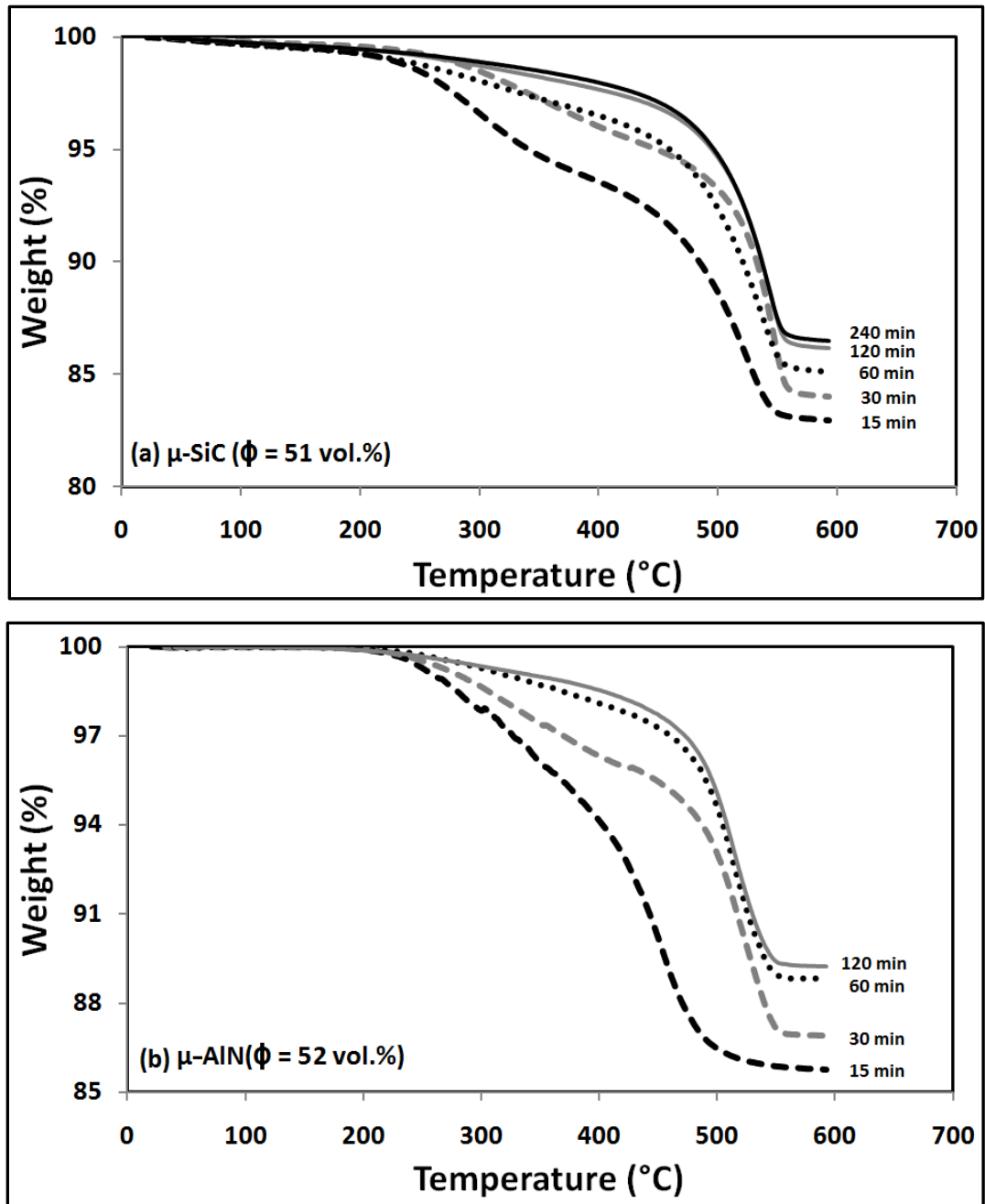


Figure 6.5: TGA runs on solvent-debound monomodal μ - SiC (a) and μ -AlN (b) samples ($\psi = 1.22/\text{mm}$) indicating the increasing removal of soluble binder components with increased immersion time.

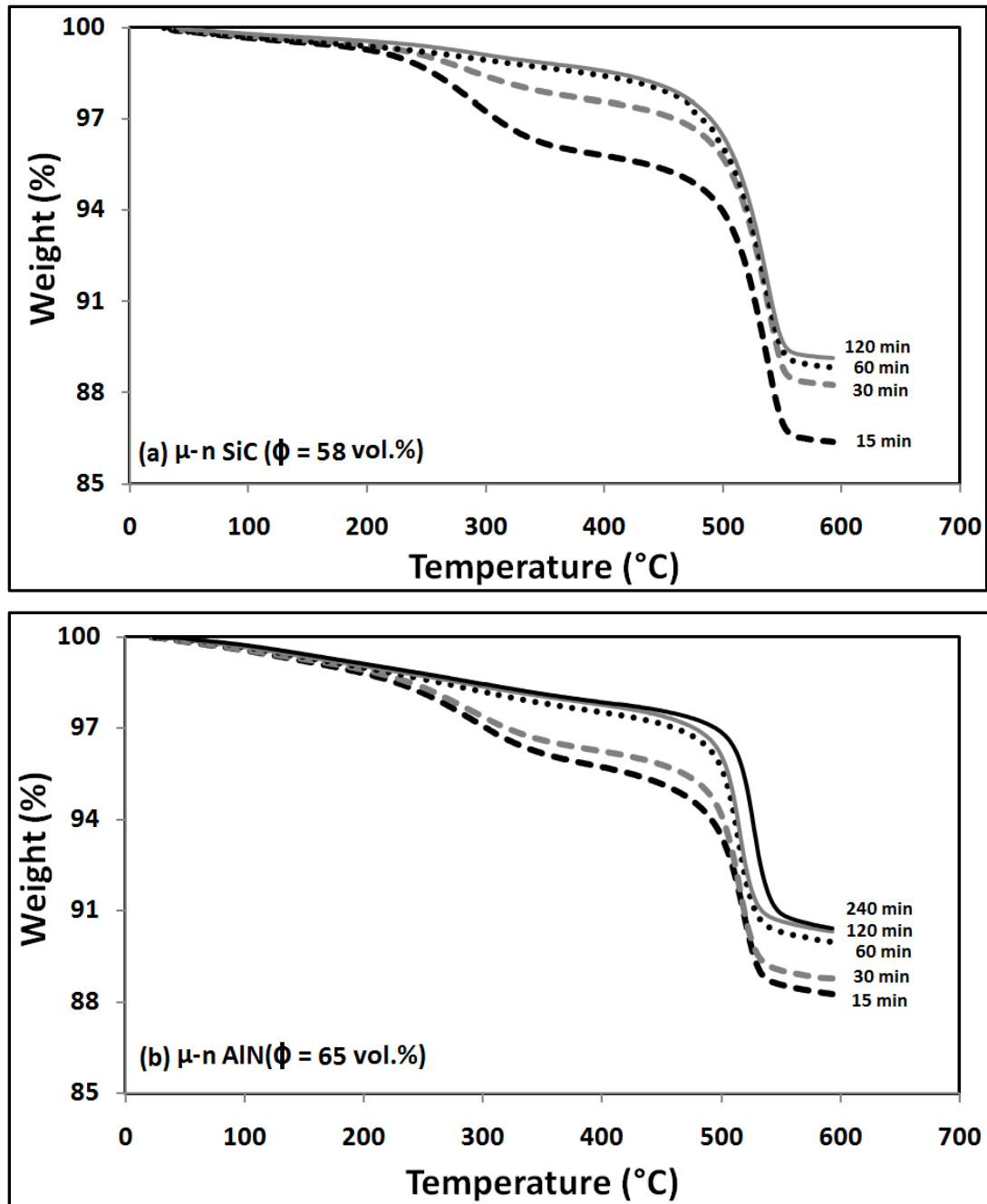


Figure 6.6: TGA runs on solvent debound bimodal μ - n SiC (a) and μ - n AlN (b) samples ($\psi = 1.22/\text{mm}$) indicating the increasing removal of soluble binder components with increased immersion time.

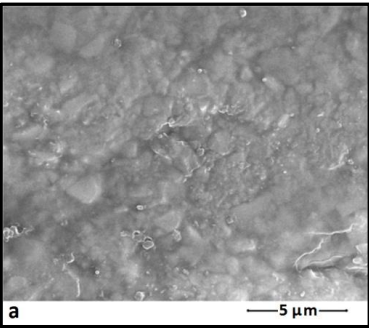
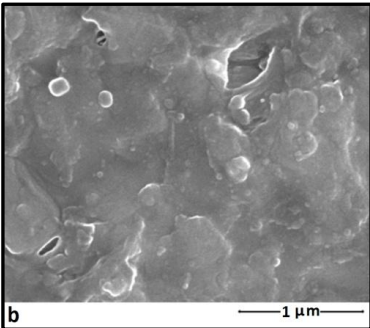
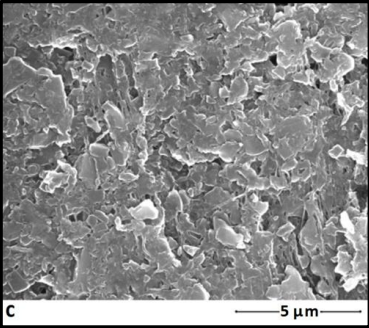
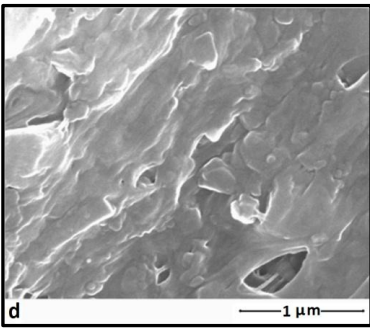
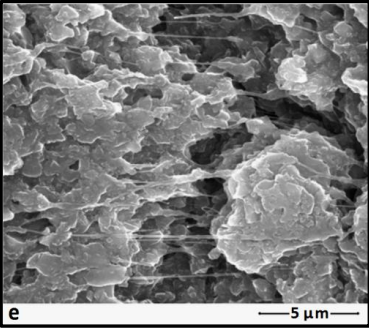
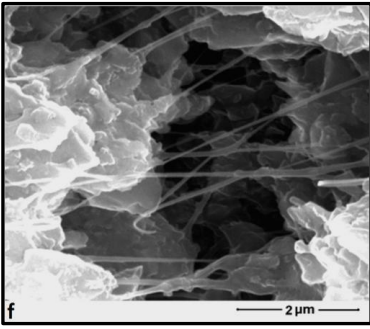
Time (min)	Surface	Core	Soluble binder extracted (%)
0			0
15			57
240			98

Figure 6.7: SEM micrographs of monomodal μ -SiC samples ($\psi = 1.22/\text{mm}$) after debinding in heptane at $60\text{ }^\circ\text{C}$ as function of immersion time.

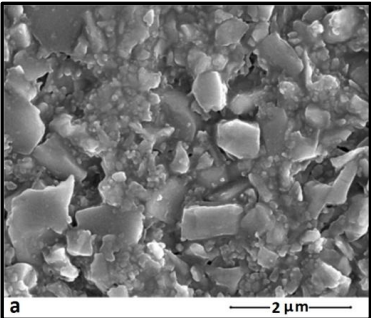
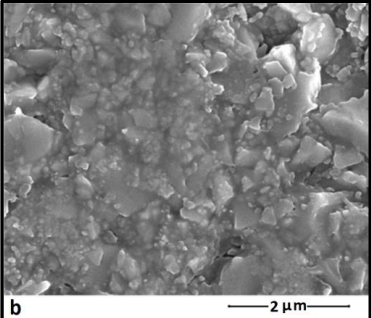
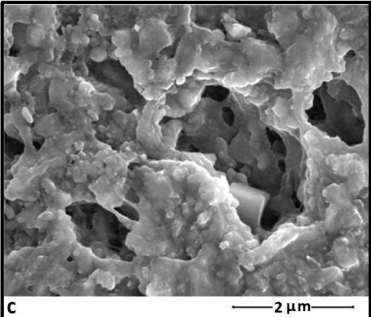
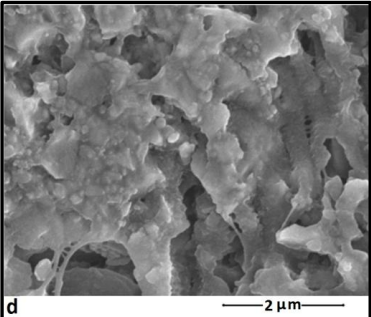
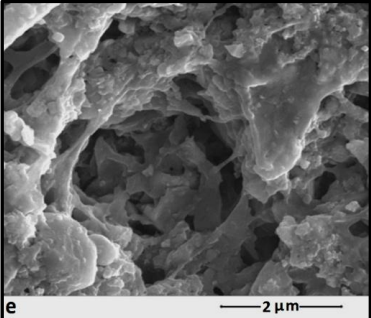
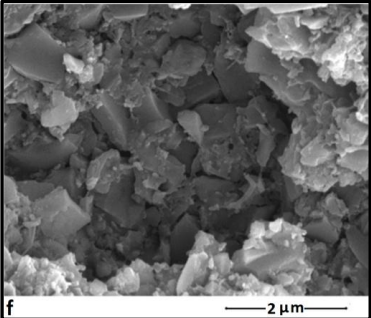
Time (min)	Surface	Core	Soluble binder extracted (%)
0			0
15			53
240			97

Figure 6.8: SEM micrographs of bimodal μ -n SiC samples ($\psi = 1.22/\text{mm}$) after debinding in heptane at 60 °C as function of immersion time.

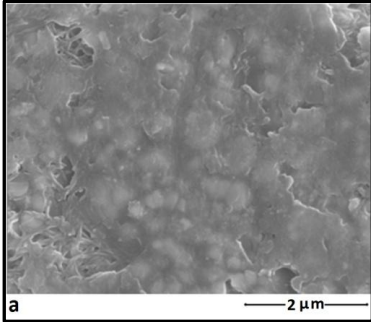
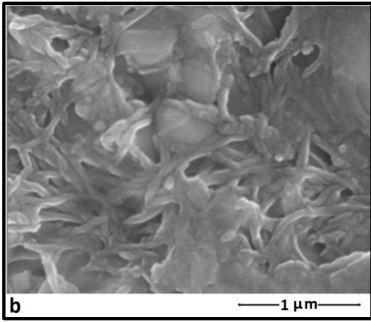
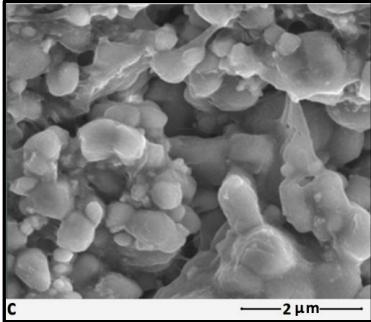
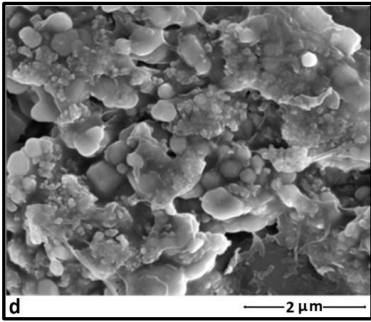
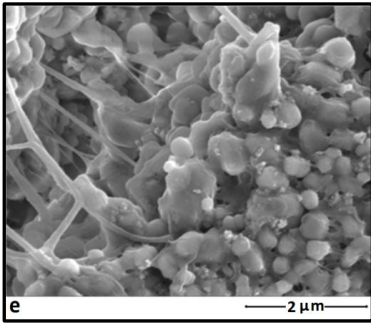
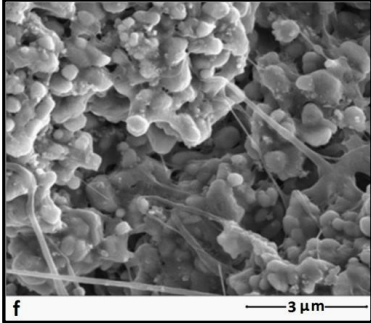
Time (min)	Surface	Core	Soluble binder extracted (%)
0			0
15			50
120			100

Figure 6.9: SEM micrographs of μ -AlN samples ($\psi = 1.22/\text{mm}$) after debinding in heptane at 40°C as function of immersion time.

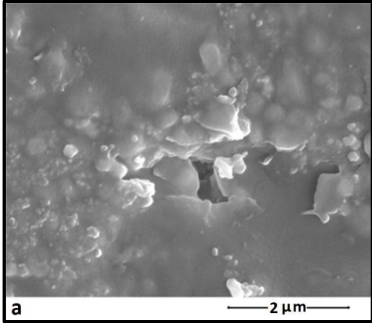
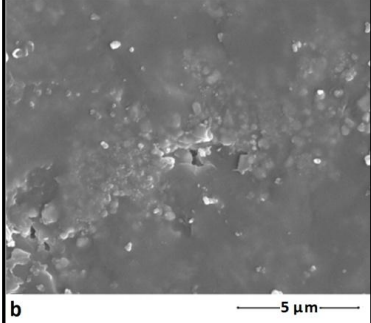
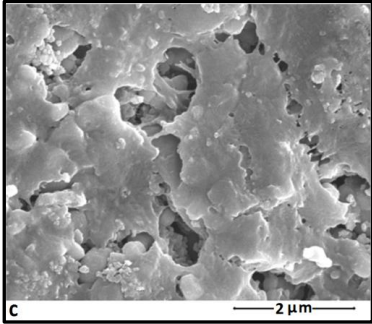
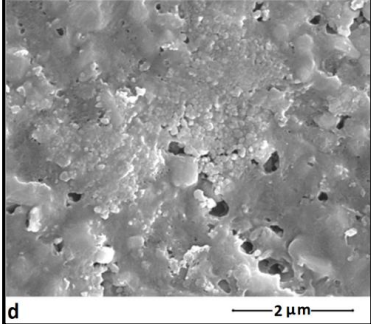
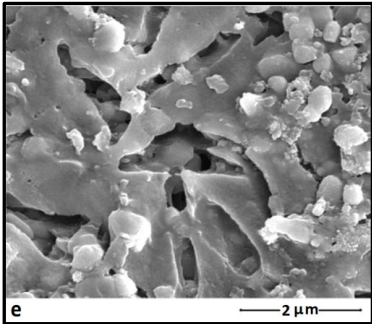
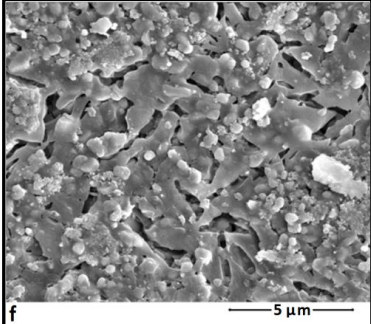
Time (min)	Surface	Core	Soluble binder extracted (%)
0			0
30			64
240			99

Figure 6.10: SEM micrographs of μ -n AlN samples ($\psi = 1.22/\text{mm}$) after debinding in heptane at 60°C as function of immersion time.

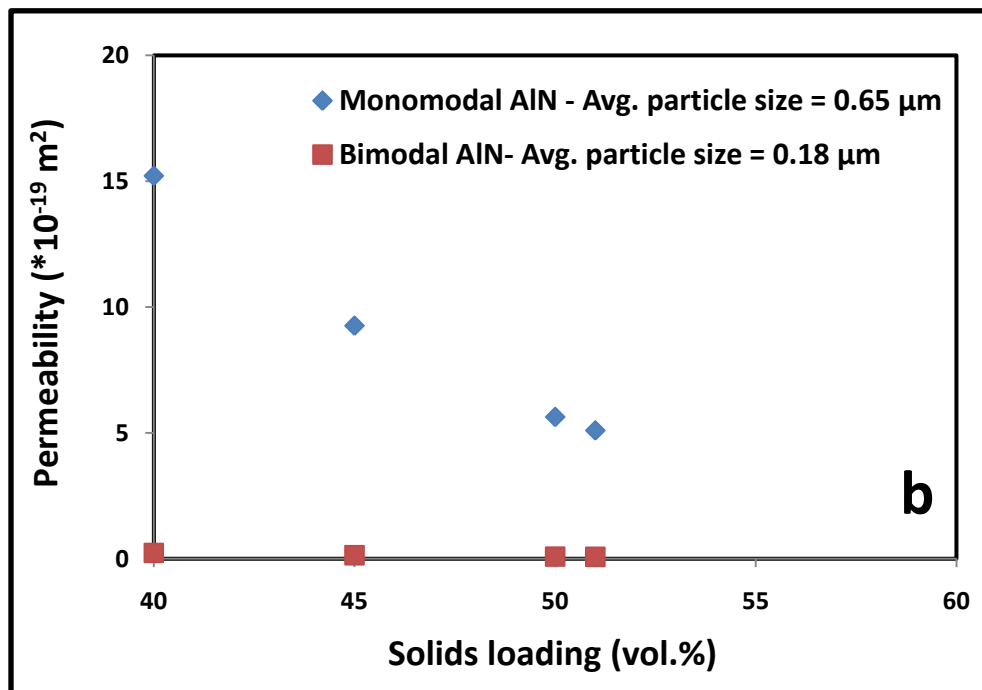
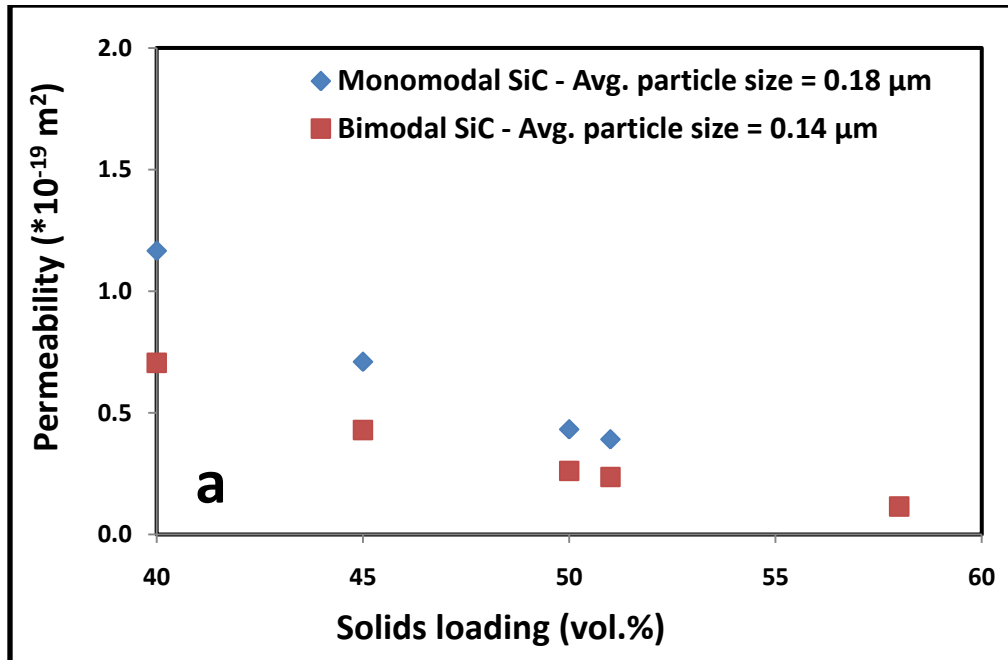


Figure 6.11: The effect of solids loading on the permeability in monomodal and bimodal SiC (a) and AlN (b) samples

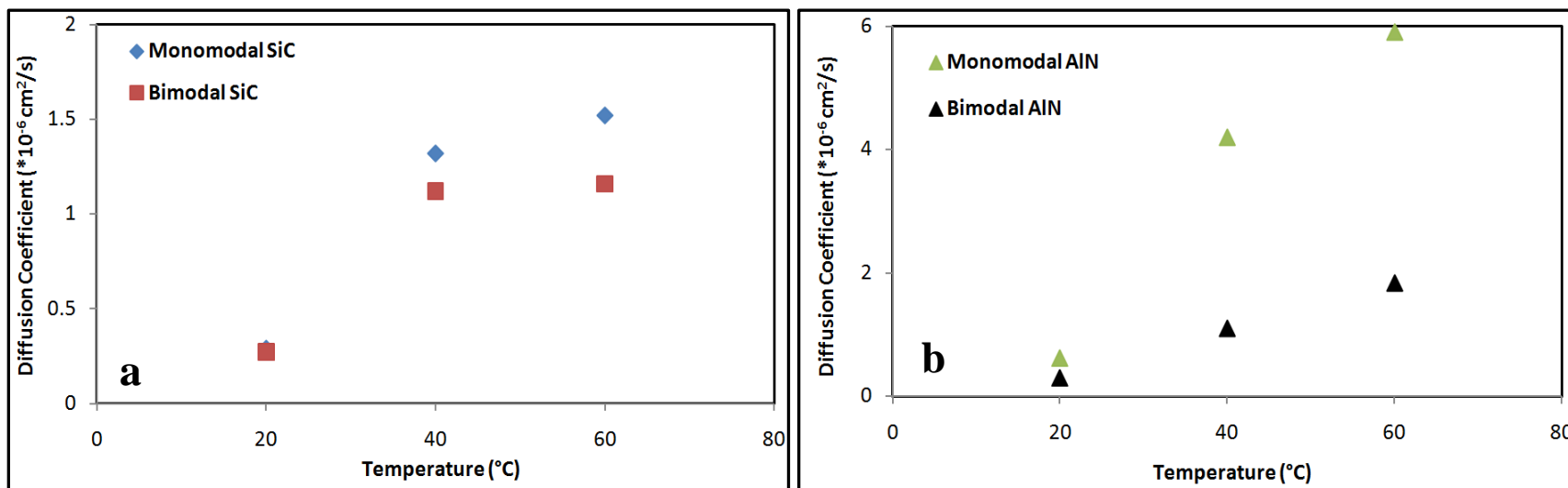


Figure 6.12: Diffusion coefficients as a function of solvent temperature for SiC (a) and AlN (b) samples (with $\psi = 1.22/\text{mm}$)

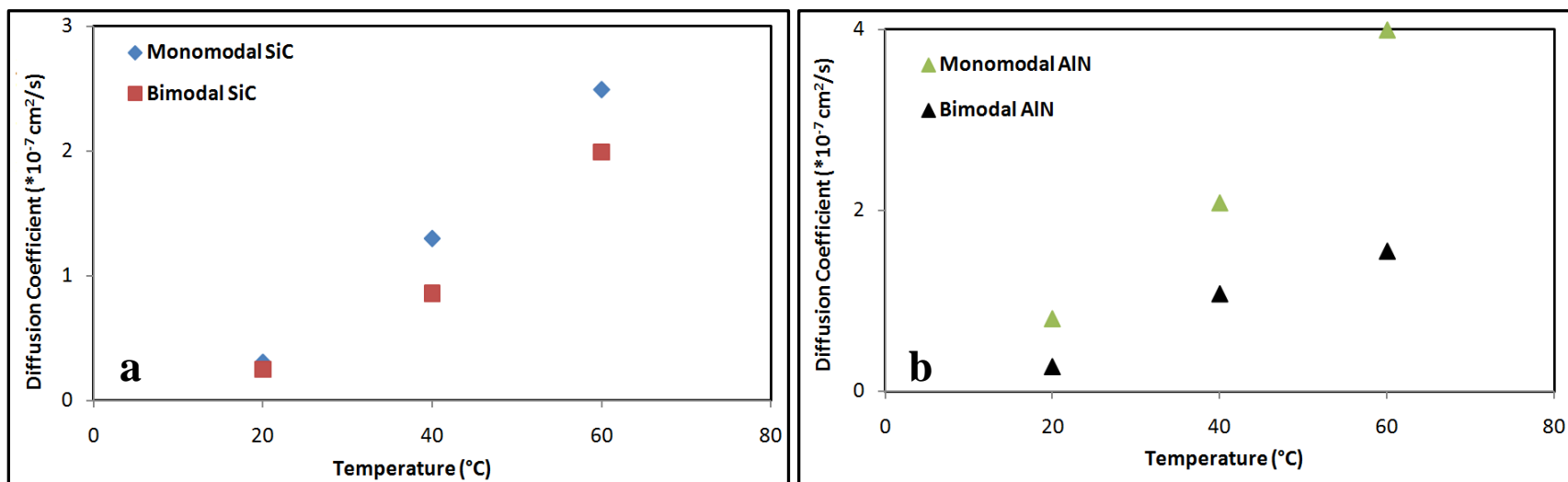


Figure 6.13: Diffusion coefficients as a function of solvent temperature for SiC (a) and AlN (b) samples (with $\psi = 0.64/\text{mm}$)

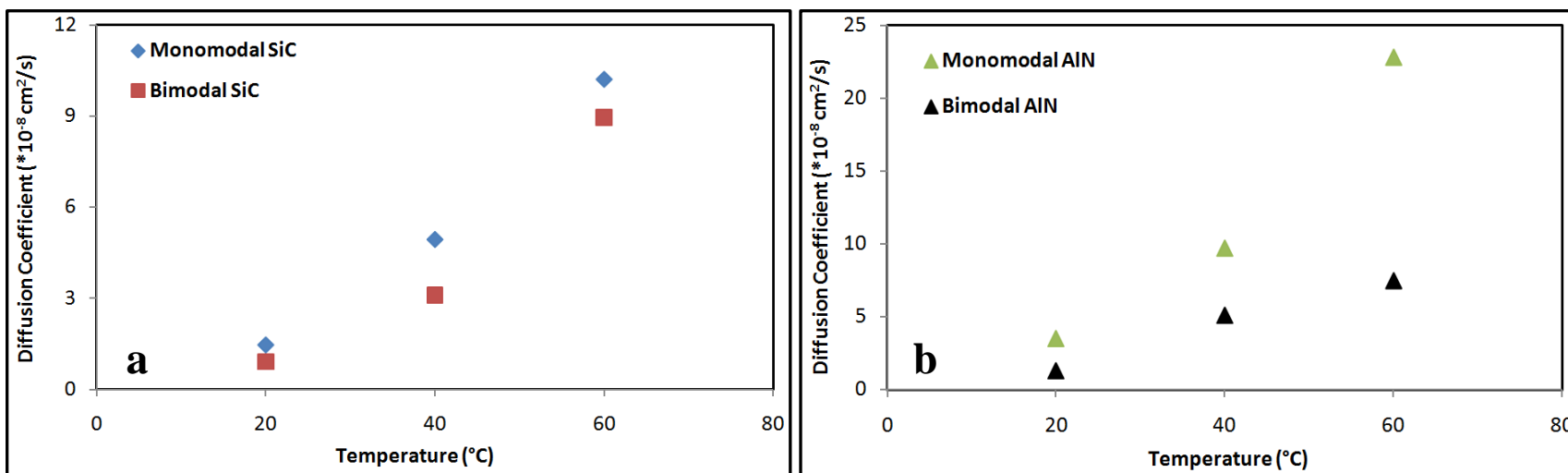


Figure 6.14: Diffusion coefficients as a function of solvent temperature for SiC (a) and AlN (b) samples ($\psi = 0.52/\text{mm}$)

Table 6.1: Literature review on binder formulations used in the multi-step debinding process

#	Author	System	Binder composition	Soluble binder content	Solvent used	Conditions mentioned	Powder particle size
1	Aggarwal et al	Niobium	-	-	Heptane	2 h @ 60 °C	-
4	Hwang et al	Alumina	30 wt.% PP, 65wt% -PW, 5wt% SA	70 wt.%		3 h @ 60 °C	1.8 μm
6	Jardiel et al	Zirconia	50 wt.% PP, 46wt% -PW, 4wt% SA	50 wt.%		3 h @ 60 °C	0.6 μm
13	Lin et al	Carbonyl Iron	40 wt.% PP, 55wt% -PW, 5wt% SA	60 wt.%		1 h @ 60 °C	4.6 μm
5	Mobellageh et al	Copper	30 wt.% PP, 65wt% -PW, 5wt% SA	70 wt.%	Hexane	3.5 h@ 60 °C	<10 μm
7	Omar et al	316L stainless steel	60 wt.% PE, 35wt% -PW, 5wt% SA	40 wt.%	Heptane	4 h @ 60 °C	12 μm
			80 wt% PEG, 20 wt.% PMMA	80 wt.%	Water	4 h @ 80 °C	
			(90, 80) wt% PEG, (10, 20) wt.% PMMA	80 to 90 wt.%		5 h @ 60 °C	24 μm
21	Wang et al	Fe-Ni-Cu	61 wt.% PW, 15 wt% SA, 12 wt.% EVA, 12 wt.% LDPE	76 wt.%	Hexane	6 h @ 40 °C	84, 25, 6μm
19	Zaky	17-4PH Stainless Steel	62 wt.% PW, 35%EVA, 3 wt.% SA	65 wt.%		2.25 h@ 50 °C	8 μm
17	Oliviera et al	Alumina	PP, PW, SA	-		4-8 h@ 60 °C	0.8 μm
18	Krauss et al		65 wt.% PEG, 30 wt.% PVB, 5 wt.% SA	70 wt.%	Water	10 h@ -	1 μm
20	Zhu et al	Tungsten Carbide	60 wt.% PW, 5 wt.% Liquid PW, 10 wt.% HDPE, 10 wt.% PP, 5 wt.% EPDM, 5 wt.% SA, 5 wt.% Dioctyl Phthalate	70 wt.%	Isooctane	5h @ 80 °C	3.2μm
13	Setasuwon et al	316L stainless steel	45 wt.% LDPE, 50 wt.% PW, 5 wt.% SA	60 wt.%	Petroleum Ether	0.75h @ 50 °C	9.58μm

Table 6.2: Composition of SiC and AlN samples tested in the current study

Sample	Avg. particle size (μm)	Solids loading (vol.%)	Soluble binder content (vol.%)	Soluble binder content (wt.%)
Monomodal SiC	0.7	51	27	11
Bimodal SiC	0.63	58	23	9
Monomodal AlN	1.1	52	26	10
Bimodal AlN	0.91	65	19	8

Table 6.3: Dissolution and diffusion coefficients of monomodal and bimodal SiC and AlN samples at room temperature with different aspect ratios.

ψ (mm ⁻¹)	Dissolution coefficient at room temperature (*10 ⁻⁸ cm ² /s)				Diffusion coefficient at room temperature (*10 ⁻⁸ cm ² /s)			
	SiC		AlN		SiC		AlN	
	μ -n	μ	μ -n	μ	μ -n	μ	μ -n	μ
0.52	0.91	2.01	2.38	4.39	1.46	0.91	1.28	3.47
0.64	4.43	6.37	4.71	8.86	2.72	3.05	2.27	6.14
1.22	6.92	9.14	10.2	14.7	2.9	2.92	2.92	8.03

Table 6.4: The effect of hold time on the % residual weight of the SiC and AlN samples during the thermal debinding

Hrs of hold at 500 °C	% residual weight in SiC		% residual weight in AlN	
	Bimodal μ -n	Monomodal μ	Bimodal μ -n	Monomodal μ
1	1.01	1.19	1	0.64
2	0.64	0.88	0.89	0.55
3	0.49	0.64	0.81	0.53
4	0.35	0.27	0.7	0.46
5	0.16	-	0.57	0.28
6	-	-	0.42	-
7	-	-	0.28	-

CHAPTER 7

The Effects of Nanoparticle Addition on the Densification and Properties of SiC

Abstract

The effects of nanoparticle addition on the pressureless sintering of injection molded and thermally debound silicon carbide (SiC) samples were studied. The influence of increased powder content and reduced particle size on the densification, microstructure and properties are discussed. The sintered parts of bimodal μ -n SiC mixtures exhibited comparable sintered density but lower shrinkage than the corresponding monomodal μ - SiC powder mixtures. Additionally, the mechanical and thermal properties sintered monomodal and bimodal SiC samples were measured and compared study with literature data on conventional monomodal μ -SiC systems.

7.1. Introduction

The development of methods to improve the densification and the ensuing thermal and mechanical properties has been a crucial issue in the processing of silicon carbide (SiC) [1-5]. Mass transport during sintering depends upon surface (ϵ_s) and grain boundary energies (ϵ_b) [6,7]. For example, the ratio ϵ_b/ϵ_s for SiC is ~ 0.97 due to the presence of covalent bonds [8]. As ϵ_b/ϵ_s approaches unity, achieving full densification becomes difficult. Consequently, several alternative techniques have been developed to improve the SiC densification. A well-explored is the inclusion of densification additives (aids) that allow liquid phase sintering [1-5, 9-12]. Solid solubility in the eutectic liquid improves transport rates responsible for grain coarsening and densification [13-14].

Prior reports investigated SiC densification by exploring material and process parameters. As mentioned earlier, the self-diffusion of SiC is extremely slow and requires various additives to assist sintering [15]. For example, Prochazka demonstrated that B and C could be used as solid-state sintering aids for SiC [16]. She and Ueno studied the effect of varying the amount of Al_2O_3 - Y_2O_3 on the porosity [9]. Similarly, Sciti and Bellosi compared the combinations of Al_2O_3 - Y_2O_3 and La_2O_3 - Y_2O_3 , as sintering aids for SiC densification [3]. Conventionally, SiC is densified by pressure-assisted sintering including hot pressing [17] and more recently plasma pressure compaction [18]. In contrast, pressureless sintering is important in the context of powder injection molding (PIM) of complex shapes. The effects of sintering temperature and hold time on the pressureless sintering have been extensively studied in the past. For example, She and Ueno [9] and Jin et al [19] reported the increase in the sintered density of SiC with the increase in the sintering temperature. On the other hand, Izhevskiy et al [11] and Rodriguez et al [20] noticed an increase in the sintered density with higher hold time at the sintering temperature. A detailed literature review on such prior work on SiC densification is reported elsewhere [21].

Our recent research work successfully demonstrated an increase in powder packing density with the addition of nanoparticles (n) to submicron (μ) particles, forming bimodal μ -n powder mixtures [22, 23]. For example, the powder content is found to increase from 53 to 65 vol.% when SiC nanoparticles are added to the monomodal submicron (μ) sized SiC powders. The implication of such nanoparticle addition is discussed in the past in the context of thermal and rheological properties of the powder-polymer mixtures, mold filling behavior and polymer removal kinetics of the injection molded bimodal μ -n SiC samples [22, 24]. In a similar manner, the effect of nanoparticle addition on the sintering of SiC at different time-temperature combinations is the focus of the current work. Further, the sintered density, shrinkage,

mechanical and thermal properties of the sintered bimodal μ -n samples are compared with that of monomodal μ - SiC samples processed under identical conditions.

7.2. Experimental Section

7.2.1 Materials

The starting powder materials contain as-received., commercially available SiC (0.7 μ m and 50 nm) with 5 wt.% AlN (20 nm) and 5 wt.% Y₂O₃ (50 nm) as the sintering additives.

7.2.2. Sample preparation

Powder injection molded bimodal μ -n SiC and monomodal μ - SiC samples were solvent and thermally debound prior to sintering. The molding and debinding conditions used are detailed elsewhere [20, 24]. Thermally debound bimodal (initial density of 1.9 g/cc (65% relative density)) and monomodal (initial density of 1.67 g/cc (51% relative density)) SiC samples with were pressureless sintered at temperatures between 1800 to 2000 °C for two different hold times of 2 and 4 hrs under argon atmosphere. The sintering conditions were selected based on the literature review on SiC densification as presented in the **Figure 7.1** [1-3, 9-11, 25-29].

7.2.3. Instrumentation

All sintered samples were diamond polished to 1 μ m surface finish prior to any characterization. The density for all the sintered samples was measured with a lab-built Archimedes density apparatus. Microstructural analysis was conducted on the surfaces of thermally debound SiC samples using a QuantaTM –FEG (FEI) dual beam scanning electron microscope (SEM) coupled with an energy dispersive X-ray spectrometer (EDS). SEM images of each sample were collected in two different magnifications for better comparison. The thermal diffusivity of the samples was measured with a LFA-457 (Netzsch) laser flash apparatus. TA Instruments- 2920 unit was used to measure the specific heat (Cp) of the sintered samples. Vickers hardness and indentation toughness of the sintered AlN samples were measured using a Leco microhardness tester.

7.3. Results and Discussion

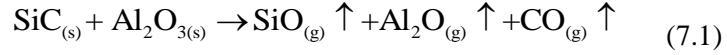
Being classified as difficult to sinter ceramic, the densification of SiC was promoted by liquid phase sintering, accompanying solution- reprecipitated SiC grains and an intergranular glassy phase [4]. Combination of AlN and Y₂O₃ is one of the most commonly reported sintering

additives for SiC and is thus used in the current study [1, 29-32]. During heating, the mixture of Y_2O_3 with the surface oxides from AlN and SiC reacts and form a rare earth alumino-silicate glass melt. With the dissolution of the small SiC particles, the resulting liquid could be regarded as Y-Si-Al-O-C glass melt. On cooling, the Y-Si-Al-O-C constitute the intergranular phases in the SiC ceramics. The liquid phase formation is accompanied by the elimination of pores which is followed by shrinkage/densification.

From the densification plots presented in the **Figure 7.2**, it can be seen that the densification of both monomodal and bimodal SiC is initiated at ~ 1550 °C. SEM studies (**Figures 7.3 and 7.4**) on these samples confirmed a liquid phase formation at ~ 1500 °C, which is ≥ 100 °C lesser than the previously reported values for monomodal μ -SiC samples as listed in the **Table 7.1** [2, 3, 9, 33-35]. The reduction in the liquid phase formation temperature for both monomodal and bimodal SiC in the current study can be attributed to the inclusion of n- Y_2O_3 and AlN as sintering additive. The increased surface area of the nanosized additive in turn may have increased the reaction rate between Al_2O_3 , Y_2O_3 and surface SiO_2 shifting the eutectic formation to relatively lower temperatures. Further sintering studies comparing bimodal SiC mixtures to those containing μ -sized additives are required to understand the effect of SiC and Y_2O_3 nanoparticles and addition on the liquid phase formation. Additionally, a novel nanorod formation is noticed with the monomodal SiC at 1550 °C (**Figure 7.4d**). This has not been previously reported in the literature. The reason for the presence of nanorods and their absence in bimodal SiC is not clear at this stage of research. Future experiments including as series of XRD analysis on the thermally debound SiC samples may explain the above mentioned behavior.

Even though the liquid phase is formed at relatively lower temperatures, densification $> 90\%$ is exhibited by both monomodal and bimodal SiC only at temperatures > 1900 °C. This may be attributed to the slower solution-precipitation of SiC from the Y-Si-Al-O-C glass melt. Additionally, varying the hold time is found to have little effect on the SiC densification for the range of times (2-4 hours) that was investigated. Bimodal SiC sintered at 1950°C showed a 97% densification which is comparable to that of monomodal SiC (96%). A comparative list of presented in the **Table 7.2** confirms the proximity of our findings on density to previously reported values [5, 9, 20, 26, 35, 37-40].

In addition to above densification trends, a decrease in density is noticed after ~ 1950 °C. This in turn can be correlated with the weight loss of upto 11% and 13% experienced by monomodal and bimodal SiC samples during sintering as shown in the **Figure 7.5**. Previous reports explained this behavior as the outcomes of the following reactions that occur at temperatures ≥ 1800 °C [35, 39].



As shown in the **Equations 7.1-7.2**, excess sintering additives present in the powder mixture reacts with SiC to form volatile monoxides of Al and Y along with CO. This material loss opens up new pores at sintering temperatures leading to reduction in the % density. **Figures 7.5a** and **7.5b**, it can be seen that the bimodal SiC samples experience more weight loss than the monomodal samples at any given sintering temperature-time conditions. This could be due to the increased reactivity brought in by the high surface area n-SiC present in the bimodal mixtures. Similar results on weight loss has been reported qualitatively in the past by She and Ueno [9], Grande et al [2], Guo et al [35], Suzuki and Sasaki [39] arguing the necessity to optimize the sintering additive content prior to SiC sintering. Sintering techniques including plasma pressure compaction and microwave sintering have been suggested in the past to combat the above issues [29]. Additionally, the reason for weight loss at temperatures between 1000 - 1800 °C is not clear at this stage of research. Future experiments including TGA-assisted-mass spectroscopy and XRD analysis are required to comparatively analyze the effect of n-SiC inclusion on the weight loss in the bimodal SiC samples.

As mentioned earlier, higher initial powder packing density (solids loading - Φ) is important for improving the sintered density and ensuing properties. Such higher green density in turn corresponds to lesser % shrinkage and thus more dimensional control. As shown in the **Figure 7.6a**, an isometric shrinkage of up to 15% is noticed in bimodal μ -n SiC samples confirming the dimensional precision. The plot is also extended to compare ~20% shrinkage noticed in the monomodal μ -SiC samples under similar sintering conditions (**Figure 7.6b**). Similar shrinkage value of 19% is reported in the past by Klemens et al for the extruded monomodal μ -SiC powder mixtures [41]. This comparison confirms the novelty of bimodal μ -n powder mixtures where higher densification is achieved yet with relatively lower shrinkage. Thus, in addition to the increased sintered densities, using bimodal μ -n SiC powder mixtures exhibited a significant lowering in the shrinkage as shown in the **Figure 7.6**. The lower shrinkage observed for bimodal samples can be directly attributed to a higher solids loading relative to the monomodal samples.

Figure 7.7 plots the Vickers hardness values obtained for bimodal (a) and monomodal (b) SiC samples sintered at different temperatures- time combinations. The hardness of SiC depends on factors such as sintered density, grain size and amount of secondary glassy phase. The Vickers hardness of both monomodal and bimodal SiC increased with increase in sintering temperature due to the corresponding densification process. A maximum hardness of 14.7 GPa and 15.1 GPa

was exhibited by monomodal and bimodal SiC samples sintered at 1950 °C for 4 hr, respectively. These values are comparatively lesser than the earlier reported measurements for monomodal SiC samples as listed in the **Table 7.3** [3, 5, 9, 29-30, 35, 38-40]. This could be due to incomplete densification as well as the increase in the weight loss of the SiC samples with the sintering temperatures as discussed earlier. Further, grain growth due to expedited liquid phase formation could also be proposed as a reason for such reduced hardness values. For example, prior reports by Sciti and Bellosi (hot pressing of monomodal μ -SiC) [3] and Bothara et al (plasma pressure compaction of monomodal n-SiC) [29] reported hardness values ≥ 20 GPa, with greater densification achieved at lower temperatures. Their work suggests the necessity for an external source (pressure, electric field) to achieve densification yet with suppressed grain growth. She and Ueno, on the other hand discussed the detrimental effect of excessive sintering additives on the properties, arguing the necessity to optimize the additives content prior to SiC sintering [9]. The measured indentation toughness of the bimodal (**Figure 7.8a**) and monomodal (**Figure 7.8 b**) SiC showed a similar trend to that of the hardness values. This is due its exhibition of a density-microstructure-property relationship similar to that of hardness values. A maximum indentation toughness of 3.4 MPa.m^{1/2} and 3.2 MPa.m^{1/2} is noticed for monomodal and bimodal SiC samples sintered at 1950 °C for 4 hr, respectively. Such lower toughness values compared to previous reports (**Table 7.3**) could be due to the combined effect of weight loss and grain growth. Future work on microstructural evolution during sintering is required to further understand the reasons for the lower properties and to find solutions to the problem.

Figure 7.9 plots the thermal diffusivity values obtained for bimodal (a) and monomodal (b) samples sintered at different temperatures. The diffusivity values were expected to be equal for monomodal and bimodal SiC samples as they show similar densification trends. However, the thermal diffusivity of bimodal samples (~ 35 mm²/s) sintered at 1950 °C were found to be higher than that of monomodal samples (~ 30 mm²/s) by 5 mm²/s. Despite the higher weight loss experienced by bimodal samples, such a rise in the thermal diffusivity values strengthens our earlier proposal of grain growth due to expedited liquid phase formation in the bimodal samples.

Figure 7.10 represents a nearly constant C_p value of 600 J/Kg.K for monomodal and bimodal SiC samples regardless of the sintering conditions. A similar C_p value of 650 J/Kg.K is reported in the past by Zhou et al for monomodal SiC system [12]. The thermal conductivity (K) is a product of thermal diffusivity, sintered density and C_p . Thus, factors such as sintered density, weight loss, grain growth and amount of intergranular glassy phase were found to affect the thermal conductivity of the given samples. These factors can explain the trends noticed in that thermal

conductivity plots (**Figure 7.11**) similar to that of the earlier discussed thermal diffusivity values. Thus, a maximum thermal conductivity of 73 W/m.K was exhibited by bimodal SiC samples sintered at 1950°C compared to that of 68 W/m.K by the monomodal samples. A detailed analysis with variations in the fabrication methods and amount and composition of sintering aids is required to further increase the thermal conductivity of bimodal SiC.

7.4. Conclusions

Bimodal μ -n and monomodal μ -SiC samples with the addition of nanosized Y_2O_3 and AlN as a sintering aid exhibited a liquid phase formation at lower temperatures than reported literature values for the pressureless sintering of SiC. The combined effect of increased powder content and reduced average particle size by nanoparticle addition are proposed as the reasons for 97% densification with only 15% shrinkage noticed in the bimodal SiC samples. A reduction noticed in the mechanical properties with an increase in the sintering temperature was attributed to the weight loss experienced by bimodal SiC samples. Higher thermal diffusivity and thermal conductivity values of bimodal SiC samples are suggested as the outcomes of higher densification and possible expedited grain growth despite the higher weight loss.

7.5. References

1. K. Biswas, J. Schneider, G. Rixecker, F. Aldinger, *Scripta Materialia*, 2005, vol. 53, 591-596
2. T. H. Grande, H. Sommerset, E. Hagen, K. Wiik, M.A. Einarsrud, *Journal of American Ceramic Society*, 1997, vol.80(4), pp. 1047-1052.
3. D. Sciti, D., A. Bellosi, *Journal of Materials Science*, 2000, vol. 35, pp. 3849-3855
4. Y. Lee, Y.W. Kim, M. Mitomo, *Journal of American Ceramic Society*, 2003, vol. 86(10), pp. 1803-1805
5. A.L. Ortiz, A.M. Bernabe, O.B. Lopez, A.D. Rodriguez, F. Guiberteau, N.P. Padture, *Journal of the European Ceramic Society*, 2004, vol.24, pp. 3245-3249
6. R.M. German, *Sintering Theory and Practice*; John Wiley and Sons, Inc.: NY, USA, 1996.
7. Y. Inomata, Proceeding of International Symposium on Ceramic Components for Engine, pp. 253, S. Somiyai, Eds., KTK Scientific Publishers: Tokyo, 1984
8. Y. Uemura, Y. Inomata, Z. Inoue, *Journal of Materials Science*, 1981, vol. 95(9), pp. 2333-2335
9. J.H. She, K. Ueno, *Materials Research Bulletin*, 1999, vol. 34, pp. 1629–1636
10. B.V. Manoj Kumar, M.H. Roh, Y.W. Kim, W. Kim, S.W. Park, W.S. Seo, *Journal of Materials Science*, 2009, vol. 44, pp. 5939-5943

11. V.A. Izhevskiy, A.H.A. Bressiani, J.C. Bressiani, *Journal of American Ceramic Society*, 2005, vol. 88, pp. 1115-1121
12. Y. Zhou, K. Hirao, M. Toriyama, Y. Yamauchi, S. Kanzaki, *Journal of American Ceramic Society*, 2001, vol. 84(7), pp. 1642-1644
13. R.M. German, *Liquid Phase Sintering*; Plenum Publication: New York, USA, 1985
14. R.M. German, P. Suri, S.J. Park, *Journal of Materials Science*, 2009, vol. 44, pp. 1-39
15. V. R.M. German, *Sintering Theory and Practice*, John Wiley and Sons, Inc., New York, NY, 1996
16. S. Prochazka, *Ceramics for High-Performance Applications*, Proc.2nd Army Materials Technology Conference, Hyannis, MS, 1973, pp. 239-52
17. T.S. Srivatsan, B.G. Ravi, M. Petraroli, T.S. Sudarshan, *International Journal of Refractory Metals and Hard Materials*, 2002, vol. 20, pp. 181-186.
18. M. Bothara, S.V. Atre, T. Sudarshan, R. Radhakrishnan, S.J. Park, R.M. German, *Metallurgical and Materials Transactions A*, 2010, vol. 41 A, pp. 3252-3261.
19. H.Y. Jin, M. Ishiyama, G.J. Qiao, J.Q. Gao, Z.H. Jin, *Materials Science and Engineering A*, 2008, vol. 483-484, pp. 270-273
20. M.C. Rodriguez, A. Munoz, A.D. Rodriguez, *Journal of the European Ceramic Society*, 2006, vol. 26, pp. 2397-2405
21. V.P. Onbattuvelli, S.V. Atre, *Materials and Manufacturing Processes*, 2011 (accepted).
22. Onbattuvelli, S. Vallury, S. Laddha, S. Atre, *PIM International*, 2010, vol.4(3), pp. 64-70.
23. V. Onbattuvelli, G. Purdy, G. Kim, S. Laddha, S. Atre, *Advances in Powder Metallurgy and Particulate Materials*, 2010, no.1, pp. 64-72.
24. V. Onbattuvelli, G. Purdy, G. Kim, S.J. Park, S. Atre, *Journal of American Ceramic Society*, 2011(submitted)
25. M. Balog, K. Sedlackova, P. Zifcak, J. Janega, *Ceramics Silikáty*, 2005, vol. 49, pp. 259-262
26. J. Gao, H. Xiao, H. Du, *Journal of Materials Science Letters*, 2002, vol.21, pp. 1835-1837
27. O.B. Lopez, A.L. Ortiz, F. Guiberteau, *Journal of American Ceramic Society*, 2005, vol.88(8), pp. 2159-2163
28. M. Herrmann, R. Neher, K. Brandt, S. Hoehn, *Journal of the European Ceramic Society*, 2010, vol. 30, pp.1495-1501
29. M. Bothara, *Sintering of nanocrystalline silicon carbide in plasma pressure compaction system*; PhD Thesis, Oregon State University: USA 2007
30. M. Nader, F. Aldinger, M.J. Hoffmann, *Journal of Materials Science*, 1999, vol. 34, pp. 1197-1204
31. G. Rixecker, K. Biswas, I. Wiedmann, F. Aldinger, *Journal of Ceramic Processing Research*, 2009, vol.1(1), pp. 12-19
32. Y.W. Kim, J.Y. Kim, S.H. Rhee, D.Y. Kim, *Journal of the European Ceramic Society*, 2000, vol. 20, pp. 945-949

33. S.G. Lee, W.H. Shim, J.Y. Kim, Y.W. Kim, W.T. Kwon, *Journal of Material Science Letters*, 2001, vol. 20, pp. 143-146
34. Can, M. Herrmann, D.S. McLachlan, I., Sigalas, J. Adler, *Journal of the European Ceramic Society*, 2006, vol.26, pp.1707–1712
35. X.Z. Guo, H. Yang, *Journal of Zhejiang University Science*, 2005, vol.6B(3), pp. 213-218
36. X. He, Y. Guo, Z. Yu, Y. Zhou, D. Jia, *Materials Science and Engineering A*, 2009, vol. 527, pp. 334–338
37. V.V. Pujar, R.P., Jensen, N.P. Padture, *Journal of Materials Science Letters*, 2000, vol.19, pp. 1011-1014
38. G. Magnani, L. Beaulardi, L. Pilotti, *Journal of the European Ceramic Society*, 2005, vol.25, pp. 1619–1627
39. K. Suzuki, M.Sasaki, *Journal of the European Ceramic Society*, 2005, vol.25, pp. 1611–1618
40. Y. Zhang, J. Han, L. Hu, *Materials Science & Engineering A*, 2008, vol.480, pp. 62-67
41. F. J. Clemens, V. Wallquist, W. Buchser, M. Wegmann, T. Graule, *Ceramics International*, 2007, vol.33, pp. 491–496

List of Figures

Figure 7.1: Processing window for sintering conditions for SiC based on literature reports

Figure 7.2: Effect of sintering temperature on the densification of bimodal (a) and monomodal (b) SiC

Figure 7.3: SEM images revealing the transition of bimodal SiC samples from thermally debound stage to the onset of liquid phase formation, (a) 500 °C, (b) 1100 °C, (c) 1300 °C and (d) 1550 °C

Figure 7.4: SEM images revealing the transition of monomodal SiC samples from thermally debound stage to the onset of liquid phase formation, (a) 500 °C, (b) 1100 °C, (c) 1300 °C and (d) 1550 °C

Figure 7.5: Weight loss experienced by bimodal (a) and monomodal (b) SiC as a function of sintering temperature

Figure 7.6: Shrinkage experienced by bimodal (a) and monomodal (b) SiC as a function of sintering temperature

Figure 7.7: Vickers hardness of bimodal (a) and monomodal (b) SiC as a function of sintering temperature

Figure 7.8: Indentation toughness of bimodal (a) and monomodal (b) SiC as a function of sintering temperature

Figure 7.9: Thermal diffusivity of bimodal (a) and monomodal (b) SiC as a function of sintering temperature

Figure 7.10: C_p of bimodal (a) and monomodal (b) SiC as a function of sintering temperature

Figure 7.11: Thermal conductivity of bimodal (a) and monomodal (b) SiC as a function of sintering temperature

List of Tables

Table 7.1: Literature review on liquid phase formation temperature for SiC densification

Table 7.2: Prior reports on additive-assisted pressureless sintering of SiC

Table 7.3: Prior reports on the mechanical properties of monomodal SiC

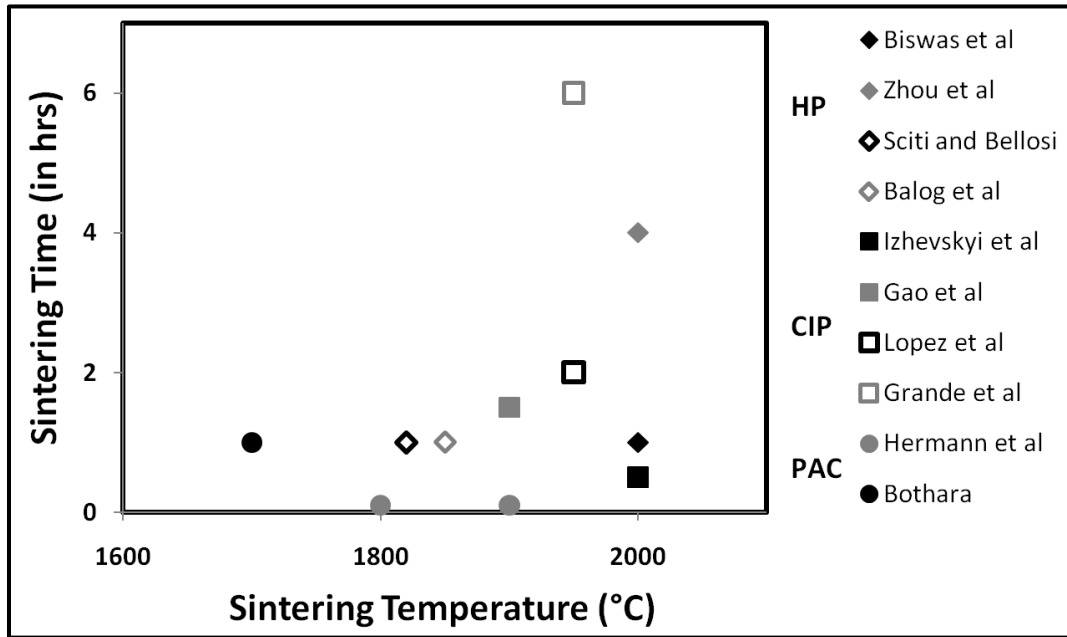


Figure 7.1: Processing window for sintering conditions for SiC based on literature reports

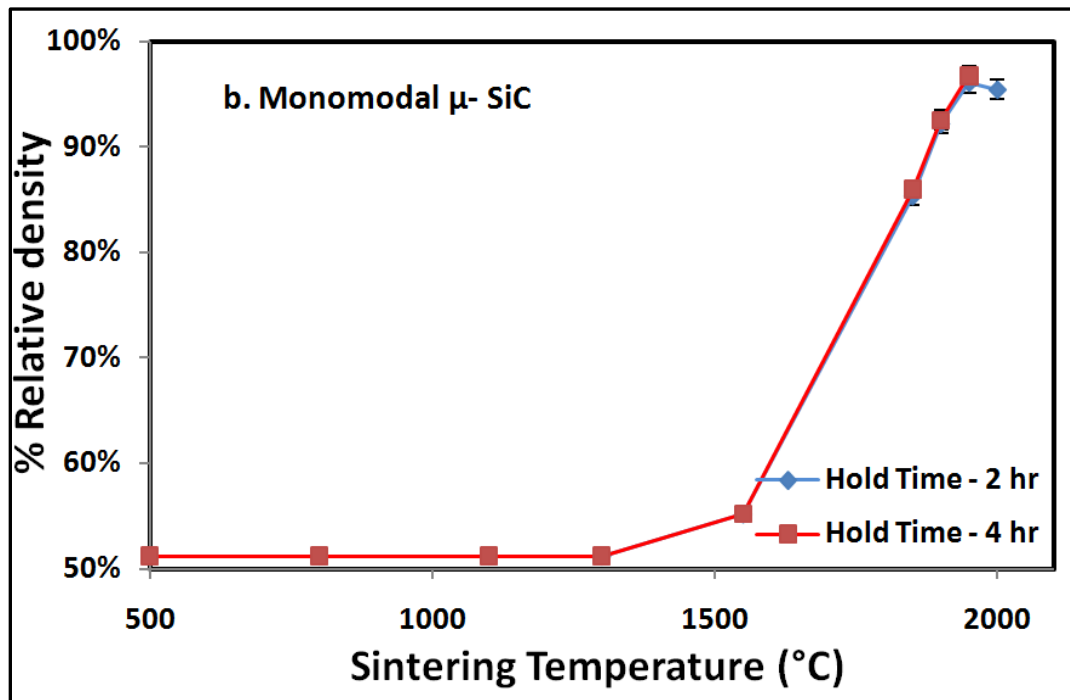
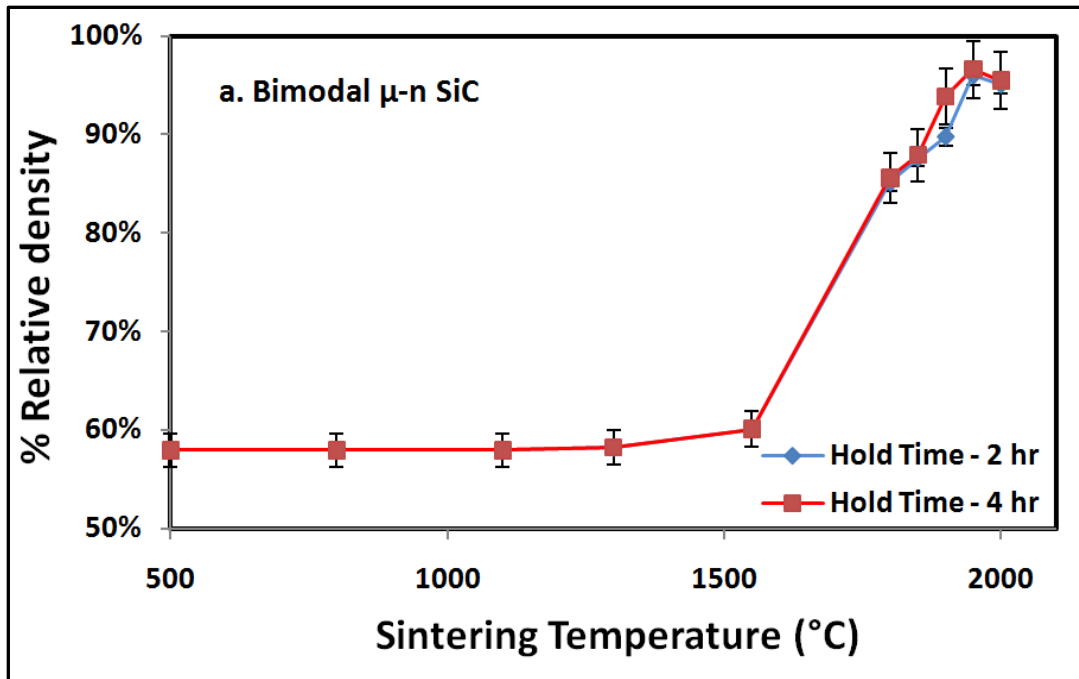


Figure 7.2: Effect of sintering temperature on the densification of bimodal (a) and monomodal (b) SiC

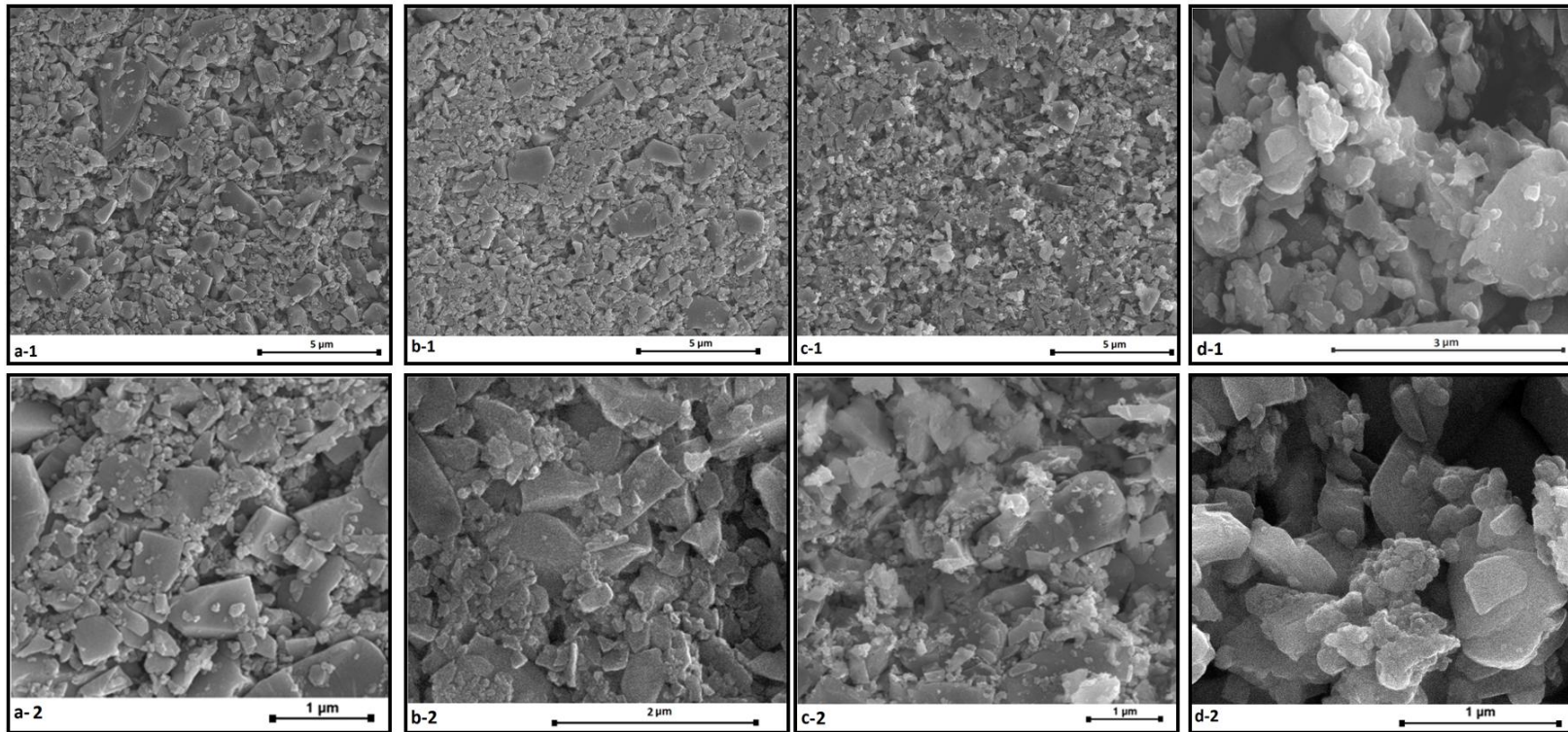


Figure 7.3: SEM images revealing the transition of bimodal SiC samples from thermally debound stage to the onset of liquid phase formation, (a) 500 °C, (b) 1100 °C, (c) 1300 °C and (d) 1550 °C

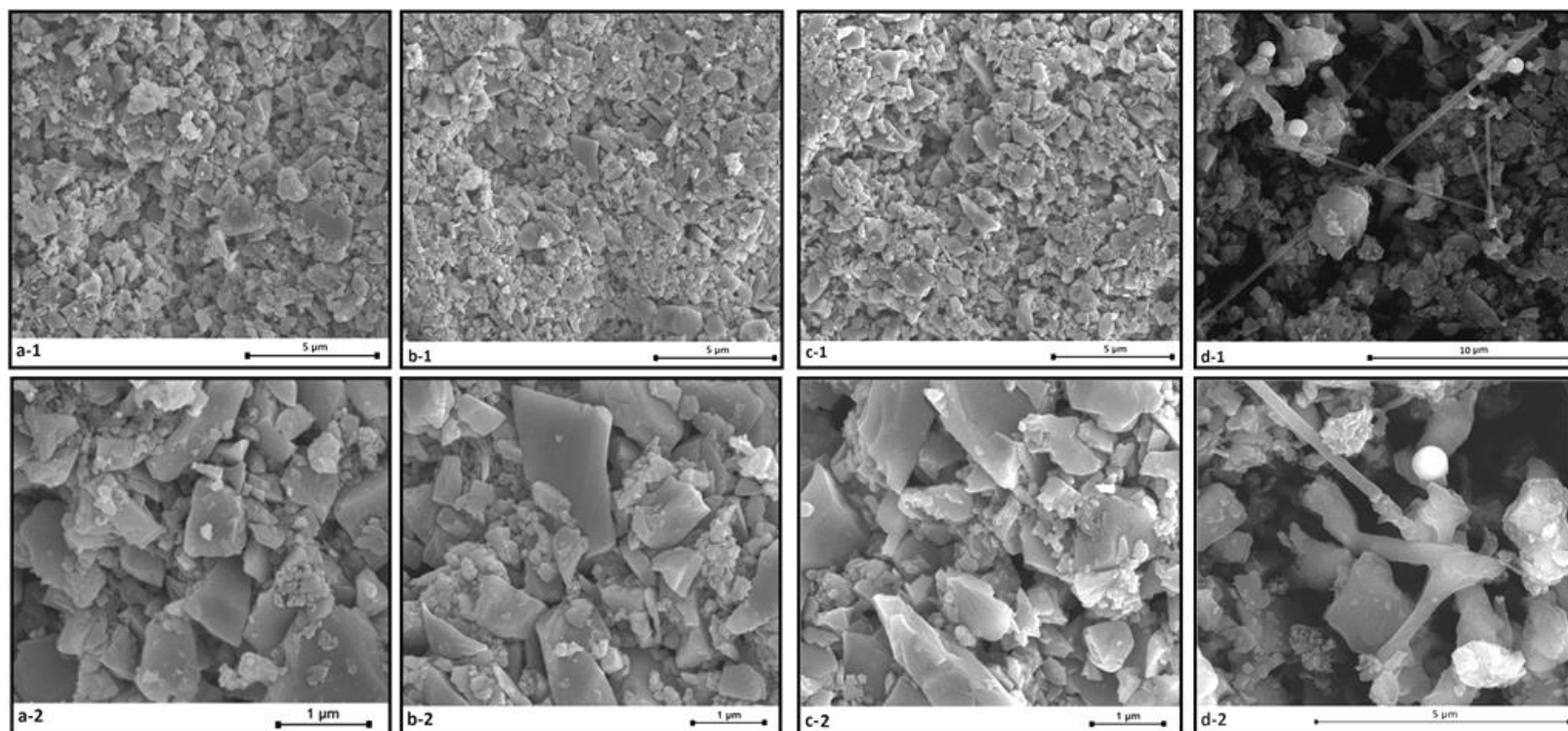


Figure 7.4: SEM images revealing the transition of monomodal SiC samples from thermally debound stage to the onset of liquid phase formation, (a) 500 °C, (b) 1100 °C, (c) 1300 °C and (d) 1550 °C.

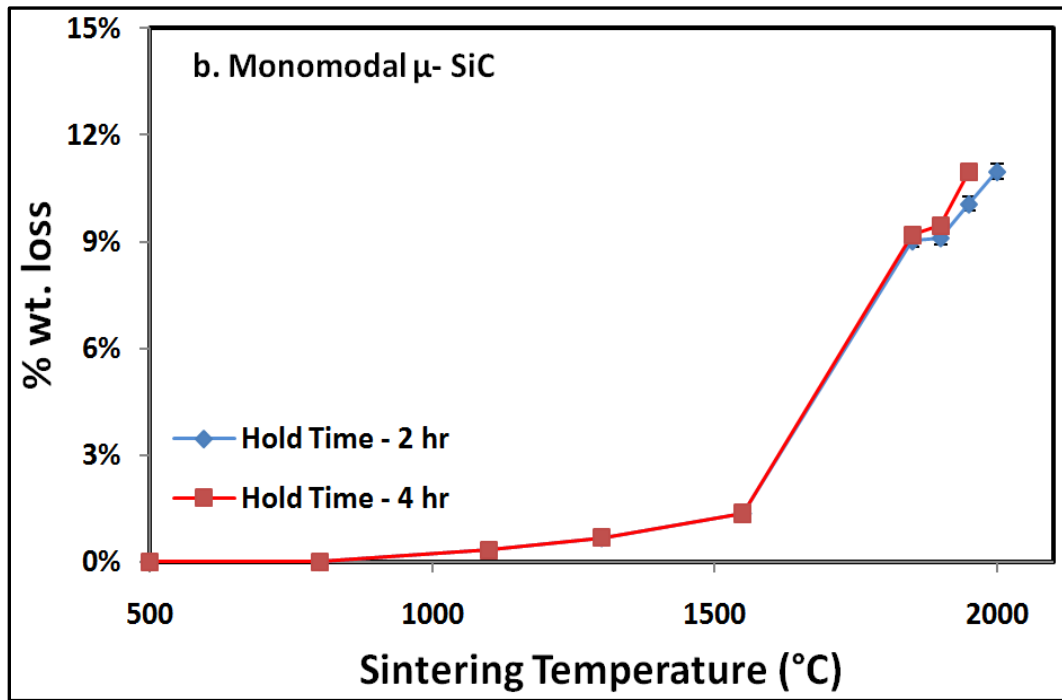
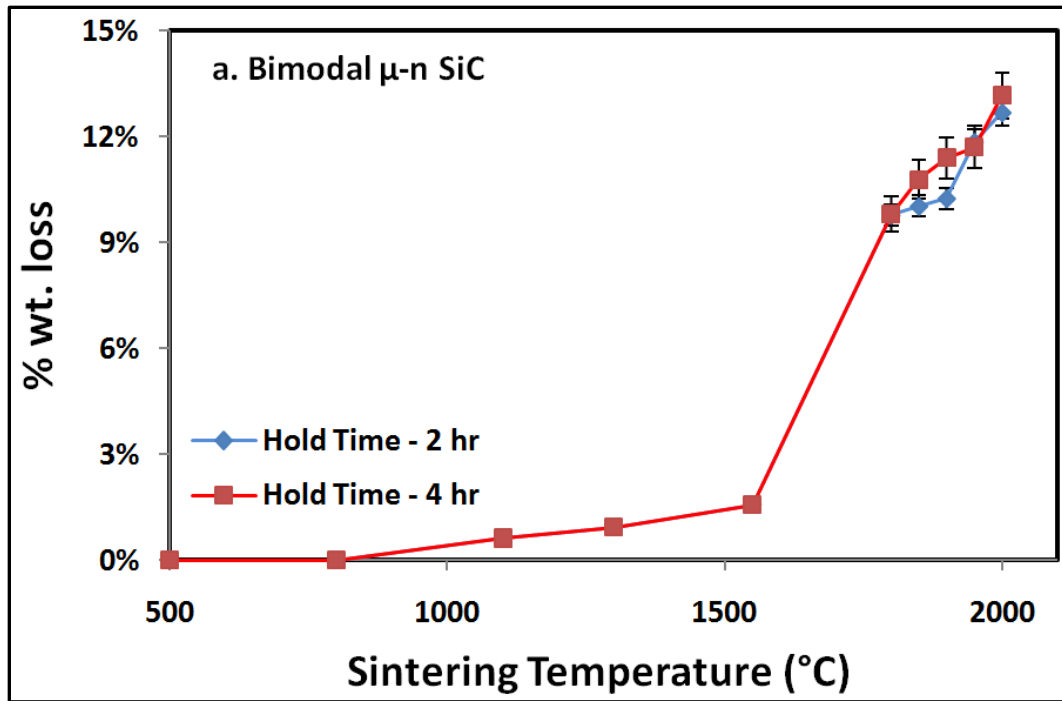


Figure 7.5: Weight loss experienced by bimodal (a) and monomodal (b) SiC as a function of sintering temperature

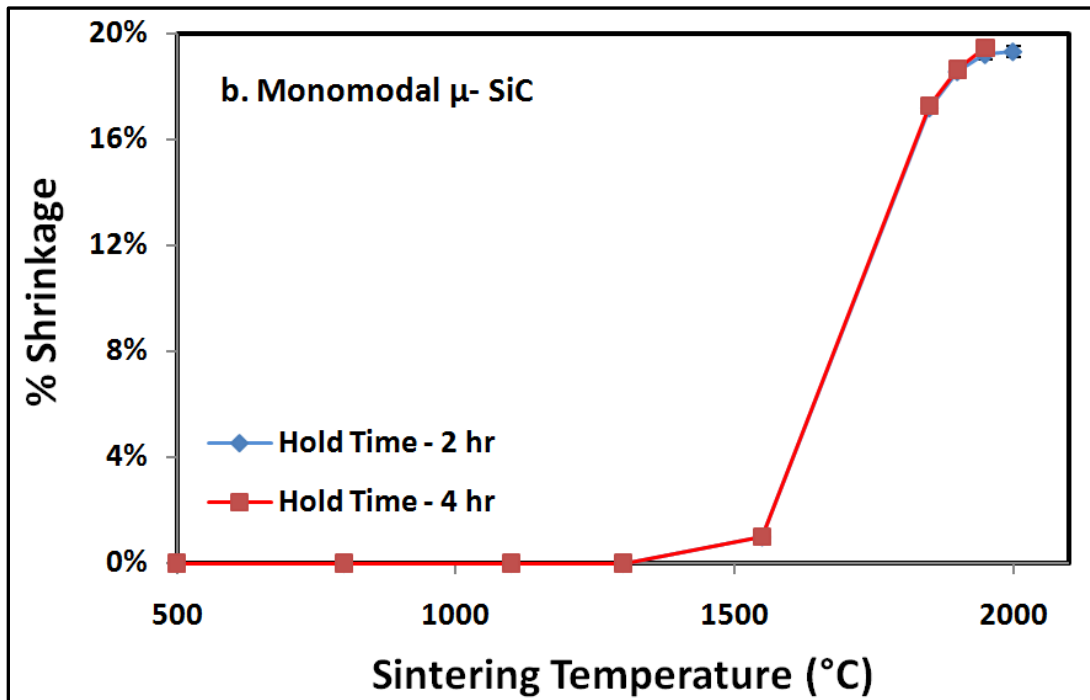
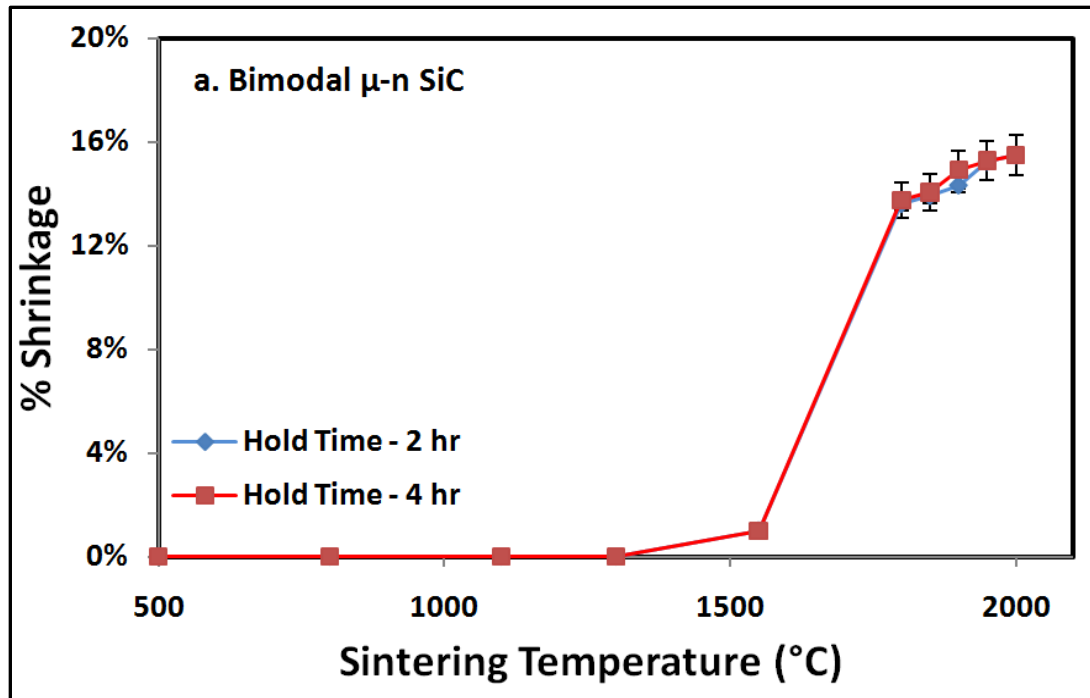


Figure 7.6: Isometric shrinkage of bimodal (a) and monomodal (b) SiC as a function of sintering temperature

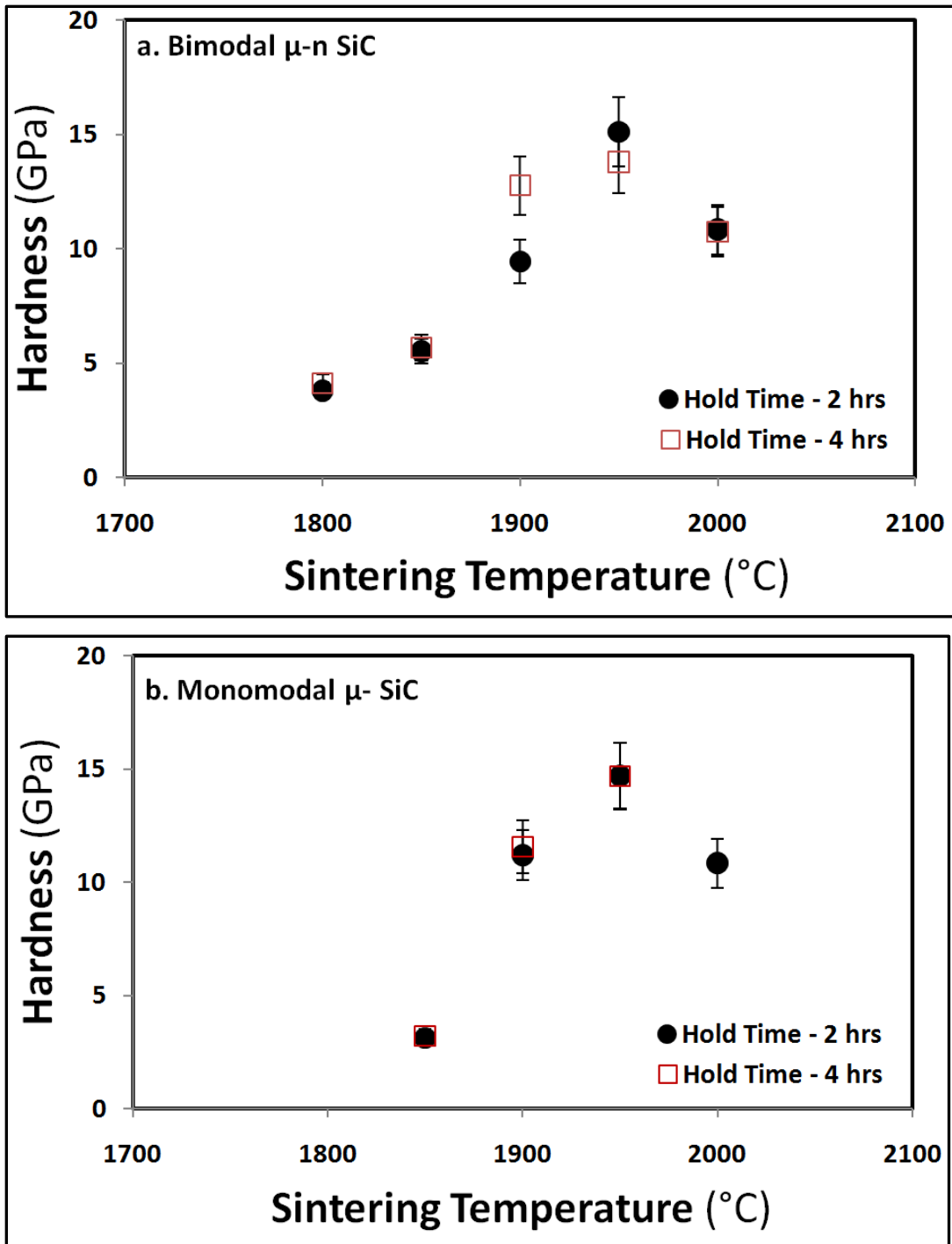


Figure 7.7: Vickers hardness of bimodal (a) and monomodal (b) SiC as a function of sintering temperature

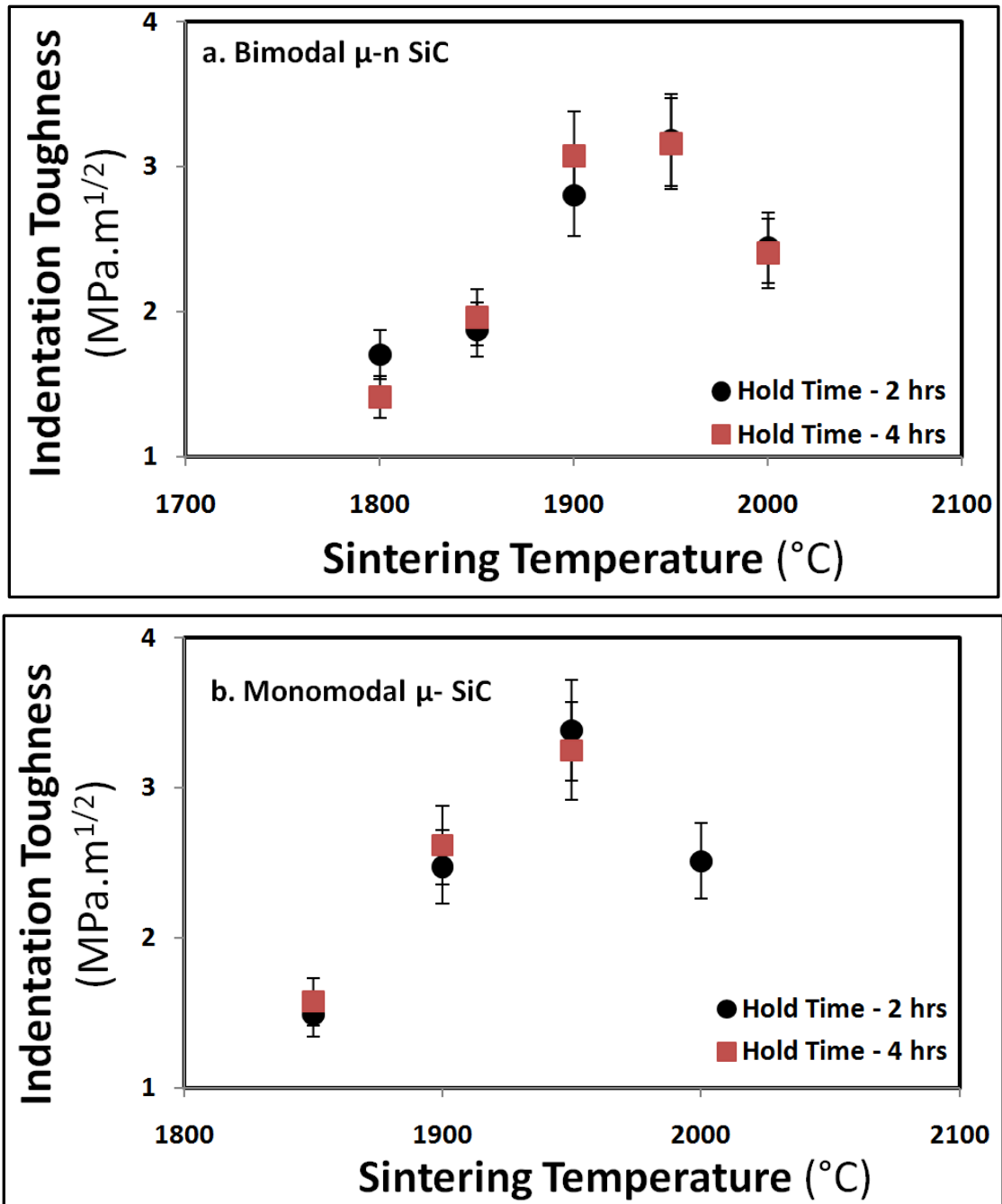


Figure 7.8: Indentation toughness of bimodal (a) and monomodal (b) SiC as a function of sintering temperatures

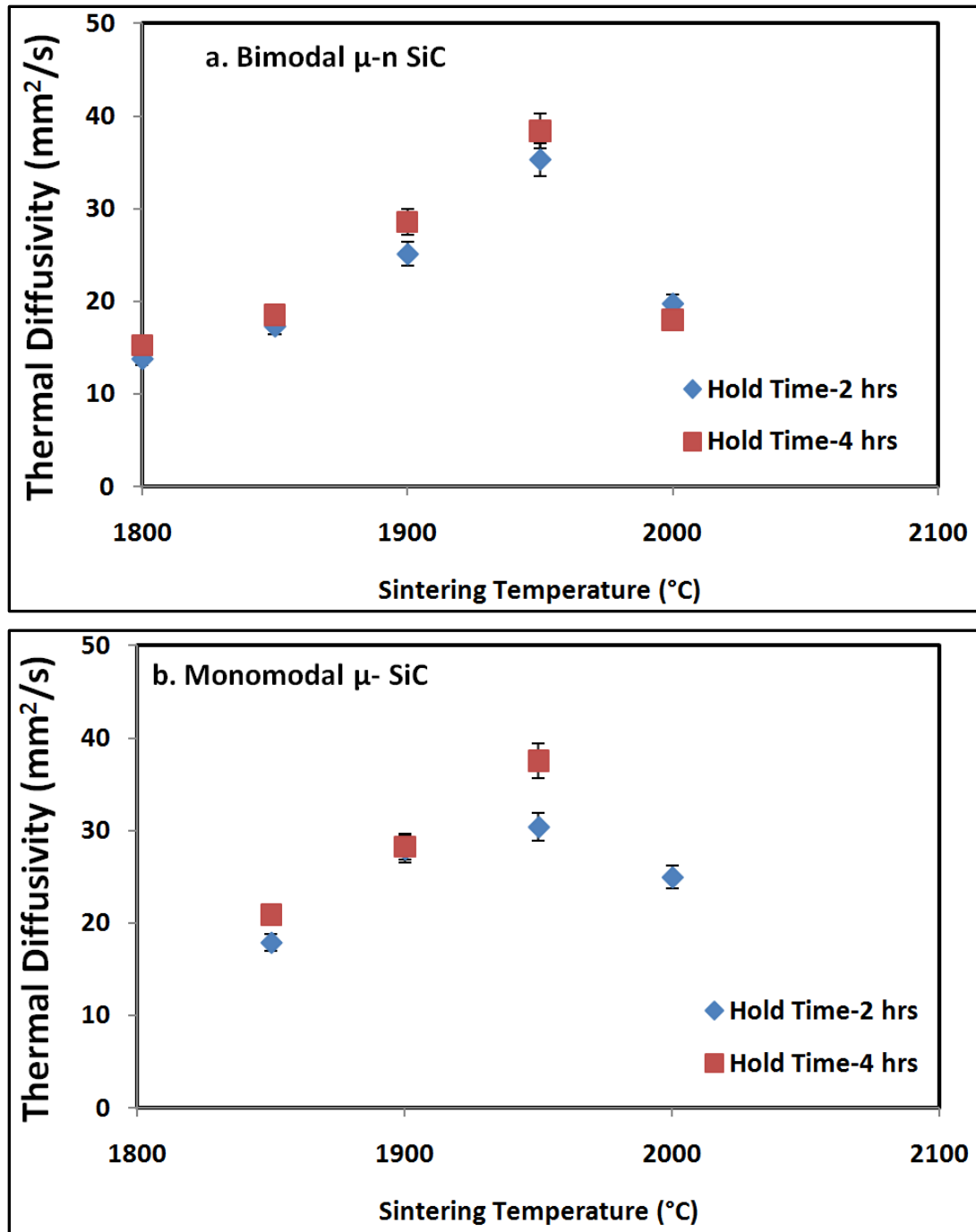


Figure 7.9: Thermal diffusivity of bimodal (a) and monomodal (b) SiC as a function of sintering temperatures

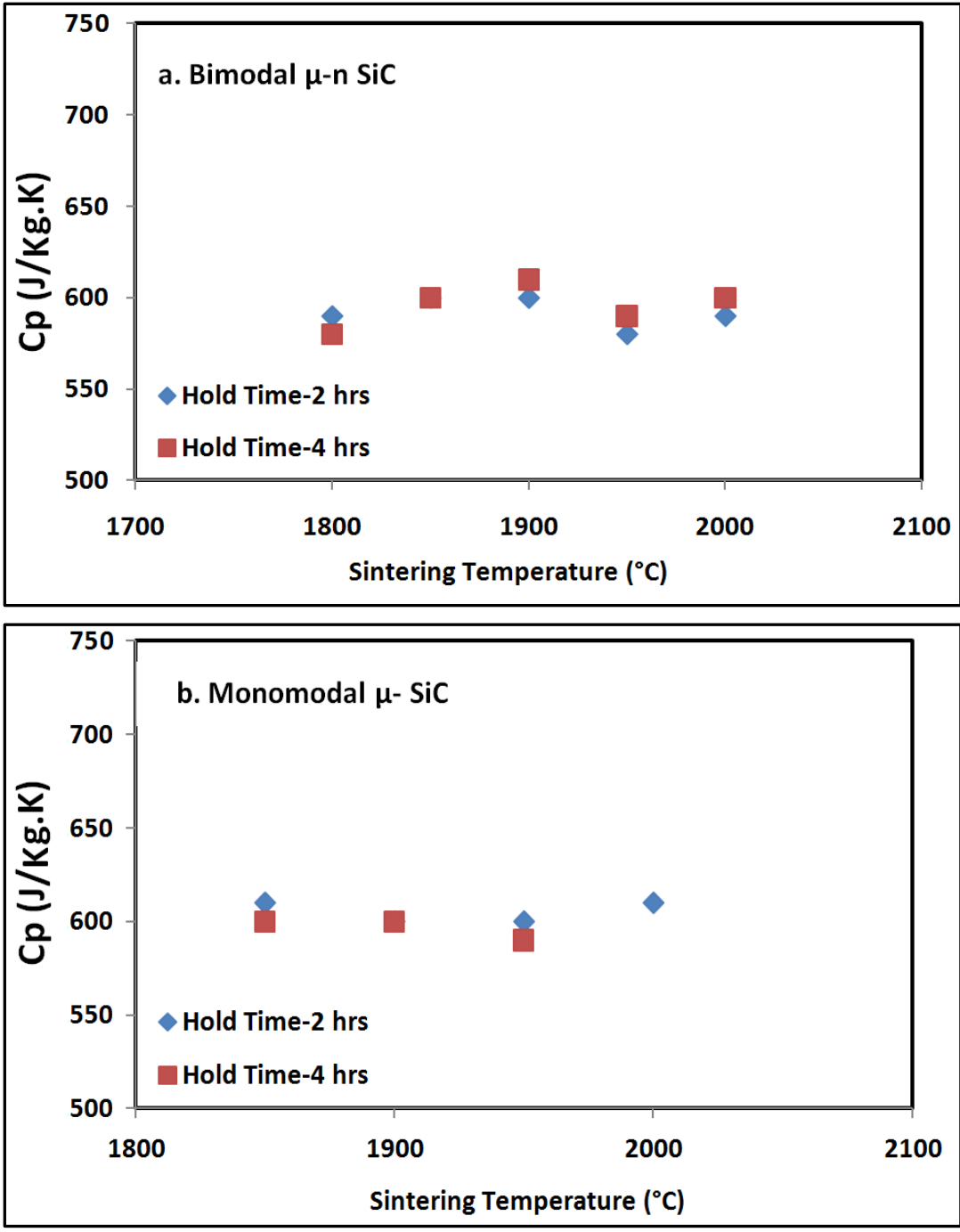


Figure 7.10: C_p of bimodal (a) and monomodal (b) SiC as a function of sintering temperatures

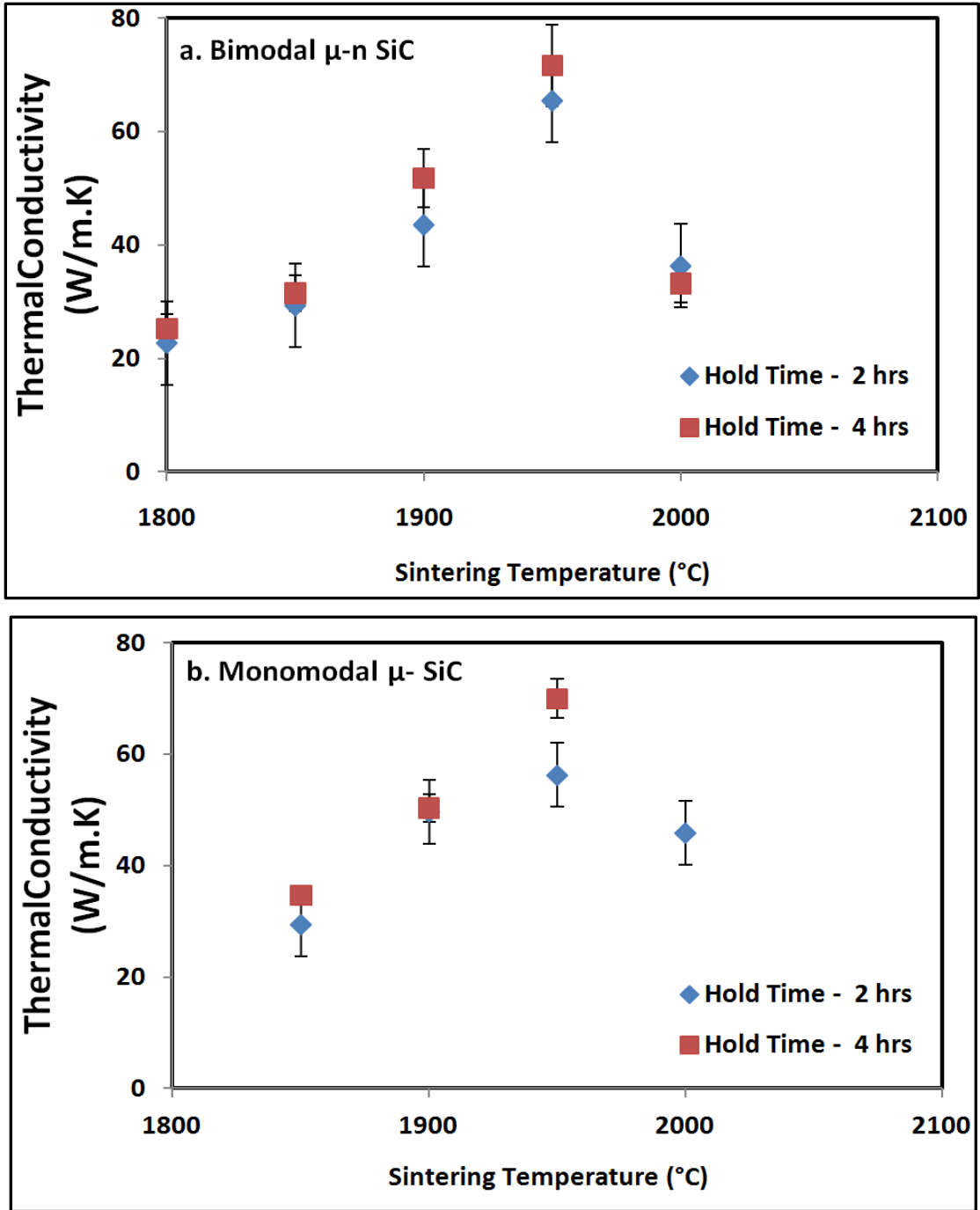


Figure 7.11: Thermal conductivity of bimodal (a) and monomodal (b) SiC as a function of sintering temperatures

Table 7.1: Literature review on the liquid phase formation temperature for SiC densification

Ref. #	Author	Initial SiC particle size (μm)	Type of sintering additive	Liquid phase formation temperature
2	Grande et al	α - 0.6	4.72% Al_2O_3 -2.73% Y_2O_3	1820°C
3	Sciti and Bellosi	-	6 % Al_2O_3 -4% Y_2O_3	1710 °C
33	Lee et al	β -0.27	5.3% Y_2O_3 -4.7% Al_2O_3	1800 °C
34	Can et al	-	5% Y_2O_3 -5% Al_2O_3	1600 °C
35	Guo et al	α - 0.75	6.25% Al_2O_3 - 3.75% Y_2O_3	1760 °C
36	He et al	β -0.8	6% MgO -1% Al_2O_3 -1% Y_2O_3	
9	She and Ueno	α - 0.6	6.25% Al_2O_3 - 3.75% Y_2O_3	

Table 7.2: Prior reports on additive-assisted pressureless sintering of SiC

Ref. #	Author	SiC Particle Size (μm)	Sintering aid		Net shaping and densification (with pressure in MPa)	Sintering Conditions			% relative density
			Nature	% content		Atm.	Temp ($^{\circ}\text{C}$)	Hold time (hrs)	
5	Ortiz et al	-	$\text{Al}_2\text{O}_3\text{-Y}_2\text{O}_3$	14.92-11.22	UP (50) + CIP (350)	Ar	1950	1	98%
9	She and Ueno	α - 0.6	$\text{Al}_2\text{O}_3\text{-Y}_2\text{O}_3$	6.25-3.75	UP (3) + CIP (200)	Ar	2000	1	98%
26	Gao et al	-	$\text{Al}_2\text{O}_3\text{-Y}_2\text{O}_3$	5-5	UP (25) + CIP (200)	N_2	1900	1.5	98%
35	Guo et al	α - 0.75	$\text{Al}_2\text{O}_3\text{-Y}_2\text{O}_3$	6.25-3.75	UP (100) + CIP (250)	Vac.	1860	0.75	96.1%
37	Pujar et al	-	$\text{Al}_2\text{O}_3\text{-Y}_2\text{O}_3$	12.5-7.5	UP (50) + CIP (350)	Ar	1900	0.5	96%
38	Magnani et al	β -0.72	$\text{Al}_2\text{O}_3\text{-Y}_2\text{O}_3$	6--4	UP (67) + CIP (250)	Ar	1875	0.5	97.1%
39	Suzuki & Sasaki	-	Al_2O_3	15	UP (20) + CIP (200)	N_2	1950	5	97%
20	Rodriguez et al	-	$\text{Al}_2\text{O}_3\text{-Y}_2\text{O}_3$	5--5	UP	Ar	1950	1	98.8%
								3	97.3%
								5	96.7%
								7	94.9%
40	Zhang et al	α - 0.5	$\text{Al}_2\text{O}_3\text{-Y}_2\text{O}_3$	4.5-4.5	-	N_2	1950	1	98%

Table 7.3: Prior reports on the mechanical properties of monomodal SiC

Ref. #	Author	Sintering aid		Sintering Conditions			% relative density	Toughness (MPa. m ^{1/2})	Hardness (GPa)
		Nature	% content	Atm.	Temp (°C)	Hold time (hrs)			
3	Sciti and Bellosi	Al ₂ O ₃ -Y ₂ O ₃	6-4	-	1780	0.5	98%	3.1	22
5	Ortiz et al	Al ₂ O ₃ -Y ₂ O ₃	14.92-11.22	Ar	1950	1	98%	3.3	17.3
9	She and Ueno	Al ₂ O ₃ -Y ₂ O ₃	6.25-3.75	Ar	1900	1	98%	7.5	19.5
					1950		97.5%	6.5	18
					2000		97%	6	17
29	Manish Bothara	AlN- Y ₂ O ₃	5-5	Ar	1700	1	99.6%	5	20
30	Nader et al	AlN-Y ₂ O ₃	2.95-10.34	N ₂	1925	14	-	2.8	-
35	Guo et al	Al ₂ O ₃ -Y ₂ O ₃	6.25-3.75	Vac.	1860	0.75	96.1%	5.2	20
38	Magnani et al	Al ₂ O ₃ -Y ₂ O ₃	6--4	Ar	1875	0.5	97.1%	4.5	21
39	Suzuki & Sasaki	Al ₂ O ₃	15	N ₂	1950	5	97%	4.3	21.9
40	Zhang et al	Al ₂ O ₃ -Y ₂ O ₃	4.5-4.5	N ₂	1950	1	98%	2	-

CHAPTER 8

The Effects of Nanoparticle Addition on the Sintering and Properties of Bimodal AlN

Abstract

The effects of nanoparticle addition on the pressureless sintering of injection molded and debound bimodal aluminum nitride (AlN) samples were studied. Variations in the densification, microstructure and properties owing to the increased powder content and reduced particle size are discussed. The results indicate the formation of liquid phase at 1500 °C in the bimodal AlN samples, a temperature that is at least 100°C lower than typically reported values in the literature. This in turn shifted the pressureless sintering to a relatively lower temperature of 1650 °C exhibiting $\geq 99\%$ densification yet only with 14% isometric shrinkage. Additionally, thermal and mechanical properties of the sintered bimodal AlN samples are presented and compared with sintering studies on conventional monomodal AlN systems reported in the literature.

8.1. Introduction

Aluminum nitride (AlN) has attracted considerable attention as a substrate material for electronic packaging because of its excellent properties, such as high thermal conductivity and coefficient of thermal expansion that are well matched to that of silicon [1-4]. These properties make AlN an excellent material to replace alumina (Al_2O_3) and beryllia (BeO) used for the manufacture of semiconductor devices [5, 6]. AlN also has the potential to be used as heat sink for high operating temperature applications, LED thermal management, laser diode heat spreaders, optoelectronic parts, cutting tools, ignition modules, and casting crucibles [5-8]. In order to translate the above mentioned thermal properties into demanding applications, it is necessary to net-shape AlN into fully dense microstructures.

Prior reports investigated AlN densification by exploring material and process parameters. AlN is a covalently-bonded material and requires sintering additives to enhance densification. Thus, prior reports on material parameters focused on the effect of varying the type and amount of sintering additives on the densification behavior of AlN. For example, Surnev et al studied the effect of varying the amount of yttria (Y_2O_3) as the sintering aid over the final density [9]. Similarly, Molisani et al compared the efficiency of Y_2O_3 and calcium oxide (CaO), as sintering aids for the AlN densification [10]. Sintering temperature and hold time were the commonly studied process parameters in the past. For example, Zhou et al [11] and Li et al [12] reported the increase in the sintered density with the increase in the sintering temperature. On the other hand, Kume et al noticed a decrease in the sintered density with higher hold time at the sintering temperature [13]. A brief literature review on AlN densification is presented by our research group elsewhere [14].

One research issue that is least explored till date is the effect of initial powder packing density on the final sintered density of AlN ceramics [15]. Our prior research work successfully demonstrated an increase in powder content with the addition of nanoparticles, forming bimodal μ -n powder mixtures [16, 17]. For example, the powder content was found to increase from 54 to 71 vol.% when AlN nanoparticles are added to the monomodal submicron (μ) sized AlN powders. The implication of such nanoparticle additions has been discussed in the past in the context of powder-polymer mixture (feedstock) properties, mold filling behavior and polymer removal kinetics of the injection molded bimodal μ -n AlN and SiC samples [16, 18]. In a similar manner, the effect of nanoparticle addition on the sintering behavior of AlN at different time-temperature combinations was discussed in the current work. These sintering experiments reveal that bimodal μ -n AlN powder mixtures display liquid phase formation at relatively lower

temperatures. The sintered density, shrinkage, thermal and mechanical properties of the resulting sintered bimodal μ -n samples are compared with that of the previously reported sintering studies on conventional monomodal AlN samples.

8.2. Experimental Section

8.2.1. Materials

The starting powder materials contain as-received, commercially available AlN (1.1 μ m and 20 nm) with 5 wt.% Y_2O_3 (50 nm) as the sintering additives.

8.2.2. Sample preparation

Powder injection molded bimodal μ -n AlN samples were solvent and thermally debound prior to sintering. The molding and debinding conditions used are detailed elsewhere [16, 18]. Thermally debound bimodal AlN samples with an initial density of 2.15 g/cc (65% relative density) were pressureless sintered at different temperatures upto 1900 °C for 4 hrs under nitrogen atmosphere.

8.2.3. Instrumentation

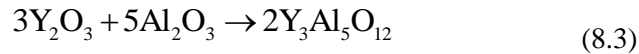
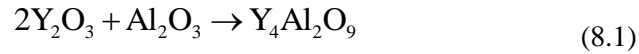
The density for all the sintered samples was measured with a lab-built Archimedes apparatus. Microstructural analysis was conducted on the fracture surfaces of sintered AlN samples using a QuantaTM –FEG (FEI) dual beam scanning electron microscope (SEM) coupled with an energy dispersive X-ray spectrometer (EDS). SEM images of each sample were presented in two different magnifications for better comparison. The thermal diffusivity of the samples was measured with a LFA-457 (Netzsch) laser flash apparatus. TA Instruments- 2920 unit was used to measure the specific heat (Cp) of the sintered samples. Vickers hardness and indentation toughness of the sintered AlN samples were measured via Leco microhardness tester.

8.3. Results and Discussion

From the densification plot represented in the **Figure 8.1**, it can be seen that the densification of the bimodal μ -n AlN is initiated at \sim 1500 °C. SEM studies on these samples confirmed a liquid phase formation at \sim 1500 °C (**Figure 8.2**). A shift in the densification towards lower sintering temperatures can be correspondingly expected. This in turn explains the \geq 99% densification of bimodal AlN samples at 1650 °C (**Figure 8.3a**). Similarly, a 95 % densification at 1600 °C is reported in the past by Panchula and Ying for a monomodal n-AlN system [23]. They proposed two likely mechanisms that could be held responsible for the low-temperature densification of

ultrafine AlN systems. Firstly, an Al-Y-O-N liquid could form and promote material transport via liquid-phase sintering. Secondly, solid-state grain boundary diffusion could increase due to the higher surface area of n-AlN, which in turn expedites Y₂O₃ doping at the grain boundaries. This hypothesis could be supported with the observed AlN grain growth as a function of temperature (**Figures 8.3b-d**). Further research including XRD analysis and a comparative study with an injection molded monomodal μ-AlN system is required to analyze the effects of the nanoparticle addition on the sintering behavior of AlN.

The densification of AlN is facilitated by liquid phase sintering, accompanying solution-reprecipitation between the AlN and the liquid phase [6]. Y₂O₃ is the most commonly reported sintering additive for AlN and is thus used in the current study [1-4, 9, 10, 15]. AlN typically contains dissolved oxygen in its lattice. At lower temperatures, this dissolved oxygen exists in the form of aluminum oxynitride, Al₉N₇O₃. Raghavan et al [19] and Klemens et al [20] state that these oxygen impurities diffuse through the grain boundary to react with Y₂O₃, forming yttrium aluminates with a smaller yttrium-to-aluminum atomic ratio Y/Al. **Equations 8.1-8.3** explain the formation of major liquid phase, yttrium aluminum garnet (YAG) (Y₃Al₅O₁₂) and other secondary aluminate phases by reacting Y₂O₃ and Al₂O₃.



Zhou et al state that during AlN sintering, Y₄Al₂O₉ is first formed [11]. At the high temperatures, the major secondary phases were found to be YAlO₃ and Y₃Al₅O₁₂ (yttrium aluminum garnet - YAG). In particular, YAG formation is the result of reduction in the oxygen vacancies, which in turn enhances the growth of AlN grains. **Table 8.1** provides a review of prior reports mentioning the onset temperature of YAG formation for conventional monomodal AlN systems [1, 3, 9, 15, 21, 22]. It can be seen that the onset of liquid phase formation in the present study is comparatively lower by at least 100 °C than what is discussed in prior reports.

In addition to the observation that grain growth occurs with increase in temperature, a decrease in density is noticed after 1650 °C in the SEM images. This in turn can be correlated with the weight loss experienced by bimodal AlN samples during sintering as shown in the **Figure 8.4**. Such weight loss could be due to the reaction between the excess Y₂O₃ present in the mixture with the YAG to form YAlO₃ at elevated temperatures, as shown in **Equation 8.4**.



The $YAlO_3$ in turn breaks down to form volatile monoxides of Al and Y along with O_2 as shown in the **Equation 8.5** [10]. This material loss opens up new pores at sintering temperatures leading to reduction in the % density. Similar results on AlN densification has been reported qualitatively in the past by Molisani et al [10], Panchula and Ying [23] and Olhero et al [24] arguing the necessity to optimize the Y_2O_3 content prior to AlN sintering. Additionally, the reason for weight loss at temperatures between 1000 - 1600 °C is not clear at this stage of research. Future experiments including TGA-assisted–mass spectroscopy and XRD analysis are required to explain the effect of nanoparticle addition on the weight loss in the bimodal AlN samples.

As mentioned earlier, a higher initial powder packing density (solids loading, Φ) is important for improving the sintered density and ensuing properties. The higher green density in turn results in lesser shrinkage and consequently more dimensional control following sinter densification. As shown in the **Figure 8.5**, an isometric shrinkage of up to 14% is noticed in our samples corresponding to 99% densification. The plot is also extended to compare the shrinkage reported in the literature for AlN densification [1, 22, 24, 25]. This comparison confirms the value of bimodal μ -n powder mixtures where, in addition to liquid phase formation at lower temperature; maximum densification can be achieved with relatively lower shrinkage.

Figure 8.6 plots the thermal diffusivity values obtained for bimodal AlN samples sintered at different temperatures. The thermal diffusivity of the bimodal AlN is expected to increase with the temperature due to the grain growth detailed earlier in the SEM images. In contrast, fluctuations are noticed which could be explained as the combined outcome of simultaneous grain boundary loss and weight loss. A maximum thermal diffusivity of 33 mm²/s is noticed for the bimodal AlN samples sintered at 1700 °C and 1900 °C. A similar trend was explained in the past by Suzuki and Sakka [22] and Olhero et al [24] for monomodal AlN samples. In addition to the weight loss explained earlier, the use of excessive amount of sintering additives was found detrimental to the sintered properties due to higher content of intergranular glassy phase. This is once again evident from the comparative study presented in the **Figure 8.7**, where the C_p of the AlN sintered under similar condition is more dependent on the amount of Y_2O_3 used.

For most solid materials with a perfect crystal lattice, thermal diffusion is primarily controlled by the transfer of thermal elastic waves, otherwise known as *phonons*. It has been suggested that thermal diffusivity is limited by intrinsic phonon scattering of the microstructure [26, 27].

Imperfections such as grain boundaries, pores and impurities (secondary phases in liquid phase sintering) are unavoidably present in nearly all materials. The phonons tend to scatter when collided with these imperfections leading to reduction in the thermal diffusivity values. The thermal conductivity (K) is a product of thermal diffusivity, sintered density and C_p . Thus, factors such as sintered density, weight loss, grain growth and amount of intergranular glassy phase were found to affect the thermal conductivity of the given samples. Despite the fact that bimodal AlN samples revealed $\geq 99\%$ densification, the higher amount of liquid phase additives, smaller grain size and higher wt. loss could account for the lower “K” value of 71 W/m.K compared to that of previous reports (**Figure 8.8**). A detailed analysis with variations in the fabrication techniques and amount and composition of sintering aids is required to explore the possibility to increase the “K” of bimodal AlN.

In addition to thermal properties, the effect of sintering temperature on the mechanical properties of bimodal AlN was studied. A maximum Vickers hardness of 10.2 GPa and indentation toughness of $2.3 \text{ MPa.m}^{1/2}$ is noticed for the AlN samples sintered at $1650 \text{ }^\circ\text{C}$. Similar values of hardness equivalent to 11.5 GPa and toughness of $3 \text{ MPa.m}^{1/2}$ is reported in the past [28, 29]. Additionally, as shown in the **Figure 8.9**, both the Vickers hardness and indentation toughness reduced with increase in temperatures, possibly due to porosity formation following weight loss. Similar results with mechanical properties were reported by Lopez et al [30] and She and Ueno [31] for monomodal SiC systems. However, absence of any detailed analysis of mechanical properties of sintered AlN in the literature diminished the possibility for a comparative study. Hence, measurements on sintered monomodal μ -AlN samples are required to study the effect of nanoparticle addition on the mechanical properties of AlN.

8.4. Conclusions

Bimodal μ -n AlN samples exhibited liquid phase formation at lower temperatures compared to that of the conventional monomodal μ -AlN samples. This in turn shifted the densification to a relative lower sintering temperature although with a reduced isometric shrinkage. The combined effect of increased powder content and reduced average particle size by nanoparticle addition is proposed as the reason for such behavior. Reduction noticed in the mechanical properties with the increase in the sintering temperatures was correlated with the microstructural evolution. Fluctuations in the thermal diffusivity values and lower thermal conductivity values are suggested as the possible outcome of the weight loss during sintering despite AlN densification and grain growth.

8.5. References:

1. K.H. Lin, Y.C. Lin, S.T. Lin, *Journal of Materials Processing Technology*, 2008, vol. 201, pp. 701-705
2. A. F. Junior, D. Shanafield, *Journal of Materials Science: Materials in Electronics*, 2005, vol. 16, pp. 139-144.
3. M. Medraj, Y. Baik, W.T. Thompson R.A.L. Drew, *Journal of Materials Processing Technology*, 2005, vol. 161, pp. 415-422
4. X. Du, M. Qin, F. Akhtar, P. Fengg, X. Qu, *Rare Metals*, 2008, vol.27 (1) pp. 70-73.
5. Y. Baik, R.A.L. Drew, *Key Engineering Materials*, 1996, vol.122-124, pp. 553-570
6. A.V. Virkar, T.B. Jackson, K.L. More, R.A. Cutler, *Journal of American Ceramic Society*, 1997, vol. 80, pp.1421-1435
7. D. Palit, A.M. Meier, *Journal of Materials Science*, 2006, vol. 41, pp.7197-7209
8. I.-L. Tangen, Y. Yu, T. Grande, R. Hoier, M.-A. Einarsrud, *Journal of American Ceramic Society*, 2004, vol. 87, pp. 1734
9. S. Surnev, D. Lepkova, A. Yoleva, *Materials Science and Engineering B*, 1991, vol.10(3), pp. 5-40
10. A. L. Molisani, H.N. Yoshimura, H. Goldenstein, K. Watari, *Journal of the European Ceramic Society*, 2006, vol.26, pp. 3431–3440
11. H. Zhou, Y. Liu, W. Miao, Y. Wu, *Journal of Materials Science*, 1999, vol. 34, pp.6165-6168.
12. X.L. Li, H.A. Ma, Y.J. Zheng, Y. Liu, G.H. Zuo, W.Q. Liu, J.G. Li, X. Jia, *Journal of Alloys and Compounds*, 2008, vol. 463, pp. 412–416.
13. S. Kume, M. Yasuoka, N.Omura, K. Watari, *Journal of American Ceramic Society*, 2005, vol.88 (11), pp. 3229-3231
14. V.P. Onbattuvelli, S.V. Atre, *Materials and Manufacturing Processes*, 2011 (accepted)
15. J.Y. Qiu, Y. Hotta, K. Watari, *Journal of American Ceramic Society*, 2006, vol.89(1), pp. 377-380
16. V. Onbattuvelli, S. Vallury, S. Laddha, S. Atre, *PIM International*, 2010, vol.4(3), pp. 64-70
17. V. Onbattuvelli, G. Purdy, G. Kim, S. Laddha, S. Atre, *Advances in Powder Metallurgy and Particulate Materials*, 2010, no.1, pp. 64-72.
18. V. Onbattuvelli, G. Purdy, G. Kim, S.J. Park, S. Atre, *Journal of American Ceramic Society*, 2011(submitted)
19. S. Raghavan, H. Wang, W. D. Porter, R. B. Dinwiddie, M. J. Mayo, “*Acta Materialia*”, 2001, vol. 49, pp. 169-79
20. P.G. Klemens, R. Dinwiddie, “*Thermal Conductivity*”, 23rd Edition, Technomic Publication, 1996, pp.209
21. C.F. Chen, M.E. Perisse, A.F. Ramirez, N.P. Padture, H.M. Chan, *Journal of Material Science*, 1994, vol. 29, pp. 1595-1600
22. T.S., Suzuki, Y. Sakka, *Scripta Materialia*, 2005, vol.52, pp. 583-586

23. M.L. Panchula, J.Y. Ying, *Journal of American Ceramic Society*, 2003, vol. 86, pp. 1121-1127
24. S.M. Olhero, P. Miranzo, J.M.F. Ferreira, *Journal of the European Ceramic Society*, 2006, vol. 26, pp. 2475–2483.
25. X. Luo, J. Li, B. Zhang, W. Li, H. Zhuang, *Journal of American Ceramic Society*, 2006, vol. 89(3), pp. 836-841
26. F. Cernuschi, P.G. Bison, S. Marinetti, P. Scardi, *Acta Materialia*, 2008, vol. 56, pp. 4477-88.
27. B. K. Jang, Y. Sakka, *Journal of Alloys and Compounds*, 2008, vol. 463, pp. 493–7
28. Ferro-Ceramic Grinding Inc., MA, USA, *Ceramic Components Directory*, 2008, pp. 13-14
29. J.W. McCauley, *Weapons and Materials Research Directorate*, 2002, ARL-TR-2740, pp. 8
30. J.H. She, K. Ueno, *Materials Research Bulletin*, 1999, vol. 34, pp. 1629–1636
31. O.B. Lopez, A.L. Ortiz, F. Guiberteau, *Journal of American Ceramic Society*, 2005, vol.88(8), pp. 2159-2163

List of Figures

Figure 8.1: Effect of sintering temperature on the pressureless densification of AlN

Figure 8.2: SEM images revealing the transition of bimodal AlN samples from thermally debound stage to the onset of liquid phase formation

Figure 8.3: SEM images revealing the grain growth in the bimodal AlN samples with the increase in the sintering temperatures

Figure 8.4: Effect of sintering temperature on weight loss during AlN densification

Figure 8.5: Effect of sintering temperature on shrinkage during AlN densification

Figure 8.6: Thermal diffusivity of AlN samples as a function of sintering temperature

Figure 8.7: C_p of AlN samples as a function of sintering temperature

Figure 8.8: Thermal conductivity of AlN samples as a function of sintering temperature

Figure 8.9: Mechanical properties of bimodal AlN samples as a function of sintering temperature

List of Tables

Table 8.1: Literature review on YAG formation temperature for AlN densification

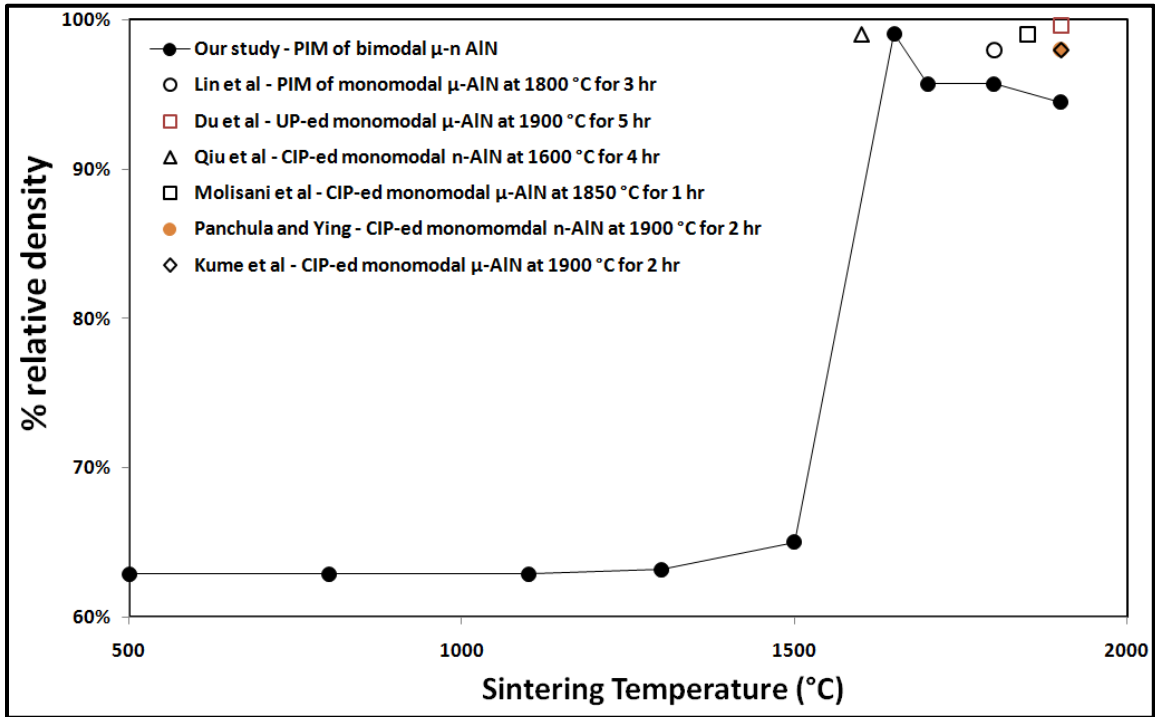


Figure 8.1: Effect of sintering temperature on the pressureless densification of AlN

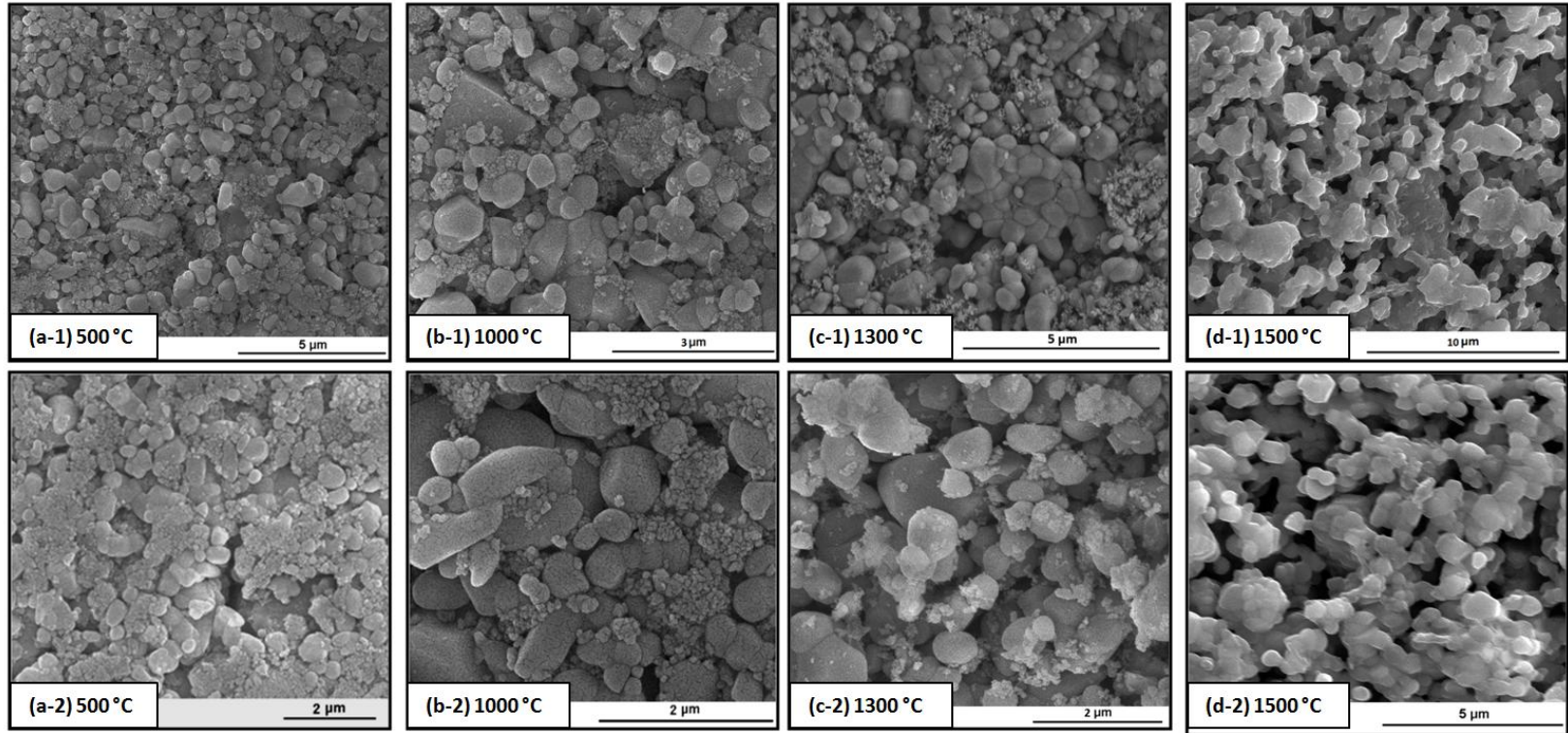


Figure 8.2: SEM images revealing the transition of bimodal AlN samples from thermally debound stage to the onset of liquid phase formation

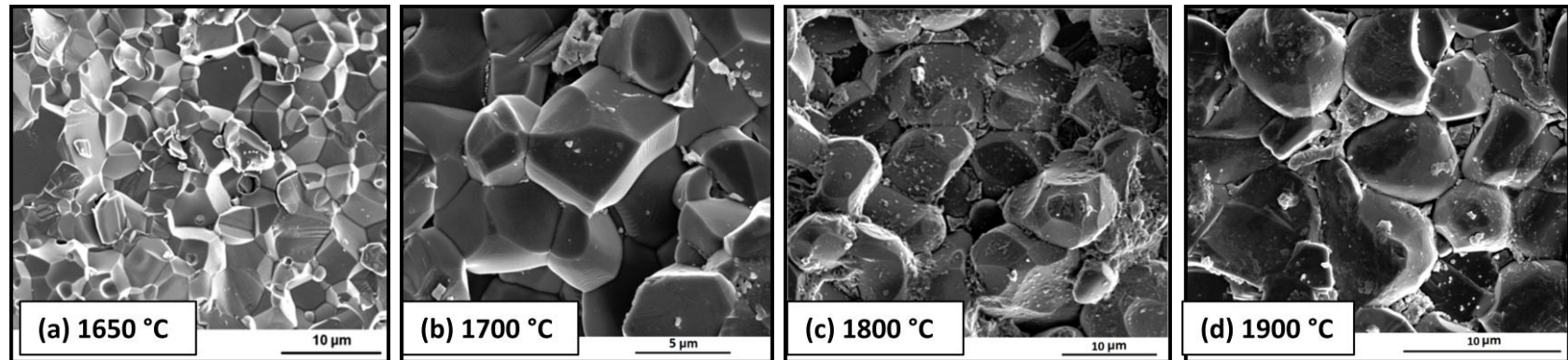


Figure 8.3: SEM images revealing the grain growth in the bimodal AlN samples with the increase in the sintering temperatures

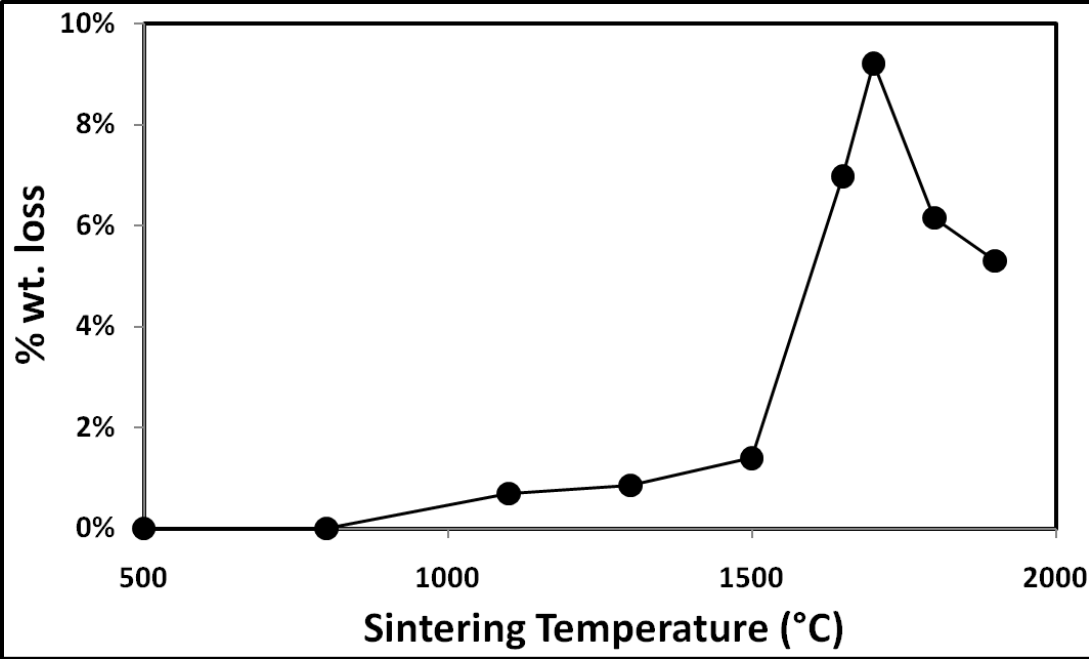


Figure 8.4: Effect of sintering temperature on weight loss during AlN densification

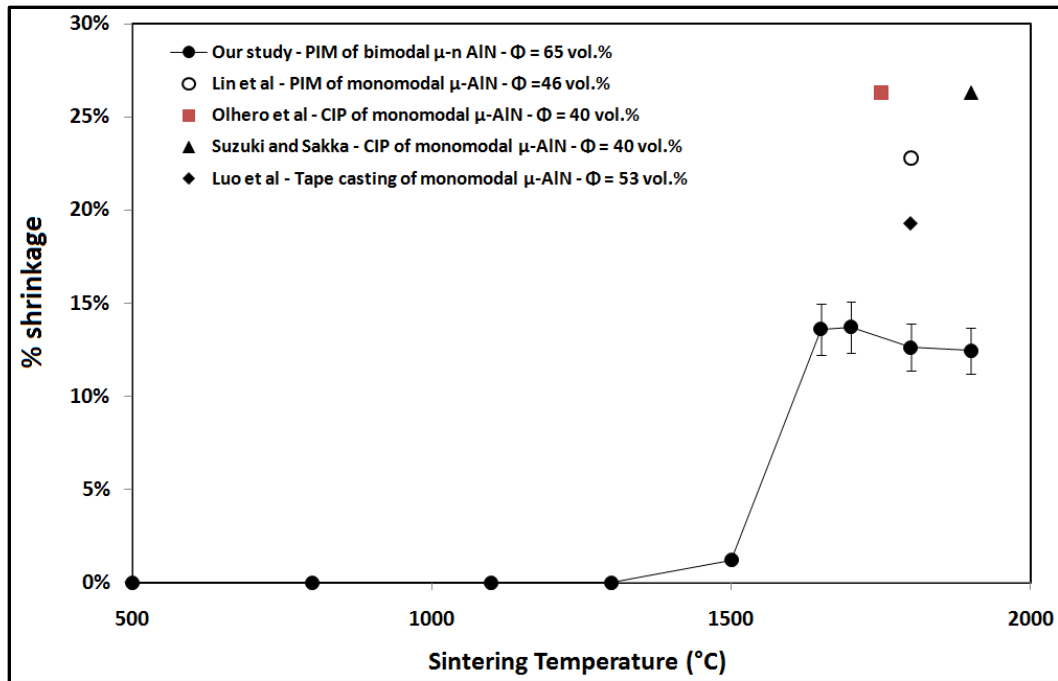


Figure 8.5: Effect of sintering temperature on shrinkage during AIN densification

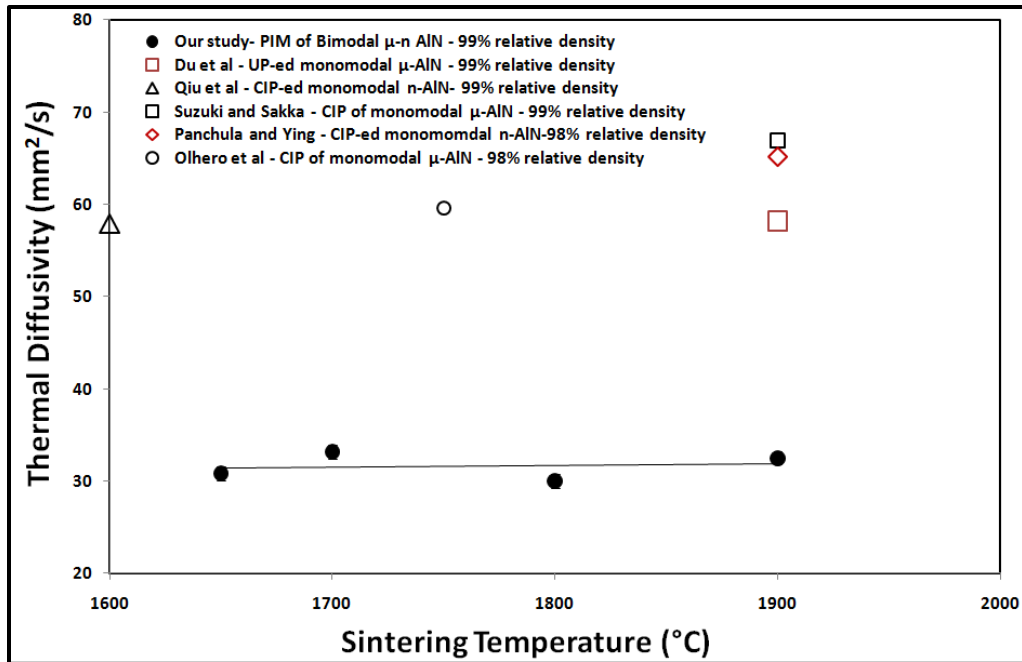


Figure 8.5: Thermal diffusivity of AlN samples as a function of sintering temperature

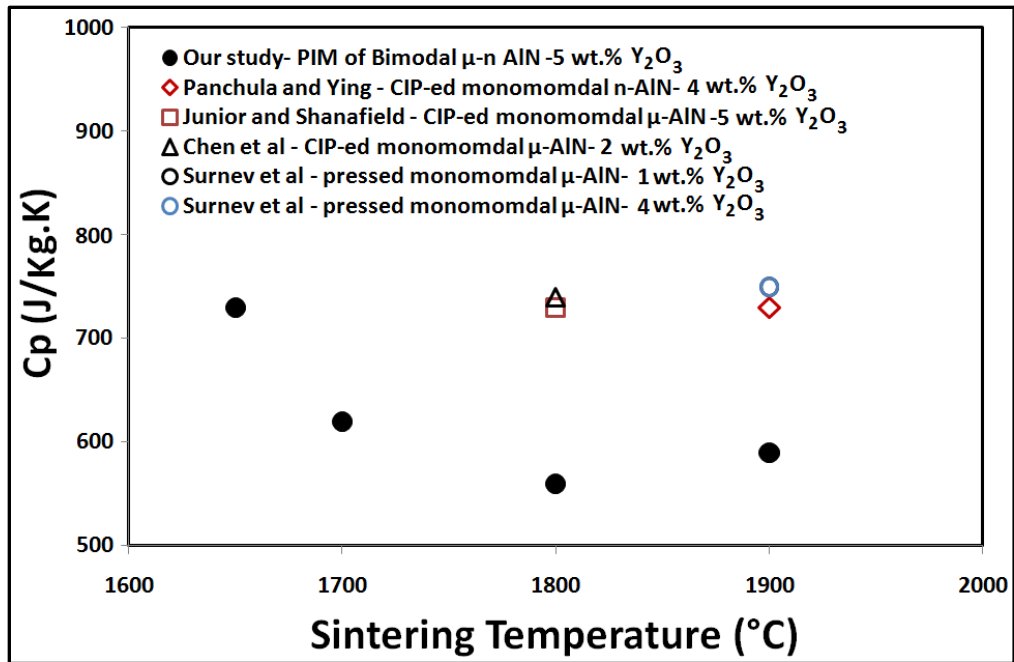


Figure 8.6: C_p of AlN samples as a function of sintering temperature

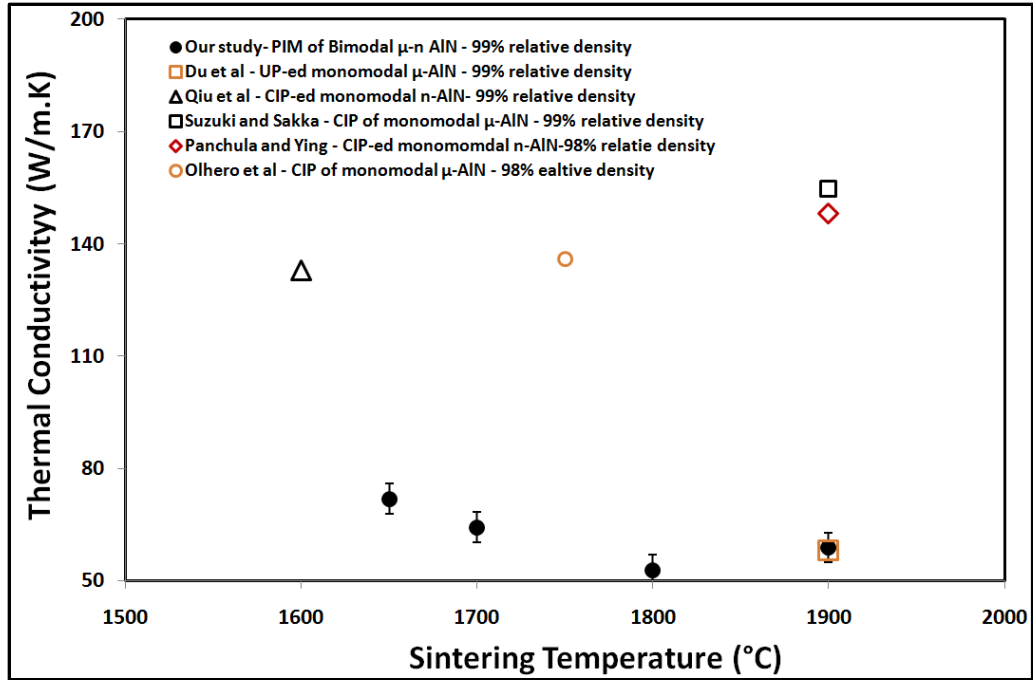


Figure 8.7: Thermal conductivity of AlN samples as a function of sintering temperature

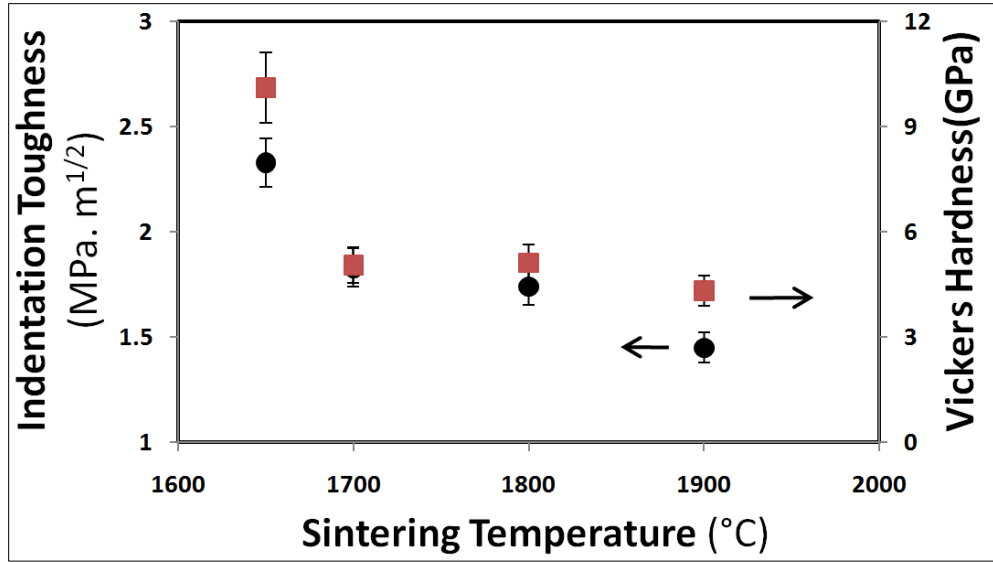


Figure 8.8: Mechanical properties of bimodal AlN samples as a function of sintering temperature

Table 8.1: Literature review on YAG formation temperature for AlN densification

Ref. #	Author	Initial AlN particle size (μm)	Y₂O₃ content	YAG formation temperature
1	Lin et al	1.5 μm	3 wt.%	1720 °C
3	Medraj et al	0.3 μm	1.36 wt.%	1782°C
			7.59 wt.%	1847°C
9	Molisani et al	0.92 μm	1.8 wt.%	1760 °C
15	Qiu et al	0.1 μm	3.5 wt.% (+2 wt.% CaO)	1600 °C
21	Chen et al	1.22 μm	2 wt.%	1800 °C
22	Suzuki and Sakka	0.7 μm	5 wt.%	1760 °C

CHAPTER 9

Conclusions and Future Work

9.1. Conclusions

SiC and AlN are difficult to sinter ceramics. The current dissertation successfully demonstrated the extension of powder injection molding concept to the difficult to sinter ceramics such as SiC and AlN. During the course of this research, effort is taken to conduct an in-depth study on the effects of nanoparticle addition on the powder injection molding (PIM) of SiC and AlN powder-polymer mixtures. The following are some of the important conclusions obtained from this work.

9.1.1. Powder bimodality

Bimodal mixtures of nanoscale (n) and sub-micrometer (μ) particles were found to have significantly increased powder volume fraction (solids loading) in the mixtures for injection molding. SEM micrographs revealed that the nanoparticles fit into the interstitial spaces between the microparticles for the AlN and SiC systems. Additionally, reduced torque values at comparable solids loading confirmed the increased particle packing in bimodal μ -n mixtures. Subsequently, a maximum powder content of 71 vol.% in the powder-polymer mixture was achieved for the bimodal AlN mixture containing 82 wt.% μ -AlN and 18 wt.% n-AlN. Similarly, a maximum powder content of 65 vol.% in the powder-polymer mixture was achieved with a particular bimodal mixture containing 90 wt.% μ -SiC and 10 wt.% n-SiC. Comparative experiments for monomodal 100 wt.% μ -SiC and μ -AlN systems, resulted in a maximum powder content of only 53 vol.% and 54 vol.%, respectively.

9.1.2. Properties of powder-polymer mixtures

The thermal, rheological and pressure-volume-temperature (PVT) properties of monomodal and bimodal powder-polymer mixtures were measured. The bimodal powder-polymer mixtures revealed a reduction in the C_p values and an expedited thermal degradation compared to monomodal mixtures. The specific volume of bimodal mixtures showed lower thermal expansion relative to monomodal mixtures. Rheological measurements concluded a reduced fluidity for the bimodal mixtures due to their increased powder content. Coefficient values obtained from the viscosity models indicated that additional shear stress is required to initiate the pseudo-plastic behavior in bimodal μ -n mixtures. Comparative studies were conducted on the powder-polymer mixtures containing equal powder content based on the theoretical models. It was inferred that at

lower solids loading, the nanoparticle addition was found to reduce the viscosity of the resulting bimodal mixtures. Mold filling simulation studies indicated that the higher viscosity of bimodal mixtures (resulting from the increased solids loading) posed challenges. The higher viscosity of the bimodal mixtures led to slower melt velocity which in turn increased the fill time and shear stress along the mold walls.

9.1.3. Polymer removal of injection molded bimodal samples

A two-step debinding was chosen to expedite the polymer removal process. The initial binder removal by solvent debinding leaves interpenetrating pore channels, which are then used to escape the decomposed gas during subsequent thermal debinding. Bimodal SiC and AlN samples exhibited slower polymer removal behavior compared to monomodal samples irrespective of the debinding conditions. The combined effect of increased powder content and reduced average particle size by nanoparticle addition is inferred as the reason for such behavior. Theoretical models indicated that the effect of particle size on solvent debinding was minimized at higher powder content, for the samples under consideration. Debinding conditions including solvent temperature, immersion time and part geometry were varied to calculate the diffusion coefficients (D_c). Nanoparticle addition in the bimodal samples also exhibited delay in the completion of the thermal debinding cycles.

9.1.4. Densification and properties of bimodal μ -n SiC

The effects of nanoparticle addition on the pressureless sintering of injection molded and thermally debound SiC samples were studied. Bimodal μ -n and monomodal μ -SiC samples with the addition of nanosized Y_2O_3 and AlN as a sintering aid exhibited a liquid phase formation at ~ 1550 °C. This is at least 100 °C lesser than previously reported values for monomodal μ -SiC samples with microscale sintering additives. When sintered at 1950 °C for 4 hours, 97% densification with only 15% shrinkage was noticed in the bimodal SiC samples. In contrast, nearly 20% shrinkage in dimensions was observed for monomodal μ -SiC samples for a comparable sintered density (96% theoretical). A combined effect of increased powder content and reduced average particle size by nanoparticle addition was proposed as the reasons for such behavior. A reduction was noticed in the mechanical properties with an increase in the sintering temperature above a certain temperature, which was attributed to the weight loss experienced by bimodal SiC samples. Higher thermal diffusivity and thermal conductivity values were observed for bimodal SiC samples and were attributed as the outcomes of higher densification and possible expedited grain growth despite the higher weight loss.

9.1.5. Densification and properties of bimodal μ -n AlN

The effects of nanoparticle addition on the pressureless sintering of injection molded and debound bimodal AlN samples were studied. Bimodal μ -n AlN samples exhibited a liquid phase formation at lower temperature of ~ 1500 °C compared to that of the conventional monomodal μ -AlN samples with microscale additives that have been reported in the literature. Consequently, densification appeared to occur at a relative lower sintering temperature of ~ 1650 °C, exhibiting $> 99\%$ relative density with only 14% isomeric shrinkage. A maximum Vickers hardness of 10.2 GPa and indentation toughness of $2.3 \text{ MPa}\cdot\text{m}^{1/2}$ were measured for the AlN samples sintered at 1650 °C. Further sintering at higher temperatures reduced the mechanical and thermal properties. Bimodal AlN samples were found to have a maximum thermal conductivity value of only 71 W/m.K which could be the possible outcome of weight loss experienced during sintering.

9.2.Directions for future research

The current work successfully reported the novel concept μ -n powder bimodality. The research was also extended to confirm the technical feasibility of injection molding bimodal SiC and AlN samples. During the course of research, various interesting results were obtained which in turn could open new opportunities for research areas that need to be explored in the future.

9.2.1. Effect of varying the binder composition

One factor that was kept constant in the current work was the composition of the binder mixture. Despite the fact that the powder bimodality had increased the solids loading, higher viscosity was exhibited by the bimodal samples. This in turn extended its impact on the flow and mold filling behavior of the bimodal mixtures. Thus, varying the binder composition and/or content could help us achieve higher powder content, lower viscosity. This in turn opens up a new research window on analyzing the effect of varying the binder composition on formulation and processing of powder-polymer mixtures. The research should also be extended to analyze the debinding behavior of these newly formulated mixtures.

9.2.2. Effect of varying the initial particle size

As mentioned in the Chapter 4, one particular bimodal μ -n powder ratio exhibited maximum powder content for both SiC and AlN systems. This ratio in turn could be shifted by varying the initial size of the micro and nanoparticles. Additionally, one could expect a change in the

maximum powder content of the resulting bimodal mixtures. Thus a future research is required to understand the effect of initial particle size on the powder content of the powder-polymer mixtures which in turn dominates the processing and properties of the resulting samples.

9.2.3. Effect of nanosized sintering additives

In addition to the concept of powder bimodality, the current work also involved nanosized sintering additives in both monomodal and bimodal SiC and AlN samples. In the cases of both monomodal AlN and SiC, a novel nanorod formation was noticed at 1550 °C and 1100 °C respectively, as shown in the **Figure 9.1**. The EDS studies (Tables 9.1 and 9.2) on these nanorods indicate compositions similar to that of the corresponding liquid phase in AlN and SiC, respectively. Additionally, an isometric shrinkage of 1.5% and 1% is noticed in AlN and SiC respectively. This has not been previously reported in the literature. The reason for the presence of nanorods and their absence in bimodal samples is not clear at this stage of research. Thus, a comparative study on the current monomodal systems with that of monomodal systems with μ -sized sintering additives is required to understand the importance of the nanorod formation. Further, the influence of nanoscale sintering additives on microstructure, sintering behavior, and properties need to be better understood.

9.2.4. Green micromachining of injection molded bimodal samples

Unlike machining of sintered ceramics, green micromachining occurs at significantly lower cutting forces and is capable of rapidly creating high precision structures. With the development of new bimodal formulations exhibiting lower dimensional shrinkage, the opportunity to introduce high precision microfeatures in the injection molded samples has been demonstrated in initial studies. **Figure 9.2** demonstrates microfeatures with dimension $\sim 10X$ the size of the starting AlN particle size. Thus a novel hybrid processing approach of combining green micromachining with PIM could have huge application in the tool making as well as prototyping short run components. **Figure 9.3** demonstrates the ability of green micromachined samples to preserve complex microfeatures following sintering. A detailed future research involving variations in the binder formulation is required to experiment the fabrication of microscale features by green micromachining.

9.2.5. Extension of powder bimodality concept to other systems

As mentioned earlier, the current research has successfully established the technical feasibility of a novel approach to net-shaping difficult-to-sinter ceramics into complex shapes with dense microstructures. Additionally, as shown in the **Figure 9.4**, the powder injection molding alone

currently holds a market of over US\$ 1 billion and requires technical advancements to ensure continued growth [1]. Thus, the principles developed from this research can be applied to other ceramic and metal powder systems and applications. This can be achieved through the use of the standardized process, process design tools and controls, engineered material and process attributes and resulting precision and properties, as identified in this dissertation. For example, the concept of bimodality has been successfully extended to net-shape barium titanate (BaTiO_3) with dense microstructures for ultracapacitor applications. This project resulted in the development of novel compositions of BaTiO_3 containing nanoscale additives accompanied by improvements in the net-shaping and properties, as shown in the **Figure 9.5**. The sintered dimensions of microwell features below $3\ \mu\text{m}$ in (**Figure 9.5c**) are the smallest dimensions ever reported for PIM. A more in-depth study of the structure, processing and properties of such features is recommended for the future.

9.2.6. Densification of bimodal $\mu\text{-n}$ SiC and AlN under pressure and electric field

As mentioned in the **Chapters 2 and 3**, extensive research had been done in the past on the densification of SiC in the presence of an external field (pressure and electric field). For example, Bothara et al reported 99.6% densification for SiC plasma –pressure compacted at $1600\ ^\circ\text{C}$ for 30 min [2]. In addition, such samples exhibited no weight loss and hence better properties such as 20 GPa Vickers hardness. Thus, coupling the concept of powder bimodality with an external field assisted sintering can open up new research ventures in the difficult to sinter ceramics like SiC and AlN.

9.3. References

1. R. M. German , *PIM International*, 2008, vol.2 (2), pp. 45-51
2. M. Bothara, *Sintering of nanocrystalline silicon carbide in plasma pressure compaction system*; PhD Thesis, Oregon State University: USA 2007

List of Figures

Figure 9.1: Nanorod formation in monomodal AlN at 1100 °C (a) and monomodal SiC at 1550 °C (b).

Figure 9.2: Micromachined green bimodal μ -n AlN samples

Figure 9.3: Sintered micromachined bimodal μ -n AlN samples

Figure 9.4: Global market for powder injection molded products

Figure 9.5: SEM micrographs of sintered microchannels (a), microgrids (b) and microwells (c) net-shaped by PIM of bimodal μ -n BaTiO₃

List of Tables

Table 9.1: Elemental composition of the nanorods formed during the monomodal AlN sintering

Table 9.2: Elemental composition of the nanorods formed during the sintering of monomodal SiC

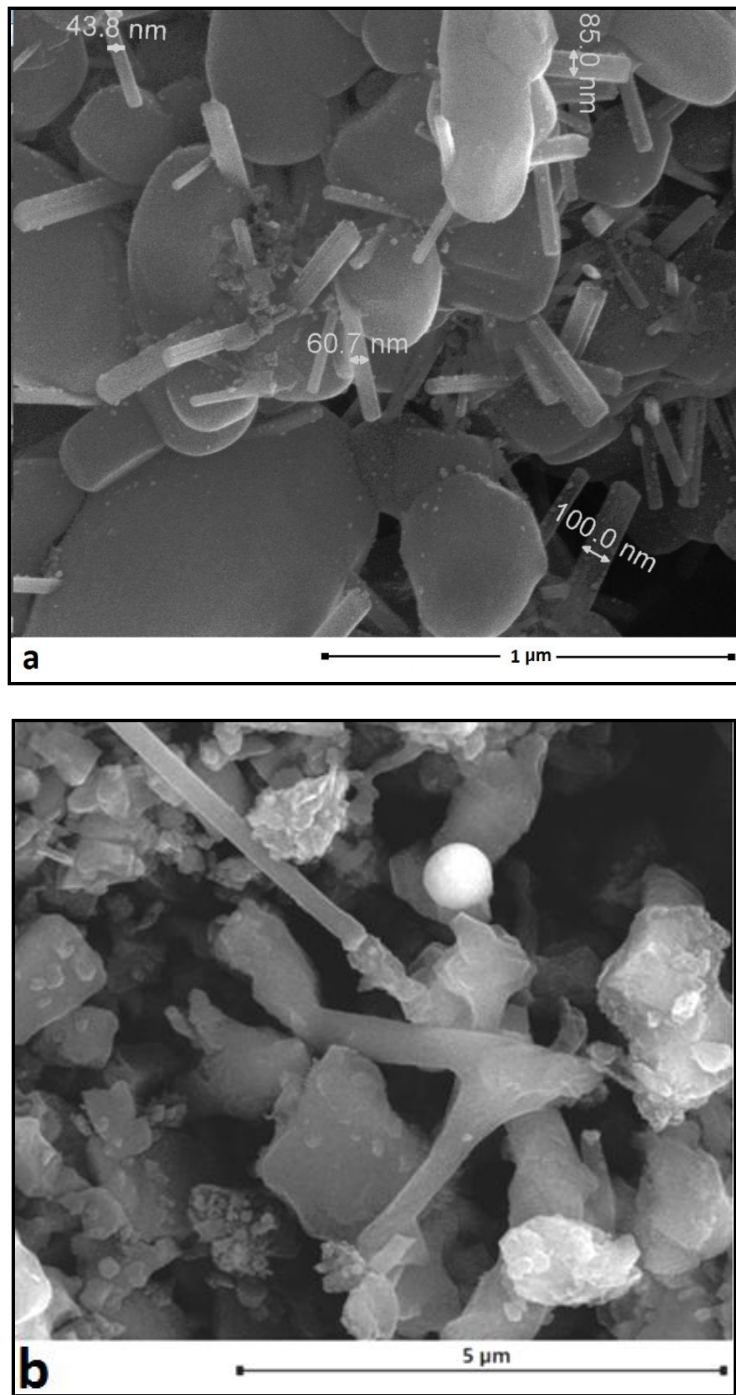


Figure 9.1: Nanorod formation in monomodal AlN at 1100 °C (a) and monomodal SiC at 1550 °C (b).

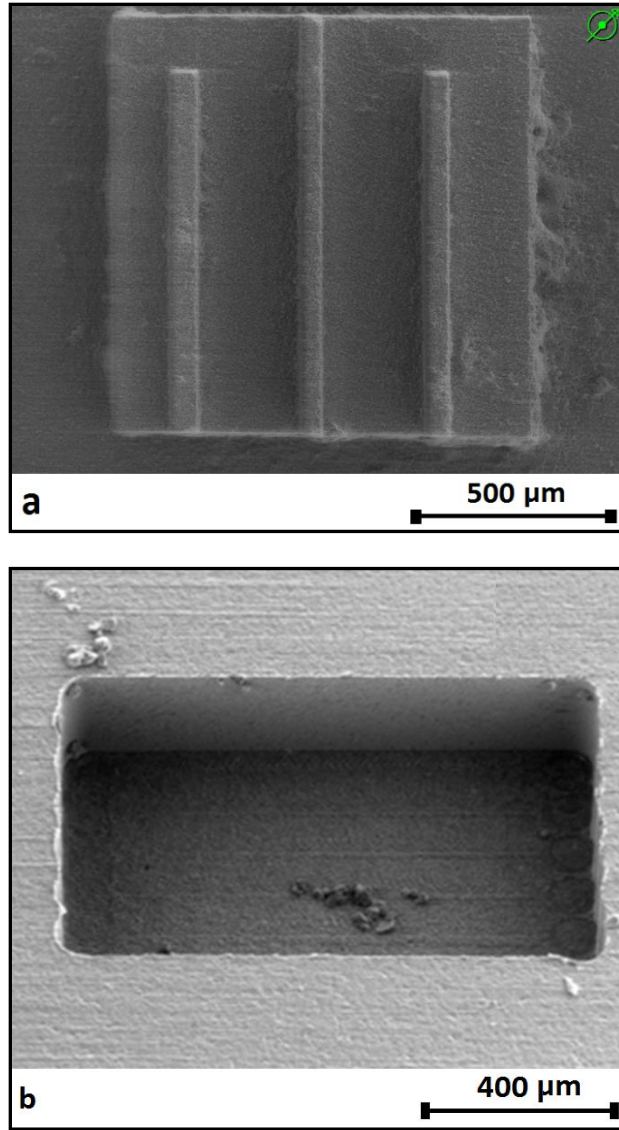


Figure 9.2: Micromachined green bimodal μ -n AlN samples

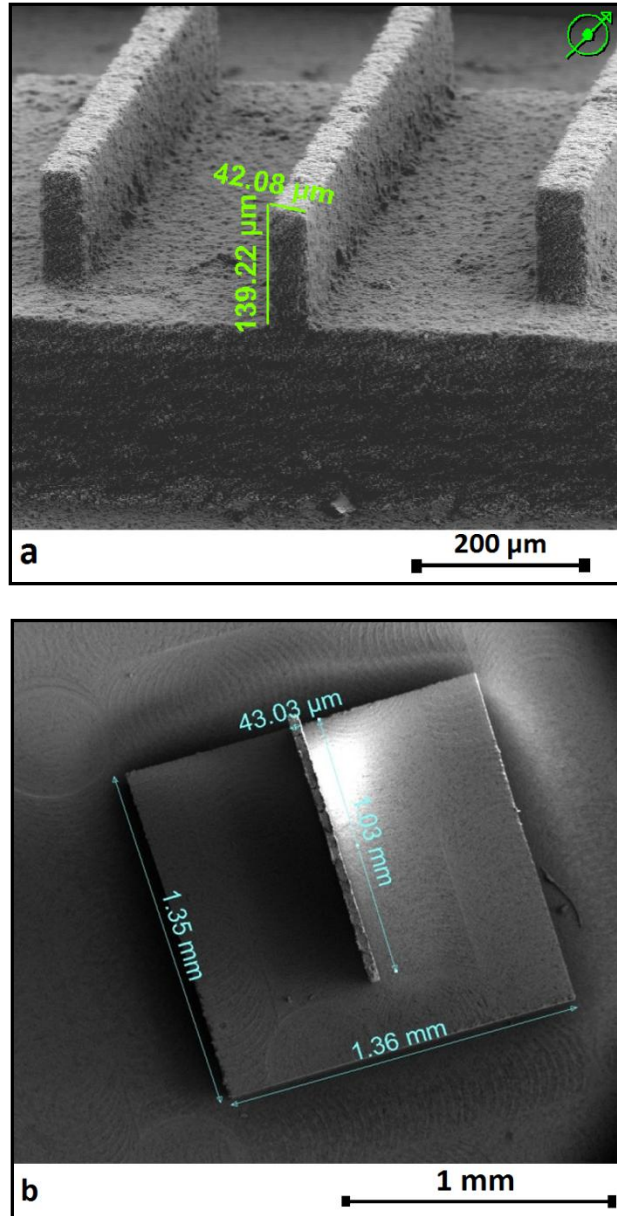


Figure 9.3: Sintered micromachined bimodal μ -n AlN samples

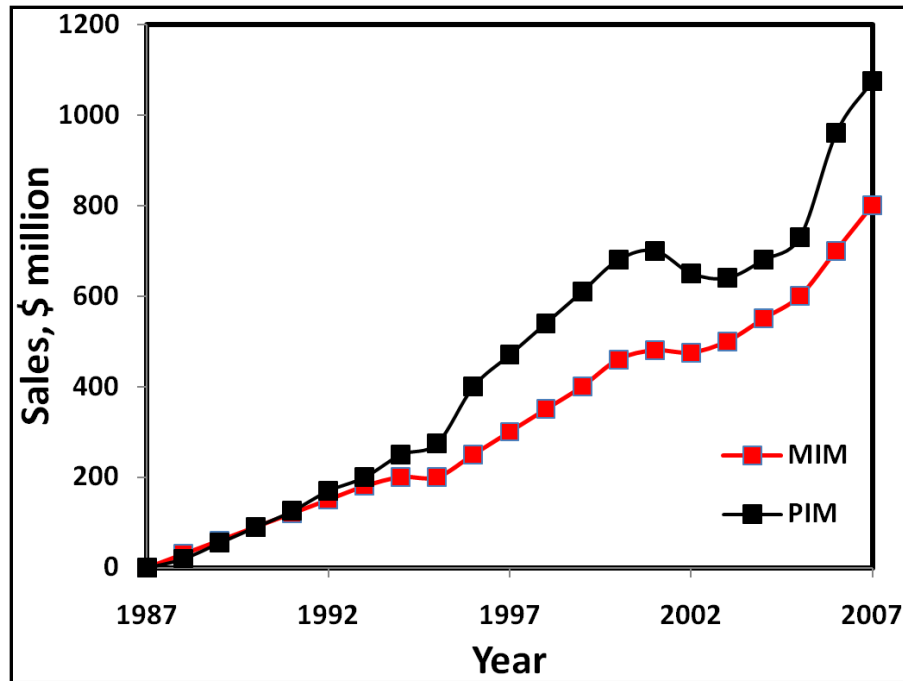


Figure 9.4: Global market for powder injection molded products

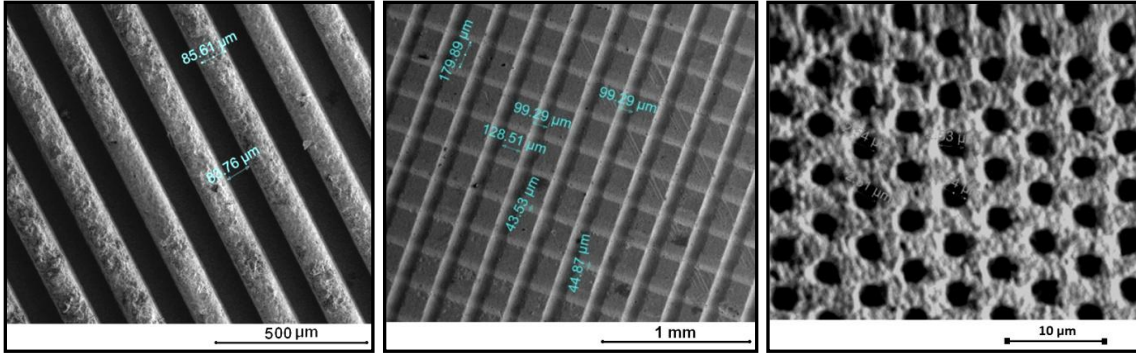


Figure 9.5: SEM micrographs of sintered microchannels (a), microgrids (b) and microwells (c) net-shaped by PIM of bimodal μ -n BaTiO_3

Table 9.1: Elemental composition of nanorods formed during the monomodal AlN sintering

Element	Wt.%	At.%
Al	59.46	58.89
N	13.86	26.44
O	3.73	6.23
Y	22.15	6.66
C	0.8	1.78

Table 9.2: Elemental composition of nanorods formed during the sintering of monomodal SiC

Element	Wt.%	At.%
Si	63.03	49.82
C	19.29	35.65
Al	2.99	2.46
N	3.96	6.28
O	2.73	3.78
Y	8.00	2.00

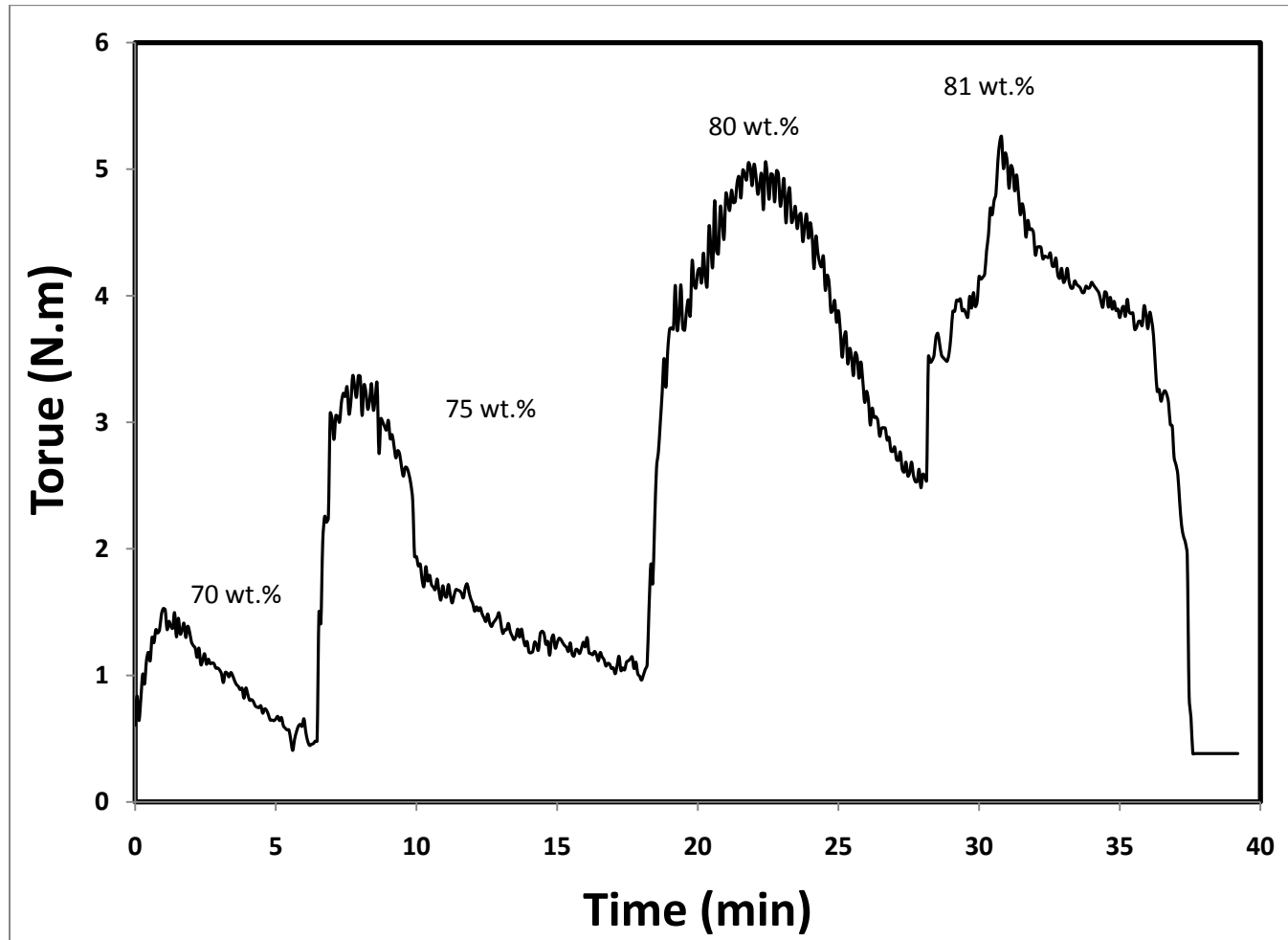
Appendix A

Torque Rheometry

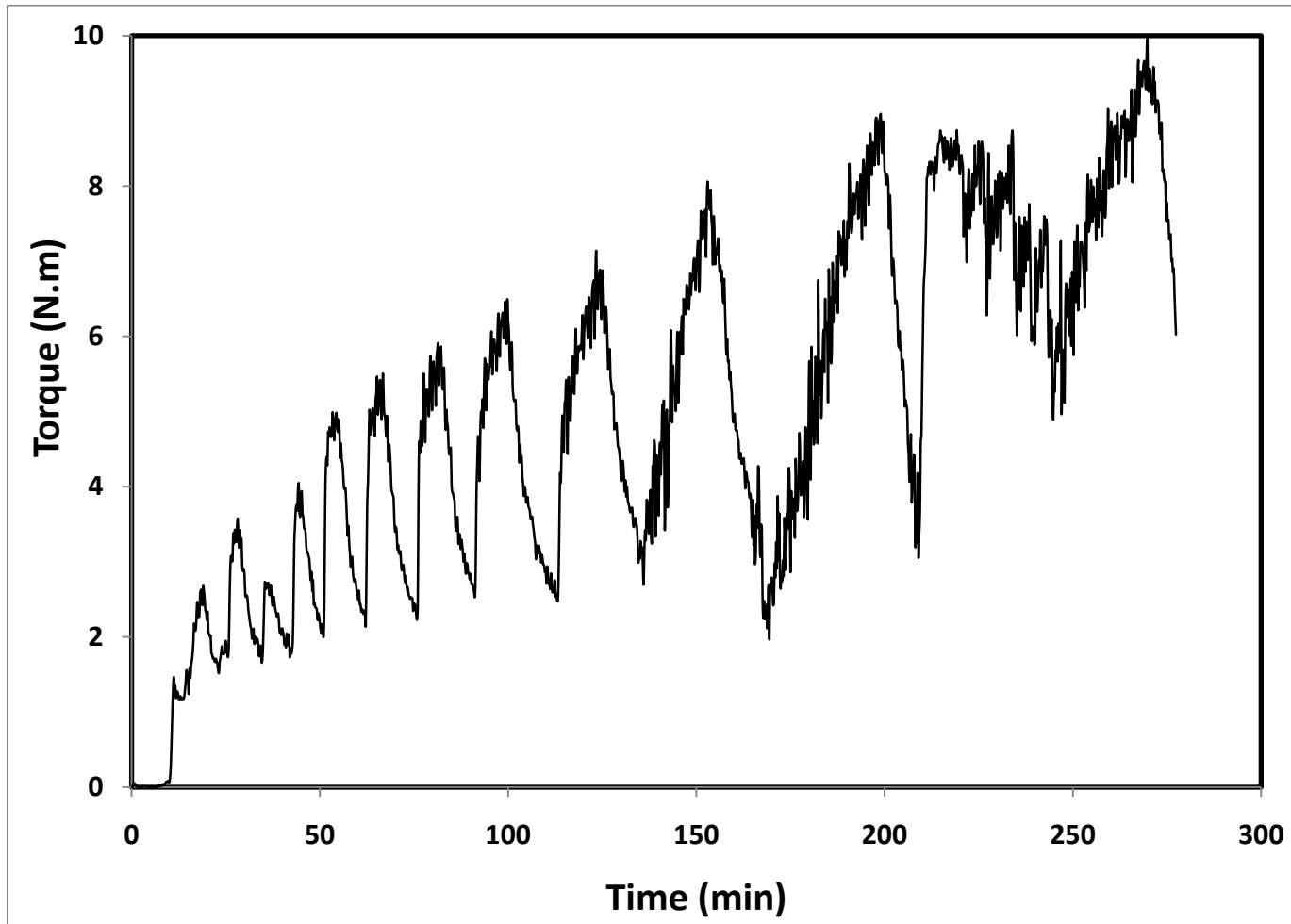
PIM of SiC and AlN commences with the preparation of the powder-polymer mixture. The homogeneity and applicability of this mixture is dependent on the powder/polymer ratio. Increasing the powder/polymer ratio will result in an increase in the mixture viscosity, leading to potential difficulties during the molding stage. On the other hand, too much polymer could result in distortion and incomplete densification. Thus, it is required to regulate the powder-polymer ratio in such a way that the powder fraction will be as high as possible to obtain a mixture that will still be homogenous and easy to process. The maximum powder-polymer ratio that will result in a homogeneous fluid is designated with the term *critical solids loading* in the PIM industry.

A torque rheometer (Intelli-Torque Plasti-Corder from CW Brabender) was used to determine the critical solids loading of the SiC and AlN powder-polymer mixtures.. The mixing conditions including zone temperatures (160 °C), screw speed (40 rpm), powder addition rate (1 wt.%) were kept the same for all the torque rheometry trails (Appendix A1-A13). With nanoparticle addition, a bimodal powder mixture showing the maximum critical solids loading was determined and used in further processing steps.

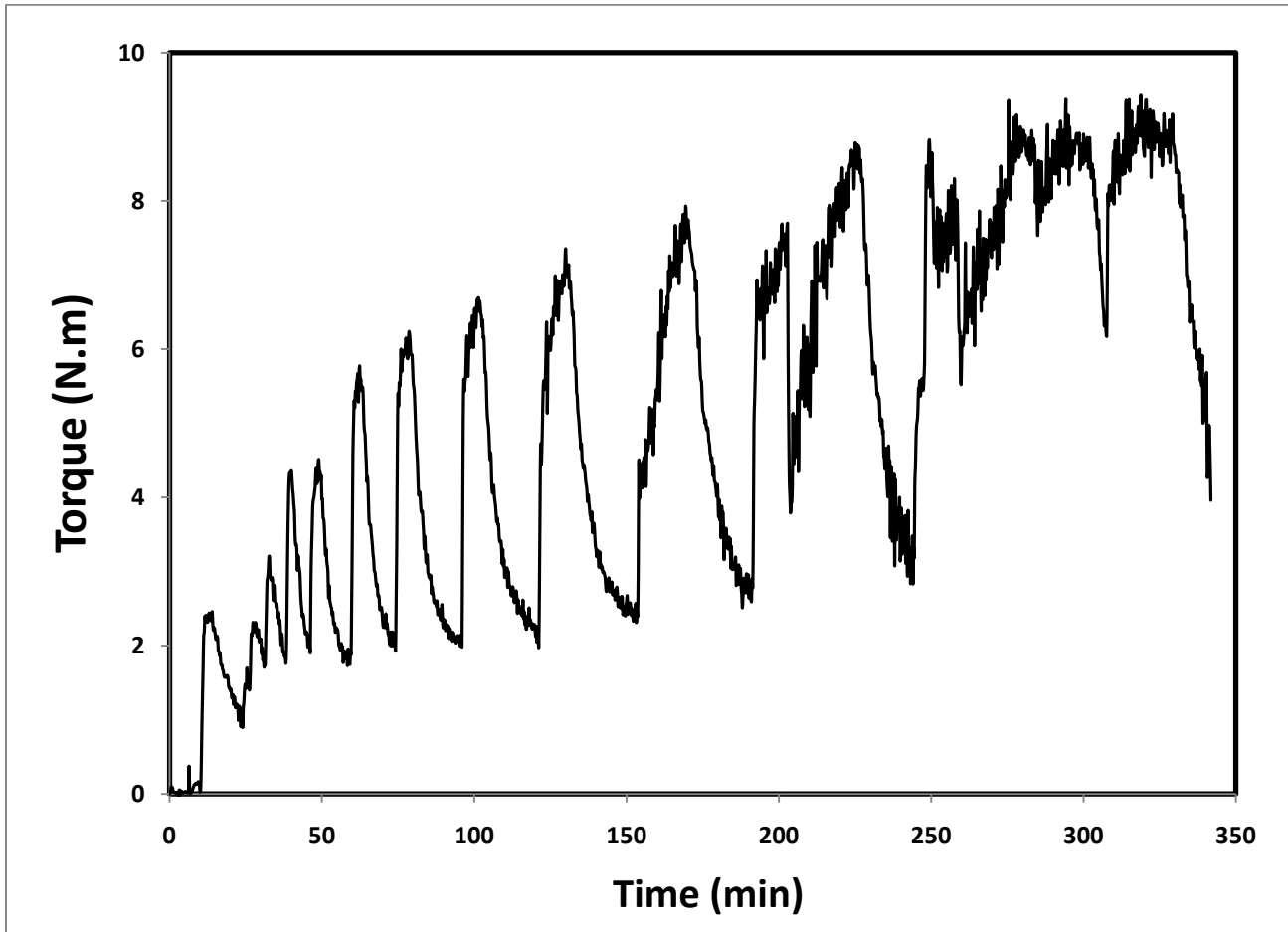
A1: Monomodal - 100% μ -SiC



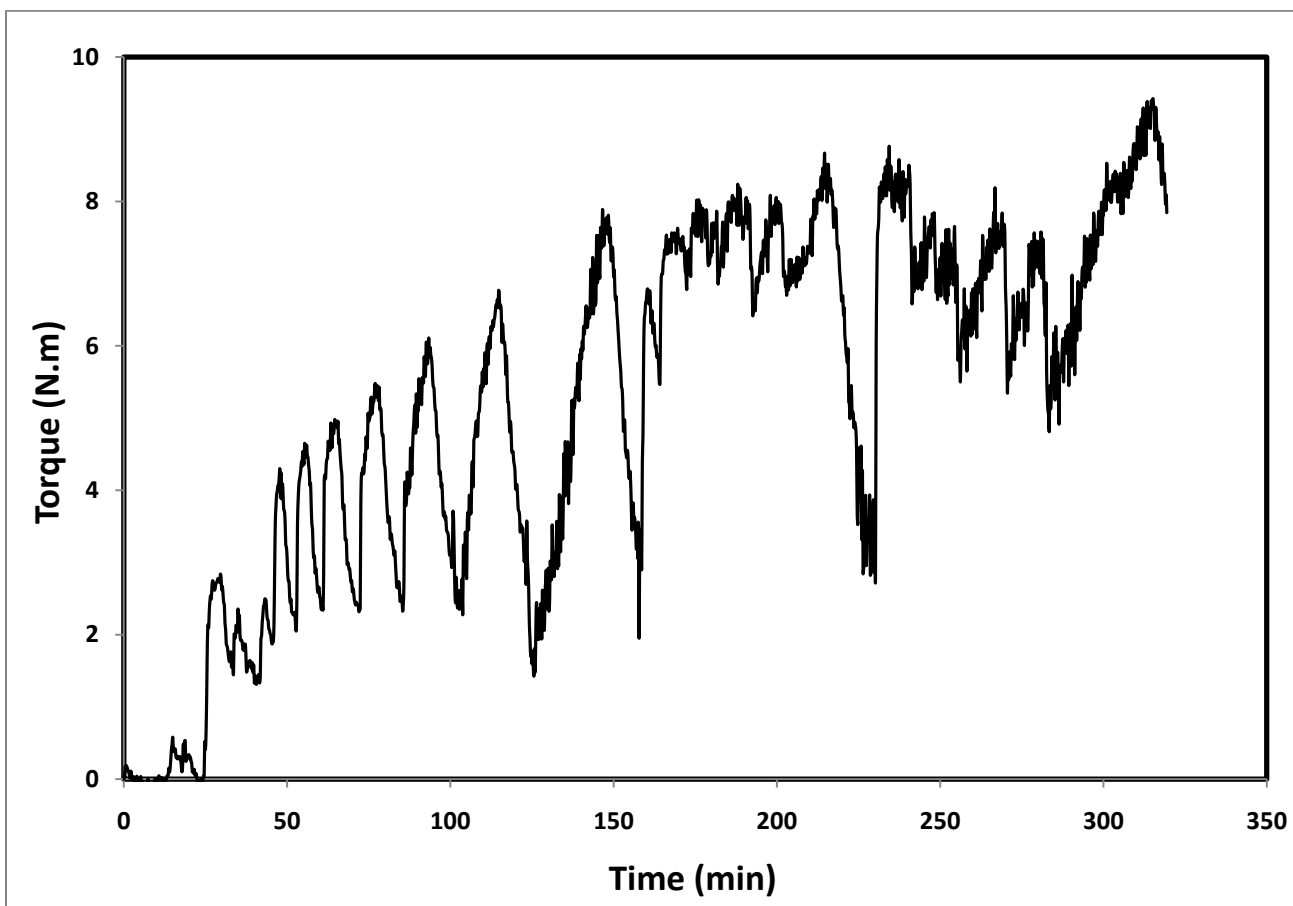
A2: Bimodal - 95% μ -SiC - 5 wt. % n-SiC



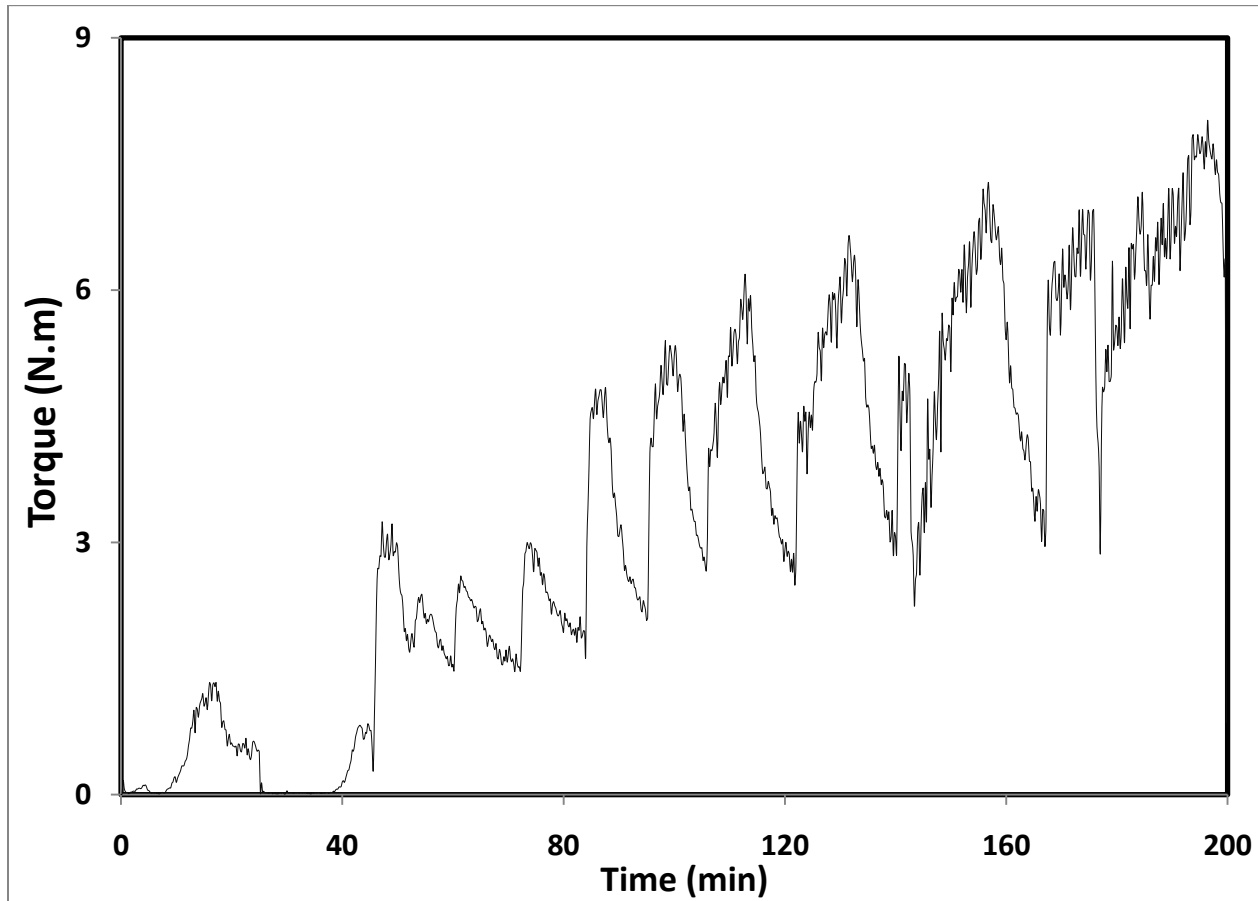
A3: Bimodal - 90% μ -SiC - 10 wt. % n-SiC



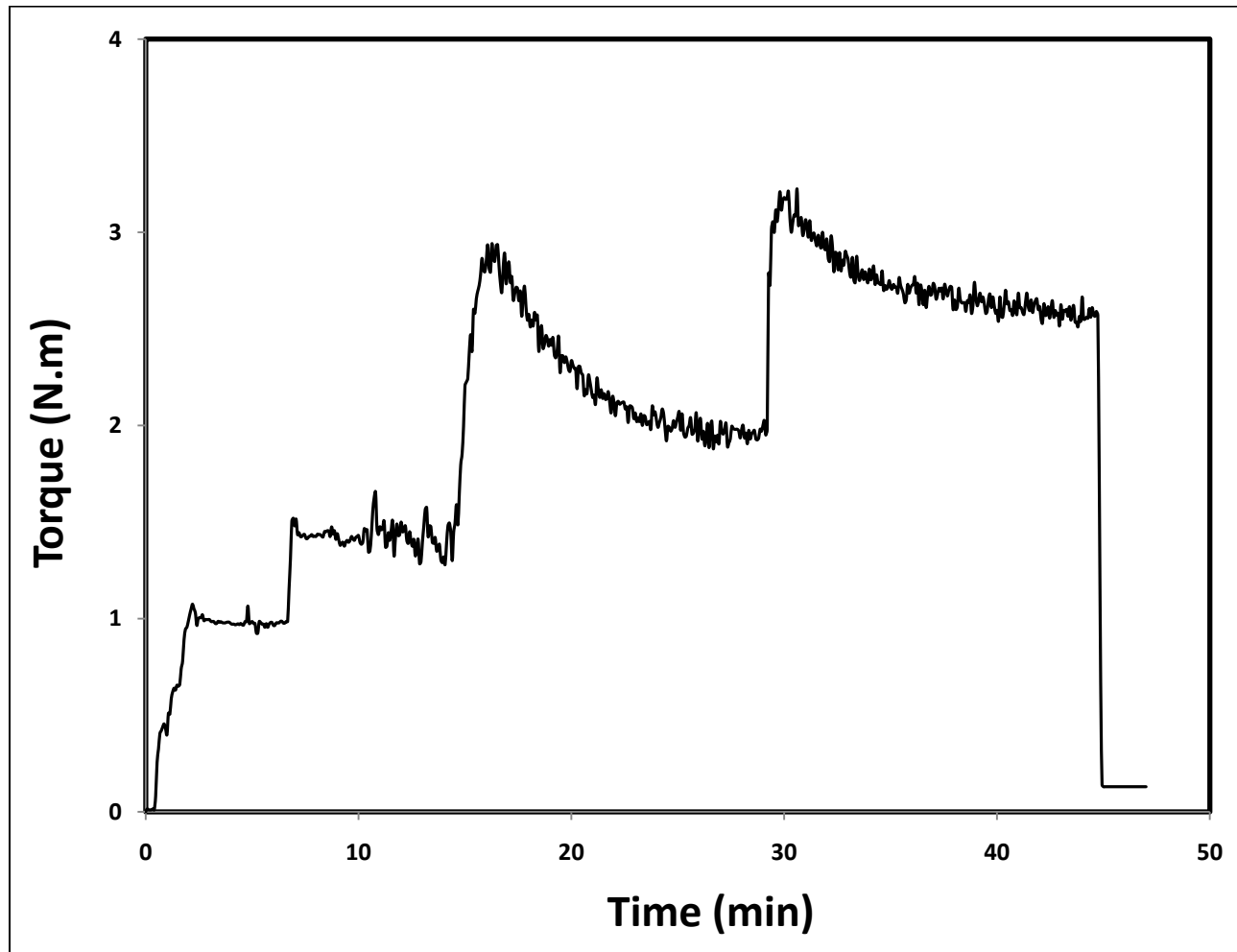
A4: Bimodal - 87% μ -SiC - 13 wt.% n-SiC



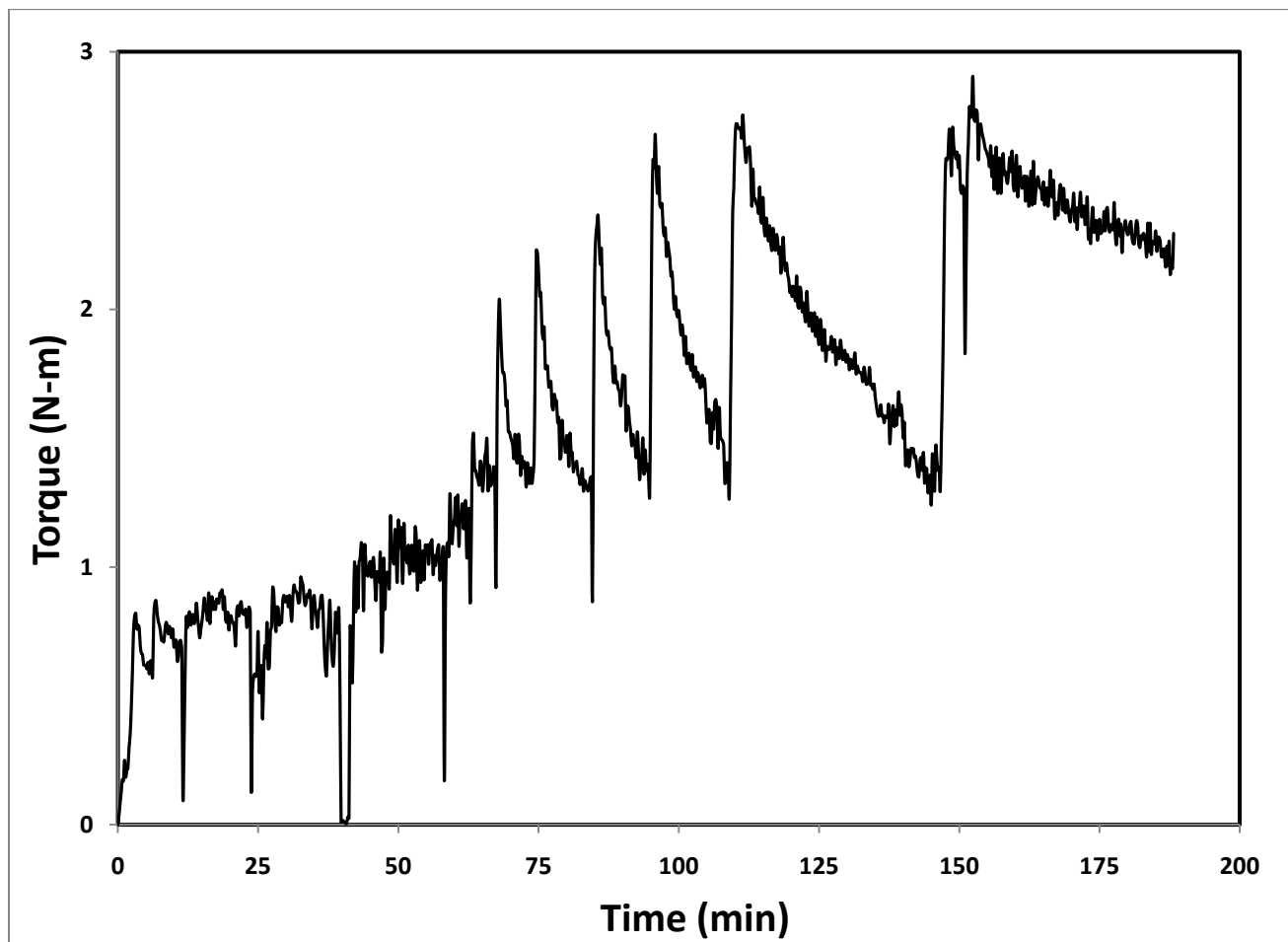
A5: Bimodal - 85% μ -SiC - 15 wt.% n-SiC



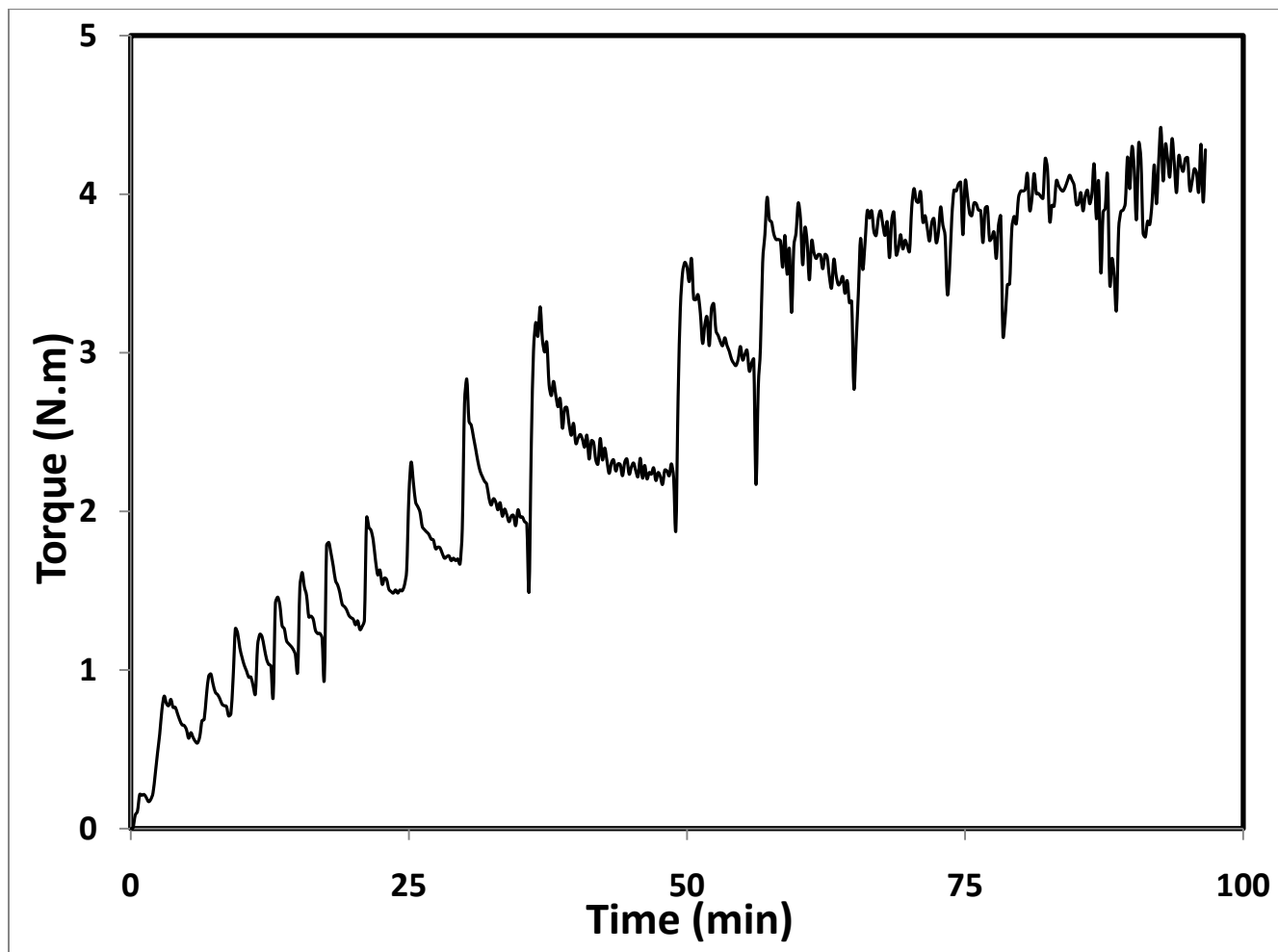
A6: Monomodal - 100% μ -AlN



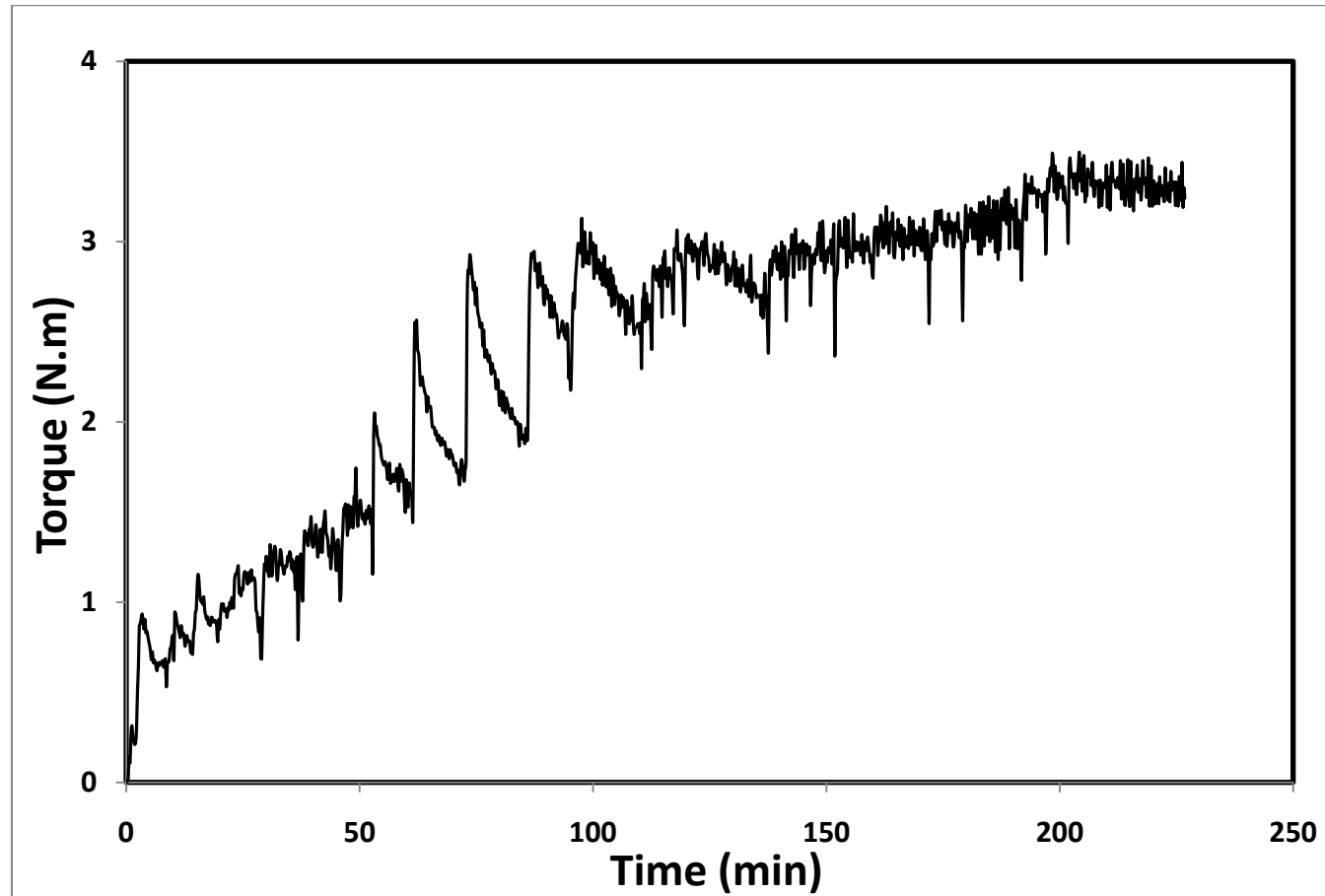
A7: Bimodal - 95% μ -AlN - 5 wt.% n-AlN



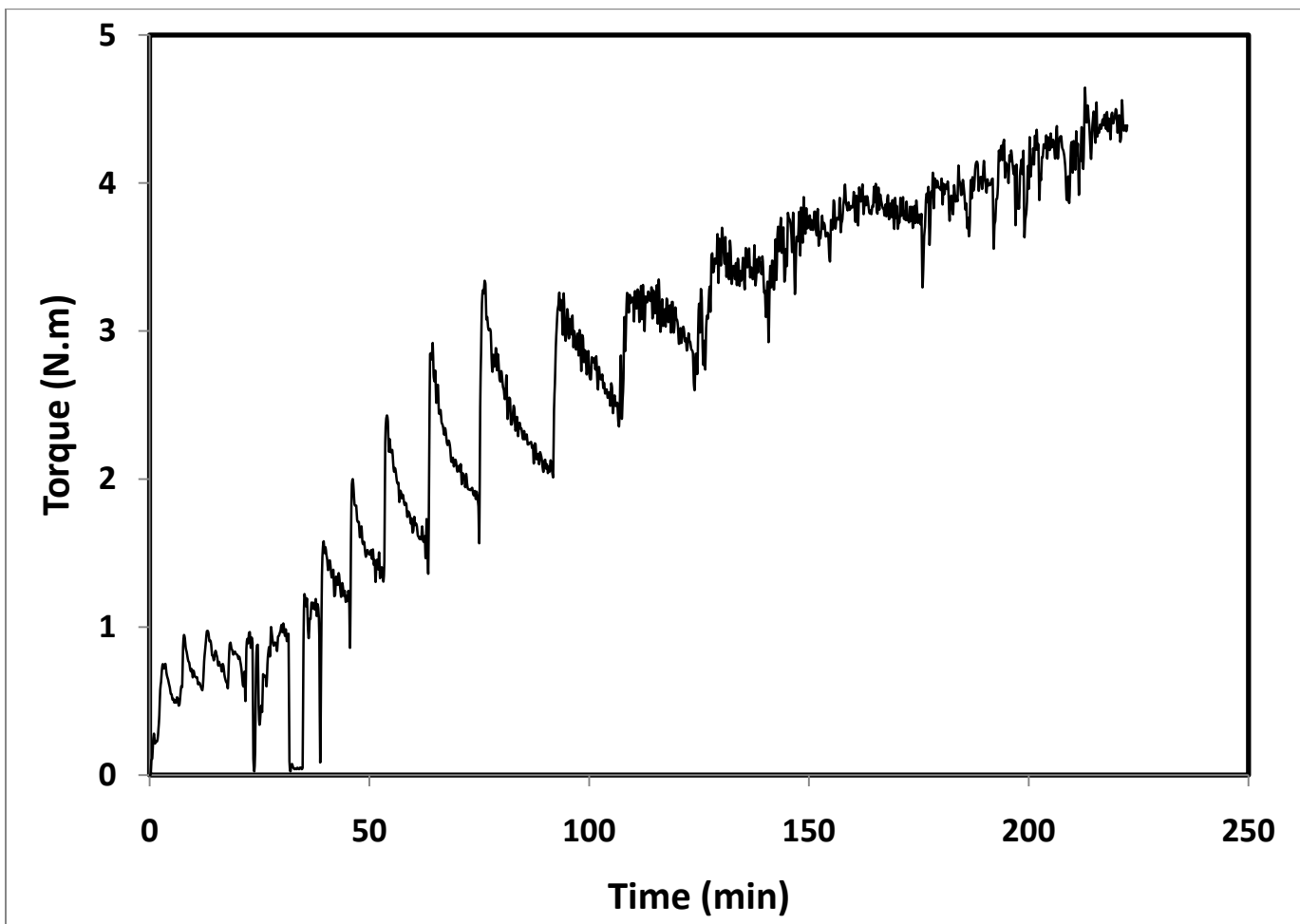
A8: Bimodal - 92% μ -AlN - 8 wt.% n-AlN



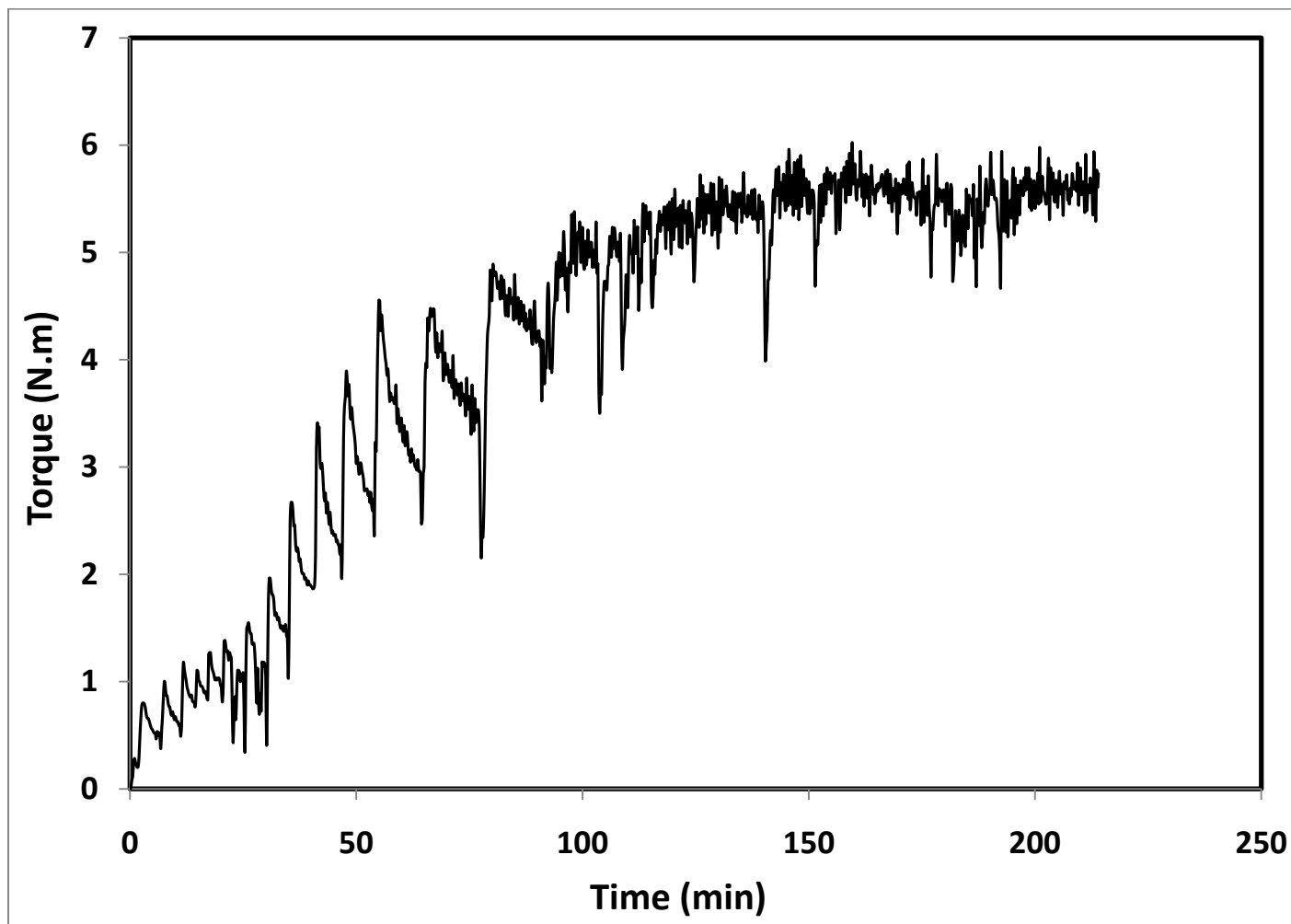
A9: Bimodal - 90% μ -AlN – 10 wt.% n-AlN



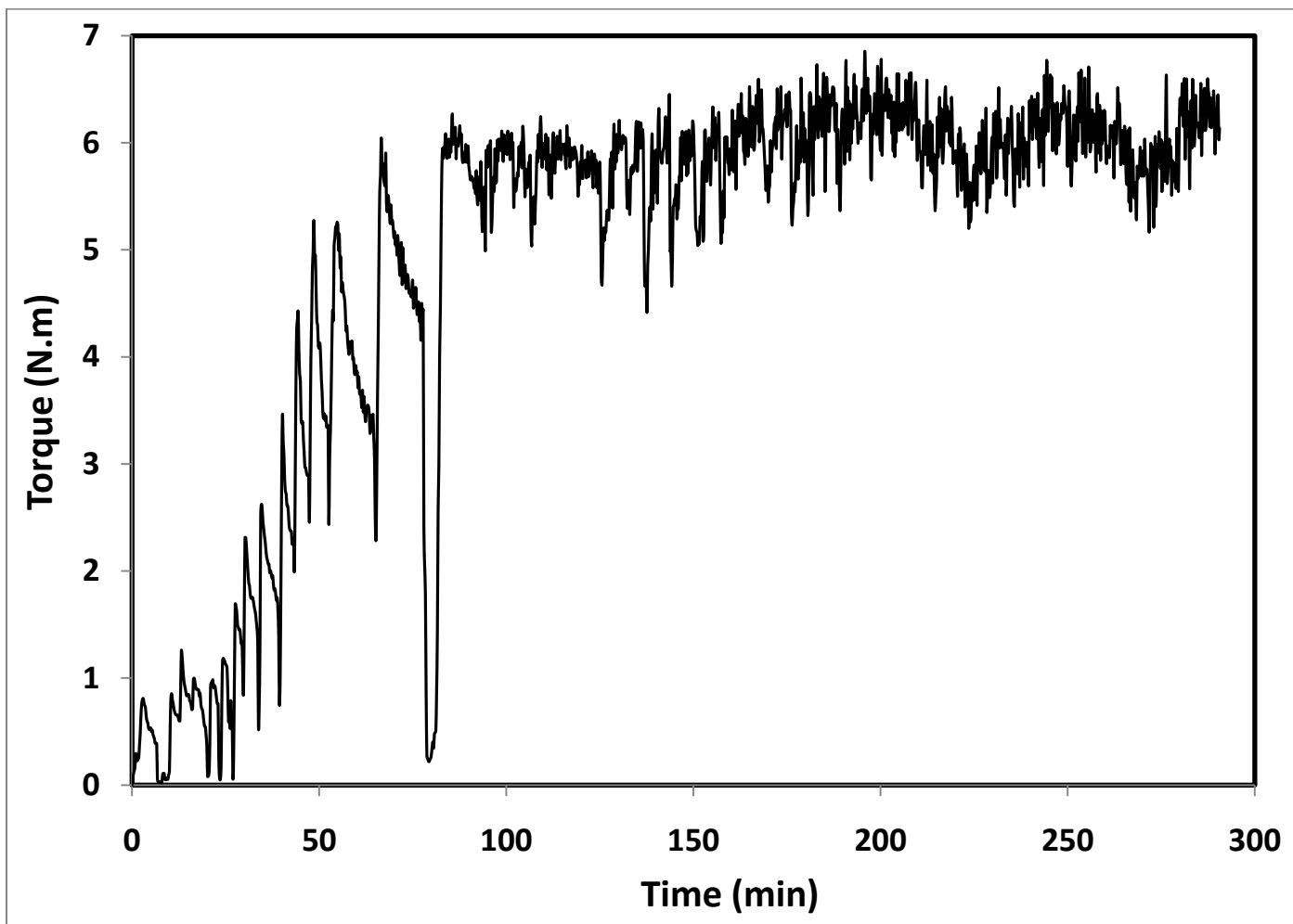
A10: Bimodal - 87% μ -AlN - 13 wt.% n-AlN



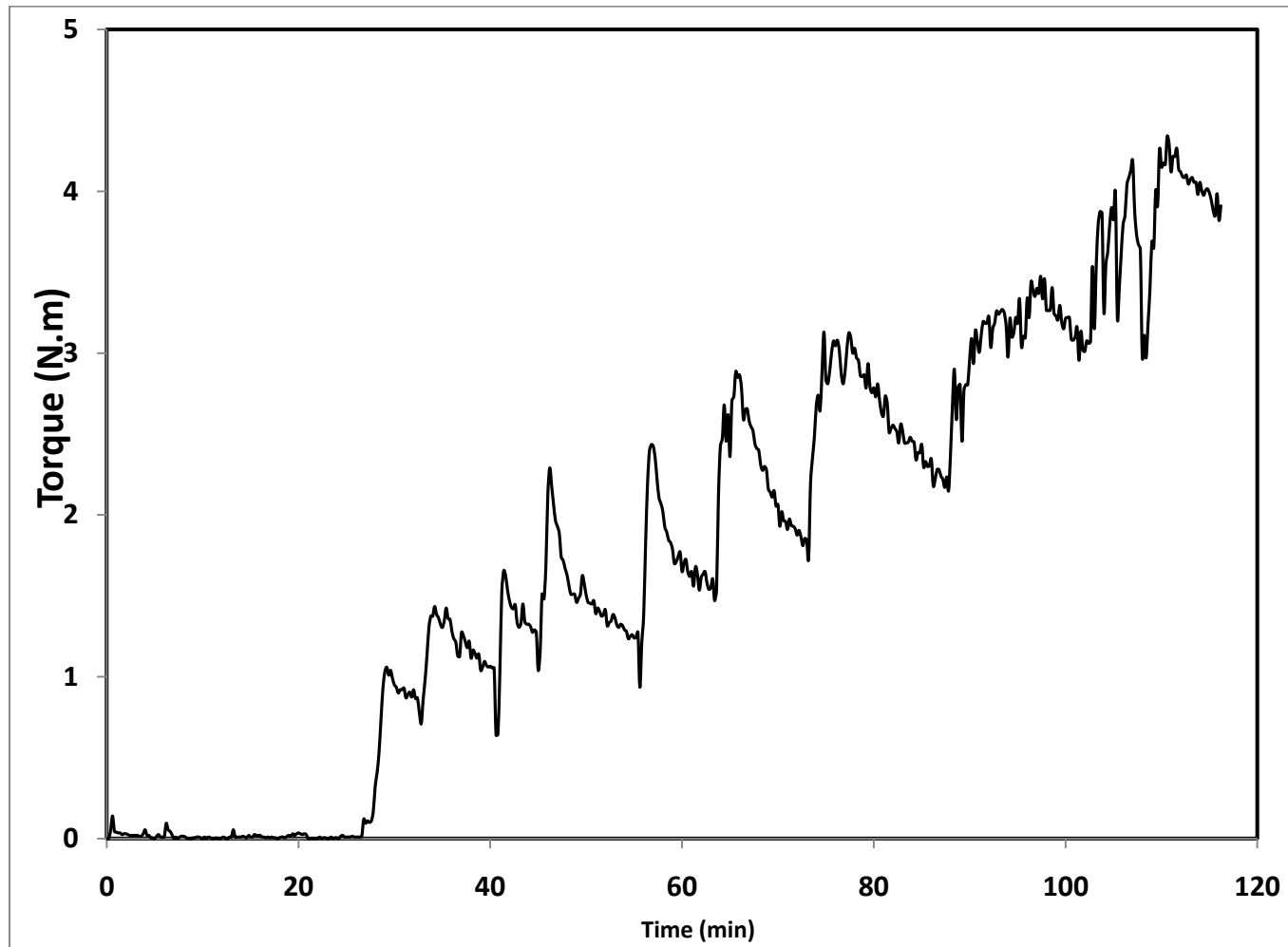
A11: Bimodal - 85% μ -AlN - 15 wt.% n-AlN



A12: Bimodal - 82% μ -AlN - 18 wt.% n-AlN



A13: Bimodal - 80 wt. % μ -AlN - 20 wt. % n-AlN



Appendix B

Mixing Scale-Up by Twin-Screw Extrusion

The scaling up of powder-polymer mixture (feedstock) with a solids loading < critical solids loading was performed using twin-screw extrusion. All the scale-up were conducted in a co-rotating 27 mm twin screw extruder (Entek Extruders). The process specifications for all the powder-polymer mixture scale-up are listed in the following table,

Table B.1: Conditions used for scaling up of all powder-binder formulations

Extruder Specifications	μ-SiC	μ-AlN	μ-n SiC	μ-n AlN
Screw Diameter (Co-Rotating)	27 mm			
L/D	40			
Flight Depth	4.3			
Barrels/Zones involved	10			
Zone Temperature	160 °C			
Screw Speed	180	260 rpm		
Extrusion Rate	20 lb/hr	30 lb/hr		
Cooling System	Air-cooled conveyor belt system			

Appendix C1

Properties of Monomodal μ - SiC Feedstock

Feedstock composition		
Materials	Particle size	Weight (%)
SiC	0.7 μ m	72
AlN	20 nm	8
Y ₂ O ₃	50 nm	8
Multi-component binder system	-	20

Client	Valmikanathan Onbattuveli
Company	Oregon State University
Address	Hall Corvallis, OR United States
Sample Received	2/25/2009
Sample Source	Oregon State University
Report Prepared	3/4/2009
Prepared By	
Title	Engineer
Issued By	
Title	Operations Manager

DatapointLabs is accredited by the American Association for Laboratory Accreditation (A2LA Certificate # 1242.01), and maintains a quality system in accordance with ISO/IEC 17025. Any opinions or interpretations expressed in this report are outside the scope of the accreditation.

The results in this report relate only to the items tested. This report shall not be reproduced except in full without the written approval of DatapointLabs.

DatapointLabs cannot be held liable under any circumstances for damages arising out of the use of this information or for claims in excess of that originally paid for the testing. DatapointLabs disclaims all other warranties, either express or implied, including implied warranties of merchantability or fitness for a particular purpose.



<http://www.datapointlabs.com>

95 Brown Road, Ithaca, NY 14850
Phone: 607-266-0405 Fax: 607-266-0168
Toll-Free (U.S.): 1-888-328-2422

This data is available in True Digital format



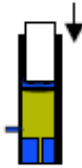
C-MOLD/Moldflow TestPak™ Results

< 14898.21000.udb

Analysis	Property & T-CODE	Value	Units
Filling & Cooling	Cross/WLF Model (01313):		
	n	0.15861	
	τ'	2.808E+04	Pa
	D1	1.741E+18	Pa*s
	D2	263	K
	D3	0	K/Pa
	A1	37.73	
	A2	51.60	K
	Juncture Loss Constants (01360):		
	C1		Pa^(1-C2)
	C2		
	Melt Density (01000)	1852	kg/m ³
	Melt Specific Heat (01100)	1204	J/kg*K
	Melt Thermal Conductivity (01200)	2.445	W/m*K
	Transition Temperature (01500)	325	K
	Specific Heat Table (01101)	See Page 7	
	Thermal Conductivity Table (01201)	See Page 8	
Post-Filling	Two-Domain Tait PVT Model (01004):		
	b5	3.440E+02	K
	b6	1.050E-07	K/Pa
	b1m	5.154E-04	m ³ /kg
	b2m	3.087E-07	m ³ /kg*K
	b3m	2.832E+08	Pa
	b4m	5.235E-03	1/K
	b1s	5.031E-04	m ³ /kg
	b2s	1.910E-07	m ³ /kg*K
	b3s	3.719E+08	Pa
	b4s	6.730E-03	1/K
	b7	1.229E-05	m ³ /kg
	b8	6.162E-02	1/K
b9	8.500E-09	1/Pa	
Shrink / Warp - Uncorrected Stress	Anisotropic Mechanical Properties (01602)		
	Modulus E ₁ (flow direction)		MPa
	Modulus E ₂ (transverse direction)		MPa
	Poisson's ratio ν_{12}		
	Poisson's ratio ν_{23}		
	Shear Modulus G		MPa
	Anisotropic Thermal Expansion (01702)		
CLTE α_1 (flow direction)		x 10E-6/°C	
CLTE α_2 (transverse direction)		x 10E-6/°C	

TestPaks™ is a trademark of Datapoint Labs. C-MOLD and Moldflow are trademarks of Moldflow Corporation.

Viscosity



Method	ASTM D 3835: 2008 Determination of Properties of Polymeric Materials by Means of a Capillary Rheometer	
Instrument	Goettfert Rheograph 2003 Capillary Rheometer	
Specimen	type drying other preparation	pellets none none
Parameters	initial pressure barrel diameter die entry angle die inner diameter die length preheating time	0 MPa 12 mm 180 ° 1 mm 20 mm 6 min
Data Correction	Rabinowitsch	
Precision	temperature die inner diameter die length	+/- 0.1 °C +/- 0.0089 mm +/- 0.025 mm
Uncertainty	per standard	

Polymer rheology characterizes the complex flow behavior of plastics. A capillary rheometer measures viscosity as a function of temperature and shear rate. The Goettfert rheometer utilizes direct measurement of melt pressures through a side mounted pressure transducer.

Data are modeled using empirical or semi-empirical equations.

Viscosity Data

140 °C		150 °C		160 °C	
Shear Rate s ⁻¹	Viscosity Pa·s	Shear Rate s ⁻¹	Viscosity Pa·s	Shear Rate s ⁻¹	Viscosity Pa·s
12	5627.90	12	6145.48	12	6411.75
88	911.47	44	1812.87	50	1705.77
121	632.00	93	1108.54	153	668.29
179	548.99	264	443.35	395	276.80
341	328.09	505	249.02	600	170.98
780	201.27	860	177.42	813	180.97
2071	91.40	2010	93.90	2176	81.10
4174	50.47	4423	47.22	4909	39.44
9683	27.69	12356	21.05		
22438	13.42	57574	4.68		

Cross/WLF Model (C-MOLD, Moldflow)

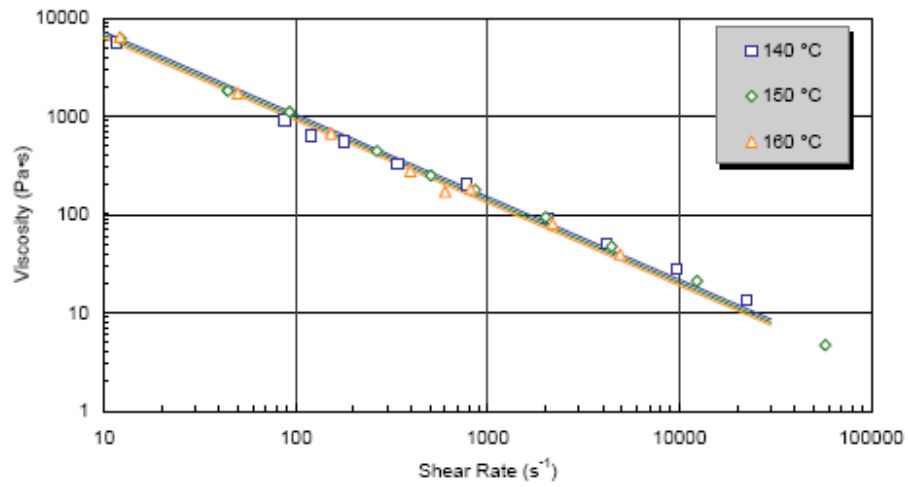
$$\eta(T, \dot{\gamma}) = \frac{\eta_0(T)}{1 + \left(\frac{\eta_0 \dot{\gamma}}{\tau^*}\right)^n}, \text{ where}$$

$$\eta_0(T) = D_1 \exp\left(-\frac{A_1(T - D_2)}{A_2 + (T - D_2)}\right)$$

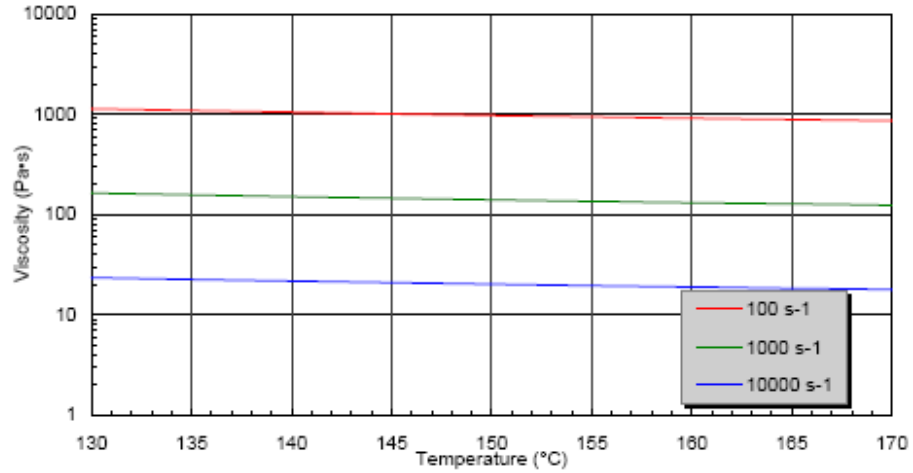
Coefficients (SI units)

n	0.15861
τ^*	28082.455
D1	1.74E+18
D2	263
A1	37.73
A2	51.6

Viscosity vs Shear Rate



Viscosity vs Temperature



Specific Heat



Method	Based on ASTM E1269: 2005 Determining Specific Heat Capacity by Differential Scanning Calorimetry	
Instrument	Perkin Elmer DSC7	
Specimen	type drying other preparation	pellets none out from pellet
Parameters	purge gas purge gas purity purge gas rate cooling rate initial temperature final temperature equilibration times sample weight sample pans	N2 99.99 % 25 ml/min 20 °C/min 160 °C 20 °C 4 min 9.99 mg Al, volatile
Calibration Standards	temperature heat flow specific heat	In, Zn In sapphire
Notes: Two peaks were observed. Transition analysis temperatures and specific heat data are for larger peak.		

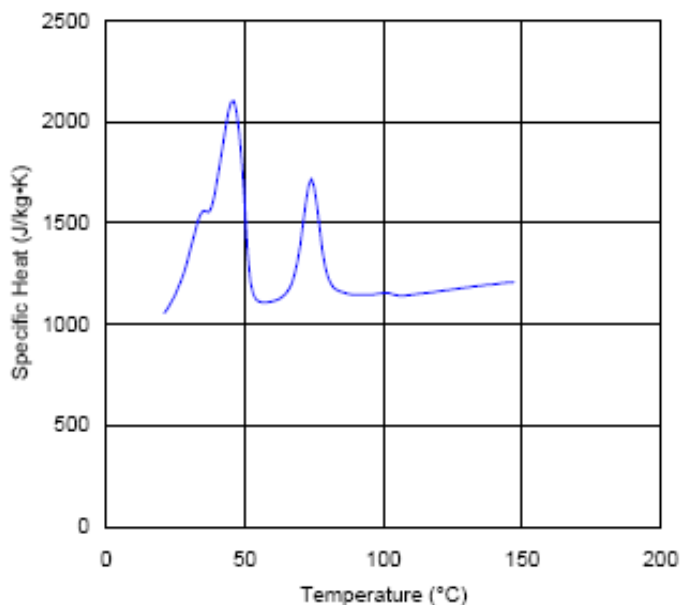
Heat capacity is a thermodynamic quantity and is a measure of the amount of heat retained by the material. The DSC can measure this property over a range of temperatures and in both solid and melt states.

Transition Analysis

extrapolated onset	52 °C
peak	46 °C
extrapolated end	33 °C

Specific Heat Data

Temp °C	Cp J/kg·K
150	1200
101	1156
57	1108
46	2105
23	1098
31	1402
30	1350



Thermal Conductivity

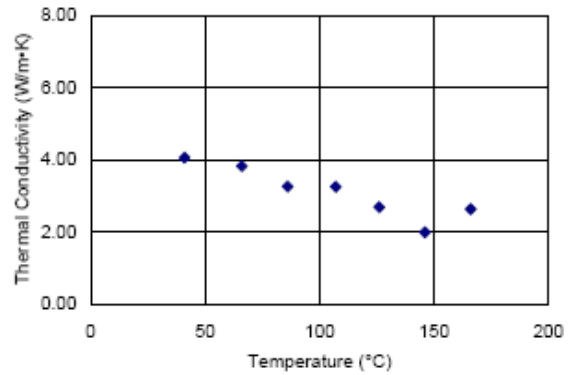


Method	ASTM D 5930: 2001 Thermal Conductivity of Plastics by Means of a Transient Line-Source Technique	
Instrument	K-System II Thermal Conductivity System	
Specimen	type drying other preparation	pellets none none
Parameters	calibration material probe constant probe length loading temperature initial temperature final temperature probe voltage acquisition time	60,000 cstk PDMS 0.743 50 mm 140 °C 160 °C 30 °C 4 V 45 s
Uncertainty	per standard	

Thermal conductivity is a measure of the rate of heat conduction of the material. It is a critical property for heat transfer calculations. The line-source method measures thermal conductivity in both melt and solid state.

Thermal Conductivity Data

Temp °C	k W/m·K
166	2.639
146	1.997
126	2.698
107	3.255
86	3.263
66	3.835
41	4.072



PVT



Method	Non-standard. Pressure-specific volume-temperature measurements using high-pressure dilatometry	
Instrument	Gnomix PVT apparatus	
Specimen	type drying other preparation	pellets 4 hrs, 70°C/vacuum see note below
Parameters	solid density method immersion liquid pVT confining fluid max temperature measurement type heating rate	ASTM D792 water mercury 160 °C isothermal heating scan approx. 3 °C/min

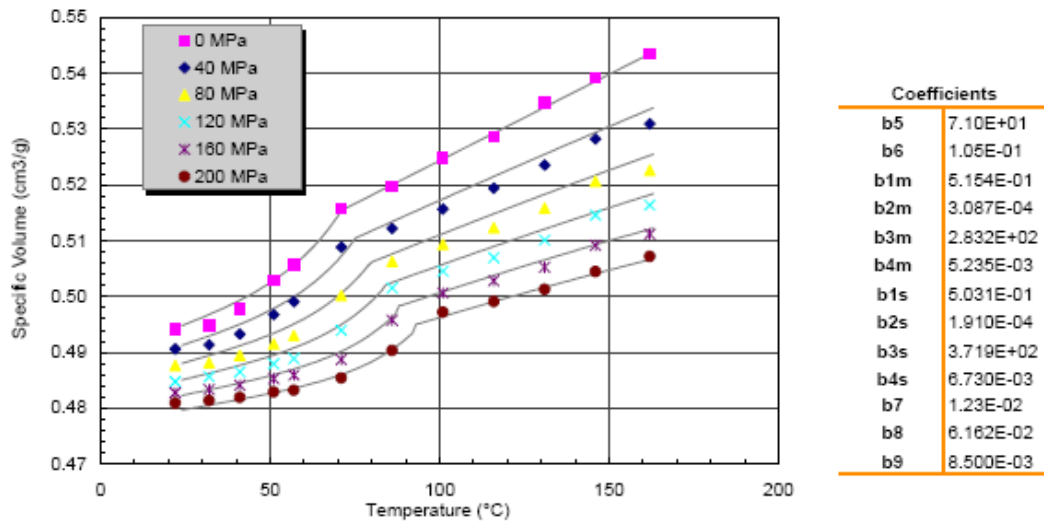
PVT data are equation-of-state thermodynamic properties that describe the compressibility and volumetric expansion of the material. Dilatometry measures the change in volume of a specimen subjected to different temperatures and pressures.

Notes: PVT specimen was cut from a plug that was manufactured by Datapoint Labs from pellets supplied by the client.

Pressure-Volume-Temperature Data

Specific Volume cm ³ /g						
Temp °C	Pressure MPa					
	0	40	80	120	160	200
22	0.4941	0.4906	0.4876	0.4847	0.4828	0.4809
32	0.4949	0.4913	0.4881	0.4856	0.4833	0.4814
41	0.4978	0.4933	0.4895	0.4865	0.4841	0.4819
51	0.5029	0.4988	0.4915	0.4880	0.4853	0.4829
57	0.5057	0.4991	0.4930	0.4889	0.4859	0.4832
71	0.5157	0.5089	0.5002	0.4940	0.4887	0.4854
88	0.5197	0.5122	0.5063	0.5016	0.4958	0.4903
101	0.5248	0.5157	0.5094	0.5046	0.5006	0.4972
116	0.5287	0.5194	0.5124	0.5070	0.5028	0.4991
131	0.5347	0.5236	0.5159	0.5102	0.5053	0.5013
146	0.5392	0.5283	0.5207	0.5146	0.5092	0.5045
162	0.5436	0.5310	0.5227	0.5164	0.5112	0.5072

Modified Two-Domain Tait Model (C-MOLD, Moldflow)



Modified Two-Domain Tait Equation

$$v(T, p) = v_0(T) \left(1 - C \ln \left(1 + \frac{p}{B(T)} \right) \right) + v_t(T, p), T_t(p) = b_5 + b_6 p$$

$$\text{for } T > T_t(p): v_0(T) = b_{1m} + b_{2m}(T - b_5), B(T) = b_{3m} \exp(-b_{4m}(T - b_5)), v_t(T, p) = 0$$

$$\text{for } T < T_t(p): v_0(T) = b_{1s} + b_{2s}(T - b_5), B(T) = b_{3s} \exp(-b_{4s}(T - b_5)), v_t(T, p) = b_7 \exp(b_8(T - b_5) - b_9 p)$$

No-Flow Temperature

	Method	non-standard Moldflow specification; no-flow temperature defined by extrudate flow < 2 mm/min	
	Instrument	Goettfert Capillary Rheometer	
Specimen	type	pellets	
	drying	none	
	other preparation	none	
Parameters	equivalent load	172 kg	
	barrel diameter	12 mm	
	initial pressure	0 MPa	
	test temperature	140 °C	
	dwel time	6 min	
	die inner diameter	1 mm	
	die length	20 mm	
	die entry angle	180 °	

The no-flow temperature provides a measure of the solidification temperature of the melt. During the test, a molten specimen is cooled under constant load; the no-flow temperature is one at which flow ceases to occur.

Results

No-Flow Temperature	66 °C
---------------------	-------

Appendix C2

Properties of Monomodal μ - AlN Feedstock

Feedstock composition		
Materials	Particle size	Weight (%)
AlN	1.1 μm	76
Y_2O_3	50 nm	4
Multi-component binder system	-	20

Client	Valmikanathan Onbattuveli
Company	Oregon State University
Address	Hall Corvallis, OR United States
Sample Received	3/6/2009
Sample Source	Oregon State University
Report Prepared	3/11/2009
Prepared By	
Title	Engineer
Issued By	
Title	Operations Manager

DatapointLabs is accredited by the American Association for Laboratory Accreditation (A2LA Certificate # 1242.01), and maintains a quality system in accordance with ISO/IEC 17025. Any opinions or interpretations expressed in this report are outside the scope of the accreditation.

The results in this report relate only to the items tested. This report shall not be reproduced except in full without the written approval of DatapointLabs.

DatapointLabs cannot be held liable under any circumstances for damages arising out of the use of this information or for claims in excess of that originally paid for the testing. DatapointLabs disclaims all other warranties, either express or implied, including implied warranties of merchantability or fitness for a particular purpose.



<http://www.datapointlabs.com>

95 Brown Road, Ithaca, NY 14850
Phone: 607-266-0406 Fax: 607-266-0168
Toll-Free (U.S.): 1-888-328-2422

This data is available in True Digital format



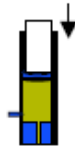
C-MOLD/Moldflow TestPak™ Results

< 14922.21000.udb

Analysis	Property & T-CODE	Value	Units
Filling & Cooling	Cross/WLF Model (01313):		
	n	0.37760	
	τ'	1.178E+02	Pa
	D1	8.777E+10	Pa·s
	D2	263	K
	D3	0	K/Pa
	A1	14.24	
	A2	51.60	K
	Juncture Loss Constants (01360):		
	C1		Pa ^{1-(1-C2)}
	C2		
	Melt Density (01000)	1943	kg/m ³
	Melt Specific Heat (01100)	1201	J/kg·K
	Melt Thermal Conductivity (01200)	2.202	W/m·K
	Transition Temperature (01500)	326	K
	Specific Heat Table (01101)		See Page 7
	Thermal Conductivity Table (01201)		See Page 8
Post-Filling	Two-Domain Tait PVT Model (01004):		
	b5	3.310E+02	K
	b8	1.650E-07	K/Pa
	b1m	4.834E-04	m ³ /kg
	b2m	2.998E-07	m ³ /kg·K
	b3m	2.865E+08	Pa
	b4m	4.818E-03	1/K
	b1s	4.686E-04	m ³ /kg
	b2s	9.700E-08	m ³ /kg·K
	b3s	5.791E+08	Pa
	b4s	1.260E-03	1/K
	b7	1.485E-05	m ³ /kg
	b8	1.101E-01	1/K
b9	2.118E-08	1/Pa	
Shrink / Warp - Uncorrected Stress	Anisotropic Mechanical Properties (01602)		
	Modulus E ₁ (flow direction)		MPa
	Modulus E ₂ (transverse direction)		MPa
	Poisson's ratio ν_{12}		
	Poisson's ratio ν_{23}		
	Shear Modulus G		MPa
	Anisotropic Thermal Expansion (01702)		
	CLTE α_1 (flow direction)		x 10E-6/°C
CLTE α_2 (transverse direction)		x 10E-6/°C	

TestPaks™ is a trademark of Datapoint Labs. C-MOLD and Moldflow are trademarks of Moldflow Corporation.

Viscosity



Method	ASTM D 3835: 2008 Determination of Properties of Polymeric Materials by Means of a Capillary Rheometer	
Instrument	Goettfert Rheograph 2003 Capillary Rheometer	
Specimen	type drying other preparation	pellets none none
Parameters	initial pressure barrel diameter die entry angle die inner diameter die length preheating time	0 MPa 12 mm 180 ° 1 mm 20 mm 6 min
Data Correction	Rabinowitsch	
Precision	temperature die inner diameter die length	+/- 0.1 °C +/- 0.0069 mm +/- 0.025 mm
Uncertainty	per standard	

Polymer rheology characterizes the complex flow behavior of plastics. A capillary rheometer measures viscosity as a function of temperature and shear rate. The Goettfert rheometer utilizes direct measurement of melt pressures through a side mounted pressure transducer.

Data are modeled using empirical or semi-empirical equations.

Viscosity Data

140 °C		150 °C		160 °C	
Shear Rate s ⁻¹	Viscosity Pa·s	Shear Rate s ⁻¹	Viscosity Pa·s	Shear Rate s ⁻¹	Viscosity Pa·s
11	1188.94	11	1024.48	11	1050.83
30	599.80	31	498.11	29	578.00
77	331.05	69	308.43	76	311.42
153	199.41	145	197.27	173	185.99
311	129.81	332	110.43	300	118.03
689	80.88	747	65.39	746	69.71
1434	52.81	1335	47.10	1479	42.53
2932	33.11	2839	31.40	2786	30.47
6869	21.52	6868	18.85	6914	18.72
13113	14.90	13574	12.69	14453	11.49

Cross/WLF Model (C-MOLD, Moldflow)

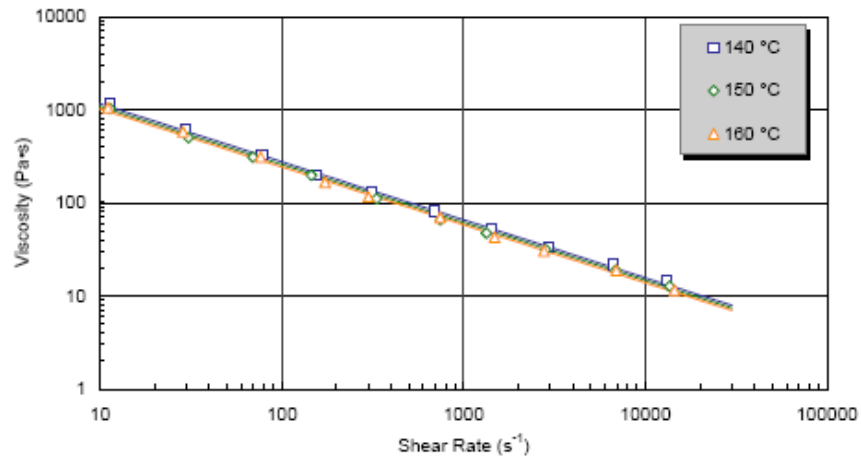
$$\eta(T, \dot{\gamma}) = \frac{\eta_0(T)}{1 + \left(\frac{\eta_0 \dot{\gamma}}{\tau^*} \right)^{1-n}}, \text{ where}$$

$$\eta_0(T) = D_1 \exp \left(- \frac{A_1(T - D_2)}{A_2 + (T - D_2)} \right)$$

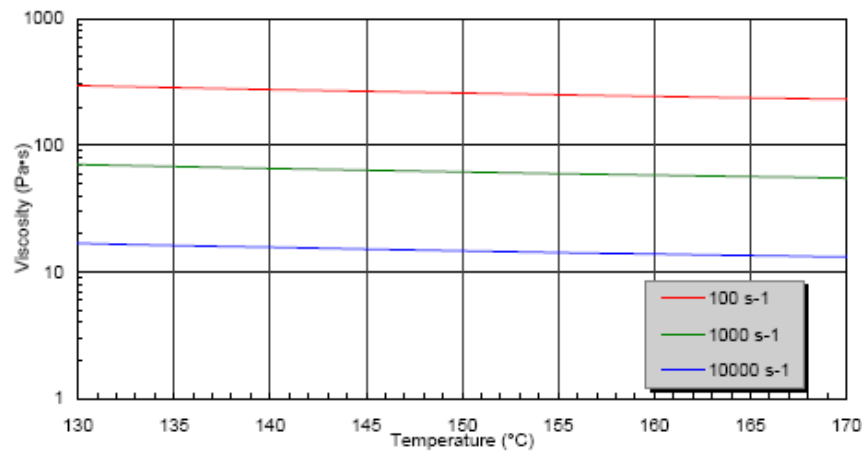
Coefficients (SI units)

n	0.37760
τ*	117.773
D1	8.78E+10
D2	263
A1	14.24
A2	51.8

Viscosity vs Shear Rate



Viscosity vs Temperature



Specific Heat



Method	Based on ASTM E1269: 2005 Determining Specific Heat Capacity by Differential Scanning Calorimetry	
Instrument	Perkin Elmer DSC7	
Specimen	type	pellets
	drying	none
	other preparation	cut from pellet
Parameters	purge gas	N2
	purge gas purity	99.99 %
	purge gas rate	25 ml/min
	cooling rate	20 °C/min
	initial temperature	160 °C
	final temperature	0 °C
	equilibration times	4 min
	sample weight	10.57 mg
	sample pans	Al, volatile
Calibration Standards	temperature	In, Zn
	heat flow	In
	specific heat	sapphire

Heat capacity is a thermodynamic quantity and is a measure of the amount of heat retained by the material. The DSC can measure this property over a range of temperatures and in both solid and melt states.

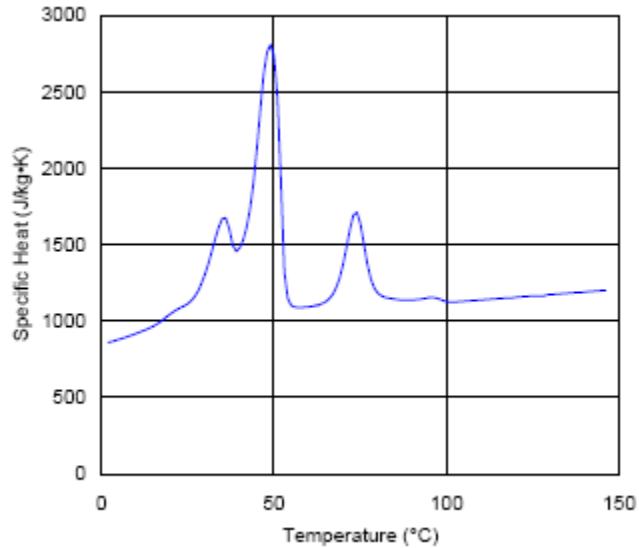
Notes: Two peaks were observed. Transition analysis temperatures and specific heat data are for larger peak.

Transition Analysis

extrapolated onset	53 °C
peak	49 °C
extrapolated end	41 °C

Specific Heat Data

Temp °C	Cp J/kg•K
150	1210
101	1125
58	1090
49	2811
31	1377
25	1114
10	918



Thermal Conductivity

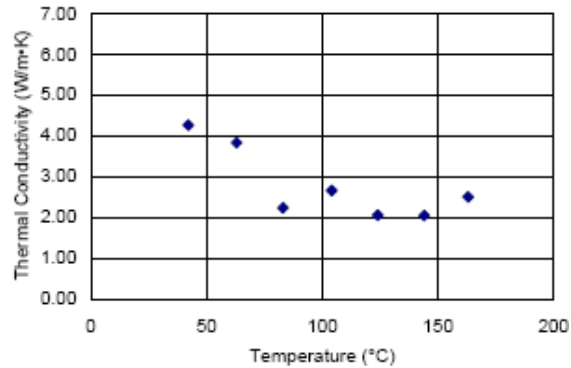


Method	ASTM D 5930: 2001 Thermal Conductivity of Plastics by Means of a Transient Line-Source Technique	
Instrument	K-System II Thermal Conductivity System	
Specimen	type	pellets
	drying	none
	other preparation	none
Parameters	calibration material	60,000 cstk PDMS
	probe constant	0.743
	probe length	50 mm
	loading temperature	150 °C
	initial temperature	160 °C
	final temperature	30 °C
	probe voltage	3.5 V
	acquisition time	45 s
Uncertainty	per standard	

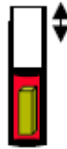
Thermal conductivity is a measure of the rate of heat conduction of the material. It is a critical property for heat transfer calculations. The line-source method measures thermal conductivity in both melt and solid state.

Thermal Conductivity Data

Temp °C	k W/m·K
163	2.503
144	2.045
124	2.058
104	2.661
83	2.234
63	3.834
42	4.283



PVT



Method	Non-standard. Pressure-specific volume-temperature measurements using high-pressure dilatometry	
Instrument	Gnomix PVT apparatus	
Specimen	type drying other preparation	pellets 4 hrs, 50°C/vacuum see note below
Parameters	solid density method immersion liquid pVT confining fluid max temperature measurement type heating rate	ASTM D792 water mercury 160 °C isothermal heating scan approx. 3 °C/min

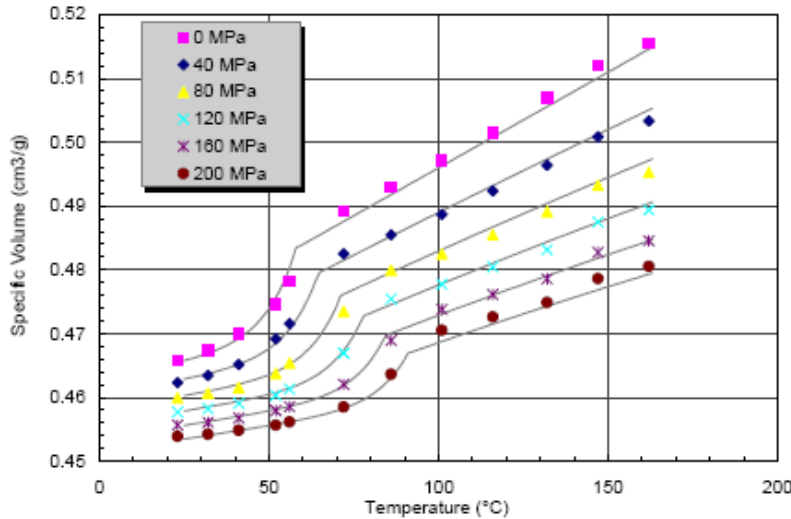
PVT data are equation-of-state thermodynamic properties that describe the compressibility and volumetric expansion of the material. Dilatometry measures the change in volume of a specimen subjected to different temperatures and pressures.

Notes: PVT specimen was cut from a plug that was manufactured by Datapoint Labs using pellets supplied by client.

Pressure-Volume-Temperature Data

Temp °C	Specific Volume cm ³ /g					
	0	40	80	120	160	200
23	0.4658	0.4623	0.4600	0.4577	0.4557	0.4539
32	0.4674	0.4634	0.4607	0.4582	0.4561	0.4542
41	0.4700	0.4652	0.4615	0.4591	0.4568	0.4549
52	0.4747	0.4692	0.4638	0.4603	0.4580	0.4557
58	0.4782	0.4716	0.4654	0.4613	0.4586	0.4562
72	0.4892	0.4825	0.4735	0.4670	0.4621	0.4585
86	0.4930	0.4855	0.4799	0.4754	0.4689	0.4636
101	0.4971	0.4887	0.4825	0.4778	0.4738	0.4705
116	0.5014	0.4924	0.4855	0.4805	0.4761	0.4726
132	0.5069	0.4964	0.4891	0.4832	0.4786	0.4749
147	0.5120	0.5009	0.4933	0.4875	0.4827	0.4786
162	0.5154	0.5033	0.4952	0.4894	0.4846	0.4806

Modified Two-Domain Tait Model (C-MOLD, Moldflow)



Coefficients	
b5	5.80E+01
b6	1.65E-01
b1m	4.834E-01
b2m	2.998E-04
b3m	2.865E+02
b4m	4.818E-03
b1s	4.688E-01
b2s	9.700E-05
b3s	6.791E+02
b4s	1.260E-03
b7	1.49E-02
b8	1.101E-01
b9	2.118E-02

Modified Two-Domain Tait Equation

$$v(T, p) = v_0(T) \left(1 - C \ln \left(1 + \frac{p}{B(T)} \right) \right) + v_i(T, p), T_i(p) = b_5 + b_6 p$$

$$\text{for } T > T_i(p): v_0(T) = b_{1m} + b_{2m}(T - b_5), B(T) = b_{3m} \exp(-b_{4m}(T - b_5)), v_i(T, p) = 0$$

$$\text{for } T < T_i(p): v_0(T) = b_{1s} + b_{2s}(T - b_5), B(T) = b_{3s} \exp(-b_{4s}(T - b_5)), v_i(T, p) = b_7 \exp(b_8(T - b_5) - b_9 p)$$

Model Terms	Units
specific volume, v	cm ³ /g
pressure, P	MPa
temperature, T	°C

No-Flow Temperature

	Method	non-standard Moldflow specification; no-flow temperature defined by extrudate flow < 2 mm/min	
	Instrument	Goettfert Capillary Rheometer	
Specimen	type	pellets	
	drying	none	
Parameters	other preparation	none	
	equivalent load	172 kg	
	barrel diameter	12 mm	
	initial pressure	0 MPa	
	test temperature	140 °C	
	dwel time	6 min	
	die inner diameter	1 mm	
	die length	20 mm	
die entry angle	180 °		

The no-flow temperature provides a measure of the solidification temperature of the melt. During the test, a molten specimen is cooled under constant load; the no-flow temperature is one at which flow ceases to occur.

Results

No-Flow Temperature	61 °C
---------------------	-------

Appendix C3

Properties of Bimodal μ -n SiC Feedstock

Feedstock composition		
Materials	Particle size	Weight (%)
SiC	0.7 μ m	67.2
	20 nm	7.5
AlN	20 nm	4.15
Y ₂ O ₃	50 nm	4.15
Multi-component binder system	-	17

Client	Valmikanathan Onbattuvelli
Company	Oregon State University
Address	Hall Corvallis, OR United States
Sample Received	6/11/2010
Sample Source	Oregon State University
Report Prepared	6/16/2010
Prepared By	
Title	Engineer
Issued By	
Title	Operations Manager

DatapointLabs is accredited by the American Association for Laboratory Accreditation (A2LA Certificate # 1242.01), and maintains a quality system in accordance with ISO/IEC 17025. Any opinions or interpretations expressed in this report are outside the scope of the accreditation.

The results in this report relate only to the items tested. This report shall not be reproduced except in full without the written approval of DatapointLabs.

DatapointLabs cannot be held liable under any circumstances for damages arising out of the use of this information or for claims in excess of that originally paid for the testing. DatapointLabs disclaims all other warranties, either express or implied, including implied warranties of merchantability or fitness for a particular purpose.



DatapointLabs

<http://www.datapointlabs.com>

95 Brown Road, Ithaca, NY 14850
Phone: 607-266-0405 Fax: 607-266-0168
Toll-Free (U.S.): 1-888-328-2422

This data is available in True Digital format

dds
matereality
www.matereality.com

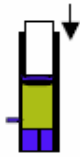
C-MOLD/Moldflow TestPak™ Results

16881.21000.udb

Analysis	Property & T-CODE	Value	Units
Filling & Cooling	Cross/WLF Model (01313):		
	n	0.06498	
	τ^*	1.278E+05	Pa
	D1	1.000E+20	Pa·s
	D2	263	K
	D3	0	K/Pa
	A1	42.69	
	A2	51.60	K
	Juncture Loss Constants (01360):		
	C1		Pa ^(1-C2)
	C2		
	Melt Density (01000)	1987	kg/m ³
	Melt Specific Heat (01100)	1250	J/kg·K
	Melt Thermal Conductivity (01200)	2.325	W/m·K
	Transition Temperature (01500)	325	K
	Specific Heat Table (01101)	See Page 7	
	Thermal Conductivity Table (01201)	See Page 8	
Post-Filling	Two-Domain Tait PVT Model (01004):		
	b5	3.350E+02	K
	b6	1.600E-07	K/Pa
	b1m	4.750E-04	m ³ /kg
	b2m	2.328E-07	m ³ /kg·K
	b3m	3.190E+08	Pa
	b4m	4.844E-03	1/K
	b1s	4.628E-04	m ³ /kg
	b2s	1.534E-07	m ³ /kg·K
	b3s	5.000E+08	Pa
	b4s	1.000E-02	1/K
	b7	1.220E-05	m ³ /kg
	b8	9.026E-02	1/K
b9	1.590E-08	1/Pa	
Shrink / Warp - Uncorrected Stress	Anisotropic Mechanical Properties (01602)		
	Modulus E ₁ (flow direction)		MPa
	Modulus E ₂ (transverse direction)		MPa
	Poisson's ratio ν_{12}		
	Poisson's ratio ν_{23}		
	Shear Modulus G		MPa
	Anisotropic Thermal Expansion (01702)		
	CLTE α_1 (flow direction)		x 10E-6/°C
CLTE α_2 (transverse direction)		x 10E-6/°C	

TestPaks™ is a trademark of Datapoint Labs. C-MOLD and Moldflow are trademarks of Moldflow Corporation.

Viscosity



Method	ASTM D 3835: 2008 Determination of Properties of Polymeric Materials by Means of a Capillary Rheometer	
Instrument	Goettfert Rheograph 2003 Capillary Rheometer	
Specimen	type drying other preparation	pellets none none
Parameters	initial pressure barrel diameter die entry angle die inner diameter die length preheating time	0 MPa 12 mm 180 °C 1 mm 20 mm 6 min
Data Correction		
Precision	temperature die inner diameter die length	+/- 0.1 °C +/- 0.0069 mm +/- 0.025 mm
Uncertainty	per standard	

Polymer rheology characterizes the complex flow behavior of plastics. A capillary rheometer measures viscosity as a function of temperature and shear rate. The Goettfert rheometer utilizes direct measurement of melt pressures through a side mounted pressure transducer.

Data are modeled using empirical or semi-empirical equations.

Notes: Pressures were quite unstable during all testing temperatures.

Viscosity Data

140 °C		160 °C		180 °C	
Shear Rate s ⁻¹	Viscosity Pa·s	Shear Rate s ⁻¹	Viscosity Pa·s	Shear Rate s ⁻¹	Viscosity Pa·s
10	19984.50	10	20715.70	10	16328.80
20	9931.34	20	10388.30	20	8164.42
50	3969.48	50	4177.11	50	3273.29
100	1984.74	100	2064.13	100	1630.54
200	998.48	200	1013.74	200	812.22
500	433.59	500	405.50	500	326.11
1000	233.26	1000	236.92	1000	188.07
2000	116.94	2000	125.80	2000	98.62
5000	59.23	5000	52.03	5000	48.97
10000	29.62	10000	30.53	10000	26.01

Cross/WLF Model (C-MOLD, Moldflow)

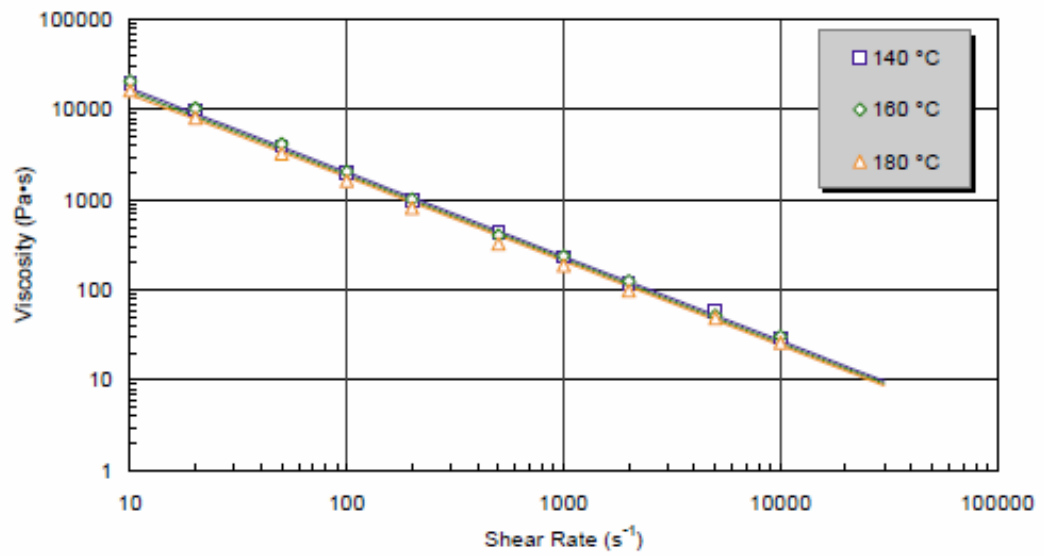
$$\eta(T, \dot{\gamma}) = \frac{\eta_0(T)}{1 + \left(\frac{\eta_0 \dot{\gamma}}{\tau^*}\right)^{1-n}}, \text{ where}$$

$$\eta_0(T) = D_1 \exp\left[-\frac{A_1(T - D_2)}{A_2 + (T - D_2)}\right]$$

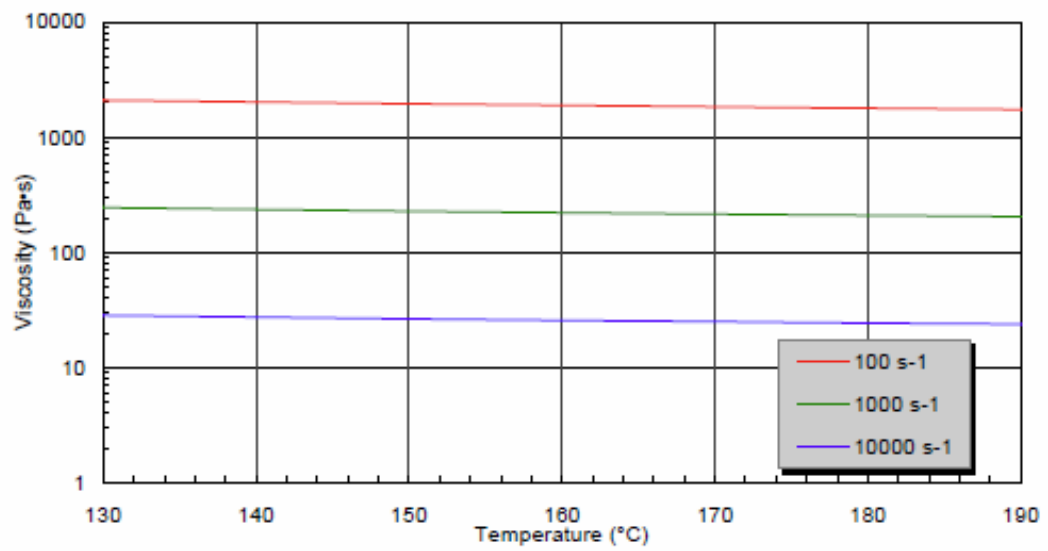
Coefficients (SI units)

n	0.06498
τ*	127756.7
D1	1E+20
D2	263
A1	42.69
A2	51.6

Viscosity vs Shear Rate



Viscosity vs Temperature



Specific Heat



Method	Based on ASTM E1269: 2005 Determining Specific Heat Capacity by Differential Scanning Calorimetry	
Instrument	Perkin Elmer DSC7	
Specimen	type drying other preparation	pellets none cut from pellet
Parameters	purge gas purge gas purity purge gas rate cooling rate initial temperature final temperature equilibration times sample weight sample pans	N2 99.99 % 25 ml/min 20 °C/min 180 °C -10 °C 4 min 6.43 mg Al, volatile
Calibration Standards	temperature heat flow specific heat	In, Zn In sapphire

Heat capacity is a thermodynamic quantity and is a measure of the amount of heat retained by the material. The DSC can measure this property over a range of temperatures and in both solid and melt states.

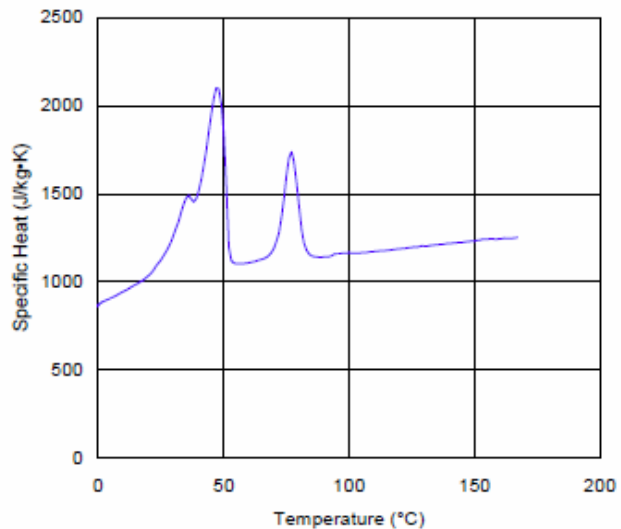
Notes: An additional peak was observed in the 60° to 90°C range.

Transition Analysis

extrapolated onset	52 °C
peak	47 °C
extrapolated end	36 °C

Specific Heat Data

Temp °C	Cp J/kg·K
170	1252
111	1174
57	1105
47	2100
26	1149
18	1013
0	871



Thermal Conductivity

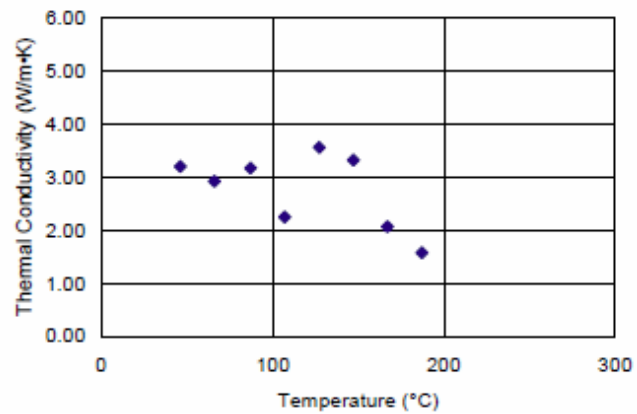


Method	ASTM D 5930: 2001 Thermal Conductivity of Plastics by Means of a Transient Line-Source Technique	
Instrument	K-System II Thermal Conductivity System	
Specimen	type	pellets
	drying	none
	other preparation	none
Parameters	calibration material	60,000 cstk PDMS
	probe constant	0.796
	probe length	50 mm
	loading temperature	180 °C
	initial temperature	180 °C
	final temperature	30 °C
	probe voltage	3.5 V
	acquisition time	45 s
Uncertainty	per standard	

Thermal conductivity is a measure of the rate of heat conduction of the material. It is a critical property for heat transfer calculations. The line-source method measures thermal conductivity in both melt and solid state.

Thermal Conductivity Data

Temp °C	k W/m•K
187	1.579
167	2.070
147	3.327
127	3.568
107	2.252
87	3.176
66	2.926
46	3.210



PVT



Method	Non-standard. Pressure-specific volume-temperature measurements using high-pressure dilatometry	
Instrument	Gnomix PVT apparatus	
Specimen	type drying other preparation	plaque none cut from plaque
Parameters	solid density method immersion liquid PVT confining fluid max temperature measurement type heating rate	ASTM D792 water Mercury 180 °C isothermal heating scan approx. 3 °C/min

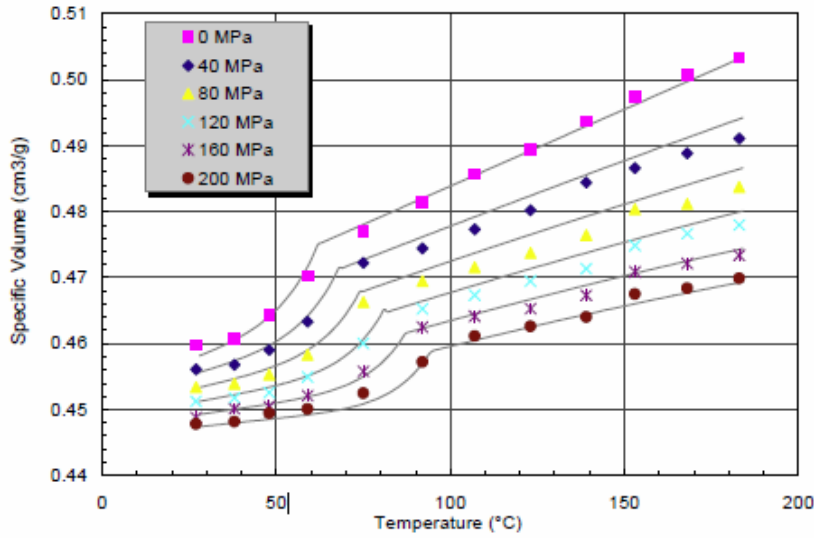
PVT data are equation-of-state thermodynamic properties that describe the compressibility and volumetric expansion of the material. Dilatometry measures the change in volume of a specimen subjected to different temperatures and pressures.

Pressure-Volume-Temperature Data

Specific Volume cm³/g

Temp °C	Pressure MPa					
	0	40	80	120	160	200
27	0.4598	0.4561	0.4534	0.4512	0.4488	0.4478
38	0.4607	0.4568	0.4539	0.4517	0.4501	0.4482
48	0.4644	0.4590	0.4553	0.4528	0.4505	0.4494
59	0.4703	0.4633	0.4583	0.4549	0.4521	0.4501
75	0.4771	0.4723	0.4663	0.4600	0.4558	0.4525
92	0.4815	0.4745	0.4695	0.4653	0.4625	0.4572
107	0.4857	0.4773	0.4716	0.4674	0.4642	0.4612
123	0.4894	0.4802	0.4738	0.4695	0.4653	0.4626
139	0.4937	0.4844	0.4765	0.4714	0.4673	0.4640
153	0.4973	0.4866	0.4804	0.4749	0.4708	0.4675
168	0.5007	0.4888	0.4812	0.4767	0.4722	0.4684
183	0.5034	0.4911	0.4838	0.4780	0.4734	0.4699

Modified Two-Domain Tait Model (C-MOLD, Moldflow)



Coefficients	
b5	6.20E+01
b6	1.60E-01
b1m	4.750E-01
b2m	2.328E-04
b3m	3.190E+02
b4m	4.844E-03
b1s	4.628E-01
b2s	1.534E-04
b3s	5.000E+02
b4s	1.000E-02
b7	1.22E-02
b8	9.026E-02
b9	1.590E-02

Modified Two-Domain Tait Equation

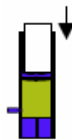
$$v(T, p) = v_0(T) \left(1 - C \ln \left(1 + \frac{P}{B(T)} \right) \right) + v_i(T, p), T_i(p) = b_5 + b_6 p$$

$$\text{for } T > T_i(p): v_0(T) = b_{1m} + b_{2m}(T - b_5), B(T) = b_{3m} \exp(-b_{4m}(T - b_5)), v_i(T, p) = 0$$

$$\text{for } T < T_i(p): v_0(T) = b_{1s} + b_{2s}(T - b_5), B(T) = b_{3s} \exp(-b_{4s}(T - b_5)), v_i(T, p) = b_7 \exp(b_8(T - b_5) - b_9 p)$$

Model Terms	Units
specific volume, v	cm ³ /g
pressure, P	MPa
temperature, T	°C

No-Flow Temperature



Method	non-standard Moldflow specification; no-flow temperature defined by extrudate flow < 2 mm/min	
Instrument	Goettfert Capillary Rheometer	
Specimen	type	pellets
	drying	none
	other preparation	none
Parameters	equivalent load	172 kg
	barrel diameter	12 mm
	initial pressure	0 MPa
	test temperature	140 °C
	dwel time	6 min
	die inner diameter	1 mm
	die length	20 mm
	die entry angle	180 °

The no-flow temperature provides a measure of the solidification temperature of the melt. During the test, a molten specimen is cooled under constant load; the no-flow temperature is one at which flow ceases to occur.

Results

No-Flow Temperature	58 °C
---------------------	-------

Appendix C4

Properties of Bimodal μ -n AlN Feedstock

Feedstock composition		
Materials	Particle size	Weight (%)
AlN	1.1 μ m	70
	20 nm	10.75
Y ₂ O ₃	50 nm	4.25
Multi-component binder system	-	15

Client	Valmikanathan Onbattuvelli
Company	Oregon State University
Address	Hall Corvallis, OR United States
Sample Received	8/11/2010
Sample Source	Oregon State University
Report Prepared	8/17/2010
Prepared By	
Title	Engineer
Issued By	
Title	Operations Manager

DatapointLabs is accredited by the American Association for Laboratory Accreditation (A2LA Certificate # 1242.01), and maintains a quality system in accordance with ISO/IEC 17025. Any opinions or interpretations expressed in this report are outside the scope of the accreditation.

The results in this report relate only to the items tested. This report shall not be reproduced except in full without the written approval of DatapointLabs.

DatapointLabs cannot be held liable under any circumstances for damages arising out of the use of this information or for claims in excess of that originally paid for the testing. DatapointLabs disclaims all other warranties, either express or implied, including implied warranties of merchantability or fitness for a particular purpose.



<http://www.datapointlabs.com>

95 Brown Road, Ithaca, NY 14850
Phone: 607-266-0405 Fax: 607-266-0168
Toll-Free (U.S.): 1-888-328-2422

This data is available in True Digital format



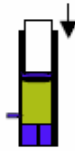
C-MOLD/Moldflow TestPak™ Results

16882.21000.udb

Analysis	Property & T-CODE	Value	Units
Filling & Cooling	Cross/WLF Model (01313):		
	n	0.05342	
	τ^*	1.782E+05	Pa
	D1	9.133E+19	Pa·s
	D2	263	K
	D3	0	K/Pa
	A1	29.54	
	A2	51.60	K
	Juncture Loss Constants (01360):		
	C1		Pa ^{1-C2}
	C2		
	Melt Density (01000)	2137	kg/m ³
	Melt Specific Heat (01100)	1411	J/kg·K
	Melt Thermal Conductivity (01200)	2.914	W/m·K
	Transition Temperature (01500)	326	K
	Specific Heat Table (01101)	See Page 7	
	Thermal Conductivity Table (01201)	See Page 8	
Post-Filling	Two-Domain Tait PVT Model (01004):		
	b5	3.360E+02	K
	b6	1.450E-07	K/Pa
	b1m	4.457E-04	m ³ /kg
	b2m	1.861E-07	m ³ /kg·K
	b3m	3.430E+08	Pa
	b4m	4.028E-03	1/K
	b1s	4.368E-04	m ³ /kg
	b2s	1.494E-07	m ³ /kg·K
	b3s	5.000E+08	Pa
	b4s	1.000E-02	1/K
	b7	8.936E-06	m ³ /kg
	b8	1.306E-01	1/K
b9	2.221E-08	1/Pa	
Shrink / Warp - Uncorrected Stress	Anisotropic Mechanical Properties (01602)		
	Modulus E ₁ (flow direction)		MPa
	Modulus E ₂ (transverse direction)		MPa
	Poisson's ratio ν_{12}		
	Poisson's ratio ν_{23}		
	Shear Modulus G		MPa
	Anisotropic Thermal Expansion (01702)		
	CLTE α_1 (flow direction)		x 10E-6/°C
CLTE α_2 (transverse direction)		x 10E-6/°C	

TestPaks™ is a trademark of DatapointLabs. C-MOLD and Moldflow are trademarks of Moldflow Corporation.

Viscosity



Method	ASTM D 3835: 2008 Determination of Properties of Polymeric Materials by Means of a Capillary Rheometer	
Instrument	Goettfert Rheograph 2003 Capillary Rheometer	
Specimen	type drying other preparation	pellets none none
Parameters	initial pressure barrel diameter die entry angle die inner diameter die length preheating time	0 MPa 12 mm 180 °C 1 mm 20 mm 6 min
Data Correction		
Precision	temperature die inner diameter die length	+/- 0.1 °C +/- 0.0069 mm +/- 0.025 mm
Uncertainty	per standard	

Polymer rheology characterizes the complex flow behavior of plastics. A capillary rheometer measures viscosity as a function of temperature and shear rate. The Goettfert rheometer utilizes direct measurement of melt pressures through a side mounted pressure transducer.

Data are modeled using empirical or semi-empirical equations.

Notes: Pressures were unstable during all of this testing.

Viscosity Data

140 °C		160 °C		180 °C	
Shear Rate s ⁻¹	Viscosity Pa·s	Shear Rate s ⁻¹	Viscosity Pa·s	Shear Rate s ⁻¹	Viscosity Pa·s
10	28260.20	10	50997.10	10	32231.20
20	27539.70	20	25650.90	20	17456.00
50	11468.70	50	5471.77	50	9038.20
100	7126.74	100	3914.52	100	4574.06
200	2494.66	200	1795.43	200	1783.21
500	798.34	500	884.28	500	903.82
1000	398.12	1000	421.94	1000	612.45
2000	220.45	2000	169.46	2000	232.96
5000	102.10	5000	62.90	5000	68.51
10000	56.85	10000	44.21	10000	36.46

Cross/WLF Model (C-MOLD, Moldflow)

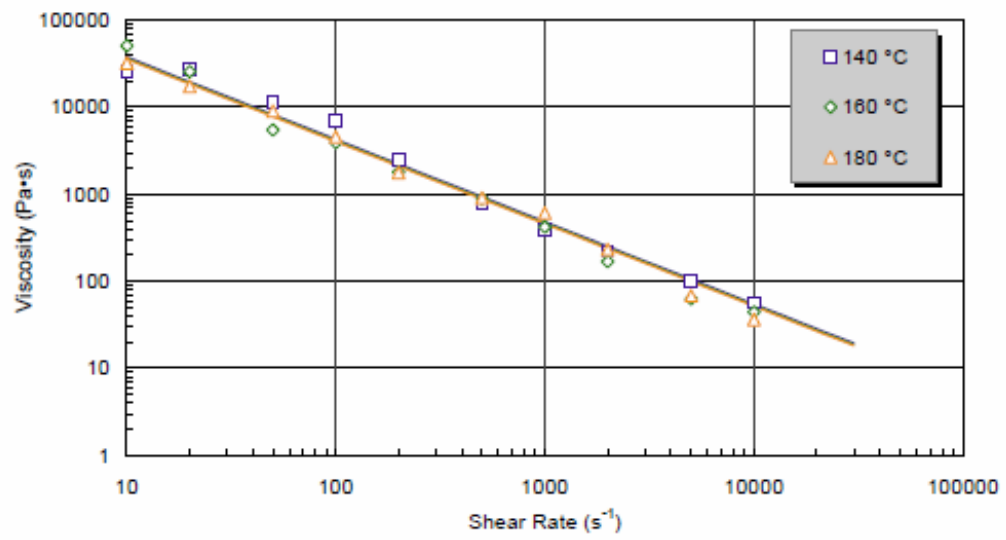
$$\eta(T, \dot{\gamma}) = \frac{\eta_0(T)}{1 + \left(\frac{\eta_0 \dot{\gamma}}{\tau^*}\right)^{1-n}}, \text{ where}$$

$$\eta_0(T) = D_1 \exp\left[-\frac{A_1(T - D_2)}{A_2 + (T - D_2)}\right]$$

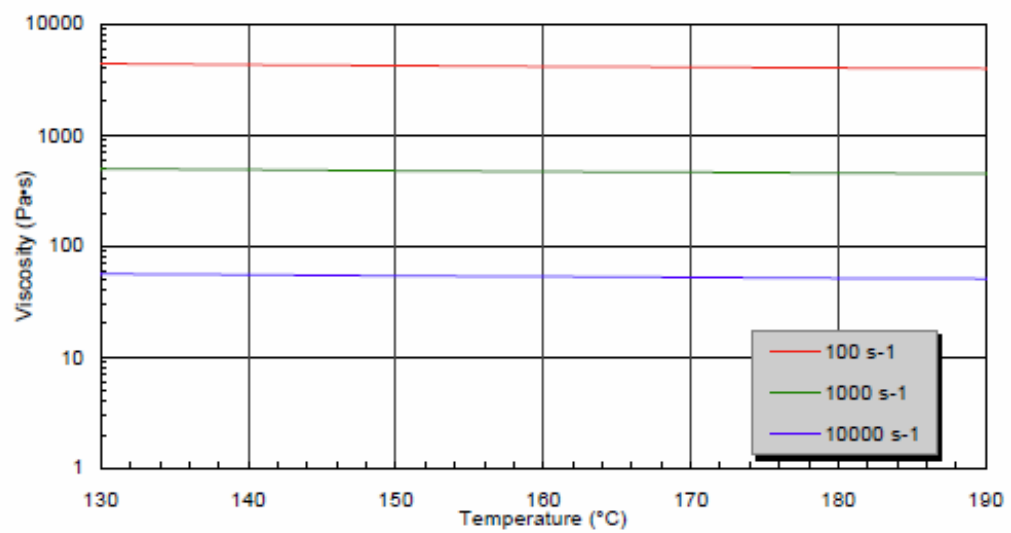
Coefficients (SI units)

n	0.05342
τ*	178204.72
D1	9.133E+19
D2	263
A1	29.54
A2	51.6

Viscosity vs Shear Rate



Viscosity vs Temperature



Specific Heat



Method	Based on ASTM E1269: 2005 Determining Specific Heat Capacity by Differential Scanning Calorimetry	
Instrument	Perkin Elmer DSC7	
Specimen	type drying other preparation	pellets none cut from pellet
Parameters	purge gas purge gas purity purge gas rate cooling rate initial temperature final temperature equilibration times sample weight sample pans	N2 99.99 % 25 ml/min 20 °C/min 180 °C -10 °C 4 min 8.71 mg Al, volatile
Calibration Standards	temperature heat flow specific heat	In, Zn In sapphire

Heat capacity is a thermodynamic quantity and is a measure of the amount of heat retained by the material. The DSC can measure this property over a range of temperatures and in both solid and melt states.

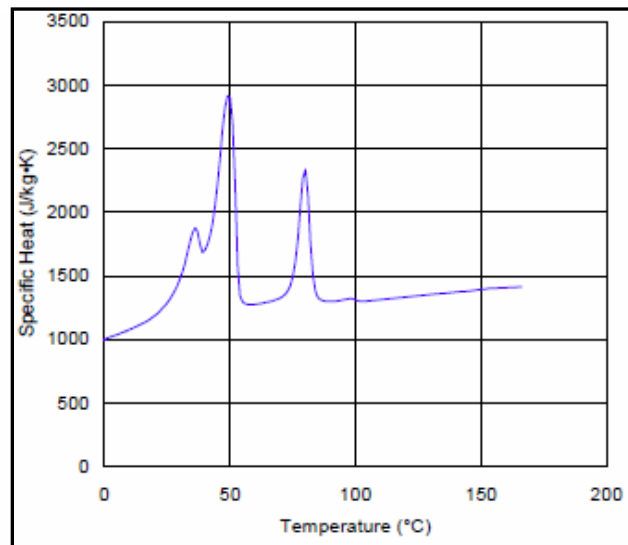
Notes: An additional peak was observed in the 60° to 90°C range.

Transition Analysis

extrapolated onset	53 °C
peak	49 °C
extrapolated end	40 °C

Specific Heat Data

Temp °C	Cp J/kg·K
170	1413
111	1315
58	1274
49	2915
30	1472
20	1186
0	998



Thermal Conductivity

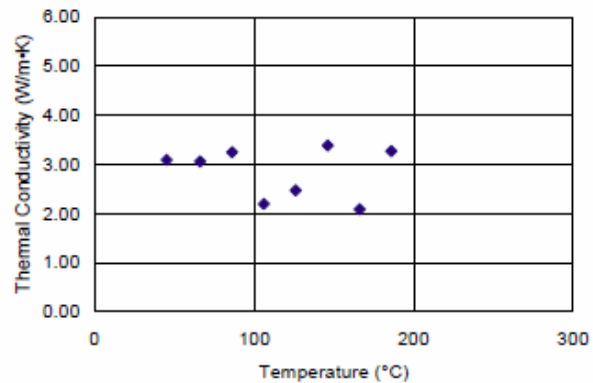


Method	ASTM D 5930: 2001 Thermal Conductivity of Plastics by Means of a Transient Line-Source Technique	
Instrument	K-System II Thermal Conductivity System	
Specimen	type drying other preparation	pellets none none
Parameters	calibration material probe constant probe length loading temperature initial temperature final temperature probe voltage acquisition time	60,000 cstk PDMS 0.798 50 mm 180 °C 180 °C 30 °C 3.5 V 45 s
Uncertainty	per standard	

Thermal conductivity is a measure of the rate of heat conduction of the material. It is a critical property for heat transfer calculations. The line-source method measures thermal conductivity in both melt and solid state.

Thermal Conductivity Data

Temp °C	k W/m·K
186	3.270
166	2.090
146	3.383
126	2.474
106	2.196
86	3.251
66	3.062
45	3.092



PVT



Method	Non-standard. Pressure-specific volume-temperature measurements using high-pressure dilatometry	
Instrument	Gnomix PVT apparatus	
Specimen	type drying other preparation	plaque none cut from plaque
Parameters	solid density method immersion liquid PVT confining fluid max temperature measurement type heating rate	ASTM D792 water Mercury 180 °C isothermal heating scan approx. 3 °C/min

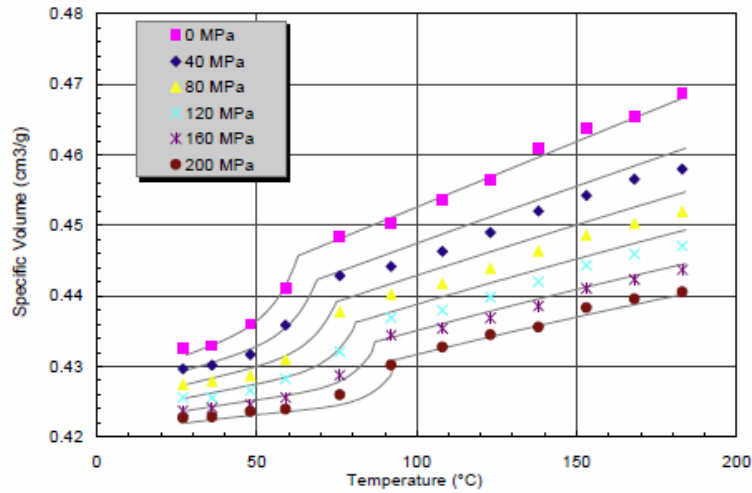
PVT data are equation-of-state thermodynamic properties that describe the compressibility and volumetric expansion of the material. Dilatometry measures the change in volume of a specimen subjected to different temperatures and pressures.

Pressure-Volume-Temperature Data

Specific Volume cm³/g

Temp °C	Pressure MPa					
	0	40	80	120	160	200
27	0.4326	0.4296	0.4274	0.4256	0.4237	0.4227
36	0.4329	0.4302	0.4279	0.4256	0.4241	0.4228
48	0.4360	0.4317	0.4287	0.4266	0.4246	0.4236
59	0.4411	0.4359	0.4310	0.4282	0.4256	0.4239
76	0.4484	0.4429	0.4377	0.4321	0.4287	0.4260
92	0.4503	0.4442	0.4402	0.4369	0.4344	0.4302
108	0.4536	0.4463	0.4417	0.4379	0.4354	0.4327
123	0.4565	0.4490	0.4439	0.4398	0.4369	0.4345
138	0.4609	0.4520	0.4463	0.4420	0.4385	0.4356
153	0.4638	0.4542	0.4486	0.4443	0.4411	0.4383
168	0.4654	0.4565	0.4502	0.4460	0.4423	0.4396
183	0.4687	0.4580	0.4519	0.4471	0.4437	0.4406

Modified Two-Domain Tait Model (C-MOLD, Moldflow)



Coefficients	
b5	8.30E+01
b6	1.45E-01
b1m	4.457E-01
b2m	1.881E-04
b3m	3.430E+02
b4m	4.028E-03
b1s	4.388E-01
b2s	1.494E-04
b3s	5.000E+02
b4s	1.000E-02
b7	8.94E-03
b8	1.308E-01
b9	2.221E-02

Modified Two-Domain Tait Equation

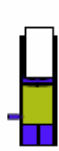
$$v(T, p) = v_0(T) \left(1 - C \ln \left(1 + \frac{P}{B(T)} \right) \right) + v_i(T, p), T_i(p) = b_5 + b_6 p$$

$$\text{for } T > T_i(p): v_0(T) = b_{1m} + b_{2m}(T - b_5), B(T) = b_{3m} \exp(-b_{4m}(T - b_5)), v_i(T, p) = 0$$

$$\text{for } T < T_i(p): v_0(T) = b_{1s} + b_{2s}(T - b_5), B(T) = b_{3s} \exp(-b_{4s}(T - b_5)), v_i(T, p) = b_7 \exp(b_8(T - b_5) - b_9 p)$$

Model Terms	Units
specific volume, v	cm ³ /g
pressure, P	MPa
temperature, T	°C

No-Flow Temperature



Method	non-standard	
	Moldflow specification; no-flow temperature defined by extrudate flow < 2 mm/min	
Instrument	Goettfert Capillary Rheometer	
Specimen	type	pellets
	drying	none
Parameters	other preparation	none
	equivalent load	172 kg
	barrel diameter	12 mm
	initial pressure	0 MPa
	test temperature	140 °C
	dwelt time	6 min
	die inner diameter	1 mm
	die length	20 mm
	die entry angle	180 °

The no-flow temperature provides a measure of the solidification temperature of the melt. During the test, a molten specimen is cooled under constant load; the no-flow temperature is one at which flow ceases to occur.

Results

No-Flow Temperature	58 °C
---------------------	-------

Appendix C5

Properties of The Multi-Component Binder Mixture

Feedstock composition	
Materials	Weight (%)
Paraffin wax	50
Propylene	35
Stearic acid	5
Low density polyethylene – g – maleic anhydride	10

Client	Valmikanathan Onbattuvelli
Company	Oregon State University
Address	Hall □ Corvallis, OR United States
Sample Received	3/26/2009
Sample Source	Oregon State University
Report Prepared	4/9/2009
Prepared By	
Title	Engineer
Issued By	
Title	Operations Manager

DatapointLabs is accredited by the American Association for Laboratory Accreditation (A2LA Certificate # 1242.01), and maintains a quality system in accordance with ISO/IEC 17025. Any opinions or interpretations expressed in this report are outside the scope of the accreditation.

The results in this report relate only to the items tested. This report shall not be reproduced except in full without the written approval of DatapointLabs.

DatapointLabs cannot be held liable under any circumstances for damages arising out of the use of this information or for claims in excess of that originally paid for the testing. DatapointLabs disclaims all other warranties, either express or implied, including implied warranties of merchantability or fitness for a particular purpose.



<http://www.datapointlabs.com>

95 Brown Road, Ithaca, NY 14850
Phone: 607-266-0405 Fax: 607-266-0168
Toll-Free (U.S.): 1-888-328-2422

This data is available in True Digital format



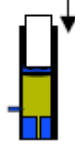
C-MOLD/Moldflow TestPak™ Results

< 14979.21000.udb

Analysis	Property & T-CODE	Value	Units
Filling & Cooling	Cross/WLF Model (01313):		
	n	0.40120	
	τ^*	7.936E+02	Pa
	D1	4.293E+23	Pa*s
	D2	333	K
	D3	0	K/Pa
	A1	78.13	
	A2	51.60	K
	Juncture Loss Constants (01360):		
	C1		Pa^(1-C2)
	C2		
	Melt Density (01000)	705	kg/m ³
	Melt Specific Heat (01100)	2589	J/kg*K
	Melt Thermal Conductivity (01200)	0.159	W/m*K
	Transition Temperature (01500)	372	K
	Specific Heat Table (01101)	See Page 7	
	Thermal Conductivity Table (01201)	See Page 8	
Post-Filling	Two-Domain Tait PVT Model (01004):		
	b5	3.360E+02	K
	b6	1.465E-07	K/Pa
	b1m	1.255E-03	m ³ /kg
	b2m	1.344E-06	m ³ /kg*K
	b3m	1.256E+08	Pa
	b4m	5.867E-03	1/K
	b1s	1.170E-03	m ³ /kg
	b2s	9.568E-07	m ³ /kg*K
	b3s	2.396E+08	Pa
	b4s	4.155E-03	1/K
	b7	8.458E-05	m ³ /kg
	b8	6.688E-02	1/K
b9	1.397E-08	1/Pa	
Shrink / Warp - Uncorrected Stress	Anisotropic Mechanical Properties (01602)		
	Modulus E ₁ (flow direction)		MPa
	Modulus E ₂ (transverse direction)		MPa
	Poisson's ratio ν_{12}		
	Poisson's ratio ν_{23}		
	Shear Modulus G		MPa
	Anisotropic Thermal Expansion (01702)		
	CLTE α_1 (flow direction)		x 10E-6/°C
CLTE α_2 (transverse direction)		x 10E-6/°C	

TestPaks™ is a trademark of Datapoint Labs. C-MOLD and Moldflow are trademarks of Moldflow Corporation.

Viscosity



Method	ASTM D 3835: 2008 Determination of Properties of Polymeric Materials by Means of a Capillary Rheometer	
Instrument	Instron 5582 Electromechanical UTM	
Specimen	type drying other preparation	powder none none
Parameters	initial pressure barrel diameter die entry angle die inner diameter die length preheating time	0 MPa 12 mm 180 ° 1 mm 20 mm 6 min
Data Correction		
Precision	temperature die inner diameter die length	+/- 0.1 °C +/- 0.0089 mm +/- 0.025 mm
Uncertainty	per standard	

Polymer rheology characterizes the complex flow behavior of plastics. A capillary rheometer measures viscosity as a function of temperature and shear rate. The Goettfert rheometer utilizes direct measurement of melt pressures through a side mounted pressure transducer.

Data are modeled using empirical or semi-empirical equations.

Notes: This material had totally unstable pressures throughout all testing.

Viscosity Data

140 °C		150 °C		160 °C	
Shear Rate s ⁻¹	Viscosity Pa·s	Shear Rate s ⁻¹	Viscosity Pa·s	Shear Rate s ⁻¹	Viscosity Pa·s
80	46.66	80	25.23	80	7.62
160	38.08	160	22.85	160	5.71
400	28.24	400	12.98	400	4.87
800	19.47	800	8.73	800	1.87
		1600	4.10		

Cross/WLF Model (C-MOLD, Moldflow)

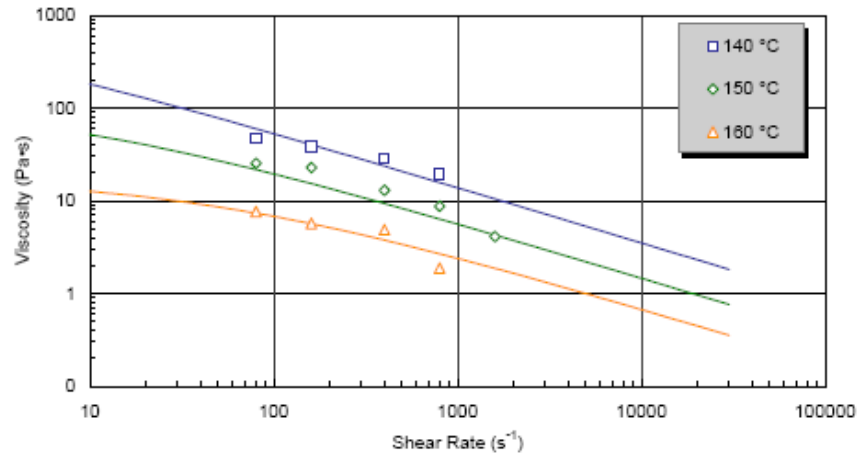
Coefficients (SI units)

$$\eta(T, \dot{\gamma}) = \frac{\eta_0(T)}{1 + \left(\frac{\eta_0 \dot{\gamma}}{\tau^*}\right)^{1-n}}, \text{ where}$$

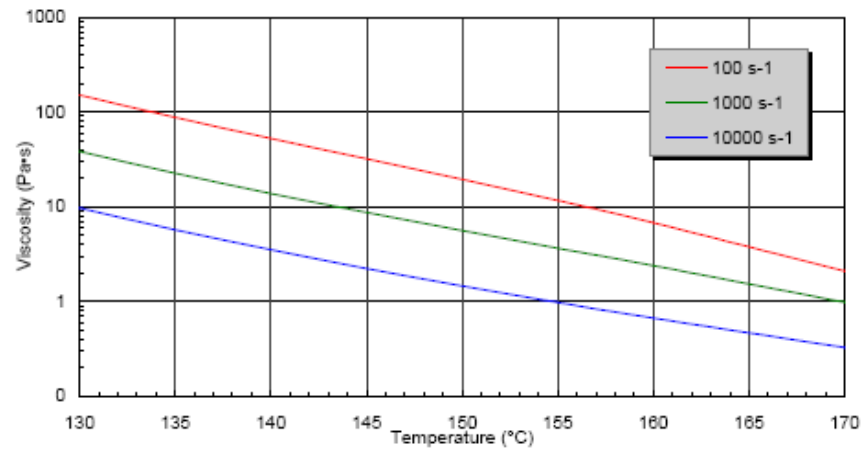
$$\eta_0(T) = D_1 \exp\left\{-\frac{A_1(T - D_2)}{A_2 + (T - D_2)}\right\}$$

n	0.40120
τ^*	793.461
D1	4.29E+23
D2	333
A1	78.13
A2	51.6

Viscosity vs Shear Rate



Viscosity vs Temperature



Specific Heat



Method	Based on ASTM E1269: 2005 Determining Specific Heat Capacity by Differential Scanning Calorimetry	
Instrument	Perkin Elmer DSC7	
Specimen	type drying other preparation	pellets none cut from pellet
Parameters	purge gas purge gas purity purge gas rate cooling rate initial temperature final temperature equilibration times sample weight sample pans	N2 99.99 % 25 ml/min 20 °C/min 180 °C 0 °C 4 min 5.63 mg Al, volatile
Calibration Standards	temperature heat flow specific heat	In, Zn In sapphire

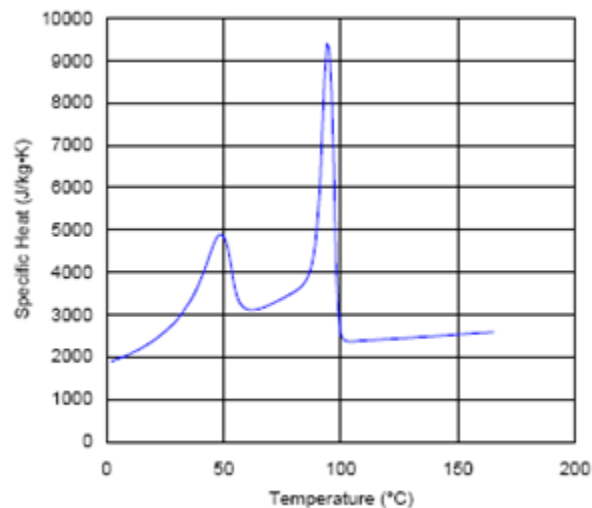
Heat capacity is a thermodynamic quantity and is a measure of the amount of heat retained by the material. The DSC can measure this property over a range of temperatures and in both solid and melt states.

Transition Analysis

extrapolated onset	99 °C
peak	95 °C
extrapolated end	89 °C

Specific Heat Data

Temp °C	Cp J/kg·K
170	2598
134	2473
104	2371
95	9298
79	3505
49	4894
10	2077



Thermal Conductivity

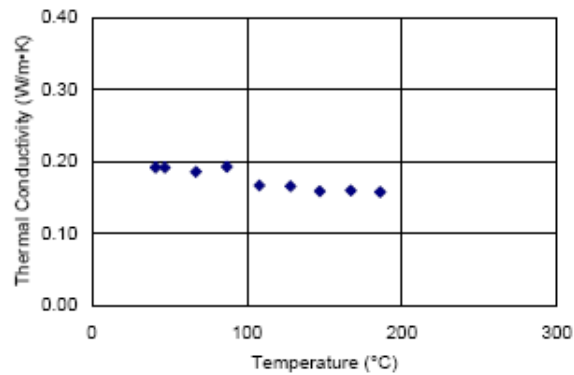


Method	ASTM D 5930: 2001 Thermal Conductivity of Plastics by Means of a Transient Line-Source Technique	
Instrument	Instron 8872 Servohydraulic UTM	
Specimen	type	powder
	drying	none
	other preparation	none
Parameters	calibration material	60,000 cstk PDMS
	probe constant	0.743
	probe length	50 mm
	loading temperature	180 °C
	initial temperature	180 °C
	final temperature	30 °C
	probe voltage	4 V
	acquisition time	45 s
Uncertainty	per standard	

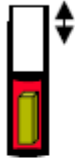
Thermal conductivity is a measure of the rate of heat conduction of the material. It is a critical property for heat transfer calculations. The line-source method measures thermal conductivity in both melt and solid state.

Thermal Conductivity Data

Temp °C	k W/m·K
186	0.158
167	0.160
147	0.159
128	0.166
108	0.167
87	0.193
67	0.188
47	0.192
41	0.192



PVT



Method	Non-standard. Pressure-specific volume-temperature measurements using high-pressure dilatometry	
Instrument	Gnomix PVT apparatus	
Specimen	type drying other preparation	pellets none see note below
Parameters	solid density method immersion liquid pVT confining fluid max temperature measurement type heating rate	ASTM D792 water mercury 180 °C isothermal heating scan approx. 3 °C/min

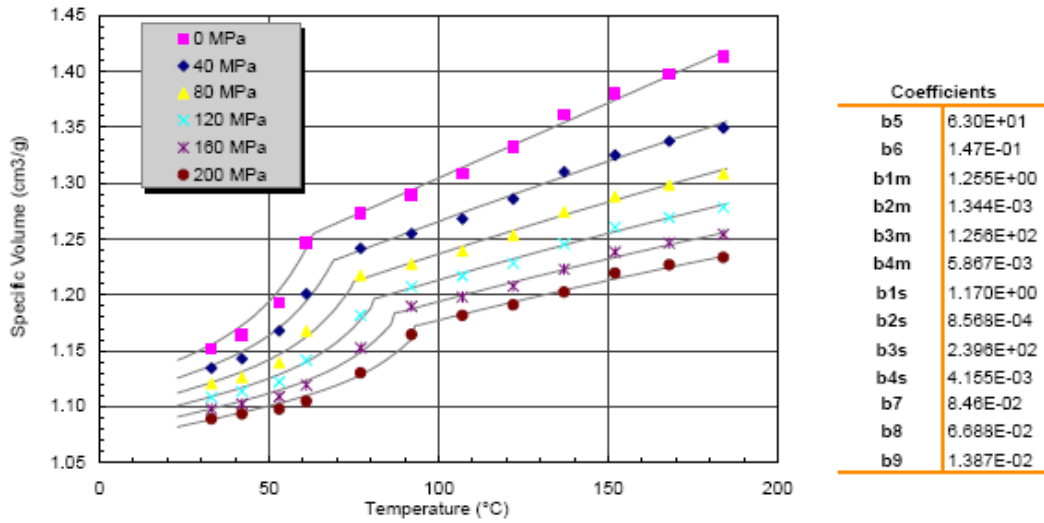
PVT data are equation-of-state thermodynamic properties that describe the compressibility and volumetric expansion of the material. Dilatometry measures the change in volume of a specimen subjected to different temperatures and pressures.

Notes: Specimen was cut from a plug that was manufactured by Datapoint Labs from pellets supplied by client.

Pressure-Volume-Temperature Data

Specific Volume cm ³ /g						
Temp °C	Pressure MPa					
	0	40	80	120	160	200
33	1.1521	1.1346	1.1207	1.1084	1.0980	1.0890
42	1.1640	1.1428	1.1261	1.1136	1.1024	1.0934
53	1.1929	1.1678	1.1394	1.1221	1.1090	1.0979
61	1.2467	1.2011	1.1678	1.1415	1.1194	1.1049
77	1.2733	1.2418	1.2174	1.1819	1.1527	1.1301
92	1.2897	1.2549	1.2277	1.2074	1.1898	1.1645
107	1.3088	1.2682	1.2393	1.2169	1.1981	1.1817
122	1.3324	1.2861	1.2534	1.2283	1.2079	1.1911
137	1.3615	1.3101	1.2745	1.2456	1.2229	1.2025
152	1.3805	1.3251	1.2882	1.2607	1.2385	1.2194
168	1.3975	1.3378	1.2983	1.2693	1.2464	1.2270
184	1.4138	1.3497	1.3085	1.2783	1.2542	1.2336

Modified Two-Domain Tait Model (C-MOLD, Moldflow)



Modified Two-Domain Tait Equation

$$v(T, p) = v_0(T) \left(1 - C \ln \left(1 + \frac{P}{B(T)} \right) \right) + v_i(T, p), T_i(p) = b_5 + b_6 p$$

$$\text{for } T > T_i(p): v_0(T) = b_{1m} + b_{2m}(T - b_5), B(T) = b_{3m} \exp(-b_{4m}(T - b_5)), v_i(T, p) = 0$$

$$\text{for } T < T_i(p): v_0(T) = b_{1s} + b_{2s}(T - b_5), B(T) = b_{3s} \exp(-b_{4s}(T - b_5)), v_i(T, p) = b_7 \exp(b_8(T - b_5) - b_9 p)$$

Model Terms	Units
specific volume, v	cm ³ /g
pressure, P	MPa
temperature, T	°C

No-Flow Temperature

	Method	non-standard Moldflow specification; no-flow temperature defined by extrudate flow < 2 mm/min	
	Instrument	Goettfert Capillary Rheometer	
Specimen	type	drying	pellets
	other preparation	none	none
Parameters	equivalent load	172 kg	
	barrel diameter	12 mm	
	initial pressure	0 MPa	
	test temperature	140 °C	
	dwel time	6 min	
	die inner diameter	1 mm	
	die length	20 mm	
	die entry angle	180 °	

The no-flow temperature provides a measure of the solidification temperature of the melt. During the test, a molten specimen is cooled under constant load; the no-flow temperature is one at which flow ceases to occur.

NOTE: No Flow temperature is taken from DSC data.

Results

No-Flow Temperature	47 °C
---------------------	-------

Appendix D

Injection Molding of Multi-Slotted Parts

The molten powder-polymer mixture (feedstock) was injected at 165 °C in an Arburg 221M injection molding machine. The injection molding conditions used are listed in the **Table D1**. The dimensions of the injection molded multi-slotted channel parts are mentioned in the **Tables D2a –d**.

Table D1: Conditions for injection molding multi-slotted parts from 4 different feedstocks

Molding Conditions		μ-SiC	μ-AlN	μ-n SiC	μ-n AlN
Temperature	Hopper	325 +/- 5 °F			
	Zone 1 -3	325 +/- 5 °F			
	Nozzle	335 +/- 5 °F			
	Mold Side A, B	60 +/- 5 °F			
Injection	Speed	1.03 * 10 ⁻² in/s			
	Pressure	13000 psi		10500 psi	11000 psi
	Delay	0.1 seconds		0.5 seconds	0.1 seconds
Holding	Pressure 1	7000 psi		8000 psi	7000 psi
	Time 1	0.7 s			
	Pressure 2, 3	3625 psi		4000 psi	
	Time 2, 3	0.7s		0.1 s	0.7 s
Ejection Delay		0.1 s			
Ejector retraction Delay		0.1s		10 s	0.1 s
Ejector retraction Speed		7.6"/s			
Retracted distance		5 mm			

Table D2a: Mass, density and dimensions of the injection molded μ -SiC multi-slotted parts

	Wt. (g)	L (mm)	B (mm)	H (mm)	Channel Separation (mm)	Channel Width (mm)	Channel Length (mm)	Vol. (cc)	Density (g/cc)
Avg. (50 Samples)	3.74	37.99	25.28	2.03	1.03	0.99	9.32	1.81	2.07
St. Dev.	0.01	0.02	0.03	0.02	0.009	0.003	0.006	0.02	0.01

Table D2b: Mass, density and dimensions of the injection molded μ -AlN multi-slotted parts

	Wt. (g)	L (mm)	B (mm)	H (mm)	Channel Separation (mm)	Channel Width (mm)	Channel Length (mm)	Vol. (cc)	Density (g/cc)
Avg. (50 Samples)	3.86	37.9	25.32	2.03	1.04	0.99	9.32	1.83	2.11
St. Dev.	0.01	0.08	0.04	0.01	0.006	0.005	0.006	0.03	0.03

Table D2c: Mass, density and dimensions of the injection molded bimodal μ -n SiC multi-slotted parts

	Wt. (g)	L (mm)	B (mm)	H (mm)	Channel Separation (mm)	Channel Width (mm)	Channel Length (mm)	Vol. (cc)	Density (g/cc)
Avg. (30 Samples)	3.88	38.25	25.49	2.03	1.04	0.99	9.32	1.84	2.11
St. Dev.	0.02	0.04	0.03	0.01	0.006	0.005	0.006	0.03	0.02

Table D2d: Mass, density and dimensions of the injection molded bimodal μ -n AlN multi-slotted parts

	Wt. (g)	L (mm)	B (mm)	H (mm)	Channel Separation (mm)	Channel Width (mm)	Channel Length (mm)	Vol. (cc)	Density (g/cc)
Avg. (40 Samples)	4.21	38.27	25.51	2.03	1.04	0.99	9.32	1.85	2.28
St. Dev.	0.01	0.02	0.02	0.01	0.008	0.005	0.004	0.04	0.03

Appendix E

Solvent Debinding of Injection Molded Multi-Slotted Parts

During debinding, the binder has to be removed from the molded parts in the shortest time with the least distortion. In the present work, the debinding protocol consisted of solvent immersion followed by thermal removal. Solvent debinding takes advantage of the solubility of low molecular weight constituents (e.g. paraffin wax and stearic acid in the present case) in organic solvents (e.g. heptanes in the present case). Solvent extraction creates porosity in the injection molded samples. A large amount of open pores, after solvent debinding, allows the degraded products during thermal debinding to diffuse to the surface easily. Therefore, the thermal removal of insoluble binder components will be finished in a much shorter period without distorting the samples. Consequently, the combination of solvent debinding and thermal debinding can be time saving. **Tables E1-E4** lists the dimensions of solvent debound SiC and AlN samples.

Table E1: Mass, density and dimensions of the debound μ -SiC multislotted parts

	Dewaxed mass (g)	Brown mass (g)	L (mm)	B (mm)	H (mm)	Channel Separation (mm)	Channel Width (mm)	Channel Length (mm)
Avg. (50 Samples)	3.4	2.97	37.77	25.19	2.03	1.03	0.99	9.26
St. Dev.	0.01	0.02	0.04	0.01	0.02	0.005	0.006	0.003

Table E2: Mass, density and dimensions of the debound μ -AlN multislotted parts

	Dewaxed mass (g)	Brown mass (g)	L (mm)	B (mm)	H (mm)	Channel Separation (mm)	Channel Width (mm)	Channel Length (mm)
Avg. (50 Samples)	3.44	3.09	37.26	24.94	2.03	1.01	0.97	9.24
St. Dev.	0.01	0.01	0.08	0.03	0.02	0.007	0.006	0.001

Table E3: Mass, density and dimensions of the “solvent debound” bimodal μ -n SiC multichannel parts

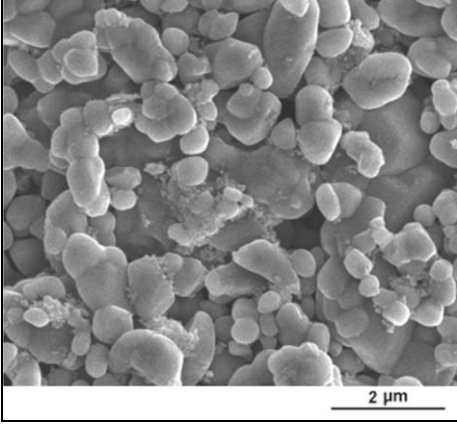
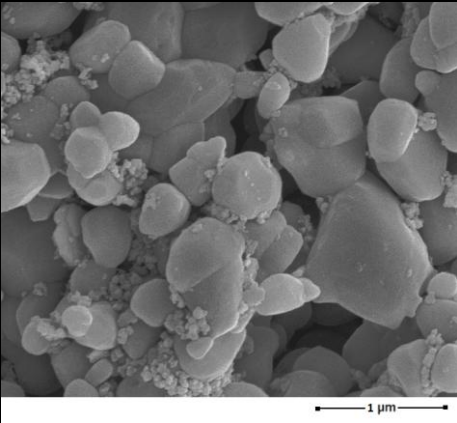
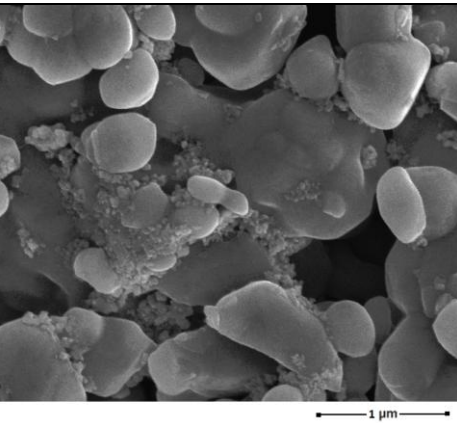
	Dewaxed mass (g)	Brown mass (g)	L (mm)	B (mm)	H (mm)	Channel Separation (mm)	Channel Width (mm)	Channel Length (mm)
Avg. (30 Samples)	3.53	3.19	38.25	25.49	2.03	1.04	0.99	9.32
St. Dev.	0.02	0.02	0.04	0.03	0.01	0.006	0.005	0.006

Table E4: Mass, density and dimensions of the “solvent debound” bimodal μ -n AlN multichannel parts

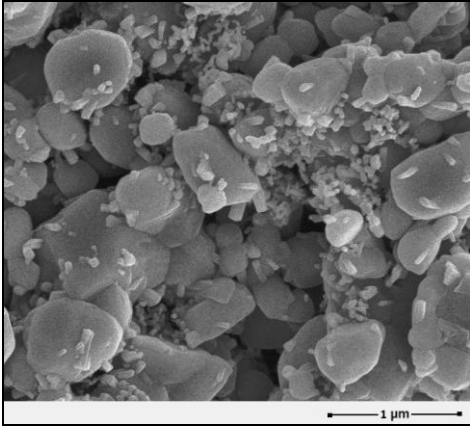
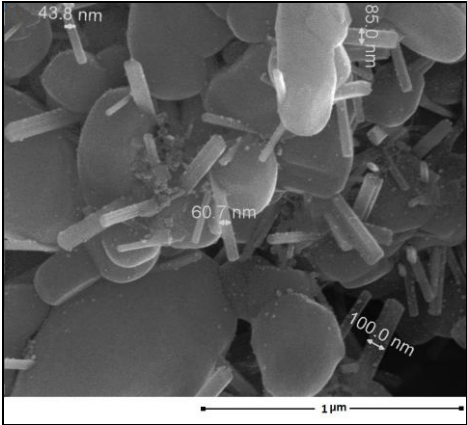
	Dewaxed mass (g)	Brown mass (g)	L (mm)	B (mm)	H (mm)	Channel Separation (mm)	Channel Width (mm)	Channel Length (mm)
Avg. (30 Samples)	3.94	3.57	38.27	25.51	2.03	1.04	0.99	9.32
St. Dev.	0.01	0.01	0.02	0.02	0.01	0.008	0.005	0.004

Appendix F

Pre-Sintering of Thermally Debound Monomodal μ -AlN Samples

Pre-sintering conditions	SEM Micrographs	% shrinkage			%wt. loss
		l	b	h	
500 °C, 5 hr		Nil			
800 °C, 4 hr					
1000 °C, 4 hr					

Pre-sintering of thermally debound monomodal μ -AlN samples

Pre-sintering conditions	SEM Micrographs	% shrinkage			%wt. loss
		l	b	h	
1100 °C, 4 hr		1.95	1.78	2.17	0
1150 °C, 4 hr		2.01	1.86	2.48	0.1

Appendix G

Vickers Hardness of Sintered SiC and AlN samples

Vickers hardness of the sintered SiC and AlN samples was measured in accordance with ASTM E384 using a Leco microhardness tester. A NIST traceable calibration steel block and a stage micrometer were used to calibrate the microhardness tester prior to the hardness measurements. A Vickers indenter with a test load of 1000g was applied on the sample surface, polished down to 1 μm , for 15 s. Figure G-1 shows a typical indentation obtained. D1 and D2 are the lengths of the indentation diagonals in number of divisions of the scale of the indenter. D is the average of D1 and D2 and is multiplied by a factor to obtain D in μm . Ten such measurements were taken for each sample.

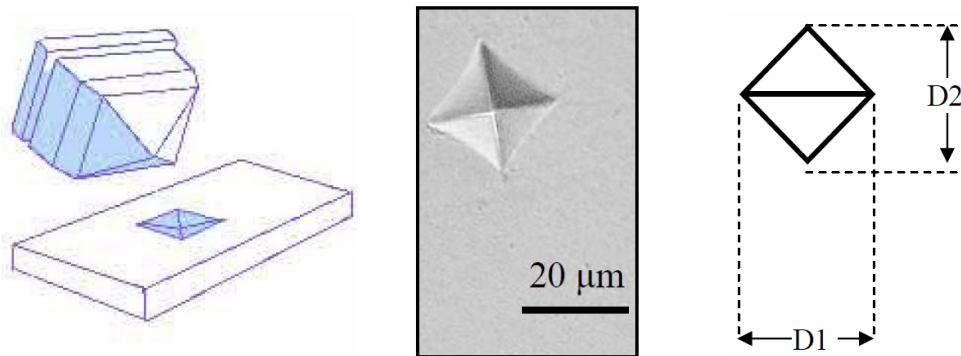


Figure G-1: Typical indentation obtained during Vickers indentation experiment

The Vickers Hardness (HV) in GPa was calculated using the equation (ASTM C-1327)

$$HV = 0.0018544 * (P/D^2)$$

where P = load in N, and, D = average length of diagonal in mm.

Monomodal SiC – 1850°C – 2 hrs

#	D ₁ (μm)	D ₂ (μm)	HV ₁ (kg/mm ²)	HV ₂ (kg/mm ²)	Avg. HV(kg/mm ²)
1	203	211	333	308	321
2	213	206	302	323	313
3	209	214	314	300	307
4	201	208	340	317	329
5	216	202	294	336	315
6	207	209	320	314	317
Avg. HV(kg/mm²)					317
Avg. HV(GPa)					3.11
St. Dev (GPa)					0.07

Monomodal SiC – 1850°C – 4 hrs

#	D ₁ (μm)	D ₂ (μm)	HV ₁ (kg/mm ²)	HV ₂ (kg/mm ²)	Avg. HV(kg/mm ²)
1	197	209	353	314	334
2	201	211	340	308	324
3	202	206	336	323	330
4	213	199	302	346	324
5	207	201	320	340	330
6	198	213	350	302	346
Avg. HV(kg/mm²)					328
Avg. HV(GPa)					3.21
St. Dev (GPa)					0.04

Monomodal SiC – 1900°C – 2 hrs

#	D ₁ (μm)	D ₂ (μm)	HV ₁ (kg/mm ²)	HV ₂ (kg/mm ²)	Avg. HV(kg/mm ²)
1	113	105	1074	1244	1203
2	109	108	1155	1176	1166
3	112	107	1093	1198	1145
4	105	111	1244	1193	1179
5	119	104	969	1268	1119
6	103	117	1293	1002	1146
Avg. HV(kg/mm²)					1160
Avg. HV(GPa)					11.36
St. Dev (GPa)					0.29

Monomodal SiC – 1900°C – 4 hrs

#	D ₁ (μm)	D ₂ (μm)	HV ₁ (kg/mm ²)	HV ₂ (kg/mm ²)	Avg. HV(kg/mm ²)
1	112	105	1093	1244	1170
2	109	108	1155	1176	1166
3	100	112	1372	1093	1183
4	105	109	1244	1155	1200
5	102	114	1318	1055	1187
6	109	107	1155	1198	1177
Avg. HV(kg/mm²)					1181
Avg. HV(GPa)					11.57
St. Dev (GPa)					0.12

Monomodal SiC – 1950°C – 2 hrs

#	D ₁ (μm)	D ₂ (μm)	HV ₁ (kg/mm ²)	HV ₂ (kg/mm ²)	Avg. HV(kg/mm ²)
1	94	97	1552	1458	1503
2	96	94	1488	1552	1520
3	97	92	1458	1621	1540
4	95	96	1520	1488	1504
5	93	96	1586	1488	1537
6	97	101	1458	1345	1402
Avg. HV(kg/mm²)					1501
Avg. HV(GPa)					14.71
St. Dev (GPa)					0.5

Monomodal SiC – 1950°C – 4 hrs

#	D ₁ (μm)	D ₂ (μm)	HV ₁ (kg/mm ²)	HV ₂ (kg/mm ²)	Avg. HV(kg/mm ²)
1	93	98	1586	1428	1507
2	96	95	1488	1520	1504
3	97	95	1458	1520	1489
4	93	96	1586	1488	1537
5	96	97	1488	1458	1473
6	94	99	0	1400	1476
Avg. HV(kg/mm²)					1498
Avg. HV(GPa)					14.68
St. Dev (GPa)					0.23

Monomodal SiC – 2000°C – 2 hrs

#	D ₁ (μ m)	D ₂ (μ m)	HV ₁ (kg/mm ²)	HV ₂ (kg/mm ²)	Avg. HV(kg/mm ²)
1	140	103	700	1293	997
2	131	117	799	1002	900
3	137	112	731	1093	912
4	123	121	907	937	922
5	131	116	799	1019	909
6	129	122	824	922	873
Avg. HV(kg/mm²)					919
Avg. HV(GPa)					9.0
St. Dev (GPa)					0.41

Bimodal SiC – 1800°C – 2 hrs

#	D ₁ (μ m)	D ₂ (μ m)	HV ₁ (kg/mm ²)	HV ₂ (kg/mm ²)	Avg. HV(kg/mm ²)
1	191	189	376	384	380
2	193	179	368	428	398
3	188	195	388	361	374
4	190	191	380	376	378
5	186	192	396	372	384
6	181	189	419	384	402
Avg. HV(kg/mm²)					386
Avg. HV(GPa)					3.78
St. Dev (GPa)					0.11

Bimodal SiC – 1800°C – 4 hrs

#	D ₁ (μ m)	D ₂ (μ m)	HV ₁ (kg/mm ²)	HV ₂ (kg/mm ²)	Avg. HV(kg/mm ²)
1	182	189	414	384	399
2	177	185	438	401	420
3	186	183	396	410	408
4	173	182	458	414	436
5	189	183	384	410	397
6	175	171	448	469	459
Avg. HV(kg/mm²)					420
Avg. HV(GPa)					4.11
St. Dev (GPa)					0.24

Bimodal SiC – 1850°C – 2 hrs

#	D ₁ (μm)	D ₂ (μm)	HV ₁ (kg/mm ²)	HV ₂ (kg/mm ²)	Avg. HV(kg/mm ²)
1	163	151	516	602	559
2	153	155	586	571	579
3	149	154	618	578	598
4	158	161	549	529	539
5	146	162	643	523	583
6	157	169	556	480	518
Avg. HV(kg/mm²)					563
Avg. HV(GPa)					5.51
St. Dev (GPa)					0.29

Bimodal SiC – 1850°C – 4 hrs

#	D ₁ (μm)	D ₂ (μm)	HV ₁ (kg/mm ²)	HV ₂ (kg/mm ²)	Avg. HV(kg/mm ²)
1	145	160	652	536	594
2	161	151	529	602	566
3	152	156	594	564	579
4	153	149	586	618	602
5	151	157	602	556	579
6	149	163	618	516	557
Avg. HV(kg/mm²)					580
Avg. HV(GPa)					5.68
St. Dev (GPa)					0.16

Bimodal SiC – 1900°C – 2 hrs

#	D ₁ (μm)	D ₂ (μm)	HV ₁ (kg/mm ²)	HV ₂ (kg/mm ²)	Avg. HV(kg/mm ²)
1	114	125	1055	878	967
2	109	128	1155	837	996
3	110	123	1134	907	1021
4	125	121	878	937	908
5	119	134	969	764	867
6	123	119	1074	969	1022
Avg. HV(kg/mm²)					964
Avg. HV(GPa)					9.44
St. Dev (GPa)					0.62

Bimodal SiC – 1900°C – 4 hrs

#	D ₁ (μm)	D ₂ (μm)	HV ₁ (kg/mm ²)	HV ₂ (kg/mm ²)	Avg. HV(kg/mm ²)
1	104	95	1268	1520	1394
2	109	104	1155	1268	1211
3	100	102	1372	1318	1345
4	105	99	1244	1400	1322
5	101	104	1345	1268	1307
6	103	107	1293	1198	1246
Avg. HV(kg/mm²)					1304
Avg. HV(GPa)					12.78
St. Dev (GPa)					0.65

Bimodal SiC – 1950°C – 2 hrs

#	D ₁ (μm)	D ₂ (μm)	HV ₁ (kg/mm ²)	HV ₂ (kg/mm ²)	Avg. HV(kg/mm ²)
1	94	92	1552	1621	1587
2	95	99	1520	1400	1460
3	87	92	1812	1621	1717
4	93	96	1586	1488	1537
5	91	97	1656	1458	1557
6	96	102	1488	1318	1403
Avg. HV(kg/mm²)					1544
Avg. HV(GPa)					15.13
St. Dev (GPa)					1.06

Bimodal SiC – 1950°C – 4 hrs

#	D ₁ (μm)	D ₂ (μm)	HV ₁ (kg/mm ²)	HV ₂ (kg/mm ²)	Avg. HV(kg/mm ²)
1	92	97	1621	1458	1540
2	106	99	1221	1400	1311
3	98	101	1428	1345	1387
4	93	95	1586	1520	1553
5	101	102	1345	1318	1331
6	104	99	1268	1400	1334
Avg. HV(kg/mm²)					1409
Avg. HV(GPa)					13.81
St. Dev (GPa)					1.07

Bimodal SiC – 2000°C – 2 hrs

#	D ₁ (μm)	D ₂ (μm)	HV ₁ (kg/mm ²)	HV ₂ (kg/mm ²)	Avg. HV(kg/mm ²)
1	122	102	1093	1318	1206
2	115	107	1037	1198	1118
3	107	114	1198	1055	1127
4	113	111	1074	1113	1094
5	111	116	1113	1019	1066
6	119	112	969	1093	1031
Avg. HV(kg/mm²)					1107
Avg. HV(GPa)					10.85
St. Dev (GPa)					0.59

Bimodal SiC – 2000°C – 4 hrs

#	D ₁ (μm)	D ₂ (μm)	HV ₁ (kg/mm ²)	HV ₂ (kg/mm ²)	Avg. HV(kg/mm ²)
1	121	103	937	1293	1115
2	113	129	1074	824	949
3	108	115	1176	1037	1106
4	113	107	1074	1198	1136
5	115	106	1037	1221	1129
6	119	102	969	1318	1144
Avg. HV(kg/mm²)					1097
Avg. HV(GPa)					10.75
St. Dev (GPa)					0.72

Bimodal AlN – 1650°C – 4 hrs

#	D ₁ (μm)	D ₂ (μm)	HV ₁ (kg/mm ²)	HV ₂ (kg/mm ²)	Avg. HV(kg/mm ²)
1	129	113	824	1074	949
2	121	105	937	1244	1090
3	109	122	1155	922	1039
4	133	112	775	1093	934
5	101	117	1345	1002	1174
6	119	114	969	1055	1012
Avg. HV(kg/mm²)					1033
Avg. HV(GPa)					10.12
St. Dev (GPa)					0.88

Bimodal AlN – 1700°C – 4 hrs

#	D ₁ (μm)	D ₂ (μm)	HV ₁ (kg/mm ²)	HV ₂ (kg/mm ²)	Avg. HV(kg/mm ²)
1	104	106	634	610	622
2	129	118	412	493	453
3	120	114	476	528	502
4	105	131	622	400	511
5	119	117	484	501	493
6	113	119	537	484	511
Avg. HV(kg/mm²)					515
Avg. HV(GPa)					5.05
St. Dev (GPa)					0.55

Bimodal AlN – 1800°C – 4 hrs

#	D ₁ (μm)	D ₂ (μm)	HV ₁ (kg/mm ²)	HV ₂ (kg/mm ²)	Avg. HV(kg/mm ²)
1	122	102	461	659	560
2	126	109	432	577	504
3	107	122	599	461	530
4	113	116	537	510	524
5	131	106	400	610	505
6	120	112	476	547	512
Avg. HV(kg/mm²)					523
Avg. HV(GPa)					5.12
St. Dev (GPa)					0.21

Bimodal AlN – 1900°C – 4 hrs

#	D ₁ (μm)	D ₂ (μm)	HV ₁ (kg/mm ²)	HV ₂ (kg/mm ²)	Avg. HV(kg/mm ²)
1	116	134	510	382	446
2	110	138	567	360	463
3	120	129	476	412	444
4	128	123	419	453	436
5	121	133	468	388	428
6	126	125	432	439	436
Avg. HV(kg/mm²)					442
Avg. HV(GPa)					4.33
St. Dev (GPa)					0.12

Appendix H

Indentation Toughness of Sintered SiC and AlN Samples

Using a Leco microhardness tester, a load of 1000 was applied on the sample surface, polished down to 1 μm , for 15 s. Figure H-1 shows a typical indentation obtained along with the cracks propagating at the from the ends of the indentation. The measurements were then made of the average length of the diagonals, $2a$, and the average length of the cracks along with the diagonal on the indentation 2ℓ . The crack length, c , was calculated as $c = \ell - a$. Ten such measurements were taken for each sample.

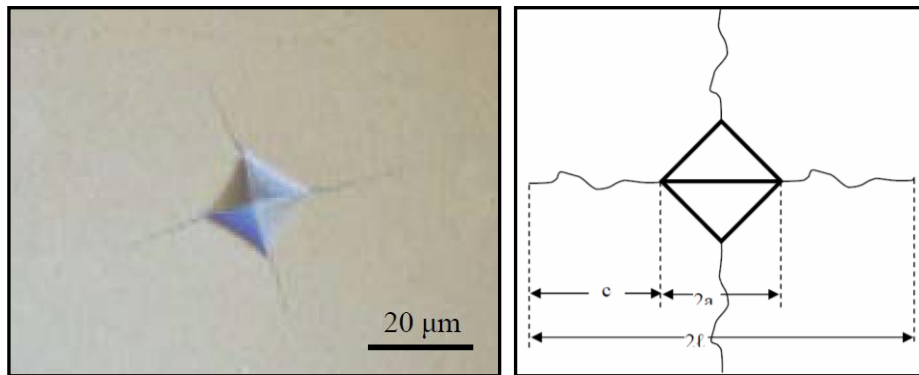


Figure H-1: Typical indentation obtained during an indentation toughness experiment. The cracks originate at the ends of the indentation.

The equation used for calculating fracture toughness (K_{IC}) was,

$$K_{IC} = \frac{0.02 * a * E^{0.4} * H^{0.6}}{\sqrt{c}}$$

Where, c = length of crack, a = average length of diagonals of the indent, E = Modulus of elasticity and H = Vickers Hardness.

Monomodal SiC – 1850°C – 2 hrs

#	2a(μm)	2l(μm)	c(μm)	K_{IC} ($\text{MPa}\cdot\text{m}^{0.5}$)
1	207	380	86.5	1.45
2	210	381	85.5	1.52
3	205	383	89	1.46
4	209	377	84	1.53
Avg. K_{IC} ($\text{MPa}\cdot\text{m}^{0.5}$)				1.49
St. Dev				0.04

Monomodal SiC – 1850°C – 4 hrs

#	2a(μm)	2l(μm)	c(μm)	K_{IC} ($\text{MPa}\cdot\text{m}^{0.5}$)
1	206	363	78.5	1.55
2	204	360	78	1.58
3	204	361	78.5	1.57
4	206	359	76.5	1.61
Avg. K_{IC} ($\text{MPa}\cdot\text{m}^{0.5}$)				1.58
St. Dev				0.03

Monomodal SiC – 1900°C – 2 hrs

#	2a(μm)	2l(μm)	c(μm)	K_{IC} ($\text{MPa}\cdot\text{m}^{0.5}$)
1	109	191	41	2.40
2	109	188	39.5	2.51
3	108	195	43.5	2.37
4	112	188	38	2.63
Avg. K_{IC} ($\text{MPa}\cdot\text{m}^{0.5}$)				2.47
St. Dev				0.12

Monomodal SiC – 1900°C – 4 hrs

#	2a(μm)	2l(μm)	c(μm)	K_{IC} ($\text{MPa}\cdot\text{m}^{0.5}$)
1	109	179	35	2.65
2	106	178	36	2.60
3	108	181	36.5	2.63
4	108	184	38	2.58
Avg. K_{IC} ($\text{MPa}\cdot\text{m}^{0.5}$)				2.62
St. Dev				0.03

Monomodal SiC – 1950°C – 2 hrs

#	2a(μm)	2l(μm)	c(μm)	K_{IC} ($\text{MPa}\cdot\text{m}^{0.5}$)
1	96	131	17.5	3.81
2	95	138	21.5	3.49
3	96	147	25.5	3.23
4	95	153	29	3.00
Avg. K_{IC} ($\text{MPa}\cdot\text{m}^{0.5}$)				3.38
St. Dev				0.34

Monomodal SiC – 1950°C – 4 hrs

#	2a(μm)	2l(μm)	c(μm)	K_{IC} ($\text{MPa}\cdot\text{m}^{0.5}$)
1	96	142	23	3.32
2	96	146	25	3.26
3	97	148	25.5	3.26
4	97	152	27.5	3.14
Avg. K_{IC} ($\text{MPa}\cdot\text{m}^{0.5}$)				3.25
St. Dev				0.07

Monomodal SiC – 2000°C – 2 hrs

#	2a(μm)	2l(μm)	c(μm)	K_{IC} ($\text{MPa}\cdot\text{m}^{0.5}$)
1	122	217	47.5	2.45
2	124	221	48.5	2.52
3	122	218	48	2.50
4	124	217	46.5	2.58
Avg. K_{IC} ($\text{MPa}\cdot\text{m}^{0.5}$)				2.51
St. Dev				0.06

Bimodal SiC – 1800°C – 2 hrs

#	2a(μm)	2l(μm)	c(μm)	K_{IC} (MPa.m ^{0.5})
1	192	329	68.5	1.70
2	191	337	73	1.68
3	189	323	67	1.74
4	185	322	68.5	1.68
Avg. K_{IC} (MPa.m^{0.5})				1.7
St. Dev				0.03

Bimodal SiC – 1800°C – 4 hrs

#	2a(μm)	2l(μm)	c(μm)	K_{IC} (MPa.m ^{0.5})
1	185	391	103	1.41
2	191	403	106	1.47
3	186	407	110.5	1.40
4	173	374	100.5	1.37
Avg. K_{IC} (MPa.m^{0.5})				1.41
St. Dev				0.04

Bimodal SiC – 1850°C – 2 hrs

#	2a(μm)	2l(μm)	c(μm)	K_{IC} (MPa.m ^{0.5})
1	152	262	55	1.89
2	160	291	65.5	1.87
3	157	283	63	1.87
4	163	297	67	1.88
Avg. K_{IC} (MPa.m^{0.5})				1.88
St. Dev				0.01

Bimodal SiC – 1850°C – 4 hrs

#	2a(μm)	2l(μm)	c(μm)	K_{IC} (MPa.m ^{0.5})
1	154	263	54.5	1.96
2	151	260	54.5	1.97
3	154	271	58.5	1.94
4	156	271	57.5	1.98
Avg. K_{IC} (MPa.m^{0.5})				1.96
St. Dev				0.02

Bimodal SiC – 1900°C – 2 hrs

#	2a(μm)	2l(μm)	c(μm)	K_{IC} (MPa.m ^{0.5})
1	117	173	28	2.81
2	123	187	32	2.84
3	127	197	35	2.80
4	121	186	32.5	2.77
Avg. K_{IC} (MPa.m^{0.5})				2.8
St. Dev				0.03

Bimodal SiC – 1900°C – 4 hrs

#	2a(μm)	2l(μm)	c(μm)	K_{IC} ($\text{MPa}\cdot\text{m}^{0.5}$)
1	101	155	27	2.96
2	102	157	27.5	3.04
3	103	158	27.5	3.07
4	105	157	26	3.22
Avg. K_{IC} ($\text{MPa}\cdot\text{m}^{0.5}$)				3.07
St. Dev				0.11

Bimodal SiC – 1950°C – 2 hrs

#	2a(μm)	2l(μm)	c(μm)	K_{IC} ($\text{MPa}\cdot\text{m}^{0.5}$)
1	90	137	23.5	3.13
2	95	149	27	3.16
3	94	149	27.5	3.10
4	99	152	26.5	3.33
Avg. K_{IC} ($\text{MPa}\cdot\text{m}^{0.5}$)				3.18
St. Dev				0.1

Bimodal SiC – 1950°C – 4 hrs

#	2a(μm)	2l(μm)	c(μm)	K_{IC} ($\text{MPa}\cdot\text{m}^{0.5}$)
1	100	148	24	3.26
2	94	151	28.5	2.88
3	102	150	24	3.41
4	102	161	29.5	3.08
Avg. K_{IC} ($\text{MPa}\cdot\text{m}^{0.5}$)				3.16
St. Dev				0.23

Bimodal SiC – 2000°C – 2 hrs

#	2a(μm)	2l(μm)	c(μm)	K_{IC} ($\text{MPa}\cdot\text{m}^{0.5}$)
1	111	191	40	2.42
2	112	197	42.5	2.44
3	114	201	43.5	2.45
4	116	206	45	2.45
Avg. K_{IC} ($\text{MPa}\cdot\text{m}^{0.5}$)				2.44
St. Dev				0.01

Bimodal SiC – 2000°C – 4 hrs

#	2a(μm)	2l(μm)	c(μm)	K_{IC} ($\text{MPa}\cdot\text{m}^{0.5}$)
1	112	190	39	2.46
2	110	198	44	2.34
3	111	200	44.5	2.35
4	116	204	44	2.47
Avg. K_{IC} ($\text{MPa}\cdot\text{m}^{0.5}$)				2.4
St. Dev				0.07

Bimodal AlN – 1650°C – 4 hrs

#	2a(μm)	2l(μm)	c(μm)	K_{IC} ($\text{MPa}\cdot\text{m}^{0.5}$)
1	86	135	24.5	2.36
2	88	141	26.5	2.32
3	84	133	24.5	2.31
4	86	137	25.5	2.32
Avg. K_{IC} ($\text{MPa}\cdot\text{m}^{0.5}$)				2.33
St. Dev				0.02

Bimodal AlN – 1700°C – 4 hrs

#	2a(μm)	2l(μm)	c(μm)	K_{IC} ($\text{MPa}\cdot\text{m}^{0.5}$)
1	153	261	54	1.87
2	130	217	43.5	1.77
3	142	238	48	1.84
4	141	236	47.5	1.83
Avg. K_{IC} ($\text{MPa}\cdot\text{m}^{0.5}$)				1.83
St. Dev				0.04

Bimodal AlN – 1800°C – 4 hrs

#	2a(μm)	2l(μm)	c(μm)	K_{IC} ($\text{MPa}\cdot\text{m}^{0.5}$)
1	124	201	38.5	1.81
2	114	189	37.5	1.68
3	120	195	37.5	1.77
4	116	192	38	1.70
Avg. K_{IC} ($\text{MPa}\cdot\text{m}^{0.5}$)				1.74
St. Dev				0.06

Bimodal AlN – 1900°C – 4 hrs

#	2a(μm)	2l(μm)	c(μm)	K_{IC} ($\text{MPa}\cdot\text{m}^{0.5}$)
1	115	206	45.5	1.39
2	110	185	37.5	1.47
3	116	197	40.5	1.49
4	114	196	41	1.46
Avg. K_{IC} ($\text{MPa}\cdot\text{m}^{0.5}$)				1.45
St. Dev				0.04

Appendix I

Thermal Conductivity of Sintered SiC and AlN Samples

The thermal conductivity (K) of a given material is a product its thermal diffusivity, density and specific heat. The thermal diffusivity is measured via laser flash apparatus (Netzsch LFA 457) where a polished 0.5” diameter sintered sample is subjected to a very short burst of radiant energy. The source of the radiant energy is usually a laser flash lamp and irradiation times are of one millisecond or less. The resulting temperature rise on the rear surface of the sample is measured and thermal diffusivity values are computed from the temperature rise versus time data.

Monomodal μ -n SiC samples- 2 hrs hold

Sintering Temperature (°C)	Density (g/cc)	Thermal Diffusivity (mm ² /s)		C _p (J/g.K)	K (W/m.K)		
		Run 1	Run 2		Run 1	Run 2	Average
1850	2.74	18.74	17.00	0.61	30.81	27.94	29.38
1900	2.96	28.45	27.50	0.6	50.52	48.85	49.68
1950	3.09	29.81	30.96	0.6	55.19	57.31	56.25
2000	3.06	24.93	24.97	0.61	45.84	45.90	45.87

Monomodal μ -n SiC samples- 4 hrs hold

Sintering Temperature (°C)	Density (g/cc)	Thermal Diffusivity (mm ² /s)		C _p (J/g.K)	K (W/m.K)		
		Run 1	Run 2		Run 1	Run 2	Average
1850	2.76	19.66	22.14	0.6	32.55	36.67	34.61
1900	2.97	28.15	28.34	0.6	50.16	50.50	50.33
1950	3.11	37.38	37.71	0.59	69.63	70.25	69.94

Bimodal μ -n SiC samples- 2 hrs hold

Sintering Temperature (°C)	Density (g/cc)	Thermal Diffusivity (mm ² /s)		C _p (J/g.K)	K (W/m.K)		
		Run 1	Run 2		Run 1	Run 2	Average
1800	2.74	13.93	13.70	0.59	22.90	22.51	22.71
1850	2.82	17.83	16.81	0.6	30.17	28.44	29.31
1900	2.89	25.10	25.14	0.6	43.52	43.60	43.56
1950	3.09	37.89	32.73	0.58	70.24	60.69	65.46
2000	3.06	19.65	19.89	0.59	36.07	36.52	36.30

Bimodal μ -n SiC samples- 4 hrs hold

Sintering Temperature (°C)	Density (g/cc)	Thermal Diffusivity (mm ² /s)		C _p (J/g.K)	K (W/m.K)		
		Run 1	Run 2		Run 1	Run 2	Average
1800	2.76	15.27	15.23	0.58	25.28	25.22	25.25
1850	2.83	18.82	18.24	0.6	31.95	30.96	31.46
1900	3.02	28.49	28.62	0.61	51.62	51.86	51.74
1950	3.11	38.47	38.33	0.59	71.78	71.52	71.65
2000	3.07	17.74	18.26	0.6	32.67	33.63	33.15

Bimodal μ -n AlN samples – 4 hrs hold

Sintering Temperature (°C)	Density (g/cc)	Thermal Diffusivity (mm ² /s)		C _p (J/g.K)	K (W/m.K)		
		Run 1	Run 2		Run 1	Run 2	Average
1650	3.23	30.73	30.81	0.73	72.46	72.65	72.55
1700	3.12	33.13	33.17	0.62	64.09	64.16	64.13
1800	3.13	29.97	30	0.56	52.51	52.58	52.55
1900	3.07	32.42	32.54	0.59	58.72	58.94	58.83